

**A Precision Measurement of the Transverse
Asymmetry $A_{T'}$ from Quasi-elastic ${}^3\text{He}(\vec{e}, e')$
process, and the Neutron Magnetic Form Factor
 G_m^n at low Q^2**

by

Wang Xu

B.S. Tsinghua University, P.R.China

1994

Submitted to the Department of Physics
in partial fulfillment of the requirements for the degree of

Doctor of Philosophy

at the

MASSACHUSETTS INSTITUTE OF TECHNOLOGY

June 2002

© Massachusetts Institute of Technology 2002. All rights reserved.

Author

Department of Physics

April 26, 2002

Certified by

Haiyan Gao

Associate Professor

Thesis Supervisor

Accepted by

Thomas J. Greytak

Chairman of Graduate Committee

**A Precision Measurement of the Transverse Asymmetry $A_{T'}$
from Quasi-elastic ${}^3\text{He}(\vec{e}, e')$ process, and the Neutron
Magnetic Form Factor G_M^n at low Q^2**

by

Wang Xu

Submitted to the Department of Physics
on April 26, 2002, in partial fulfillment of the
requirements for the degree of
Doctor of Philosophy

Abstract

Electromagnetic form factors are fundamental quantities in describing the underlying electromagnetic structure of nucleons. While proton electromagnetic form factors have been determined with good precision, neutron form factors are known poorly, largely due to the lack of free neutron targets. Jefferson Lab Hall A experiment E95-001, “a precise measurement of the transverse asymmetry $A_{T'}$ from the quasi-elastic ${}^3\text{He}(\vec{e}, e')$ process”, was therefore designed to determine precisely the neutron magnetic form factor, G_M^n at low momentum transfer values and was successfully completed in Spring 1999. High precision $A_{T'}$ data in the quasi-elastic region at Q^2 values of 0.1 to 0.6 (GeV/c)² were obtained using a high-pressure spin-exchange optically-pumped polarized ${}^3\text{He}$ gas target with an average polarization of 30%, a longitudinally polarized e^- beam, and two High Resolution Spectrometers: HRSe and HRSh. HRSe was employed to detect scattered electrons from the quasi-elastic kinematic region, and HRSh was employed as a elastic polarimetry to monitor the product of the beam and target polarizations.

The extraction of form factors is usually model-dependent. Significant constraints on theoretical calculations are provided by additional high precision quasi-elastic asymmetry data at Q^2 values of 0.1 and 0.2 (GeV/c)² in ${}^3\text{He}$ breakup region, where effects of final state interactions(FSI) and meson exchange currents (MEC) are expected to be large [71]. G_M^n is extracted from a non-relativistic Faddeev calculation which includes both FSI and MEC at Q^2 values of 0.1 and 0.2 (GeV/c)². The uncertainties of G_M^n at these Q^2 values are comparable to those of recent experiments with deuterium targets [58]. At the higher Q^2 values from this experiment, G_M^n is extracted from Plane-Wave Impulsive Approximation (PWIA) calculations with a relatively large theoretical uncertainty of 2-4%. Thus a reliable extraction of G_M^n from

$A_{T'}$ at higher Q^2 values (especially at Q^2 values of 0.3 and 0.4 $(GeV/c)^2$) requires improved theoretical calculations including FSI, MEC, and relativistic effects. However, those G_M^n results extracted from PWIA at higher Q^2 values from this experiment still show overall a good agreement with the most recent deuterium measurements.

The analysis of asymmetries and the extraction of G_M^n from both the Faddeev calculations and the PWIA calculations are reported in this thesis.

Thesis Supervisor: Haiyan Gao

Title: Associate Professor

Acknowledgments

An experiment and document of this magnitude can only be completed with the help of many people. I would like to gratefully acknowledge everyone who helped me along the way in both technical and emotional needs. However, I will undoubtedly forget to mention someone since so many people have supported me on this journey. The fact that some are not listed here does not mean that they are any less important than those mentioned specifically.

I would like to thank my supervisor, Prof. Haiyan Gao, for her support and patience. Haiyan possesses uncanny physical insight and ambition which is why her research is so productive. Our weekly meetings were inspiring, and I would always find some new physical insight. She guided me through the experiment and edited my thesis with great care and patience. A few people in our group have been especially helpful to me. I would like to thank Tim Black (post doc), Dipangkar Dutta (post doc), and Feng Xiong for technical support during the experiment and during data analysis. I would also like to thank Chris Crawford, Hong Xiang, Ben Clasio, Jason Seely, Lingyan Zhu, and Bin Ma for cheering me on and sharing my burden. In addition, Bill Donnelly provided invaluable theoretical insight during our long discussions in his office. I would also like to thank Dave Woodruff and Stu Galley for being so helpful in solving the computer problems.

I enjoyed working with many people at JLab, both before and during the experiment. J.P. Chen (Jlab staff) was a great source of stability and sanity during E94010, which was the experiment that ran just before E95001. J.P., Robert Michaels (Jlab staff), Ronald Gilman (Jlab staff), Ole Hansen (Jlab staff), Mei Liang (post doc), Xiaodong Jian (post doc), Liyanage Nilianga (post doc), David Prout (post doc) and Mark Jones (post doc) taught me how to setup the experiment and do the data analysis. They were a source of encouragement for myself and many others. As the thesis students, Steffen Jensen, Karl Slifer, Pibero Djawotho, Ioannis Kominis, Alexandre Deur, and I all suffered together during E94010 and E95001. We worked late and ate

junk food together. The time I spent with them at JLab was precious to me.

There are many brothers and sisters to whom I am greatly indebted because of Jesus Christ. Pastor Zhao and his wife gave me rides from my apartment to Jlab in the mornings and prepared a lunch boxes every day for two months during E95001 experiment. Shuqian drove me from Jlab to my apartment in the evening even though he lived at the College of William and Mary. Hecchin JDSN, and brothers sent me a car all the way from Boston to Newport News, VA; and Joe, Darren, and other brothers drove this car back for me. Yang's couple and Dinghua&WuYan provided a room for me to live while I was at Jlab. Pastor Paul& Becky JDSN, Pastor Sam and Byungho Hyung encouraged me to continue to move on when I was discouraged. Also many members of family of God have prayed for me and my research during this five-year journey.

Finally, I want to thank my family and my wife for their endless love and support. I would not be where I am at today without my parents; and my wife made many sacrifices during the writing of this thesis.

I would like to dedicate my thesis to those who love me so much and especially my Lord and Savior Jesus Christ.

Wang Xu

Cambridge, MA

May 7,2002

Contents

1	Physics Motivation	1
1.1	Introduction	1
1.2	Nucleon Form Factor Calculation	4
1.3	Existing Data	9
1.4	The Spin-Dependent Quasi-elastic ${}^3\vec{H}e(\vec{e}, e')$ Process	12
1.4.1	Spin-dependent Inclusive Electron Scattering	13
1.4.2	Plane-Wave Impulse Approximation (PWIA)	20
1.4.3	Non-relativistic Faddeev Calculation	25
1.5	Extraction of Nucleon Form Factor From Quasi-elastic ${}^3\vec{H}e(\vec{e}, e')$ Process	32
2	Experimental Apparatus	33
2.1	Overview	33
2.2	Polarized Electron Source	38
2.3	Beamline	39
2.3.1	The Møller Polarimeter	39
2.3.2	Beam Energy	42
2.3.3	Beam Current Monitors	45
2.3.4	Beam Position Monitor	47
2.3.5	Beam Fast Raster	48
2.4	Polarized ${}^3\text{He}$ Target	49
2.4.1	Introduction	49

2.4.2	Target Setup	52
2.5	High Resolution Spectrometers (HRS)	59
2.6	Detector Package	60
2.6.1	Vertical Drift Chamber	63
2.6.2	Scintillator	65
2.6.3	Gas Čerenkov	66
2.6.4	Shower Detector	67
2.7	Hall A Data Acquisition Aystem	68
2.7.1	Trigger Electronics	68
2.7.2	Data Acquisition	71
3	Data Analysis	75
3.1	Overview	75
3.2	The Data Analyzer	79
3.3	Quasi-Elastic Raw Asymmetry	80
3.4	Elastic Polarimetry	83
3.4.1	MCEEP	84
3.4.2	Acceptance	86
3.4.3	Energy Loss	88
3.4.4	Multiple Scattering	91
3.4.5	Bremsstrahlung	92
3.4.6	Results of $P_b P_t$	98
3.5	Dilution Factor	107
3.6	Quasi-elastic Radiative Correction and Elastic Tail Correction	113
4	False Asymmetry and Systematic Uncertainty	121
4.1	Correctable Helicity-dependent Variables	122
4.1.1	Data Acquisition Deadtime	122
4.2	Helicity-independent Variables	126
4.2.1	N_2 Asymmetry and Empty Target Cell Asymmetry	126

4.2.2	Trigger Efficiency	129
4.2.3	VDC Efficiency	137
4.3	Negligible Helicity-dependent Variables	141
4.3.1	Beam Position Shift	141
4.3.2	Beam Helicity Determination	144
4.3.3	Beam Current	147
4.3.4	Pion Contamination	151
5	Results	153
5.1	Introduction	153
5.2	Elastic Asymmetry	153
5.3	Quasi-elastic Transverse Asymmetry $A_{T'}$	154
5.4	Extraction of the Neutron Magnetic Form Factor	160
5.5	Discussion	186
6	Conclusion	191

List of Figures

1-1	Jefferson Lab precise data on proton form factor ratio $\mu_p G_e^p / G_m^p$. Data is shown in figure (solid circle: Jones <i>et al.</i> [1], and solid square: Gayou <i>et al.</i> [2]), along with various model calculations (SU(6) +CQ ff (dot): Cardarelli and Simula [20], RCQM (thick dot-dash): Schlumpf [17], GKex(02L) (dash): Lomon [13], Soliton (dot-dash): Holzwarth [24], Diquark (thick dot): Ma [21], and CBM (solid): Lu [27]).	8
1-2	The word G_m^n data since 1990. The figure shows the results of the Bonn [55](\square), the MIT-Bates [39] [40](\circ, \diamond), the NIKHEF/PSI [56](\star), and the Mainz/PSI [57](\triangle), in comparison to various model calculations. Solid: Lu <i>et al.</i> [25], dot: Meissner <i>et al.</i> [9], dash: Mergell <i>et al.</i> [7], long dot-dash: Kubis <i>et al.</i> [12], and short dot-dash: Schlumpf <i>et al.</i> [17]	11
1-3	The Born approximation	14
1-4	Definition of target spin angles with respect to the three-momentum transfer, \vec{q}	18
1-5	Feynman diagram in the Plane Wave Impulse Approximation (PWIA)	20
1-6	FSI contributions in the non-relativistic Faddeev calculation	26
1-7	Typical MEC contributions. a) Graphs for coupling a photon to a pair of correlated nucleons; b) Graphs for π or M (other than π) in flight terms; c) Graphs for the pionic coupled to a Δ or N^* intermediate state.	31
2-1	The accelerator layout	35
2-2	The Hall A Setup	37

2-3	The layers of the strained GaAs cathode and the level diagram of the conduction and valence bands	38
2-4	Møller Polarimeter Layout	40
2-5	Møller results for the beam polarization	42
2-6	The Arc Measurement Layout	43
2-7	eP Measurement Layout	44
2-8	Beam Current Monitor Layout	46
2-9	Beam Position Monitor Layout	48
2-10	The optical pumping mechanism without considering the hyperfine interaction	49
2-11	The E95-001 target system layout	53
2-12	The target cells and the target ladder	55
2-13	The effective field H_e	57
2-14	Side view of the Hall A High Resolution Spectrometer. Shown are scattering chamber and the spectrometer magnetic elements, including the dipole and the three quadrupole magnets (labeled Q1, Q2, Q3). The detectors are inside the shields house at the top of the spectrometer.	60
2-15	High Resolution Spectrometer in electron-arm (HRSE) Setup	62
2-16	High Resolution Spectrometer in hadron-arm (HRSH) Setup	62
2-17	VDC Layout	63
2-18	The scintillator planes (S1&S2) layout	65
2-19	Gas Čerenkov Detector Setup	66
2-20	The configurations of both HRSE and HRSH shower detectors	67
2-21	H-arm trigger Setup	69
2-22	E-arm trigger Setup	70
2-23	Data Acquisition Setup	72
3-1	Experiment E95-001 data analysis flow chart	78
3-2	The Quasi-elastic raw asymmetry, A_{raw} for four different configurations at $Q^2 = 0.6$ ((GeV/c) ²) plotted as an example.	82

3-3	Block diagram of the main routines called by MCEEP. Subroutines are to the right of the double arrow and are called in order reading down the page. Indented subroutines are within the main Monte-Carlo event loop. For clarify, only the main routines are shown	85
3-4	The experiment acceptance is plotted as a function of ϕ_{target} vs θ_{target} with 10mm y_{target} long scanning from $y_{target} = -60\text{mm}$ to $y_{target} = 60\text{mm}$. . .	87
3-5	The simulation acceptance is plotted as a function of ϕ_{target} vs θ_{target} with 10mm y_{target} long scanning from $y_{target} = -60\text{mm}$ to $y_{target} = 60\text{mm}$. . .	88
3-6	The distribution of the simulated elastic electron events versus e_{loss} which is denoted as the energy loss (ΔE) at $Q^2 = 0.1$ when the electron passes through the side wall of the target glass cell.	91
3-7	The internal bremsstrahlung	94
3-8	The material, which particle goes through, layout	99
3-9	The spectrometer central momentum setting P_0 and the incident energy E_e from three independent means: ep elastic(eP), 3He elastic(sim), and the optic database(optic)	101
3-10	The comparisons between data and simulation for $Q^2 = 0.1$ and 0.2 . The two-body breakup energy is about 5.5 MeV.	102
3-11	The target polarization, P_t from the NMR measurement in the upper panel, and P_t from the Møller measurement & elastic polarimetry in the lower panel.	107
3-12	Excitation energy, E_x for N_2 reference and 3He target. The most left peak is related to the ground state of N_2 and others are related to excitation states of N_2	108
3-13	The dilution factors of the empty target cell for 1 Pass kinematic in H-arm	110

3-14	The comparison among the extracted quasi-elastic cross-sections. The extracted cross-section from the simulation without radiative correction is referred to as “Born”, the extracted cross-section from the simulation with radiative correction is referred “Rad”, the cross-section from the calculation is referred to as “Cal”, and the extracted cross-section from data is referred to as “Data”. The number on the graph is the ratio of “Rad” and “Data”, and “Data” is scaled with this ratio in the graph.	118
4-1	The DAQ livetime vs. rate with respect to helicities. The hollow triangle is the DAQ livetime for helicity + and the solid square is the DAQ livetime for helicity -.	124
4-2	The comparison between the livetime and the calculated live time. The different shapes of the data points represent six different Q^2 data sets. . .	125
4-3	The definitions of the scintillator efficiencies	130
4-4	The scintillator efficiencies ($\epsilon_1 \times \epsilon_2$) vs. run number with different paddle configuration. The reason for the low determined efficiencies on the paddler 1-1 and the paddler 6-6 is because of cosmic ray contamination.	133
4-5	The difference of the scintillator efficiencies regarding the beam helicity vs. run number for the different paddle configurations.	135
4-6	Overall study of the correlation between the helicity and the scintillator efficiencies	136
4-7	The collecting process of vdc signal	137
4-8	VDC wire efficiencies & difference of efficiencies at V1 planes in H-arm (as an example)	139
4-9	The difference of vdc wire efficiencies vs. vdc planes	140
4-10	Beam spot at target position	141
4-11	The empty reference cell yields with different beam positions and their beam positions vary within a few mm	142
4-12	The variation of beam spot with helicities	143
4-13	The variation of beam spot with helicities	144

4-14	The combinations of two input high voltages of the Pockel's cell and their copy	146
4-15	The beam current summary	147
4-16	The current asymmetry form two independent instruments. Upper Graph is the result from the independent DAQ for Happex experiment (which we used during our experiment to check the current asymmetry); Lower one is the results from upstream BCM and downstream BCM	150
4-17	The particle id information on e^-/π^- using shower vs. preshower	151
5-1	The $A_{T'}$ results vs. the energy transfer, ω . The error bar is the statistical uncertainty and the error band is the systematic uncertainty.	156
5-2	The fitting process for P_0 and P_1	161
5-3	The extraction of G_m^n as a function of energy transfer ω . In the upper panel, the long-dashed line is the results from Eq. 5.5 and the dotted line is the results from Eq. 5.7. The difference between these two is plotted in the lower panel.	162
5-4	FSI effect study. The long dashed line is a relativistic pwia calculation (to distinguish non-relativistic pwia which we generate, the general pwia calculation is called relativistic pwia calculation), the dotted line is a non-relativistic Faddeev calculation with FSI effects, and the dot-dashed the non-relativistic Faddeev calculation with FSI effects corrected by relativistic effects. Comparing the long dashed line and dot-dashed line, one can find contributions due to FSI effects in $A_{T'}$	174
5-5	MEC effect study. Comparing the full calculation and the calculation with FSI effects, one can find contributions due to MEC effects in $A_{T'}$	175
5-6	MEC and FSI effects on $A_{T'}$ for ${}^3\vec{H}e(\vec{e}, e')$. The upper graph is FSI effects and the lower one is MEC effects. For MEC effects, the solid triangle is from $\frac{A_{T'}^{full} - A_{T'}^{fsi}}{A_{T'}^{full}}({}^3\vec{H}e(\vec{e}, e'))(\%)$ (0.1 - 0.4 (GeV/c) ²) and the solid square is from $\frac{(A_{T'}^{full} - A_{T'}^{fsi})(\vec{d}(\vec{e}, e'))}{A_{T'}^{full}({}^3\vec{H}e(\vec{e}, e'))}(\%)$ (0.1 - 0.6 (GeV/c) ²).	176

5-7	MEC effect on asymmetry for $\vec{d}(\vec{e}, e')$ process, $\frac{A_{T'}^{full} - A_{T'}^{fsi}}{A_{T'}^{full}}(\vec{d}(\vec{e}, e'))(\%)$ calculated by Arenhövel <i>et al.</i> [50]. The arrow points the quasi-elastic peak position.	177
5-8	Relativistic effect on cross-section. The open square is a relativistic pwia calculation and the solid triangle is a non-relativistic pwia calculation which we developed.	179
5-9	Relativistic effect on $A_{T'}$. The long dashed line is a non-relativistic pwia calculation which we developed, the dot-dashed line is the non-relativistic pwia calculation with relativistic corrections, and the dotted line is a relativistic pwia calculation.	180
5-10	Off-shell effect on $A_{T'}(1)$. The open square is a PWIA calculation using cc1 half-offshell form and the solid triangle is a PWIA calculation using on-shell form which we developed. Here Diff. is the relative difference between two calculations, which is defined as the difference over the average.	183
5-11	Off-shell effect on $A_{T'}(2)$. The open square is a PWIA calculation using cc1 half-offshell form and the solid triangle is a PWIA calculation using on-shell form which we developed. Here Diff. is the relative difference between two calculations, which is defined as the difference over the average.	184
5-12	Off-shell effect on cross-section. The open square is a PWIA calculation using cc1 half-offshell form and the solid triangle is a PWIA calculation using on-shell form which we developed.	185
5-13	The word G_m^n data since 1990. The figure shows the results of the present measurement (● This work), the Bonn [55](□), the MIT-Bates [39] [40](o,◇), the Mainz/PSI [57] [59](△,◆), and the NIKHEF/PSI [56](☆), in comparison to various model calculations. Solid: Lu <i>et al.</i> [25], dot: Lomon [13], long dash: Mergell <i>et al.</i> [7], short dash: Holzwarth [24], long dash-dot: Kubis <i>et al.</i> [12], long dash-dot: Schlumpf <i>et al.</i> [17], and short dot-dash: Bo-Qian Ma [21].	188

List of Tables

2.1	Kinematic setup for electron-arm High Resolution Spectrometer	34
2.2	Kinematic setup for hadron-arm High Resolution Spectrometer	34
2.3	Determination of beam parameters	36
2.4	Beam polarization results from Møller measurements	41
2.5	Relaxation rate of various depolarization mechanism	52
2.6	Wall thickness and window thickness of Cuervo and reference cell	56
2.7	Hall A High Resolution Spectrometer (HRS) general characteristics	61
3.1	Raw asymmetry sign with four configurations	80
3.2	The corresponding target spin direction in the lab, θ_{spin} at the quasi-elastic peak for six different kinematics as the target spin direction with respect to three momentum transfer \vec{q} , θ^* is equal to zero.	81
3.3	The target spin direction configurations for six different kinematics. Here θ^* at the quasi-elastic peak is referred to as $\theta_{\omega_{peak}}^*$ and the ω value at quasi-elastic peak, ω_{peak} is listed in the upper table.	83
3.4	The medium radiation length, X_0	100
3.5	Variation of A_{el}^{sim} for 1 Pass kinematic setting and target spin -62.5° with different cuts	103
3.6	Variation of A_{el}^{sim} for 2 Pass kinematic setting and target spin -62.5° with different cuts	103
3.7	The simulated elastic asymmetry, $ A_{el} $ for different target polarization direction, θ_{spin} and kinematic setting	104

3.8	The elastic dilution factors: f_{N2} and f_{empty} for two elastic data sets	105
3.9	Systematic uncertainty in determining $P_t P_b$ from the elastic asymmetry measurement.	106
3.10	The dilution factors: R^{N2} and R^{empty} for six Q^2 values of quasi-elastic kinematics of the experiment	112
3.11	ΔA_{rad}^{qe} , η and A^{ert} for six Q^2 values. Because η is too small for the last two Q^2 kinematic settings, A^{ert} is not necessary to calculate.	120
4.1	The false asymmetry contributions in E-arm from $N2$ and the empty target cell backgrounds	128
4.2	Helicity configuration	145
4.3	The calibration numbers of Beam Current Monitor(BCM)	148
5.1	$ A_{el}^{exp} $ results for four configurations of beam helicity & target spin at six quasi-elastic kinematic settings. -62.5° and -243.6° are the target spin directions with respect to the incident electron beam direction (convention: standing facing the beam dump, + for left side of beamline and - for right side of beamline). In/out refers to the beam half-wave plate status.	154
5.2	$A_{T'}$ results for different energy transfer, ω	158
5.3	Systematic errors in $A_{T'}$ measurement.	159
5.4	The G_m^n results for different ω bins extracted with full calculation by Golak <i>et al.</i>	165
5.5	The G_m^n results for different ω bins extracted with PWIA calculation by Salmè <i>et al.</i>	167
5.6	The uncertainties in G_m^n for six Q^2 kinematic settings. The lower limit of uncertainty of on FSI and MEC effects of PWIA calculation is the difference between full calculation and PWIA calculation, and the upper limit is equals to the uncertainty of full calculation.	170
5.7	Contribution due to FSI effects in $A_{T'}$	171
5.8	Contribution due to MEC effects in $A_{T'}$	172

5.9 The presented G_m^n results from PWIA calculation by Salmè *et al.* and full calculation by Golak *et al.* are the extracted G_m^n results at quasi-elastic peak. The bold numbers are the published G_m^n values from this experiment [58]. In addition, the extracted G_m^n results at Q^2 values of 0.3 and 0.4 $(GeV/c)^2$ from full calculation and PWIA calculation seem to suggest that FSI and MEC effects may be overestimated in full calculation at Q^2 values of 0.3 and 0.4 $(GeV/c)^2$ 187

Chapter 1

Physics Motivation

1.1 Introduction

Electromagnetic form factors of the nucleon have been a very interesting topic for a few decades, and are parametrized in terms of the Sachs form factors, $G_{m,e}$ or the Dirac and Pauli form factors, $F_{1,2}$. The Dirac and Pauli form factors, $F_{1,2}$ is related to the Sachs form factors, $G_{m,e}$ via equation 1.46. In a particular Lorentz frame, so-called the Breit (or brick wall) frame in which the transfer Q^2 equals the three-momentum transfer q^2 , the form factors, G_e and G_m are closely related to the charge and magnetic moment distribution inside the nucleon. As the value of the four-momentum transfer squared is much lower than the mass square of the pion, G_E and G_m are just the Fourier transform of the nucleon charge and magnetization densities in its rest frame, respectively. Theoretical understanding of the nuclear structure in terms of the fundamental quark and gluon degrees of freedom of Quantum Chromodynamics (QCD) is of great importance in nuclear and particle physics. While theoretical predictions of QCD have great success in the perturbative QCD region where the momentum transfer is large (i.e. $Q^2 \rightarrow \infty$); in the non-perturbative QCD region, i.e. the low momentum transfer region, the theoretical understanding based on QCD remains either very poor or unknown. Potentially, theoretical approaches

relying on the first principles of QCD, such as lattice QCD and effective field theories, may give better understandings of the nucleon electromagnetic structure. Thus, the precision measurement of the nucleon electromagnetic form factors is crucial for confronting theories and further understanding of the underlying interactions between quarks and gluons of QCD. Particularly at low Q^2 such measurement allows for both a determination of the electromagnetic radii and accurate calculations of nuclear form factors.

The proton electromagnetic form factors have been determined with good precision at low Q^2 using Rosenbluth separation of elastic electron - proton cross-sections, and more recently at higher Q^2 using a polarization transfer technique [1]. Due to the lack of a free neutron target and calculations fully including electromagnetic interaction within a complex nucleus, neutron electromagnetic form factors are determined poorly compared with proton electromagnetic form factors. The extraction of the neutron magnetic form factor, G_m^n with high precision is essential to resolve the inconsistency in the existing G_m^n data at low Q^2 from deuterium experiments. In addition, precise information on G_m^n can significantly reduce the uncertainty in determining the neutron electric form factor, G_e^n because the determination of G_e^n is via the ratio G_e^n/G_m^n from double-polarization experiments. Furthermore, precise electromagnetic form factor data are crucial for probing the strangeness content of the nucleon by measuring the parity violation asymmetry in electron scattering [73, 74]. Lastly, the nucleon form factors are closely related to the Generalized Parton Distributions(GPD's), the formalism which provides a unifying description of the fundamental quantities in hadronic structure.

This thesis reports Jefferson Lab Experiment E95-001-a precision measurement of the transverse asymmetry, A_{TV} , in the inclusive quasi-elastic scattering of longitudinally polarized electrons from a polarized 3He target at six different four momentum transfer values ($Q^2 \sim 0.1, 0.2, 0.3, 0.4, 0.5, 0.6$ (GeV/c)²), and the extraction of the

neutron magnetic form factor, G_m^n . The data taking at the Thomas Jefferson National Lab started on January 21, 1999 and completed on February 28, 1999. More than ten institutions including MIT, JLab, Caltech, Princeton, Temple, College of W&M and others collaborated on this experiment. The MIT group led the experiment (Spokespersons: H. Gao and J.-O. Hanson).

Concerning the measurement of $A_{T'}$, the systematic uncertainty which comes from the determination of the product of the beam and target polarization through the elastic measurement is the main source of systematic uncertainty. The uncertainty in extracting G_m^n , however, is dominated by the theoretical uncertainty. For the inclusive quasi-elastic scattering ${}^3\vec{H}e(\vec{e}, e')$, the theoretical limitations of the state-of-the-art three-body calculations have prevented G_m^n from being extracted with high precision at Q^2 values above 0.3 (GeV/c)^2 . The work presented here is both a challenge and an opportunity for theoretical physics in the few-body system.

In the remainder of this chapter, we first discuss nucleon electromagnetic form factor calculations, and the recent data on G_m^n in a Q^2 region, which is less than 1 (GeV/c)^2 . Subsequently, we give an overview of the basic theoretical description of the inclusive electron scattering, the existing plane-wave impulse approximation (PWIA) model calculation, and the Faddeev full calculation. Chapter 2 gives a detailed description of the experimental setup. In Chapter 3 and 4, the data analysis as well as systematic uncertainties are discussed. Chapter 5 presents the results on $A_{T'}$ and G_m^n . Also investigated and presented in Chapter 5 are theoretical uncertainties associated with the extraction of G_m^n in the framework of PWIA and the full calculation. In Chapter 6 we give brief conclusions and future outlook on this subject.

1.2 Nucleon Form Factor Calculation

In the perturbative QCD region ($Q^2 \gg 1.0 (GeV/c)^2$), the effective strong coupling constant is much less than 1 and thus calculations of QCD can be performed using perturbation method. However, in low Q^2 region, non-perturbative QCD can not be solved technically and an important approach for non-perturbative QCD is lattice QCD. In fact, there are various models and calculations of nucleon electric and magnetic form factors $G_e^{p,n}$ and $G_m^{p,n}$ at low Q^2 . Inspired by QCD, there are five semi-phenomenological models: vector meson dominance model (VDM), relativistic constituent quark model (RCQM), diquark model, Skyrme/soliton model and the MIT bag model, and the Lattice QCD calculation. Following are the discussion on these five models and one calculation.

Vector Meson Dominance Model (VDM)

It is now established that QCD is the theory of strong interactions. Even before the advent of the quark model, however, Sakurai had attempted to model the strong interactions as a gauge theory where vector mesons, such as $\rho(770)$, $\omega(780)$ and $\phi(1020)$, played the role of the gauge bosons. This model so-called vector meson dominance model(VDM), at phenomenological level, has been very successful in the areas of hadronic form factors, photo-production and absorption cross-sections, and in the vector meson exchange contribution to πN and NN scattering. These achievements imply that for low-energy phenomena, QCD may reduce to a theory with only mesonic degrees of freedom, interacting nonlinearly. In the VDM pictures of electron scattering from a hadron, a virtual photon converts to a neutral vector meson first and then couples to the hadron.

Based on this model, Iachello and coworkers [3] attempted to describe the nucleon form factor using a semi-phenomenological fit at early time. Gari and Krümpelmann [4, 5] extended VMD model to include quark dynamics at large Q^2 via perturbative QCD. In addition, Höhler *et al.* [6] fit a dispersion ansatz to e-N scattering with VMD con-

tributions from ρ , ω , ϕ , ρ' , ω' . Later on, Meissner and coworker [7–12] have extended this VMD/dispersion relation approach to include chiral perturbation theory. Among those calculations, Mergell *et al.* [7] obtain a best fit that gave a rms proton radius near 0.85 fm, closer to the accepted value of 0.86 fm, but could not do better while simultaneously fitting neutron data. Most recently, Lomon [13] extended the Gari and Krömpelman technique to include the width of the ρ meson by substituting the result of dispersion relations for the pole and the addition of $\rho'(1450)$ vector meson pole. In Fig. 1-1, this extended GK results (dash) are shown to produce a good overall fit to the recent $\mu_p G_e^p / G_m^p$ ratio data from Jefferson Lab.

Relativistic Constituent Quark Model

Ever since the proposal of the quark model in the early sixties by Gell-Mann, the modeling of the hadrons has been a very active area of theoretical research. Non-relativistic constituent quark models are successful in describing the mass spectrum of baryons. However, considering the uncertainty principle these values of the r.m.s. radius implies a quark momentum in the range 250-500 MeV, which is comparable with the light constituent quark mass in the range 210-360 MeV. The use of non-relativistic quantum mechanics is therefore inconsistent, even for static properties of the hadrons, because the relativistic corrections are of the order $\langle p^2 \rangle / m^2$ and are expected to be large. In the relativistic constituent quark models, a light front scheme is chosen, in which there are seven (maximal number) Poincare generators of kinematical character, and only the remaining three generators contain interaction, which is the minimally possible. The light-front formalism is specified by the invariant hyper-surface $x^+ = x^0 + x^3 = \text{constant}$, four vector is given by $x = (x^+, x^-, x_\perp)$, and light-front vectors are denoted by an arrow $\vec{x} = (x^+, x_\perp)$, where $x^\pm = x^0 \pm x^3$ and $x_\perp = (x^1, x^2)$.

Several authors: Chung and Coster [14], Aznauryan [15], and Schlumpf [16,17] have calculated the nucleon form factors using various version of the relativistic con-

stituent quark model (RCQM). More recent RCQM calculations have been using light front dynamics (LFCQM) and $SU(6)$ asymmetry breaking effects by the group from INFN in Rome, Cardarelli, Simula, Pace, and Salmè [18–20]. One of RCQM calculations (thick dot-dash) and LFCQM (dot) calculation are shown in Fig. 1-1, and discrepancy between data and these calculations increase as Q^2 goes higher.

Diquark Model

Measurements of deep inelastic scattering show clear flavor dependence of the nucleon structure functions. One example is the ratio of the neutron to proton structure functions $F_2^n(x)/F_2^p(x)$ which shows a large deviation from the naive quark-parton model prediction, which is $2/3$. The idea of diquark clustering, i.e. correlated of two quarks, is thus introduced phenomenologically to explain the scaling violation of the nucleon structure functions, which may be caused by the non-perturbative diquark flavor-dependent correlations. In an other word, the experimental ratio of the neutron to proton structure function can be qualitatively explained if nearly all the momentum is carried by a leading quark, which is a u quark in the case of a proton and a d quark in the case of a neutron. Because the QCD spin-spin force is attractive and strongest in spin-0 quark-quark state, a scalar diquark $((ud)_0)$ is more probable than a vector one at large momentum transfer and the scalar diquark with isospin zero remains in the scattering.

Bo-Qian Ma, Ivan Schmidt and coworkers [21], and M. Oettel and coworkers [22] calculate the nucleon electromagnetic form factors in a light cone diquark model and in covariant diquark-quark model, respectively. Similar to RCQM, diquark calculation (thick dot) falls off much faster than data do and thus is not able to describe the proton form factor ratio well as Q^2 increases.

Skyrme/Soliton Model

The Skyrme model was first proposed by T.H.R Skyrme [23] in the sixties, as a revolutionary idea for incorporating baryons in the non-linear sigma model description

of the low-energy interactions of pions. This sigma model consists of a unitary matrix valued field $U(\vec{x}, t)$ of dimension 2×2 or 3×3 depending on number of light flavors that are considered. The dynamics is described by the Lagrange density

$$L = -\frac{f_\pi^2}{4} \text{tr}(U^\dagger \partial_\mu U U^\dagger \partial_\nu U), \quad (1.1)$$

where f_π is the pion decay constant. Skyrme noted that the existence of topologically non-trivial field configurations of finite energy. These were however, unstable against collapse, which can be deduced by a simple application of scaling argument. Skyrme then added a higher derivative term to the Lagrange density rendering these configurations stable. This term is now called the Skyrme term and Skyrme Lagrange density L_{sk} is give by

$$L_{sk} = -\frac{f_\pi^2}{4} \text{tr}(U^\dagger \partial_\mu U U^\dagger \partial_\nu U) + \frac{1}{32e^2} \text{tr}([U^\dagger \partial_\mu U U^\dagger \partial_\nu U]^2), \quad (1.2)$$

where e is a new, dimensionless coupling constant. Since each derivative corresponds to a momentum, this term is clearly of higher order in the low energy approximation. Skyrme proposed the interpretation of these topological solitons(stable, localized, finite-energy solution of classical equation of motion) as nucleons and identified the winding number of the soliton with baryon number.

Holzwarth [24] has used this model to calculate the nucleon form factors and included the loop corrections. His results (dot-dash) agree very well with the recent proton $\mu_p G_e^p / G_m^p$ ratio in Fig 1-1.

MIT Bag Model

In QCD model, the color electric interaction between charged objects becomes stronger for large distances. QCD vacuum is therefore an "anti-screening" medium. As the distance gets smaller, the interaction becomes weaker. This is called asymptotic freedom. Based on these phenomena, a nucleon can be modeled as independent quarks

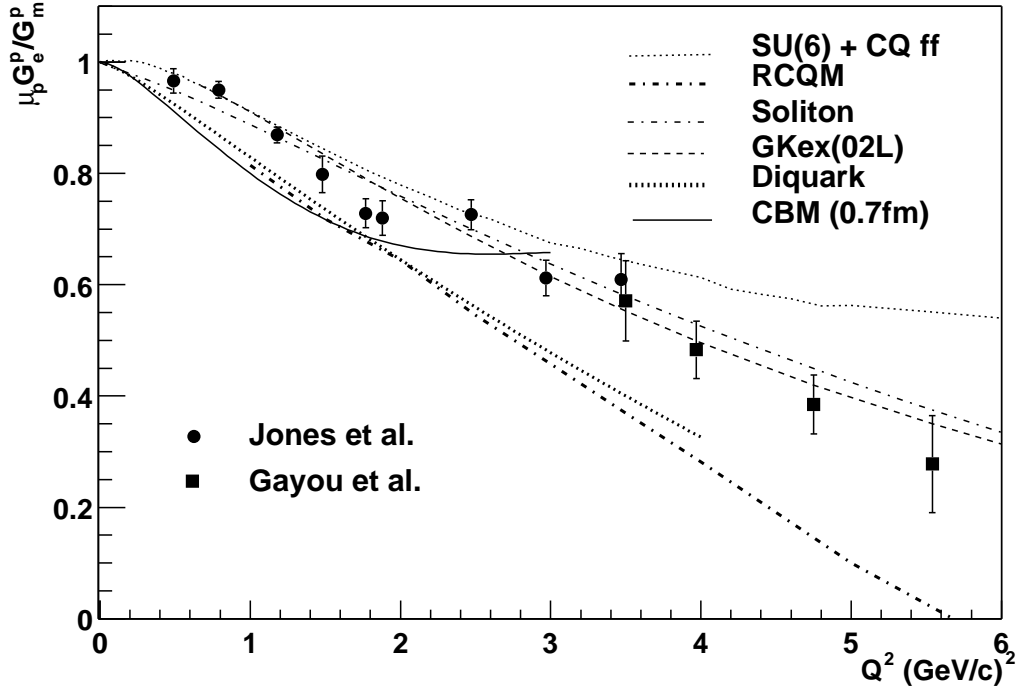


Figure 1-1: Jefferson Lab precise data on proton form factor ratio $\mu_p G_e^p / G_m^p$. Data is shown in figure (solid circle: Jones *et al.* [1], and solid square: Gayou *et al.* [2]), along with various model calculations (SU(6) +CQ ff (dot): Cardarelli and Simula [20], RCQM (thick dot-dash): Schlumpf [17], GKex(02L) (dash): Lomon [13], Soliton (dot-dash): Holzwarth [24], Diquark (thick dot): Ma [21], and CBM (solid): Lu [27]).

confined in a rigid spherical well. This model is the so-called MIT Bag model.

Lu and Thomas [25–27] have performed calculations based on a cloudy bag model (CBM) which is a bare MIT bag with a meson cloud. The introduction of the pion cloud improves the static properties of the nucleon by restoring chiral symmetry and also provides a convenient connection to πN and NN scattering. In Fig 1-1, the CBM calculation (solid) with a small bag radius of 0.7 fm gives a better agreement to the Jlab data, but the abrupt change of slope between 2 and 3 $(GeV/c)^2$ is inconsistent

with the data.

Lattice QCD

QCD is fundamentally different from QED. In QCD, there exists a rich topological structure, self-interaction is highly nonlinear, interaction between quarks increases at large distance (confinement), the strong coupling constant is much greater than 1. Currently, analytical techniques are inadequate to solve non-perturbative QCD. Thus, a technique called lattice QCD, in which path integral of the action S is numerically evaluated on space-time lattice in Euclidean space, bring a hope to solve non-perturbative QCD, yet adequate human and computer resources are highly demanded in order to solve QCD on the lattice.

A lattice gauge calculation is the most fundamental. However such calculations are still in early stage of development. Recent calculations by a few groups such as K.F. Liu *et al.* [29], W. Wilcox *et al.* [28] and G. Schierholz *et al.* [30] therefore have relatively large uncertainties.

The comparison between the previous neutron magnetic form factor, G_m^n data and some of various model calculations at Q^2 values less than 1 $(GeV/c)^2$ are included in the following section, and discussions on the most recent G_m^n results and some of the most recent model calculations are included in Chapter 5.

1.3 Existing Data

In the past, the existing world's data set is found to be internally inconsistent and with poor quality due to the lack of a free neutron target, while the proton form factors are known with good precision over a large range of Q^2 . This is true for both the electric form factor G_e^n and to a somewhat lesser degree for the magnetic form factor G_m^n . G_m^n has been determined mostly from the quasi-elastic $D(e, e')$ cross-section. The extraction of G_m^n demands a longitudinal/transverse separation and a

subtraction of the (dominant) proton magnetic contribution. The deuteron model, meson exchange currents (MEC), and final interactions (FSI) result in uncertainty of G_m^n greatly amplified by these two subsequent subtraction steps. The accuracy of G_m^n therefore is no better than 20% from these inclusive measurement. Due to all these limitations alternative techniques have been used in recent experiments.

One of the techniques is the exclusive cross-section measurement from the $D(e, e'n)$ process, which was employed most recently by Markowitz *et al.* [40] at the MIT-Bates Lab. The neutron detection efficiency is determined using the associated technique with the ${}^2H(\gamma, pn)$ reaction. Though the proton contribution is excluded, the method still depends on a deuteron model for the extraction of G_m^n . Later on, an improved method, which determines G_m^n from the ratio $R = \sigma(e, e'n) / \sigma(e, e'p)$ on the deuteron in quasi-free kinematics to minimize the uncertainty due to a deuteron model, FSI and MEC, is developed. However, the cost is the need for a precise measurement of the absolute efficiency of the neutron detector employed. The absolute neutron detection efficiency is measured either in situ using the ${}^1H(\gamma, \pi^+)n$ reaction by Bruins *et al.* [55] during a Bonn experiment, or with high accuracy using tagged neutrons produced from the $H(n, p)n$ elastic scattering by means of a high intensity neutron beam in recent NIKHEF and Mainz experiments [56, 57]. The values of G_m^n are consequently extracted with error bar as low as 1% in low Q^2 with the ratio technique. Due to the difficulty with absolute neutron efficiency determination, the G_m^n results from these improved experiments however exist a intrinsic inconsistency [60] in Figure 1-2.

The neutron magnetic form factor, G_m^n , can also be obtained from the transverse asymmetry, A_{TV} , measured in the ${}^3\vec{H}e(\vec{e}, e')$ scattering. Following a pilot experiment by Gao *et al.* [39] at MIT-Bates, more recently G_m^n is extracted with high precision in JLAB experiment E95-001 resulting from a rigorous non-relativistic 3-body calculation, which includes FSI and MEC effects.

The standard dipole parameterization of the nucleon electromagnetic form factors

are given:

$$\frac{G_m^n}{\mu_n} = \frac{G_m^p}{\mu_p} = G_e^p = G_D = \left[1 + \frac{Q^2}{0.71}\right]^{-2}, \quad (1.3)$$

where Q^2 is in $(\text{GeV}/c)^2$. Fig 1-2 shows the recent world data on $(G_m^n)^2$, in dipole

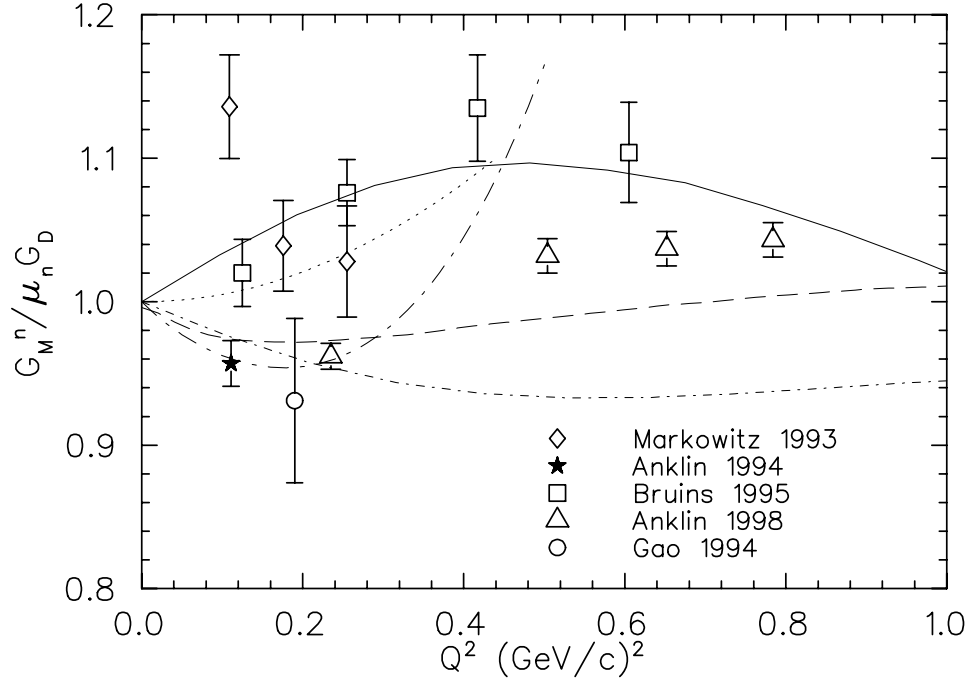


Figure 1-2: The world G_m^n data since 1990. The figure shows the results of the Bonn [55](\square), the MIT-Bates [39] [40](\circ, \diamond), the NIKHEF/PSI [56](\star), and the Mainz/PSI [57](\triangle), in comparison to various model calculations. Solid: Lu *et al.* [25], dot: Meissner *et al.* [9], dash: Mergell *et al.* [7], long dot-dash: Kubis *et al.* [12], and short dot-dash: Schlumpf *et al.* [17]

unit $((\mu_n G_D)^2)$, in the low Q^2 region including the recent Bates, Bonn and NIKHEF and Mainz data. These data clearly show a difference from the dipole expression used to remove the dominant Q^2 -dependence in G_m^n . In addition, the data from deuterium measurements do not agree with each other. Measurements by Markowitz *et al.* [40](\diamond) and Bruins *et al.* [55](\square) used three-body reactions $d(e, p)ne'$ and

$H(e, \pi)ne'$ to tag the recoiling neutron in the absolute neutron detection efficiency determination. However, the argument is that significant corrections for neutrons that miss the neutron detector are required, but these corrections were not applied [60]. The agreement between the data measured at NIKHEF and Mainz by Ankin *et al.* [56, 57](\star, Δ) and at Bates by Gao *et al.* [39](o) using different techniques at different facilities seem to support this argument. But the further investigation is needed due to the rather large statistical uncertainty associated with the measurement by Gao *et al.* [39](o). The data measured by Anklin *et al.* [56, 57](\star, Δ) and Gao *et al.* [39](o) show significant differences from a recent cloudy bag model calculation [25](solid) and a minimal vector dominance model prediction [9](dot). These data are also compared to results of the relativistic chiral perturbation theory by Kubis and Meissner [12](long dot-dash), the calculation by Mergell *et al.* [7](dash) based on a fit of the proton data using dispersion theoretical arguments, and the relativistic constituent quark model calculation by Schlumpf [17](short dot-dash). However, none of these calculations describes the data satisfactorily.

The extracted G_m^n from this work and some of the most recent model calculations are included in Chapter 5.

1.4 The Spin-Dependent Quasi-elastic ${}^3\vec{H}e(\vec{e}, e')$ Process

Inspired by the pioneering experiments using polarized 3He targets [36–39], we have for the first time measured precisely the transverse asymmetry $A_{T'}$ and have extracted neutron magnetic form factor G_m^n from the quasi-elastic ${}^3\vec{H}e(\vec{e}, e')$ process. The notable advantages of using the spin-dependent quasi-elastic ${}^3\vec{H}e(\vec{e}, e')$ process to study the structure of neutron are following: (i) an electron probe is able to sample the entire nuclear volume because the interaction between electron and nuclei are

relatively weak, and the electron-photon interaction is extremely well understood in terms of QED; (ii) the ground state ${}^3\text{He}$ is dominated by the spatially symmetric S -state [31, 32] in which the spins of two protons are paired off to satisfy the Pauli principle so that the nuclear spin is mainly carried by the unpaired neutron. Thus, the spin-dependent asymmetry is very sensitive to the neutron electromagnetic form factors at certain kinematics near the top of the quasi-elastic peak.

Recently, the full calculation with the final state interaction (FSI) effect and the meson exchange current (MEC) effect, which has been developed by the Buchum-Krakow collaboration, has made it possible to extract G_m^n with high precision at very low Q^2 values from ${}^3\vec{H}e(\vec{e}, e')$ process on top of the quasi-elastic peak, where the relativistic effect is relatively small. As Q^2 increases, although FSI effect is expected to decrease, the relativistic effect grows rapidly. So PWIA may provide a better approximation for describing the cross-section around the quasi-elastic peak and the extraction of G_m^n at higher values of Q^2 .

1.4.1 Spin-dependent Inclusive Electron Scattering

As an incident longitudinally polarized electron with four-momentum $k = (E, \vec{k})$ is scattered by a nucleus $P_A = (M_A, 0)$ with a spin S_A to $k' = (E', \vec{k}')$, the electromagnetic interaction via virtual photon exchange and the weak interaction via Z^0 boson exchange between the electron and the nucleus take place. In the medium energy range, the electromagnetic contribution dominates by many orders of magnitude due to the mass of the vector bosons and the weak coupling constant. Also among all orders of electromagnetic contributions, the first order approximation of the electromagnetic contribution, so-called the first Born Approximation as shown in Fig. 1-3, is larger by roughly two orders over the rest of all electromagnetic contributions because of the virtue of electromagnetic interaction, the α (1/137) suppression. The study of the one-photon-exchange approximation is therefore sufficient to fulfill the require-

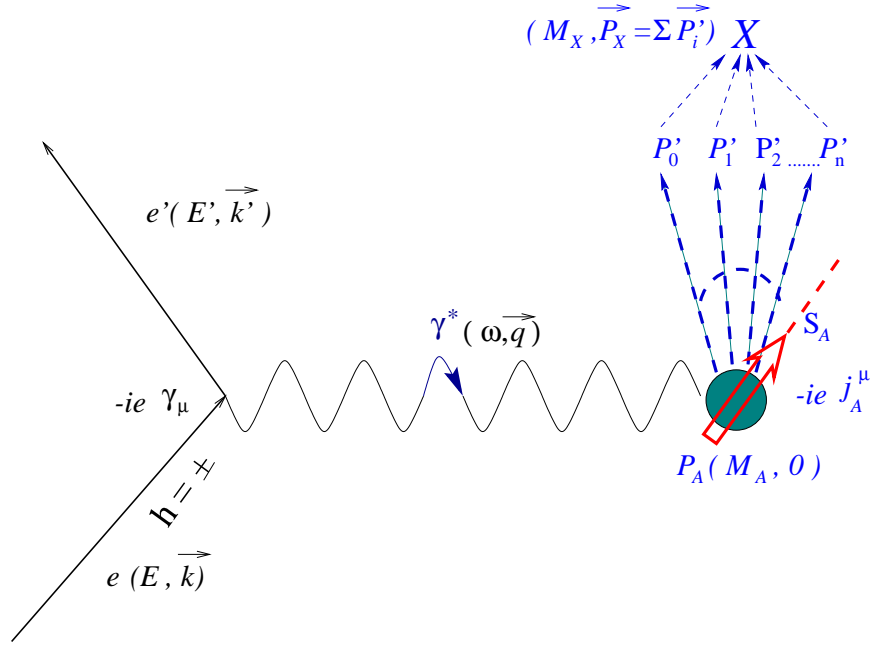


Figure 1-3: The Born approximation

ments of the experiment. The inclusive cross-section summing over initial states and averaging over all possible final states is given as:

$$d\sigma = \frac{1}{4\sqrt{(k \cdot p_A)^2 - m_e^2 M_A^2}} \sum_N \left(\int \prod_{n=1}^N \frac{d^3 k'}{(2\pi)^3 2p_n^0} \right) \sum_{s' s n'} |\mathcal{M}_{fi}|^2 (2\pi)^4 \delta^{(4)}(q + p_A - p_X). \quad (1.4)$$

Here \mathcal{M}_{fi} is the transition matrix element from the initial state $|i\rangle$ to the final state $|f\rangle$ and the square of \mathcal{M}_{fi} has the well-known form in terms of the leptonic current and hadronic current:

$$|\mathcal{M}_{fi}|^2 =$$

$$(4\pi)^2 \frac{\alpha^2}{Q^4} \underbrace{[\langle k, s | j_e^{\dagger\mu} | k' s' \rangle \langle k', s' | j_e^\nu | k' s' \rangle]}_{\eta^{\mu\nu}} \underbrace{[\langle p_A, s_A | j_A^{\dagger\mu} | X \rangle \langle X | j_A^\nu | p_A, s_A \rangle]}_{W_{\mu\nu}}, \quad (1.5)$$

where $\eta^{\mu\nu}$ and $W_{\mu\nu}$ are so-called leptonic tensor and hadronic tensor [34] respectively. From Eq. 1.5, one realizes the importance of understanding the leptonic tensor $\eta^{\mu\nu}$ and the hadronic tensor $W_{\mu\nu}$ for studying electron scattering.

Leptonic Tensor:

In terms of the Dirac spinor, the leptonic tensor is generally given as the following:

$$\eta^{\mu\nu} = \sum_{s'} \overline{u_e(k, s)} \gamma^\mu u_e(k', s') \overline{u_e(k', s')} \gamma^\nu u_e(k, s). \quad (1.6)$$

If the electron beam is longitudinally polarized, Equation 1.6 can be rewritten as:

$$\eta^{\mu\nu} = \frac{1}{2} \text{Tr}[\gamma^\mu (\not{k} + m_e) \gamma^\nu (1 + \gamma_5 \not{s}) (\not{k} + m_e)]. \quad (1.7)$$

Here, $\not{k} + m_e$ and $\not{k}' + m_e$ are the electron projectors for incoming and outgoing electrons respectively, and $1 + \gamma_5 \not{s}$ is the spin projector for the incoming electron. It is not difficult to figure out that by inserting the spin projector for the outgoing electron, one is able to calculate $A(\vec{e}, \vec{e}')B$ case. Furthermore, if we have taken the ultra-relativistic limit by dropping terms containing the electron mass, m_e , with the exception of the term containing the electron spin, $m_e s$, the leptonic tensor could be deduced as a sum of a symmetric piece and an antisymmetric piece in the following equation.

$$\eta^{\mu\nu} = 2 \left[\underbrace{[k'^\mu k^\nu + k^\mu k'^\nu - g^{\mu\nu} (k \cdot k')]}_{\text{symmetry terms}} + \underbrace{[i\epsilon^{\mu\nu\alpha\beta} (m_e s_\alpha) q_\beta]}_{\text{anti-symmetry term}} \right] \quad (1.8)$$

Hadronic Tensor:

Although the hadronic tensor can not be written explicitly without detailed knowl-

edge of the nuclear current J_A , it is still a good idea to study the general formulas for the hadronic tensor. Like the leptonic tensor, the hadronic tensor, $W^{\mu\nu}$ can be split into a symmetric piece and an anti-symmetric piece, $W^{\mu\nu} = W_s^{\mu\nu} + W_a^{\mu\nu}$. Each term satisfies parity and time-reversal invariances, and current conservation, $q_\mu W^{\mu\nu} = 0$.

The general symmetric rank-two tensor which can be constructed from the two independent 4-vectors (q, p_A) is thus

$$W_s^{\mu\nu} = \left(\frac{q^\mu q^\nu}{q^2} - g^{\mu\nu} \right) W_1 + \tilde{p}_A^\mu \tilde{p}_A^\nu \frac{W_2}{M_A^2}, \quad (1.9)$$

with two scalar functions $W_1(q^2, p_A \cdot q)$ and $W_2(q^2, p_A \cdot q)$ called the unpolarized structure functions and the abbreviation

$$\tilde{p}_A^\mu \equiv p_A^\mu - \frac{q \cdot p_A}{q^2} q^\mu. \quad (1.10)$$

In addition, it is useful to express the structure functions in terms of the elements of the hadron tensor $W^{\mu\nu}$ because $W^{\mu\nu}$ is defined in the theoretical calculation. If the rest frame of the target is chosen, where z-axis is along the three-momentum transfer $\hat{z} = \hat{q}$, and y-axis is normal to the plane spanned by the three momentum transfer and the target spin s_A , $\hat{y} = (\hat{q} \times \hat{s}_A) / |\hat{q} \times \hat{s}_A|$, the inverted expressions are given by

$$W_1 = \frac{1}{2}(W^{11} + W^{22}), \quad (1.11)$$

$$W_2 = \frac{q^4}{|\vec{q}|^4} W^{00} - \frac{1}{2} \frac{q^2}{|\vec{q}|^2} (W^{11} + W^{22}). \quad (1.12)$$

Likewise, one can construct the antisymmetric part,

$$W_a^{\mu\nu} = i\epsilon^{\mu\nu\alpha\beta} q_\alpha V_\beta. \quad (1.13)$$

For $W_a^{\mu\nu}$ satisfies current conservation, time-reversal and parity invariances, V_β must

be a pseudo-vector and so it must be a function of s_A , $s_A \cdot q$ and $s_A \cdot p_A$. However terms containing $s_A \cdot p_A$ vanish, because s_A is chosen to satisfy $s_A \cdot p_A = 0$. The general expression of V_β is

$$V_\beta = s_{A\beta} \frac{G_1}{M_A} + [(p_A \cdot q)s_{A\beta} - (s_A \cdot q)p_{A\beta}] \frac{G_2}{M_A^3} \quad (1.14)$$

with two additional polarized structure functions, $G_1(q^2, q \cdot p_A)$ and $G_2(q^2, q \cdot p_A)$ different from $W_{1/2}$ above. Similar to the unpolarized structure $W_{1/2}$, $G_{1/2}$ is also helpful to invert as

$$\frac{G_1}{M_A} = -\frac{i}{2|\vec{q}|^2} \left\{ \frac{q^2}{|\vec{q}|} \frac{1}{s_{Ax}} (W^{02} - W^{20}) + \frac{\omega}{s_{Ax}} (W^{12} - W^{21}) \right\}, \quad (1.15)$$

$$\frac{G_2}{M_A} = \frac{i}{2|\vec{q}|^2} \left\{ \frac{\omega}{|\vec{q}|} \frac{1}{s_{Ax}} (W^{02} - W^{20}) + \frac{1}{s_{Ax}} (W^{12} - W^{21}) \right\} \quad (1.16)$$

in terms of the element of $W^{\mu\nu}$. From the expressions of $G_{1/2}$ and $W_{1/2}$, one finds that all third components of $W^{\mu\nu}$ vanish. It is simply because the current conservation, $W^{3\nu} = \omega W^{0\nu} / |\vec{q}|$, and we prefer to use the zeroth components of $W^{\mu\nu}$.

The zeroth components of $W^{\mu\nu}$ correspond to the longitudinal projection, related to the nuclear charge density, and the first and the second components of $W^{\mu\nu}$ correspond to the transverse projections, related to nuclear magnetization currents. Because $W_{1/2}$ and $G_{1/2}$ mix different components of the nuclear current, introducing an equivalent set of structure functions, with separated current projections, so-called response functions, is useful from a physical point of view. The response functions are defined as:

$$R_L \equiv W^{00} \quad (1.17)$$

$$R_T \equiv W^{11} + W^{22} \quad (1.18)$$

$$R_{T'} \equiv -i \frac{1}{s_{Ax}} (W^{12} - W^{21}) \quad (1.19)$$

$$R_{TL} \equiv -i \frac{\sqrt{2}}{s_{Ax}} (W^{12} - W^{21}). \quad (1.20)$$

Inserting the response functions into equations of $W_s^{\mu\nu}$ and $W_a^{\mu\nu}$, we get

$$\begin{aligned} W^{\mu\nu} = & \frac{1}{2} \left(\frac{q^\mu q^\nu}{q^2} - g^{\mu\nu} - \frac{q^2}{|\vec{q}|^2} \frac{\tilde{p}_A^\mu \tilde{p}_A^\nu}{M_A^2} \right) R_T + \frac{q^4}{|\vec{q}|^4} \frac{\tilde{p}_A^\mu \tilde{p}_A^\nu}{M_A^2} R_L \\ & + i\epsilon^{\mu\nu\alpha\beta} q_\alpha \left\{ \frac{1}{2|\vec{q}|^2} \left(\omega s_{A\beta} - \frac{1}{M_A} [(p_A \cdot q) s_{A\beta} - (s_A \cdot q) p_{A\beta}] \right) R_{T'} \right. \\ & \left. + \frac{1}{2\sqrt{2}|\vec{q}|^3} \left(q^2 s_{A\beta} - \frac{\omega}{M_A} [(p_A \cdot q) s_{A\beta} - (s_A \cdot q) p_{A\beta}] \right) R_{TL'} \right\} \quad (1.21) \end{aligned}$$

Having written down the leptonic tensor $\eta^{\mu\nu}$ and the hadronic tensor $W^{\mu\nu}$, we are

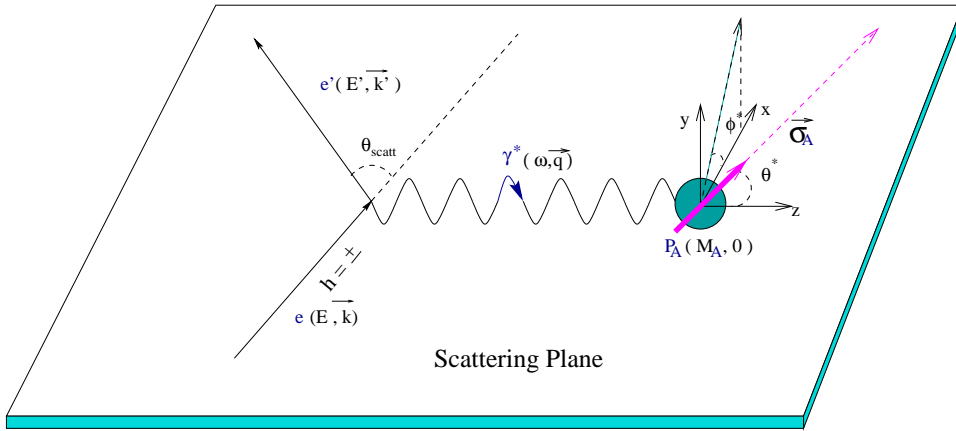


Figure 1-4: Definition of target spin angles with respect to the three-momentum transfer, \vec{q}

ready to reveal the full expression of the cross-section and asymmetry in terms of the nuclear response functions. Assuming the target spin direction is of polar angle θ^* and azimuthal angle ϕ^* with respect to the momentum transfer \vec{q} in Figure 1-4, we find the spin-dependent quasi-elastic differential cross-section:

$$\frac{d^2\sigma}{dE' d\Omega'} \propto \eta^{\mu\nu} W_{\mu\nu} \quad (1.22)$$

$$= \sigma_{Mott}\{v_L R_L + v_T R_T - h(\cos\theta^* v_{T'} R_{T'} + \sin\theta^* \cos\phi^* v_{TL'} R_{TL'})\} \quad (1.23)$$

$$\equiv \Sigma + h\Delta \quad (1.24)$$

with the kinematic factors

$$\begin{aligned} v_L &\equiv \frac{Q^4}{|\vec{q}|^4}, \\ v_T &\equiv \frac{1}{2} \frac{Q^2}{|\vec{q}|^2} + \tan^2 \frac{\theta}{2}, \\ v_{T'} &\equiv \tan \frac{\theta}{2} \sqrt{\frac{Q^2}{|\vec{q}|^2} + \tan^2 \frac{\theta}{2}}, \\ v_{TL'} &\equiv -\frac{1}{\sqrt{2}} \frac{Q^2}{|\vec{q}|^2} \tan \frac{\theta}{2}. \end{aligned} \quad (1.25)$$

Here, the symbols Σ and Δ denote the spin-independent and spin-dependent differential cross section respectively, h denotes the helicity of the polarized electron ($h = \frac{\vec{\sigma} \cdot \vec{p}}{|\vec{\sigma}| |\vec{p}|}$, $h = \pm 1$), and $Q^2 = -q^\mu q_\mu$. The so-called spin-dependent asymmetry, is defined as

$$A = \frac{\frac{d\sigma}{dE' d\Omega} h=+1 - \frac{d\sigma}{dE' d\Omega} h=-1}{\frac{d\sigma}{dE' d\Omega} h=+1 + \frac{d\sigma}{dE' d\Omega} h=-1} \quad (1.26)$$

Using the Eq. 1.26, the expression of asymmetry is given as:

$$A = \frac{\Sigma}{\Delta} = -\frac{\cos\theta^* v_{T'} R_{T'} + \sin\theta^* \cos\phi^* v_{TL'} R_{TL'}}{v_L R_L + v_T R_T}. \quad (1.27)$$

From Eq. 1.27, as $\theta^* = 0^\circ$ or $\theta^* = 90^\circ$, namely the spin direction is along or perpen-

pendicular to the momentum transfer vector \vec{q} , either the polarized response function, $R_{TL'}$ term or $R_{T'}$ term vanishes. The asymmetry corresponding to $\theta^* = 0^\circ$ is called the transverse asymmetry, $A_{T'}$. The asymmetry corresponding to $\theta^* = 90^\circ$ is called the transverse-longitudinal asymmetry, $A_{TL'}$. In experiment E95-001, we measured the transverse asymmetry, $A_{T'}$ from the inclusive quasi-elastic ${}^3\bar{H}e(\vec{e}, e')$ process.

1.4.2 Plane-Wave Impulse Approximation (PWIA)

The basic assumptions of PWIA are (Fig. 1-5):

- a single nucleon within the target nucleus totally absorbs the energy and momentum of a single virtual photon.
- the “quasi free” is valid and hence final-state interactions and various exchange current effects are ignored. The outgoing nucleon is treated as a plane wave.
- the target nucleus can be described by independent particles.

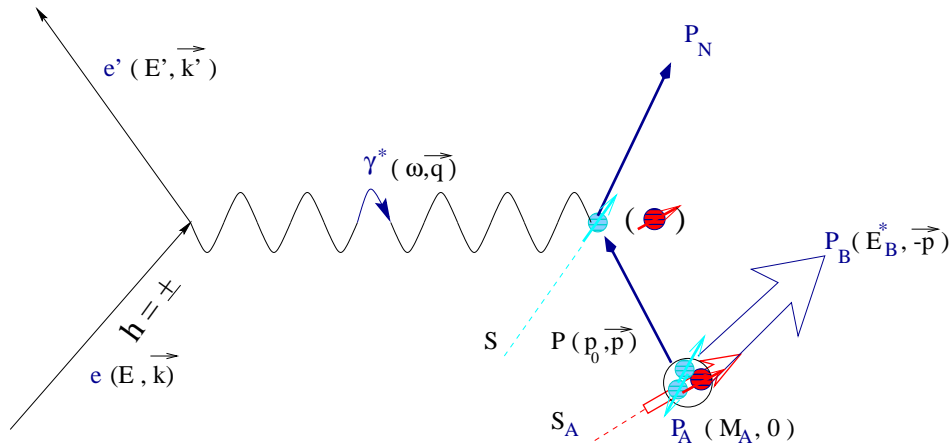


Figure 1-5: Feynman diagram in the Plane Wave Impulse Approximation (PWIA)

Thus, the one-body operator of the hadronic current is

$$\hat{J}^\mu = \sum_{mm'} \sum_{\tau\tau'} \int \int dp dp' \langle p', m', \tau' | \Gamma^\mu | p, m, \tau \rangle a_{p'm'\tau'}^\dagger a_{pm\tau}, \quad (1.28)$$

where $|p, m, \tau\rangle$ is an on-shell spinor state characterized by 3-momentum \vec{p} , 4-vector spin S^μ and the isospin τ , $a_{p'm'\tau'}^\dagger$ and $a_{pm\tau}$ are creation and annihilation operators of a single nucleon respectively, and Γ^μ is the $\gamma^* NN$ vertex operator. As the target initial state $|i\rangle = |A\rangle$ evolves to the final state $|f\rangle$, which includes a single knocked-out nucleon and the residual A-1 system $|B\rangle$, one then have for the hadronic current

$$\langle f | J^\mu | i \rangle = \sum_m \int dp \langle p_N, m_N | \Gamma^\mu | p, m \rangle \langle B | a_{pm} | A \rangle. \quad (1.29)$$

Inserting this result into the expression for the hadronic current we can write

$$W^{\mu\nu} = \sum_{mm'} W_N^{\mu\nu}(p, q) \times S(p, \Omega^*), \quad (1.30)$$

where two new quantities are introduced: the spectral function $S(p, \Omega^*)$ and the single-nucleon tensor, $W_N^{\mu\nu}$. The general formula for the spectral function [33, 35] is

$$S(p, \Omega^*) = \sum_A p(A) \sum_B \langle B | a_{p'm'} | A \rangle \langle A | a_{pm} | B \rangle, \quad (1.31)$$

which characterized the probability to find a nucleon with momentum p within the target nucleus. The solutions for the wave function of the $|A\rangle$ and $|B\rangle$ can be obtained from the Faddeev equations [51] using a realistic N-N potential. The spectral function is a Lorentz scalar and so is parameterized in terms of the available Lorentz vectors \hat{p} , spin of the struck nucleon in its rest frame, $\vec{\sigma}$ and target spin, $\vec{\sigma}_A$ as [33]:

$$S(p, \Omega^*) = \frac{1}{2} \{ f_0(p, \Omega^*) + f_1(p, \Omega^*) (\vec{\sigma} \cdot \vec{\sigma}_A) \}$$

$$+ f_2(p, \Omega^*) \left[(\vec{\sigma} \cdot \hat{p})(\vec{\sigma}_A \cdot \hat{p}) - \frac{1}{3}(\vec{\sigma} \cdot \vec{\sigma}_A) \right] \Big\}. \quad (1.32)$$

Here f_0 is the usual unpolarized spectral function and f_1 and f_2 are spin-dependent parts of the spectral function.

Regarding the single nucleon hadronic tensor

$$W^{\mu\nu}(p, q)_N = \sum_{m_N} \langle p_N, m_N | \Gamma^\mu | p, m' \rangle^* \langle p_N, m_N | \Gamma^\nu | p, m \rangle, \quad (1.33)$$

which depends directly on the $\gamma^* NN$ vertex, one can write in a form very similar to the general expression of hadronic current,

$$W_N^{\mu\nu}(p, q) = \left\{ \left(\frac{q^\mu q^\nu}{q^2} - g^{\mu\nu} \right) \tilde{W}_1 + \tilde{p}^\mu \tilde{p}^\nu \frac{\tilde{W}_2}{M^2} + i\epsilon^{\mu\nu\alpha\beta} q_\alpha \left(s_\beta \frac{\tilde{G}_1}{M} + [(p \cdot q)s_\beta - (s \cdot q)p_{A\beta}] \frac{\tilde{G}_2}{M^3} \right) \right\} \times 2M\delta(2q \cdot p + q^2), \quad (1.34)$$

where $\tilde{p} \equiv p - q(q \cdot p)/q^2$, and the δ -function ensures the quasi-elastic scattering region. s represents the 4-vector spin of the struck nucleon in the rest frame of the struck nucleon. The transformation of the s representing the boost of the vector $\vec{\sigma}$ to the momentum \vec{p} is

$$s = \left(\frac{\vec{p} \cdot \vec{q}}{M}, \vec{\sigma} + \frac{\vec{p} \cdot \vec{\sigma}}{M(M + p_N^0)} \vec{p} \right) \quad (1.35)$$

In addition, the nucleon structures can be written in terms of the elastic Sachs form factors, $G_{e/m}(q^2)$, as

$$\begin{aligned} \tilde{W}_1 &= \tau G_m^2 \\ \tilde{W}_2 &= \frac{G_e^2 + \tau G_m^2}{(1 + \tau)} \end{aligned}$$

$$\begin{aligned}\tilde{G}_1 &= \frac{G_m(G_e + \tau G_m)}{2(1 + \tau)} \\ \tilde{G}_2 &= \frac{G_m(G_m - G_e)}{4(1 + \tau)}\end{aligned}\quad (1.36)$$

where $\tau = -q^2/4M$. The sachs form factors have an intuitive interpretation. In the non-relativistic limit, they are directly related to the Fourier transformation of the charge and magnetization distribution of the nucleon, and in $Q^2 \rightarrow 0$ limit reduce to

$$G_e(Q^2 = 0) = q_{nucleon}, \quad (1.37)$$

$$G_m(Q^2 = 0) = \mu_{nucleon}, \quad (1.38)$$

where $q_{nucleon}$ is the nucleon charge and $\mu_{nucleon}$ is the magnetic moment of the nucleon.

Based on the study of the single nucleon hadronic tensor (Eqs. 1.11, 1.12, 1.15, 1.16, 1.17 - 1.20, and 1.36 - 1.36) the response functions for the single nucleon (.ie. the electron scattering from a free nucleon) therefore can be obtained in term of $G_{e/m}$:

$$R_L = (1 + \tau)G_e^2, \quad (1.39)$$

$$R_T = 2\tau G_m^2, \quad (1.40)$$

$$R_{T'} = 2\tau G_m^2, \quad (1.41)$$

$$R_{TL'} = 2\sqrt{2\tau(1 + \tau)}G_m G_e, \quad (1.42)$$

and according to Eq. 1.27 the spin-dependent asymmetry for the single nucleon is

$$A_{e\vec{N}} = -\frac{2\tau v_{T'} \cos\theta^* G_m^2 + 2\sqrt{2\tau(1 + \tau)} v_{TL'} \sin\theta^* \cos\phi^* G_m G_e}{(1 + \tau) v_L G_e^2 + 2\tau v_T G_m^2}. \quad (1.43)$$

In the process of electron scattered from $|A\rangle$, the interacting nucleon is usually kinematically off its mass shell: $E \neq \sqrt{\vec{p}^2 + M^2}$ ie if $\vec{p} = \vec{p}_N + \vec{q}$ but $\sqrt{\vec{p}^2 + M^2} \neq \omega + \sqrt{\vec{p}_N^2 + M^2}$, the struck nucleon is off-shell. The de Forest half-offshell prescription [42] are thus introduced to empirically describe the possible off-shell effect. The de Forest prescriptions involve three major steps. First the spinors are still treated as free on-shell ones in the current operator, then the vertex operator of the current operator changes according to the CC1 and CC2 prescription given as

$$\Gamma_{CC1}^\mu = (F_1 + F_2)\gamma^\mu - \frac{F_2}{2M}\bar{p} + p_N^\mu \quad (1.44)$$

$$\Gamma_{CC2}^\mu = F_1\gamma^\mu + \frac{iF_2}{2M_N}\sigma^{\mu\nu}Q_\nu \quad (1.45)$$

with F_1 and F_2 : the on-shell Pauli and Dirac form factors, respectively and $\bar{p} \equiv (\sqrt{\vec{p}^2 + M^2}, \vec{p})$. The Dirac and Pauli form factors are related to Sachs form factors in the usual way by

$$F_1 = \frac{G_m - G_e}{1 + \tau}, F_2 = \frac{G_e - \tau G_m}{1 + \tau}. \quad (1.46)$$

Therefore similar to the free nucleon case, we can get the corresponding response functions for the single off-shell nucleon (ie. the electron scattering from a free off-shell nucleon). However the response functions for the single off-shell nucleon are much more complicated than that for the single nucleon. However when the struck nucleon's momentum is small compared with nucleon mass (this is our case), a good approximation for the response functions is the following:

$$R_L = \frac{\tau(1 + \tau)}{\bar{\tau}}G_e^2, \quad (1.47)$$

$$R_T = 2\bar{\tau}G_m^2, \quad (1.48)$$

$$R_{T'} = 2\bar{\tau}G_m^2, \quad (1.49)$$

$$R_{TL'} = 2\sqrt{2\tau(1+\tau)}G_m G_e, \quad (1.50)$$

where τ is equal to $\tau = |\bar{Q}^2|/4M^2$ with $\bar{Q}^\mu = (p_N^\mu - \bar{p}^\mu)$.

Lastly, the issue of current conservation ($qJ^3 = \omega J^0$) needs to be considered. Based on the current conservation, either third-component or 0th-component can be eliminated by employing Siegert's theorem. Corresponding notations: $CC1^0$ and $CC1^3$ (or likewise, $CC2^0$ and $CC2^3$) are used. Meanwhile, the cross section from CC1 or CC2 prescriptions without enforcing the current conservation denotes as NCC1 or NCC2.

1.4.3 Non-relativistic Faddeev Calculation

Exact non-relativistic Faddeev calculations for both the ground state and the continuum of ${}^3\text{He}$ and ${}^3\text{H}$ describes well exclusive and inclusive low energy electron scattering on ${}^3\text{He}$ and ${}^3\text{H}$. The full calculation, the non-relativistic Faddeev calculations, has been developed by Golak *et al.* [52] in the non-relativistic framework, which employs Faddeev techniques to calculate the bound-state of ${}^3\text{He}$ and re-scattering effects in the final state up to all orders [44, 45, 52] (shown in Fig. 1-6), and also includes some meson exchange currents (MEC) [41] (shown in Fig. 1-7). The MEC effects in the full calculation are calculated using the prescription of Riska [54], which includes π - and ρ -like exchange terms. The exact treatment of final-state interactions (FSI) in the full calculation results in a much improved description of unpolarized pd capture and breakup channels [57]. Because of its fully non-relativistic frame work, the full calculation is not expected to be applicable at higher Q^2 .

As can be seen, the determination of the hadronic tensor or current plays the major role for the inclusive or exclusive scattering calculation. We therefore begin with the introduction of the hadronic current. Unlike the general formula of the

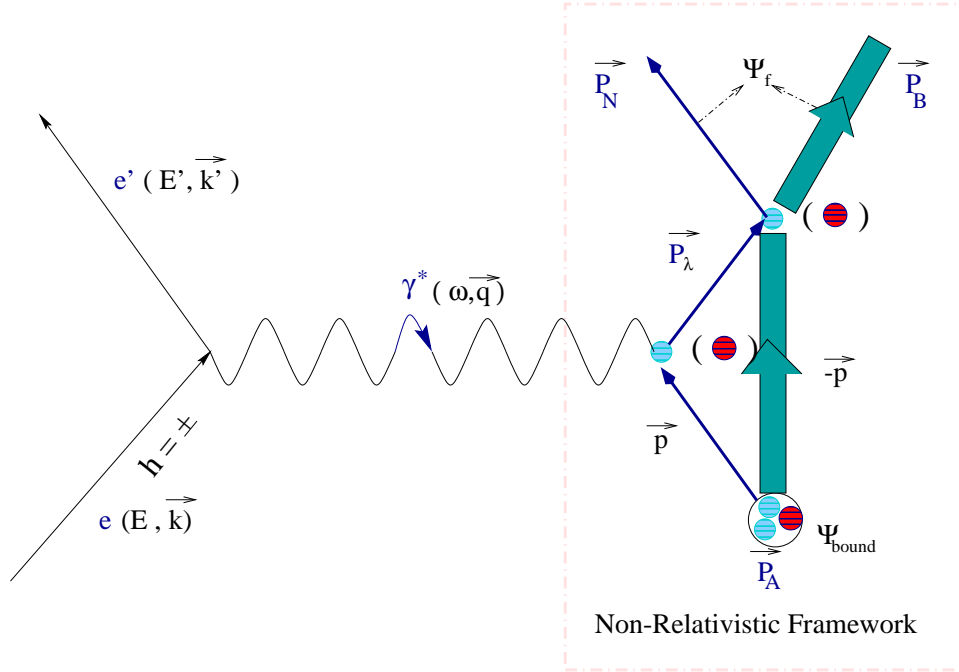


Figure 1-6: FSI contributions in the non-relativistic Faddeev calculation

current, the hadronic current in the full calculation is written as a spherical tensor

$$J^0 \equiv \langle \Phi_f | \hat{J}^0 | \Phi_{bound} \rangle, J^\pm \equiv \langle \Phi_f | \hat{J}^\pm | \Phi_{bound} \rangle, \quad (1.51)$$

where the Φ_{bound} is the ground state of target nucleus (${}^3\text{He}$), Φ_f is the final eigenstates of the 3N Hamiltonian corresponding to the two types of breakup (pd and ppn), and $J^0 \equiv \rho$.

Two schemes of the full calculation have been used to handle the final state interactions. One treats the pd and ppn breakup contributions separately and the other one is related to the optical theorem for the Compton scattering. In general, the

hadronic current is written as

$$J^{(0,\pm)} = J_{PWIA}^{(0,\pm)} + J_{rescatt}^{(0,\pm)}, \quad (1.52)$$

which separates the contribution from the plane wave approximation and from the re-scattering processes summed up to infinite order.

For the first method, the amplitudes for PWIA are

$$J_{PWIA}^{(0,\pm)} = \begin{cases} 3 \langle \phi_{pd} | (1 + P) \hat{J}^{(0,\pm)}(\vec{Q}) | \Phi_{bound} \rangle & \text{for pd breakup} \\ 3 \langle \phi_{ppn} | (1 + P) \hat{J}^{(0,\pm)}(\vec{Q}) | \Phi_{bound} \rangle & \text{for ppn breakup} \end{cases} \quad (1.53)$$

and for all re-scattering processes

$$J_{rescatt}^{(0,\pm)} = \begin{cases} 3 \langle \phi_{pd} | P \hat{J}^{(0,\pm)}(\vec{Q}) | U^{(0,\pm)} \rangle & \text{for pd breakup} \\ 3 \langle \phi_{ppn} | (1 + P) \hat{J}^{(0,\pm)}(\vec{Q}) | U^{(0,\pm)} \rangle & \text{for ppn breakup.} \end{cases} \quad (1.54)$$

Here $U^{(0,\pm)}$ obeys the Faddeev-type integral equation

$$|U^{(0,\pm)} \rangle = tG_0(1 + P)\hat{J}^{(0,\pm)}(\vec{Q})|\Phi_{bound} \rangle + tG_0P|U^{(0,\pm)} \rangle. \quad (1.55)$$

where t is the two nucleon t matrix. G_0 is the free 3N propagator, P is the sum of a cyclic and anti-cyclic permutation of the three particles, and ϕ_{pd} and ϕ_{ppn} are final channel states. In terms of the components of the hadronic currents, the response functions are thus given by

$$R_L = \sum_{m'\tau'} \int df' \delta(M + \omega - P'_0) (|J^0|^2) \equiv R_{\rho\rho}, \quad (1.56)$$

$$R_T = \sum_{m'\tau'} \int df' \delta(M + \omega - P'_0) (|J^+|^2 + |J^-|^2) \equiv R_{j+1j+1} + R_{j-1j-1}, \quad (1.57)$$

$$R_{T'} = \sum_{m'\tau'} \int df' \delta(M + \omega - P'_0) (|J^0|^2 - |J^-|^2) \equiv R_{j+1j+1} - R_{j-1j-1}, \quad (1.58)$$

$$R_{TL'} = \sum_{m'\tau'} \int df' \delta(M + \omega - P'_0) (-2\text{Re}[J^+ J^0 + J^- J^0]) \equiv -2\text{Re}[R_{j+1\rho} + R_{j-1\rho}]. \quad (1.59)$$

Since the calculation is built in a non-relativistic framework, the argument of the δ function is

$$M + \omega - P'_0 = \epsilon_{3He} + \omega - \frac{\vec{q}^2}{6M} - E_{f'} \equiv E - E_{f'}, \quad (1.60)$$

where ϵ_{3He} is the 3He binding energy (negative), the final energy P'_0 , the final total momentum $\vec{P}' = \vec{P}_N + \vec{P}_B = \vec{q}$, and $E_{f'}$ the internal energy related to the quantum numbers f' . In evaluating the response functions, we can either use the hadronic currents in Equations 1.53 and 1.54 or generalize the second method using the optical theorem.

In the following, we will derive the response functions with the optical theorem by evaluating each piece of the response function, R_{AB} , in which A and B denote either $\rho, j-1$ or $j+1$. The definition of R_{AB} is

$$R_{AB} \equiv \sum_{m'\tau'} \int df' \delta(E - E_{f'}) \langle \Phi_{f'm'\tau'}^- | A | \Phi_{bound} \rangle \langle \Phi_{f'm'\tau'}^- | B | \Phi_{bound} \rangle^* \quad (1.61)$$

$$= \sum_{m'\tau'} \int df' \langle \Phi_{bound} | B^\dagger \delta(E - E_{f'}) | \Phi_{f'm'\tau'}^- \rangle \langle \Phi_{f'm'\tau'}^- | A | \Phi_{bound} \rangle \quad (1.62)$$

$$= \langle \Phi_{bound} | B^\dagger \delta(E - E_{f'}) A | \Phi_{bound} \rangle \quad (1.63)$$

$$= \frac{1}{2\pi i} \left(\langle \Phi_{bound} | B^\dagger \frac{1}{E - i\epsilon - H} A - B^\dagger \frac{1}{E + i\epsilon - H} A | \Phi_{bound} \rangle \right) \quad (1.64)$$

$$= \frac{1}{2\pi i} \langle \Phi_{bound} | A^\dagger \frac{1}{E + i\epsilon - H} B | \Phi_{bound} \rangle^* - \frac{1}{2\pi i} \langle \Phi_{bound} | B^\dagger \frac{1}{E + i\epsilon - H} A | \Phi_{bound} \rangle. \quad (1.65)$$

We introduce

$$|\Phi_{A,B}^+\rangle \equiv \frac{1}{E + i\epsilon - H}(A \leftrightarrow B)|\Phi_{bound}\rangle. \quad (1.66)$$

The states $|\Phi_{A,B}^+\rangle$ contain all the complexity of the interaction among the three nucleons and using the Faddeev scheme, are evaluated as

$$|\Phi_{A,B}^+\rangle = G_0(1 + P)|U_{A,B}\rangle \quad (1.67)$$

with

$$|U_{A,B}\rangle = (1 + tG_0)(A \leftrightarrow B)^{(1)}|\Phi_{bound}\rangle + tG_0P|U_{A,B}\rangle. \quad (1.68)$$

Here we assumed that A or B can be decomposed as three single nucleon operators

$$(A \leftrightarrow B) = \sum_{i=1}^3 (A \leftrightarrow B)^{(i)}. \quad (1.69)$$

Now, according to the optical theorem,

$$\begin{aligned} R_{A,B} &= \frac{1}{2\pi i} (\langle \Phi_{bound} | A^\dagger G_0(1 + P) | U_B \rangle^* - \langle \Phi_{bound} | B^\dagger G_0(1 + P) | U_A \rangle) \\ &= \frac{3}{2\pi i} (\langle \Phi_{bound} | A^{(1)\dagger} G_0(1 + P) | U_B \rangle^* - \langle \Phi_{bound} | B^{(1)\dagger} G_0(1 + P) | U_A \rangle) \end{aligned} \quad (1.70)$$

In the last step we used Eq. 1.69 and the fact that the states to the left and right of A^\dagger or B^\dagger are antisymmetric.

Overall, the second method does not require summation over all the 3N continuum states for both types of breakup and is thus much superior, but one loses insight of how the response functions are built up in detail.

Another piece of information, which involves the various current exchange effects and hence is called meson exchange current (MEC) effect, is also much of importance in the full calculation. In ref. [41], one can treat MEC effect, e.g. the two-body current and the Δ resonance, as an additional correction for a single nucleon current. Following the notation of Eq. 1.69, this correction (for particle 1) is given by

$$(A \leftrightarrow B)^{(1)} = (A \leftrightarrow B)_{single}^{(1)} + (A \leftrightarrow B)_{exch}^{(23)}, \quad (1.71)$$

where the first term is the single nucleon current and $(A \leftrightarrow B)_{exch}^{23}$ is the corresponding component of a two body current acting on particles 2 and 3. The figure 1-7 shows typical meson exchange currents and resonances. Due to lack of computing power, not all the re-scattering process, meson exchange currents, and resonances have been included in the full calculation. Only important ones are considered and the effects, which are caused by the rest, however are found very small.

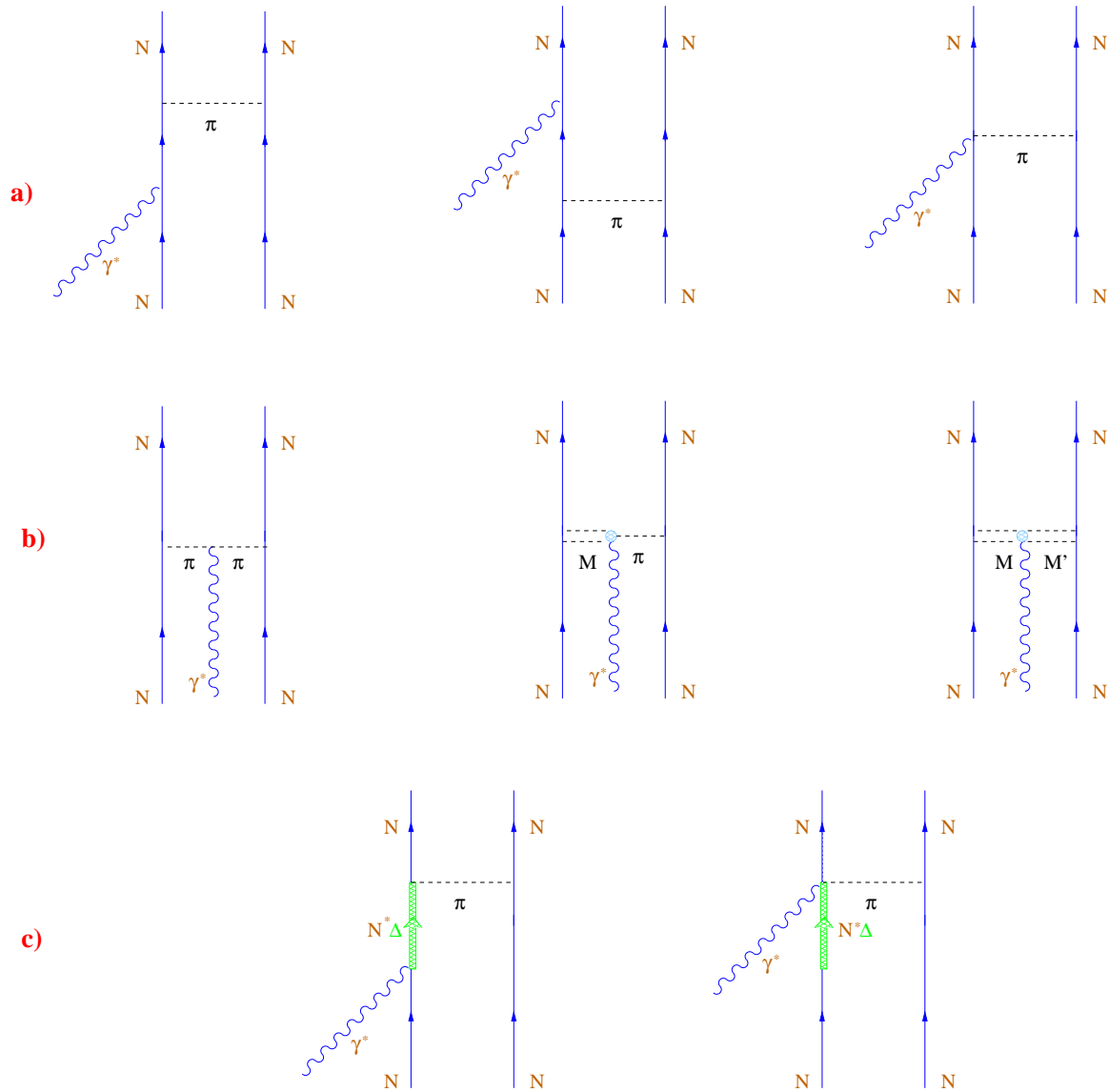


Figure 1-7: Typical MEC contributions. a) Graphs for coupling a photon to a pair of correlated nucleons; b) Graphs for π or M (other than π) in flight terms; c) Graphs for the pionic coupled to a Δ or N^* intermediate state.

1.5 Extraction of Nucleon Form Factor From Quasi-elastic ${}^3\vec{H}e(\vec{e}, e')$ Process

Because the ${}^3\text{He}$ nuclear spin is carried mainly by the neutron, $R_{T'}$ at quasi-elastic kinematics contains a dominant neutron contribution and is essentially proportional to $(G_m^n)^2$, similar to elastic scattering from a free neutron. Unlike the free neutron case, however, the unpolarized and polarized parts of the cross section contain contributions from both the protons and the neutrons. As a result, the ${}^3\text{He}$ quasi-elastic transverse asymmetry, $A_{T'}$ can be written as a function of the neutron magnetic form factor based on PWIA:

$$A_{T'}(G_m^{n\ 2}) = \frac{1 + aG_m^{n\ 2}}{b + cG_m^{n\ 2}}. \quad (1.72)$$

Here $|a| \gg 1$, and $b > c$ at low Q .

By Matching $A_{T'}$ from data and calculation around a quasi-elastic peak, one can extract G_m^n from experimental $A_{T'}$ results. The detailed discussions are included in Chapter 5. The extraction of form factors is usually model-dependent. Significant constraints on theoretical calculations are provided by high precision quasi-elastic asymmetry data at Q^2 values of 0.1 and 0.2 $(\text{GeV}/c)^2$ from H-arm in ${}^3\text{He}$ breakup region, where effects of final state interactions(FSI) and meson exchange currents (MEC) are expected to be large. For details see [71].

Chapter 2

Experimental Apparatus

2.1 Overview

The experiment to measure the transverse asymmetry $A_{T'}$ precisely in the quasi-elastic ${}^3\vec{H}e(\vec{e}, e')$ process from Q^2 value of 0.1 to 0.6 (GeV/c)² was performed at the Thomas Jefferson National Accelerator Facility. Incident longitudinally polarized electrons were scattered from the polarized ${}^3\vec{H}e$ target and the scattered electrons were detected in two identical Hall-A high resolution spectrometers (HRS): electron-arm spectrometer and hadron-arm spectrometer. The E95-001 experiment is a two single-arm experiment in which electron-arm spectrometer was employed to detect the scattered electron from the quasi-elastic kinematic, and hadron-arm spectrometer was employed as a elastic polarimetry to detect the scattered electron from the elastic kinematic. During this experiment, the incident electron beam energies of 778 MeV (1-pass) and 1727 MeV (2-pass) were used. Tab. 2.1 and Tab. 2.2 present the kinematic setups for two HRSs.

The Thomas Jefferson National Accelerator facility, the world's premier medium energy electron accelerator laboratory, is located in Newport News, VA. The facility consists of a continuous-wave electron accelerator, three complementary experimen-

Q^2 (GeV/c) ²	E (GeV)	E' (GeV)	θ (deg)
0.1	0.778	0.717	24.44
0.193	0.778	0.667	35.50
0.3	1.727	1.559	19.21
0.4	1.727	1.506	22.62
0.5	1.727	1.453	25.80
0.6	1.727	1.399	28.85

Table 2.1: Kinematic setup for electron-arm High Resolution Spectrometer

Q^2 (GeV/c) ²	E (GeV)	E' (GeV)	θ (deg)
0.1	0.778	0.760	23.73
0.2	1.727	1.691	15.04

Table 2.2: Kinematic setup for hadron-arm High Resolution Spectrometer

tal halls for different aspects of physics, a free electron laser facility and an applied research center. The CEBAF accelerator is a unique tool for exploring the transition between the region where strongly interacting (nuclear) matter can be understood as a bound state of protons and neutrons, and the region where the underlying fundamental quark and gluon structure of matter is evident. The accelerator is capable of delivering high quality continuous electron beam up to 6 GeV and is planned to be upgraded to 12 GeV in the near future. The layout of accelerator is shown in Fig. 2-1.

The electron beam used in CEBAF is generated in the following way. The 45 MeV electron beam from the injector is delivered to a race-track accelerator, which consists of two 0.4 GeV linac and two recirculation arcs. After passing the linacs and the recirculation arcs one by one, at the beam switch-yard, the beam can either be extracted and delivered into any of the three experimental halls, or kept running

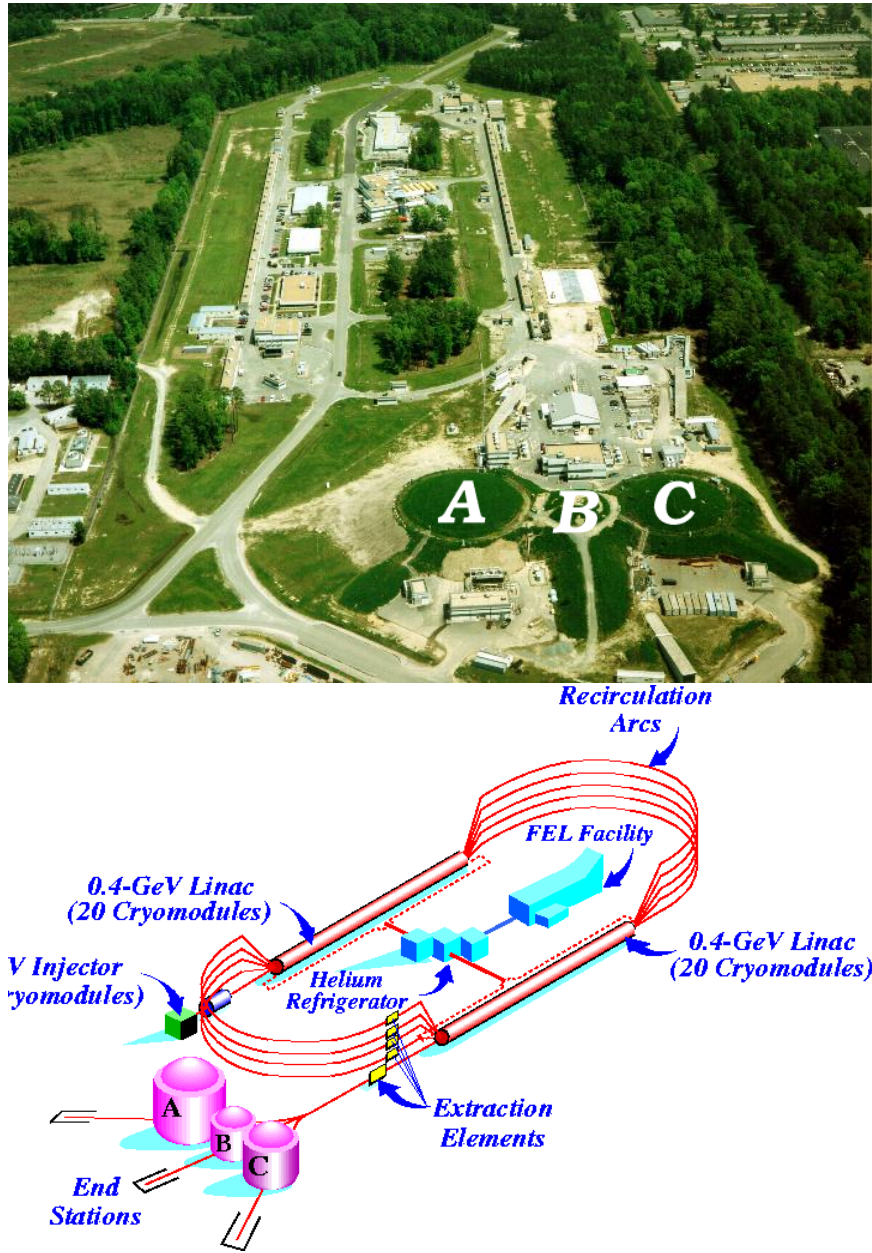


Figure 2-1: The accelerator layout

in the accelerator for additional acceleration. With each pass, an electron gains 1.2 GeV(0.8 GeV normally) at most. A grand total of 5 pass are available and the final maximum beam energy is thus 45 MeV plus 1200 MeV times 5 (number of pass) , which is 6045 MeV. Therefore, up to this stage, the facility can offer the continuous-wave beam with energy from 45 MeV to 6045 MeV. The whole beamline includes the RF cavities, the quadrupole magnets and the dipole magnets which are used to accelerate, focus and bend the electron beam respectively.

HALL A

Parameter	Method		Accuracy
Energy	ARC	Absolute	2×10^{-4}
		Relative	$\pm 1 \times 10^{-4}$
	eP	Absolute	2×10^{-4}
Energy Width	OTR*	$\frac{\Delta E}{E}(\sigma) \sim 1 \times 10^{-5}$	
Current($\geq 0.5\mu A$)	2 RF Cavities	Absolute	$\leq 2 \times 10^{-3}$
Charge($\geq 0.5\mu A$)	2 RF Cavities	Absolute	$\leq 2 \times 10^{-3}$
Position (at target)	2 BPM/Harp	Absolute	$140\mu m$
Direction (at target)	2 BPM/Harp	Absolute	$30\mu rad$
Stability (at target)	Fast Feedback*		$\leq 720Hz$ motion
Position			$\leq 20\mu m(\sigma)$
Energy			$\leq 10ppm(\sigma)$
Polarization	Møller	Absolute	$\frac{\Delta P}{P} \approx 3\%(\rightarrow 2\%)$
	Compton*	Absolute	$\frac{\Delta P}{P} \rightarrow 2\%$

*Still under development during the time of this experiment

Table 2.3: Determination of beam parameters

There are three experimental halls at Jefferson Lab (Hall A, Hall B, Hall C). Experiment E95-001 was carried out in Hall A. In this experiment, the polarized 3He target housed in the scattering chamber is located at the pivot of hall A. The beamline of Hall A is equipped by 2 beam position monitors (BPM) & Harp for monitoring beam position, raster for rastering beam, 2 beam current monitors (BCM)

for monitoring beam current, Møller Polarimeter and Compton polarimeter not fully committed then for determining beam polarization, and eP and Arc systems for measuring beam energy. The summary of control and measurement equipment along the beamline are given in Tab. 2.3 [83]. The longitudinally polarized electron beam is delivered to Hall A through the beamline and is incident onto the target. Scattered particles from target are collected and analyzed by a pair of spectrometers, which are set on two sides of the beamline and configured for different types of particles. While the spectrometers are labeled by “Electron Spectrometer” and “Hadron Spectrometer” in the Fig. 2-2, both spectrometers can detect either type of charge particles by simply switching the magnet field polarity of the magnets. For this inclusive experiment, both spectrometers are configured for e^- detection, and electronics in two arms are configured for two independent DAQ.

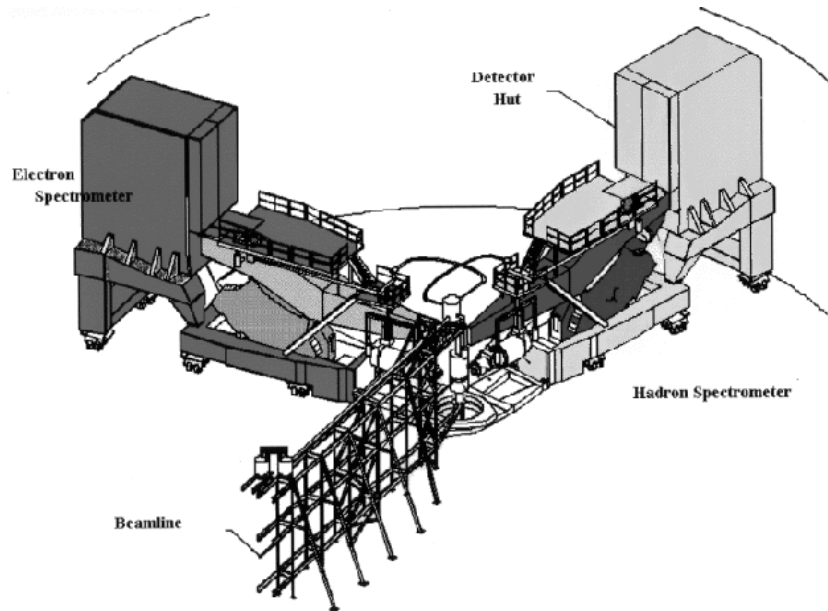


Figure 2-2: The Hall A Setup

2.2 Polarized Electron Source

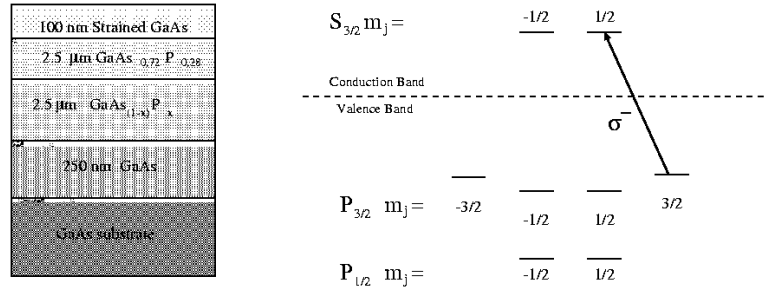


Figure 2-3: The layers of the strained GaAs cathode and the level diagram of the conduction and valence bands

The polarized electron source used at JLab is similar to the source used at SLAC [85]. The electron beam is generated by illuminating a GaAs cathode, which is placed in ultra-high vacuum, with high-intensity circularly polarized laser light. Fig. 2-3 shows that the cathode is made of various layers of GaAs combinations. The strain creates a gap in the different sub-levels of the $P_{3/2}$ electrons in the valence bands of the GaAs [84]. The left circularly polarized light with the right frequency, incident on the GaAs, only causes transition between the $P_{3/2}$ $m=3/2$ state in the valence band and the $S_{1/2}$ $m=1/2$ level of the conduction band. From there the polarized electrons diffuse to the surface and escape into the surrounding vacuum. Typically, the surface of the GaAs cathode is treated with Cs to lower the work function. The polarization of source electrons are consequently as high as 70%.

The incident laser light is circularly polarized by two Pockel's cells, one acting as a half-wave plate and the other acting as a quarter-wave plate. The helicity of the laser light is modulated by the Pockel's cell, which acts as a half-wave plate. In this way, the continuous beam helicity pulse is obtained with pulse width (or repetition rate) that can be controlled electronically to match the requirement of the accelerator and the experiment. The rate of the typical helicity pulse was about 1Hz at the beginning

of the experiment and was later changed to 30 Hz towards the end of this experiment.

2.3 Beamline

2.3.1 The Møller Polarimeter

In order to precisely determine the beam polarization, the Hall A Møller polarimeter shown in Fig 2-4 was designed to cover the electron beam energy ranging from 0.8 - 4.0 GeV. The Møller polarimeter includes a target system and an optical system. The target system consists of the vacuum chamber with a ironless magnet in which field two ferromagnetic foils in the nearly saturated states are placed, a moving system for the lifting and rotation of the target foil orientation relative to the electron beam axis, power supplies and electronic blocks for the target motion and the magnetization measurement, and software for remote operation, data acquisition and processing. The optical system of the Møller polarimeter contains three quadrupole and one dipole magnets.

The principle of the Møller polarimeter [86] is based on the fact that the spin-dependent asymmetry is proportional to the product of the beam and the target polarization for the Møller scattering process ($\vec{e} + \vec{e} \rightarrow e + e$). The target polarization value, determined from measurements of the saturation and the hysteresis curves, is used to extract the beam polarization from the measured asymmetry. The full expression of the differential cross-section depends on the beam and target polarization P_b and P_t as

$$\frac{d\sigma}{d\Omega} \propto (1 + \sum_{i=X,Y,Z} (A_{ii} \cdot P_b \cdot P_t)), \quad (2.1)$$

where $i = X, Y, Z$ defines the projections of the polarizations. Assuming the beam direction is along the Z-axis and that the scattering occurs in the scattering plane(XZ),

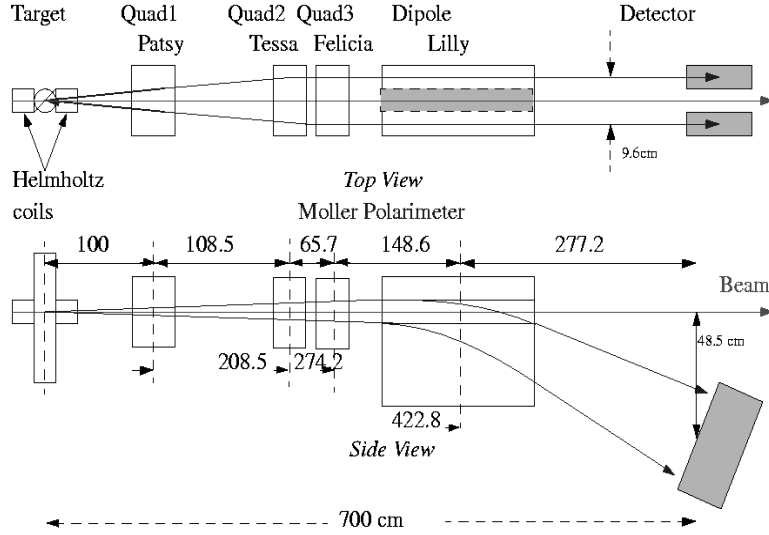


Figure 2-4: Møller Polarimeter Layout

the analyzing power can be written in terms of the scattering angle in the CM frame θ_{CM} as:

$$A_{ZZ} = -\frac{\sin^2\theta_{CM} \cdot (7 + \cos^2\theta_{CM})}{(3 + \cos^2\theta_{CM})^2}, \quad (2.2)$$

$$A_{XX} = -\frac{\sin^4\theta_{CM}}{(3 + \cos^2\theta_{CM})^2}, \quad (2.3)$$

$$A_{YY} = -A_{XX} \quad (2.4)$$

At $\theta_{CM} = 90^\circ$ the analyzing power has its maximum $A_{ZZ_{max}} = -7/9$. The main purpose of the Møller polarimeter is to measure the longitudinal component of the

beam polarization. Therefore, the practical value of the analyzing power can be very close to its maximum, $7/9$. Taking into account the angular acceptance and the background, the average value of the analyzing power for the hall A Møller polarimeter is 0.76 as determined by a Monte-Carlo simulation.

Six Møller measurements taken during E95-001 experiment are shown in Fig. 2-5. The results of these Møller measurements together with uncertainties are list in Tab. 2.4.

Date	$P_{beam}(\%)$	$err_{stat}(\%)$	$err_{sys}(\%)$
Jan. 22	70.0	2.0	3.5
Jan. 26	72.5	0.5	3.5
Jan. 31	74.2	0.3	3.5
Feb. 4	67.7	0.3	3.5
Feb. 8	69.5	0.2	3.5
Feb. 12	69.4	0.15	3.5
Feb. 19	71.3	0.15	3.5
Feb. 28	72.0	0.15	3.5

Systematic Errors

Origin	Relative error(%)
Target polarization	3.0
Target angle	0.5
Analyzing power	0.3
Transverse polarization	0.3
non-polarized background	< 1.0
deadtime	1.0
observed fluctuations	1.0
total	3.5

Table 2.4: Beam polarization results from Møller measurements

However, for experiment E95-001 Møller measurements were only used for cross-check because more precise polarimetry - elastic polarimetry was employed. The

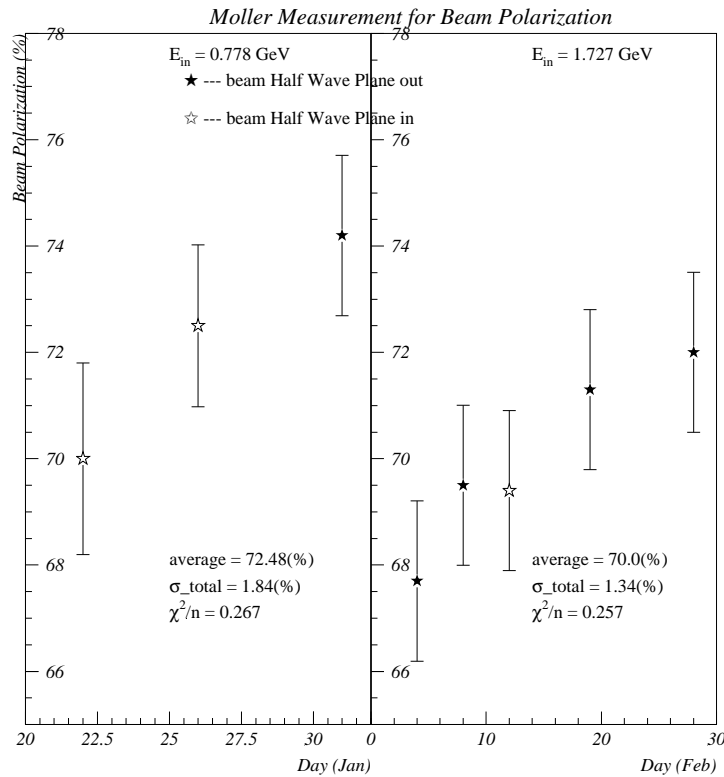


Figure 2-5: Møller results for the beam polarization

detailed discussion on the elastic polarimetry is in the next chapter.

2.3.2 Beam Energy

Beam energy can be analyzed in three independent ways for experiment E95-001: measuring the electron trajectory in a known B-field (Arc Measurement), the electron-proton elastic scattering (eP measurement), and the ^3He elastic scattering.

The Arc measurement sketched in Fig. 2-6 is performed along with an arc of beam pipe, a control electronics system and four superharp scanners near the entrance of

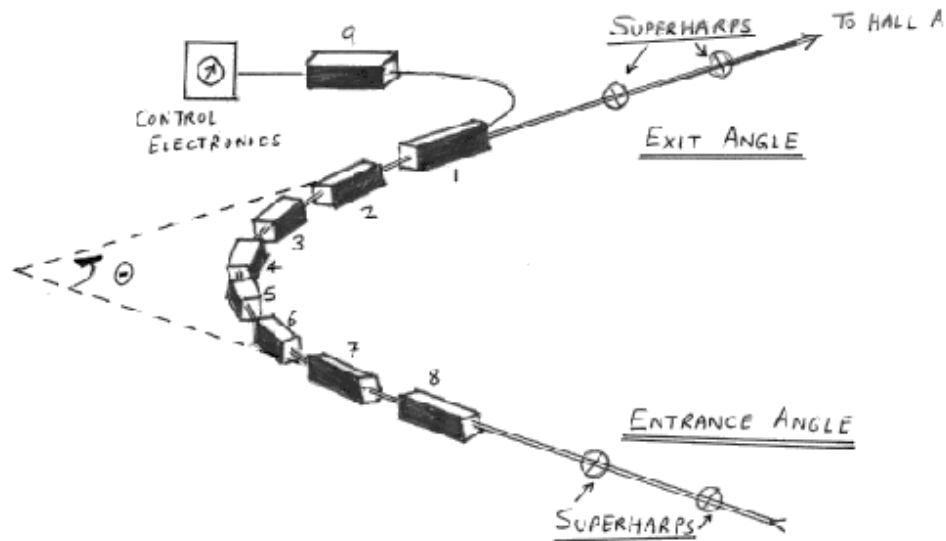


Figure 2-6: The Arc Measurement Layout

Hall A. The principle of the Arc Energy measurement is that an electron in a uniform magnetic field moves in a circle with a radius which depends on both the strength of the magnetic field and the electron's momentum (energy). The detailed relation is: $E = c \frac{\int B_{\perp} dl}{\theta_{\parallel}}$, Where B_{\perp} is the magnet field perpendicular to the electron momentum direction, dl is the path length of the electron, and θ_{\parallel} is the deflection angle of the electron after it passes through the B_{\perp} field. A superharp is the instrument to measure the beam position. Two superharps are installed on each side of the arc. These four superharps thus provide a method to precisely determine the electron deflection angle θ_{\parallel} . Along with the knowledge of the magnet field, the electron energy can be determined to the level of $\delta p/p = \pm 2 \times 10^{-4}$.

Both the eP and the ^3He energy measurements involve the well-known elastic scattering process. For the elastic scattering process, the incident energy can be determined if any two of these four quantities - the electron scattering angle, the

recoil particle angle, the scattering electron energy and the recoil particle energy are known. In the case of eP energy measurement, the electron scattering angle and the recoil proton angle are measured; in the case of the ^3He energy measurement, the electron scattering angle and energy are analyzed through one of the High Resolution Spectrometers. The more detailed discussion related to the ^3He energy measurement is described in the next chapter.

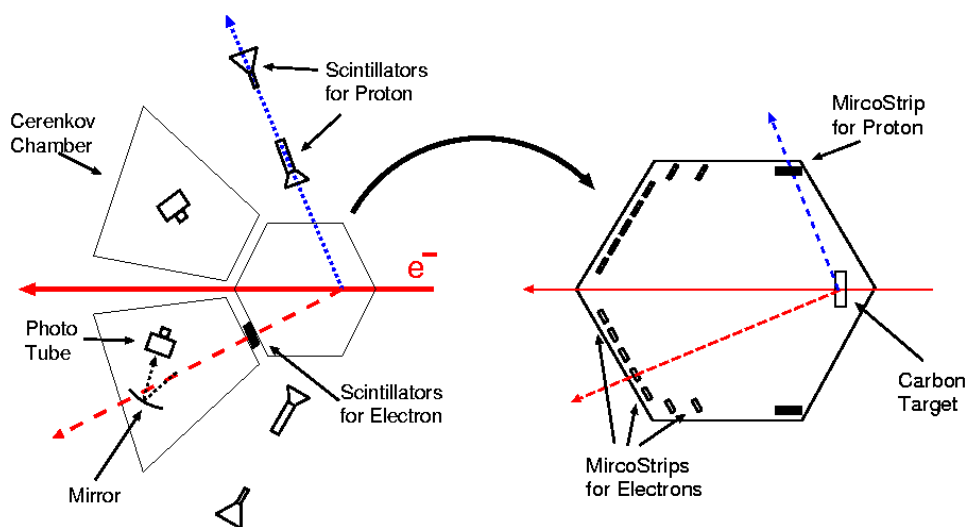


Figure 2-7: eP Measurement Layout

The schematics of the eP measurement is shown in Fig. 2-7. The eP measurement device consists of a CH_2 target, Čerenkov chambers, a Si strip detector and scintillators. A scattered particle from the target goes through the Si strip detector which gives the precise information on the position of a passing particle, then passes through a set of scintillators. From the TDC signals of the scintillators, the coincident triggers were generated and were used to define events. The scattered proton and electron can be well identified using the Čerenkov detectors. The knowledge of the electron and proton position from the Si strip detector allows for a calculation of the electron and the proton scattering angle, from which the beam energy can be calculated, and

the energy resolution of eP measurement $\delta E/E$ is about 1×10^{-4} .

2.3.3 Beam Current Monitors

In the beamline, about 24.5 meters upstream of the target, the complete beam current monitoring system, which consists of two RF cavities (BCMs) and a Unser monitor [87, 88] (shown in Fig. 2-8), was installed in a shielded and temperature stabilized enclosure. The whole assembly is contained within a large grey box. Sandwiched between two RF cavities (BCMs), the Unser monitor provides a direct measurement and absolute calibrations of the two RF cavities. The Unser monitor is a direct current transformer (DCT) consisting of two identical toroidal cores driven in opposite ways by an external source. In the absence of any DC beam current, the sense windings produce equal and opposite signals. The sum of the output signals from two windings is zero. When a DC beam current goes through the two cores, the net result is a flux imbalance between the two cores and generates an output signal which is highly linear to the beam current. The Unser monitor is calibrated by sending in a high-precision source, through a wire placed within the core to replace the beam. While the normal beam current is delivered by the accelerator, the signal is subject to noise and its offset drifts. The solution is to use the Unser monitor to calibrate the RF cavities by sending reference current. The two RF cavities are called “Upstream” and “Downstream” cavities corresponding to their positions relative to the Unser monitor. These cavities are two cylindrical wave guides made out of stainless steel, 15.48 cm in diameter and 15.24 cm in length. The resonant frequency is tuned to the 1497 MHz frequency of the JLab beam. Inside the cavity, a magnetic field probe (a loop antenna) is located in the place where the electrical field is at minimum and the magnetic field is at maximum. When the electron beam passes through, the cavity will excite the resonant transverse electromagnetic mode TM₀₁₀ at 1497 MHz and the probe will couple to this mode to provide an output signal proportional to the current.

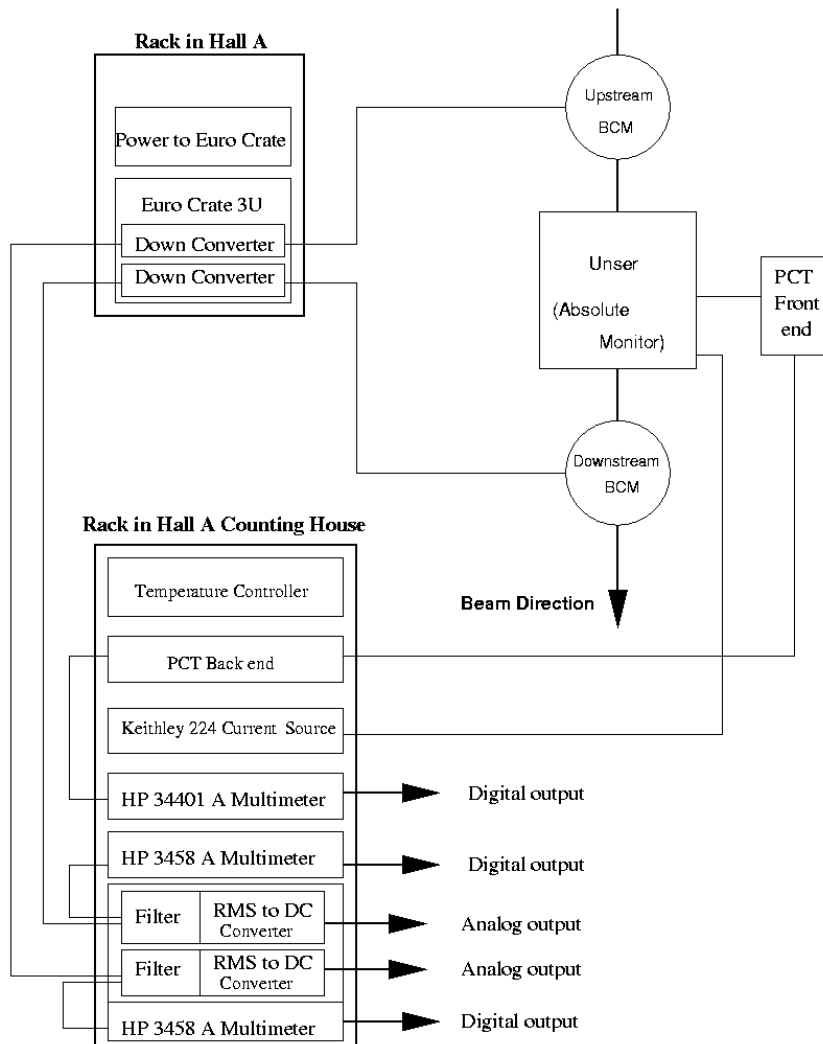


Figure 2-8: Beam Current Monitor Layout

In fact, there is another smaller antenna used to test periodically the response of the cavity by sending through a 1497 MHz calibration signal from a current source and detecting the induced current in the large antenna. The RF output signal for each cavity is down converted from 1497 MHz to 1 MHz by two converters located in the Hall. These signals are then sent to the counting house where the signals are filtered by 1 MHz bandpass filters to eliminate noise. The final signals can be taken into either EPICS datastream through a sampling digital voltmeter , or coda datastream gated by helicity state through Voltage-to-Frequency (V-to-F) converter and VME scalers. The scaler signal of V-to-F provides automatic integration over every a few seconds in a run. The magnitude of the last scaler signal in the datastream is equal to the total charge for each run multiplied by the V-to-F calibration number. The V-to-F calibration number is provided through a careful calibration using a precision voltage meter.

2.3.4 Beam Position Monitor

The position of the beam along the beamline was monitored by two beam position monitors (BPM) upstream of the target. These two BPMs (03A and 03B) are 1.1 m and 7.5 m away from the target, respectively. A BPM plotted in Fig. 2-9 is simply a cavity with four antennas at $\pm 45^\circ$ to the horizontal and vertical directions. The BPM signal picked up by each antenna is proportional to the instantaneous distance between beam and the antenna. The beam position at a BPM is thus the difference between the properly normalized and calibrated signals from two antenna on the opposite sides of the beamline. Two wire scanners (superharp) installed before the target can directly measure beam position. While the wire scanner can not be used as a online monitor of the beam position because the beam will be blocked by the wares of wirescanner as wires scan the beam, they give an absolute calibration for the two associated beam position monitors. From the two values of beam position

at the two BPMs, one can easily determine the beam position on the target and the beam direction. At a beam current of $10 \mu\text{A}$, the resolution of the beam position at the target is less than $20 \mu\text{m}$.

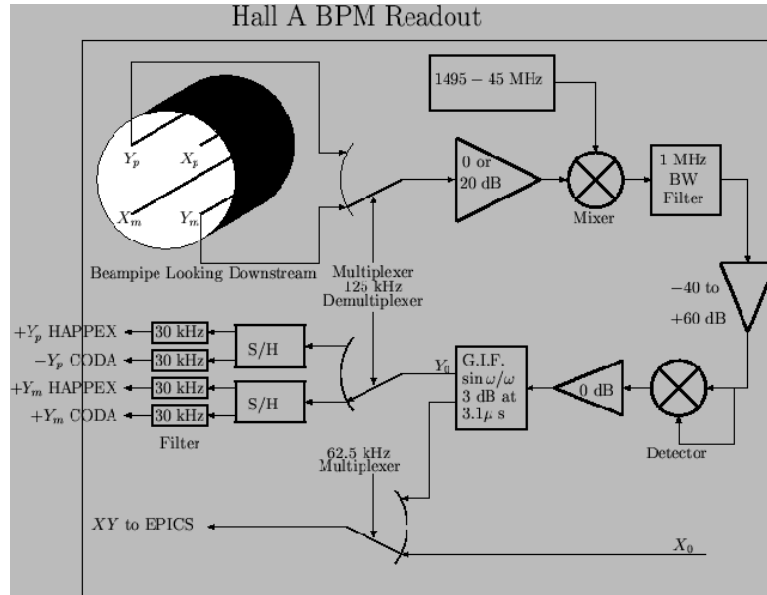


Figure 2-9: Beam Position Monitor Layout

During the entire experiment, the size of beam spot at the target was around ($3\text{mm} \times 4\text{mm}$) with beam faster raster on, and the central value of beam spot was kept within 0.5 mm to a reference beam position where the dilution from the empty reference cell was found to be the best.

2.3.5 Beam Fast Raster

In an effort to prevent damage from depositing too much power in too small an area on the target and reduce the beam-induced target density change, the beam is rastered before it impinges onto the target. The hardware for the raster system is installed 23 m upstream of the ^3He target. The system consists of two sets of steering

magnets. The first and second sets have their magnetic field oriented to deflect the beam horizontally and vertically, respectively. Both the ratio of the oscillation frequencies of the two coils and the amplitude of the driving current of the two coils were chosen so that the result of beam pattern would sweep out a 3 mm diameter disk on the target.

2.4 Polarized ^3He Target

2.4.1 Introduction

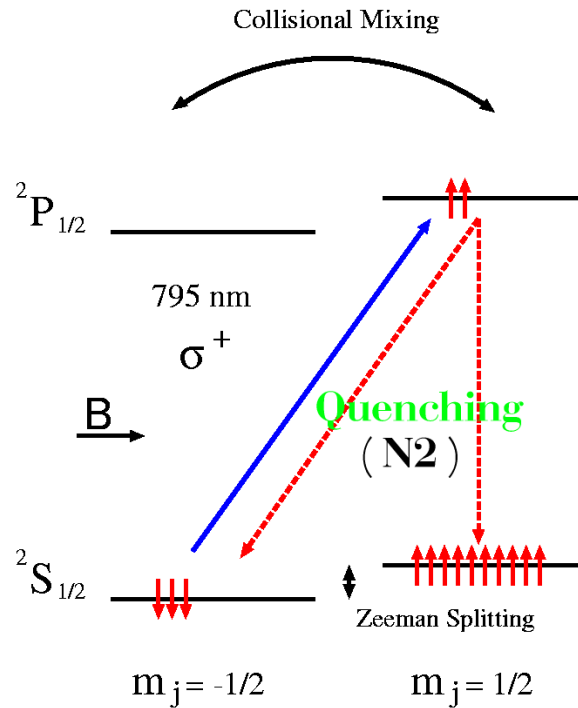


Figure 2-10: The optical pumping mechanism without considering the hyperfine interaction

Our experiment employed a polarized ^3He target as an effective source of polarized neutrons. The optical pumping process is that through transfer of angular momentum

from photons (polarized laser light) to the atomic electron, large unequal populations of atomic magnetic substates can be generated. Because the energy gap between $2S$ and $2P$ states of 3He atom is too large for the energy of laser source, practically the 3He target can not directly polarized through the optical pumping process. Two indirect methods have been developed to optically pump 3He atoms. One is referred to as the spin-spin interaction (spin-exchange collision) with an optically pumped alkali metal vapor, such as Rb vapor [98] and the other is referred to as metastability-exchange optical pump [97]. we employed the first method: spin-exchange optical pumping scheme in this experiment for a high density target.

Spin-exchange pumping scheme works as following: the electron energy state of the alkali metal atom (${}^{87}Rb$) splits into various sub-level states with the presence of a magnetic field. If ${}^{87}Rb$ atom is exposed with a circularly polarized laser at the right transition frequency in the same direction as the magnetic field, an electron from the certain sub-level energy state will be excited and the energy sub-level will become depopulated. The outer electron of ${}^{87}Rb$ atom is thus polarized along the magnetic field. Via spin-exchange collision with polarized rubidium vapor, polarization of the 3He nuclei was achieved.

In Fig. 2-10, the process of optical pumping from the magnetic sublevel $m=1/2$ of the Rb ground state neglecting hyperfine structure is depicted. As excited electrons of Rb return to the ground state, they will emit a photon at the wavelength(795nm). This photon is randomly polarized and can excite the ground state of Rb . Thus the polarization will decrease from this process, the so-called radiation trapping effect. The admixture of a small amount of N_2 gas quenches both P-state sublevels, therefore reducing the polarization losses from the radiation trapping. The amount of N_2 gas is mixed to be a couple of orders of magnitude smaller than the 3He density and a few orders of magnitude larger than Rb density in order to compromise between the quenching rate and the contribution of N_2 to the dilution factor. Only

about 5% of excited electrons are expected to decay by emitting a photon under this condition [103].

The average polarization, P_{Rb} of the Rb vapor is given in terms of the optical pumping rate, R and the spin destruction rate, Γ_{SD} :

$$P_{Rb} = \frac{R}{R + \Gamma_{SD}}. \quad (2.5)$$

The spin destruction rate constant due to the collisions with a gas species is proportional to the density of the species, so it can be written as

$$\Gamma_{SD} = k_{Rb-he}[^3He] + k_{Rb-N_2}[N_2] + k_{Rb-Rb}[Rb] \quad (2.6)$$

with spin destruction rate constants $k_{Rb-i} = \langle v\sigma_{Rb-i} \rangle$. These constants have been measured by Wagshul and Chupp [99]: $k_{Rb-he} \leq 2 \times 10^{-18} \text{cm}^3/\text{s}$, $k_{Rb-N_2} = 8 \times 10^{-18} \text{cm}^3/\text{s}$, and $k_{Rb-Rb} = 8 \times 10^{-18} \text{cm}^3/\text{s}$. The densities of the various species for our experiment are $[He] \approx 2 \times 10^{20} \text{cm}^{-3}$, $[N_2] \approx 2 \times 10^{18} \text{cm}^{-3}$ [100], and $[Rb] \approx 2.5 \times 10^{14} \text{cm}^{-3}$ [101]. So an order of magnitude of the spin destruction rate ($\frac{1}{\Gamma_{SD}}$) is 10^{-3}s . Because the optical pumping rate is about $5 \times 10^4 \text{s}^{-1} (\gg \Gamma_{SD})$, rubidium vapor is nearly 100% polarized in regions where optical absorption is occurring. The evolution of the 3He nuclear polarization due to spin exchange collision is described in the following equation:

$$P_{He}(t) = \langle P_{Rb} \rangle \frac{\gamma_{SE}}{\gamma_{SE} + \Gamma} (1 - e^{-(\gamma_{SE} + \Gamma)t}), \quad (2.7)$$

where $\langle P_{Rb} \rangle$ is the volume averaged rubidium polarization and is about 60% in our experiment, the spin exchange rate is given by $\gamma_{SE} = k_{SE}[Rb]$ with the spin exchange rate constant, $k_{SE} = (6.7 \pm 0.6) \times 10^{20} [\text{cm}^3]$ [102], and Γ is the 3He nuclear spin relaxation rate. The relaxation mechanism includes the depolarization mechanism

(the $^3\text{He} - ^3\text{He}$ magnetic dipole interaction), the wall relaxation, the relaxation due to the holding field inhomogeneities, and the beam-induced relaxation. In Table 2.5, the estimations of the various relaxation mechanisms are given [105].

relaxation rate	amount
$\Gamma_{dipolar}$	$\frac{1}{80}h^{-1}$
Γ_{wall}	$\frac{1}{60}h^{-1}$
$\Gamma_{\Delta B}$	$\frac{1}{10^4}h^{-1}$
Γ_{beam}	$\leq \frac{1}{30}h^{-1}$

Table 2.5: Relaxation rate of various depolarization mechanism

2.4.2 Target Setup

The target system shown schematically in Fig. 2-11 was used in E95-001. It consisted of four main systems: an optical pumping system, a Nuclear Magnetic Resonance (NMR) system, an Electron Paramagnetic Resonance (EPR) system (We did not really use it during this experiment), and the target.

Optical Pumping System

The complete optical pumping system comprises of two sets of Helmholtz coils used to create a magnetic holding field and the laser system used to optically pump the rubidium vapor. The two sets of the Helmholtz coils, which were perpendicular to each other, were 19 degrees off the central beamline in order not to block the scattered particles. The size of each coil is about 60 inches in diameter. The magnitude of the current for each coil could be adjusted so that both the direction and the magnitude of the holding field would satisfy the experimental requirements. In the central region of the target, the magnitude of the holding field was typically about 20-25 Gauss. The laser system used to optical pump the rubidium vapor consisted of four (seven for E94-010) diode lasers, a set of circular polarizing optics, and a set of mirrors and lenses

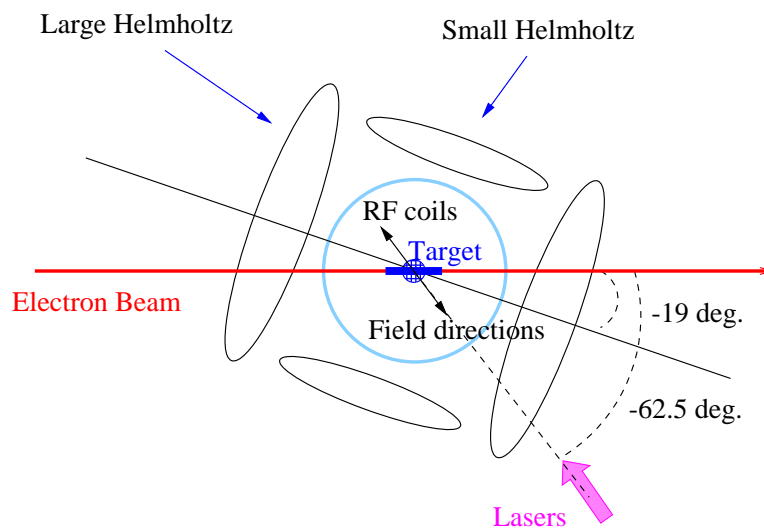
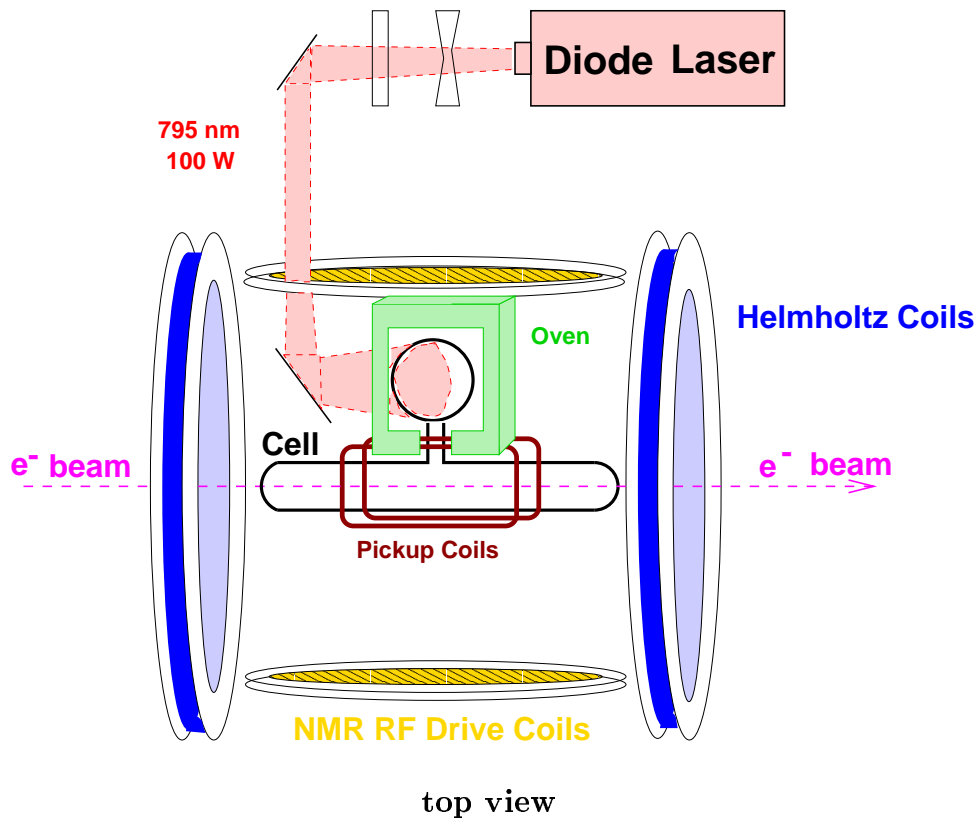


Figure 2-11: The E95-001 target system layout

to direct the light onto the target. The entire laser system was shielded in a concrete hut located near the target in Hall A. The output power of each laser was 30 Watts at a central wavelength of 795 nm. Four lasers were dedicated for optical pumping and were pointed to -62.5° with respect to the incident electron beam direction. The helicity of the lasers could be reversed remotely using a set of the half-wave plate in the laser hut, and the two polarization directions 180° with respect to each other were thus available in the experiment.

The Target

Fig 2-12 shows that there are two glass cells: the ^3He target (at the top of the ladder) and the reference target (at the bottom of the ladder) and the BeO foil (in the middle of the ladder) mounted on the target ladder. To make sure that the glass cell was not overheated by the electron beam, the BeO target was often used to check the size of the beam spot before the production run was taken. Two cells: the ^3He cell for E95-001 named Cuervo and the reference cell were made from an aluminum-silicate glass (Corning 1720¹ or GE 180²). The thickness of the glass wall and the entrance and exit windows for the two cells was measured using laser interferometry and are listed in Table 2.6 [106, 107]. The polarized ^3He target is a double-cell system filled with ^3He gas of a pressure 9.98 ± 0.21 amg.³ [105]. A spherical upper part of the ^3He target is called the pumping cell within which the optical pumping and the spin exchange process take place. The other cell of the ^3He target is the target cell which is a 40 cm long tube where the electron beam passes and thus the electron scattering takes place. In the middle, the transfer tube connects the two cells to become a one-piece- ^3He target. The reference cell and the cooling jets of ^4He were designed and constructed by our group at MIT. The reference cell is a 40cm long glass cylinder

¹ $\rho_{1720} = 2.53 \text{g/cc}$

² $\rho_{ge180} = 2.76 \text{g/cc}$

³An amagat(amg.) is the number of particles per cubic centimeter at 0° and 1 atmosphere:
 $1 \text{amg.} = 2.689 \times 10^{19} \text{cm}^{-3}$

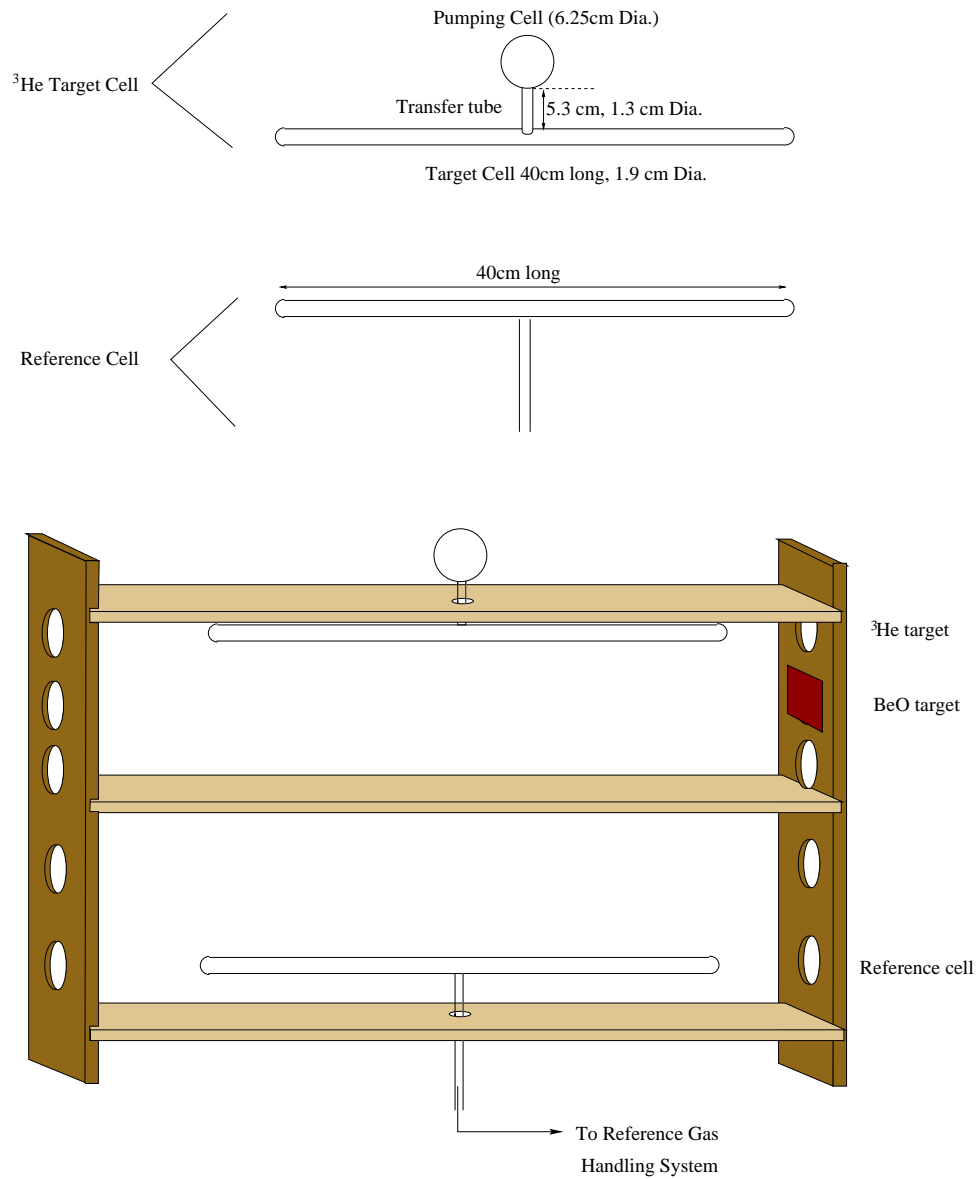


Figure 2-12: The target cells and the target ladder

Cell:**Cuervo**(GE 180)

Average wall thickness = 1.200(mm) \pm 0.020

Position along Electron side(in.)	+5.0	+1.7	-1.8	-4.0
Thickness(mm)	1.237	1.218	1.196	1.184
Position along Electron side(in.)	+4.0	+2.2	-0.5	-3.0
Thickness(mm)	1.208	1.198	1.230	1.187
Out of scattering plane(H side)	5.5	2.5	-1.5	-4.2
Thickness(mm)	1.173	1.189	1.199	1.185

Up-Window thickness(μ m)	Down-Window thickness(μ m)
130 \pm 1.3	142 \pm 1.3

Cell:**Reference Cell**(Corning 1720)

Average wall thickness(mm) = 1.171 \pm 0.032

Position along Electron side(in.)	+4.7	+2.5	-0.3	-4.0
Thickness(mm)	1.132	1.197	1.184	1.229
Position along Electron side(in.)	+0.0	-1.5	-4.0	-4.5
Thickness(mm)	1.149	1.162	1.163	1.143

Table 2.6: Wall thickness and window thickness of Cuervo and reference cell

connected to a gas handling system. Using the gas system and a remote control system, the reference cell can be evacuated or filled with either ^3He or N_2 gas up to 70 psi in the Hall A counting house. For the study of dilutions from the empty target cell and a small amount N_2 in the ^3He target for assisting the optical pumping, and the understanding of the ^3He target density in operating conditions, some data were taken with the reference cell empty, filled with ^3He or N_2 gas.

The target ladder was mounted onto a Torlon (a high temperature anti-radiation plastic) oven. Hot air flowed into the oven through a pipe which was connected to an electric coil heater. The pumping cell was inside the oven and was heated by the hot air. The oven are heated to 170-180 $^\circ\text{C}$ to produce R_b vapor to be optically pumped.

The Resistive Thermal-couple Devices (RTD) were mounted on both the pumping cell and the target cell in order to measure and regulate the temperature of oven and the target. ^4He gas from cooling jets flow through the entrance and exit windows of the target cell to remove the beam-induced heat. The oven was installed on a plastic rod that could move vertically. Through remote controlling of the motion of the rod, different targets, such as BeO target, could be put into the beamline.

The NMR System

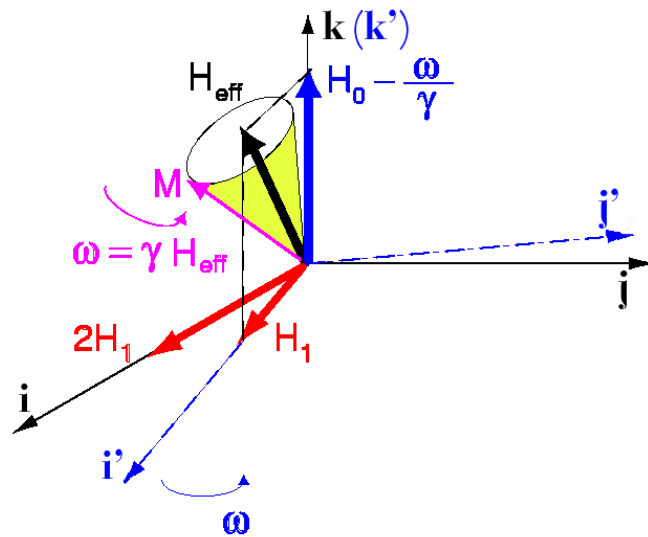


Figure 2-13: The effective field H_e

The NMR system is comprised of a computer system, a pair of pickup coils with a lock-in amplifier, and two pairs of Helmholtz coils and a pair of RF coils. Those three pair of coils are perpendicular to each other. The nuclear polarization of the ^3He target is measured throughout the experiment by the NMR system based on the Nuclear Magnetic Resonance (NMR) technique of Adiabatic Fast Passage (AFP) [109]. To explain the idea of the NMR-AFP, let us consider a free particle placed in the holding

field H ($H_z \hat{z}$) and the RF field ($2H_1 \cos(\omega_0) \hat{i}$), with spin I and magnetic moment $M = \gamma I$, where γ is the gyromagnetic ratio. In the system rotating with $\omega_0 \hat{k}$, the RF field can be decomposed into a stationary part $H_1 \hat{i}'$ and a part rotating at a frequency $2\omega, H_1 \cos 2\omega t \hat{i}' - H_1 \sin 2\omega t \hat{j}'$. As the rotating part does not affect the spin of the particle, thus the effective field (shown in Fig: 2-13) becomes

$$H_e = (H_z - \frac{\omega_0}{\gamma}) \hat{k} + H_1 \hat{i}' \quad (2.8)$$

If initially the holding field H_z is much smaller than $\frac{\omega_0}{\gamma}$, the effective field is almost parallel to the k -axis. As the magnetic field is swept through resonance until H_z is greater than $\frac{\omega_0}{\gamma}$. The effective field changes away from \hat{k} to $-\hat{k}$ and the effective field H_e equals to $H_1 \hat{i}'$ at the resonance ($H_z = \frac{\omega_0}{\gamma}$). In order that the magnetization follows the effective field adiabatically, the sweep has to be slow enough. On the other hand, the sweep can not be too slow, because the spin relaxes [110] faster near the resonance as the effective field is very small. These two constraints for AFP are given by

$$D \frac{|\Delta H_z|^2}{H_1^2} \ll \frac{\dot{H}_z}{H_1} \ll \gamma H_1. \quad (2.9)$$

Here $D \frac{|\Delta H_z|^2}{H_1^2}$ is the relaxation rate in the rotation frame and AFP refers to a technique to reverse the spin of the particle with respect to the static magnetic field ($H_z \hat{k}$). There are two ways to achieve AFP measurement, one can sweep either the hold field or the RF frequency to go through resonance. We have chosen the first approach to measure the ^3He polarization by scanning the holding field back and forth from 25 to 32 G, at rate 1.2 G/s. When the magnetic field passes through the 28.06G ($\frac{\omega_0(91kHz)}{\gamma}$), the spin precessing rapidly at RF frequency ω in the $(i \times j)$ plane of the lab frame. The magnetic flux of a pair of the pickup coils placed in the $(i \times k)$ plane will get to the maximum value, which is proportional to the polarization of ^3He target. The entire scanning process results in two peaks of NMR signals with different sign. The

strength of the NMR signals indicates the amount of the polarization of ^3He .

To obtain the polarization of ^3He from an NMR measurement, the ^3He signal is compared with the signal from an identical water sample. The thermal polarization of protons in water is given from the Boltzmann distribution by $P_{thermal} = \tanh\left(\frac{\mu_p B}{k_B T}\right)$ with the proton magnetic moment $\mu_p = 2.793\mu_N$. Though the order of magnitude of the thermal polarization is as small as 10^{-9} for a holding field B of 18 Gauss and the room temperature, this polarization can produce a measurable AFP signal that can be used to calibrate the ^3He - AFP signal. The nuclear polarization of the ^3He target is given as $P_{He} = c_w \times S_{He}$ with the water calibration constant, c_w and the magnitude of the ^3He -AFP signal, S_{He} . The c_w is roughly expressed as

$$C_w = \left(\frac{P_{thermal}}{S_w} \right) \left(\frac{(QnV\mu)_p}{(QnV\mu)_{He}} \right), \quad (2.10)$$

where Q is the quality factor of the pick-up circuit, n is the number density of spin 1/2 particles with momentum μ , and V is the volume of the cell. The corrections for c_w includes the flux corrections, Q-curve corrections etc. For detailed information about the polarized ^3He target, please refer to [105, 106].

2.5 High Resolution Spectrometers (HRS)

In order to achieve a missing energy resolution of 200-500 KeV to clearly identify nuclear final states, two Hall A spectrometers and associated instruments are designed to have high resolution and high accuracy in the determination of particle momenta and the scattering angle. This two high resolution spectrometers are an identical pair of QQDQ magnetic spectrometers which compose of three $\cos 2\theta$ superconducting quadrupole magnets, Q1, Q2 and Q3 and one superconducting dipole magnet. Each spectrometer shown in Fig. 2-14 has a vertical ending plane and a 45° bending angle. The overall optical length of the spectrometer, from target to focal plane, is 23.4 m.

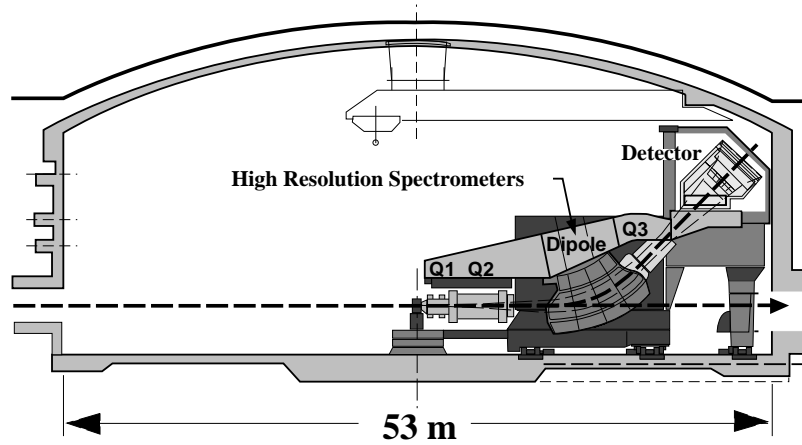


Figure 2-14: Side view of the Hall A High Resolution Spectrometer. Shown are scattering chamber and the spectrometer magnetic elements, including the dipole and the three quadrupole magnets (labeled Q1, Q2, Q3). The detectors are inside the shields house at the top of the spectrometer.

The momentum range of the spectrometer is from 0.3 (GeV/c) to 4.0 (GeV/c). The momentum acceptance is $\sim 9\%$ and momentum resolution is about 1×10^{-4} . The main characteristics of the spectrometer are listed in Tab. 2.7.

The optical property of each HRS is point-to-point in the dispersive direction. Particles traveling through a spectrometer, the position and angular coordinates of the particle tracks are measured by the vertical drift chambers. The so-called “focal plane” coordinates are used to reconstruct the coordinates of the particle track at the interaction point in the target.

2.6 Detector Package

Both Figures 2-16 and 2-15 show typical electron arm and hadron arm detector packages. In order to understand the physics behind the scattering process, it is crucial

Momentum Range	0.3 - 4.0 GeV/c
Configuration	QQDQ
Optical Length	23.4 m
Momentum Acceptance	$\pm 4.5\%$
Dispersion (D)	12.4 cm%
Radial Linear Magnification (M)	2.5
D/M	5
Momentum Resolution (FWHM)	1×10^{-4}
Angular Acceptance	
Horizontal	± 28 mr
Vertical	± 60 mr
Solid Angle:	
(rectangular approximation)	6.7 msr
(elliptical approximation)	5.3 msr
Angular Resolution: (FWHM)	
Horizontal	0.6 mr
Vertical	2.0 mr
Transverse Length Acceptance	± 5 cm
Transverse Position Resolution (FWHM)	1.5 mm
Spectrometer Angle Determination Accuracy	0.1 mr

Table 2.7: Hall A High Resolution Spectrometer (HRS) general characteristics

to precisely identify the trajectory and thus to determine the momentum and the identity of the scattering particle. The certain combination of the detectors in the detector package satisfies the requirement of individual experiment. The following components of the electron arm detector package were used for this experiment

- A pair of Vertical Drift Chamber (VDC) to locate precisely the trajectories of the particle and to determine its momentum.
- Two scintillator planes (S1 and S2) to generate the trigger and provide time-of-flight information.
- Gas Čerenkov detector for e^-/π^- separation.

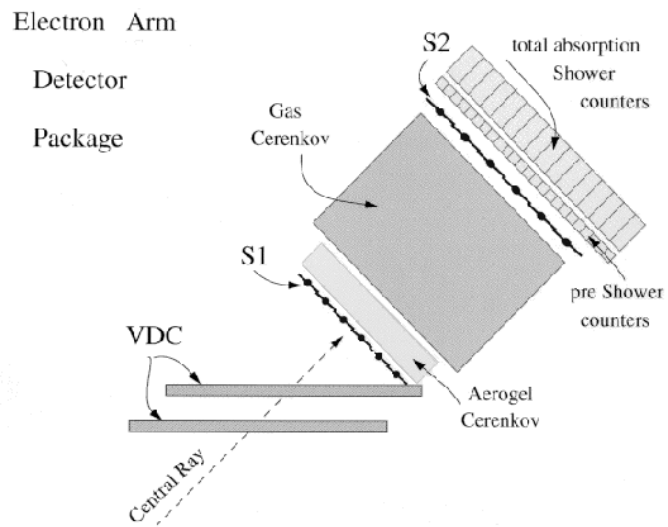


Figure 2-15: High Resolution Spectrometer in electron-arm (HRSE) Setup

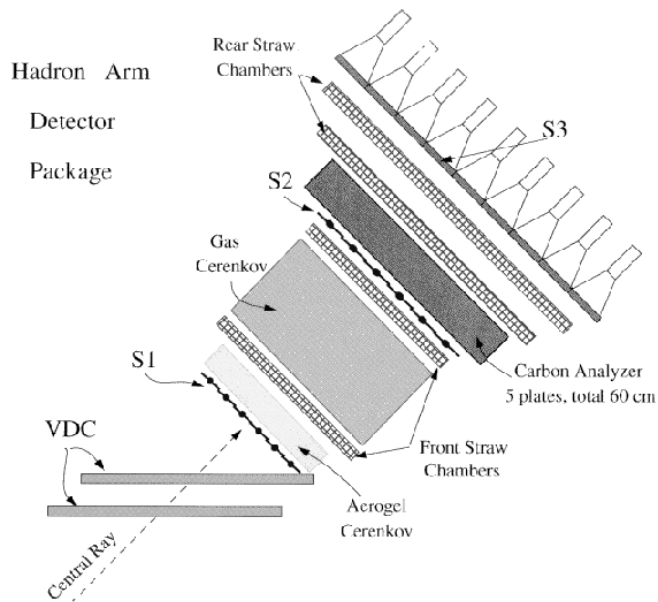


Figure 2-16: High Resolution Spectrometer in hadron-arm (HRSH) Setup

- Preshower and shower counter to provide additional e^-/π^- separation.

Except the preshower, all other detectors were included in the hadron-arm detector package. Next, we discuss the function of each individual detector.

2.6.1 Vertical Drift Chamber

The Vertical Drift Chambers for the HRS pair were constructed, commissioned and installed by MIT and JLab a few years ago. A pair of VDCs (shown in Fig. 2-17) have been playing a main role in reconstructing the trajectory and determining the momentum of a charge particle in both the electron and hadron spectrometers.

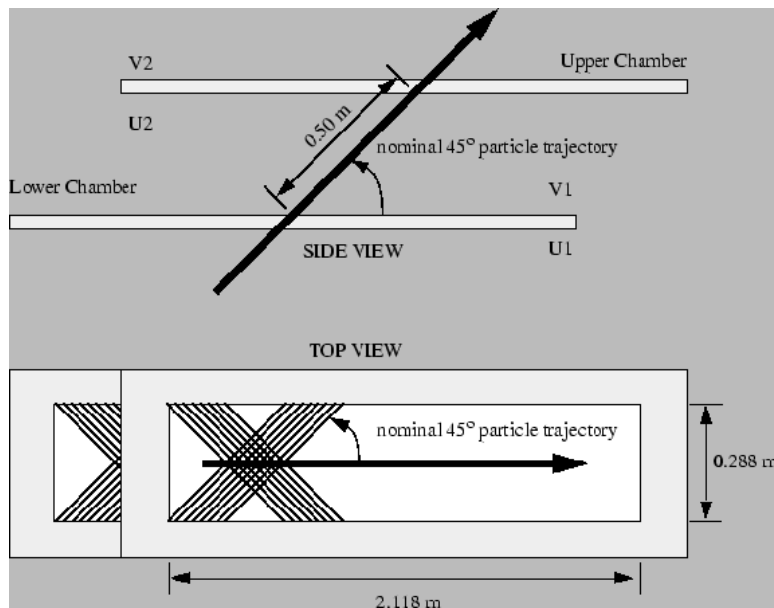


Figure 2-17: VDC Layout

Physically the VDCs locate in front of all the other detectors and behind the third quadrupole magnet. The size of each VDC is about 240 cm long, 40 cm wide and 10 cm high. The active area is 211.8 cm \times 28.8 cm. In the VDC package, the bottom

chamber is placed at the actual focal plane and the top one, which is shifted by about 35 cm with respect to the bottom one in the dispersive direction, is about 35 cm above the bottom one. The VDC wires are enclosed between two Mylar windows and form two wire planes (one U and one V) perpendicular to one another inside each chamber. Each plane contains 368 gold-plated tungsten wires each with a diameter of 20 μm . The gas flowing through the chamber was 38% ethane, 62% argon.

When a charged particle, such as an electron, passes through the chamber, the gas along the particle's track will be ionized. The electrons resulting from these ionizations follow the electric field lines generated by the cathode planes and anode wires. A high voltage between the cathode planes and anode wires is usually about -4kV. Near the wire, the field is radial and increases as $1/r$, while away from the wire the field is parallel and uniform. Away from the avalanche region, electrons gain so little energy between the collisions that they keep a constant drift velocity. When an electron gets close enough to the wires, it reaches a region where the electric field is stronger, and the electron gains enough energy to ionize more gas atoms and an electron multiplication, the so-called avalanche, occurs. As electrons finally are collected on the wire, a signal will feed into a ADC and a TDC. A TDC is used to measure the time elapsed between the initial ionization and the induction of the signal on the sense wire. Knowledge of the drift velocity of the electron in the chamber gas and the TDC information allows the drift distance and eventually the perpendicular distance between the particle trajectory and the wire to be deduced. Generally, five and six adjacent wires fire for a trajectory. Fitting the results of the distances between the trajectory and wires, the particle trajectory and the intersection point between the trajectory and the wire plane may be determined. The resolution on the electron's position at wire planes is approximately $\pm 200 \mu\text{m}$. For further information of hall A VDCs, see references [89], [90], and [91].

2.6.2 Scintillator

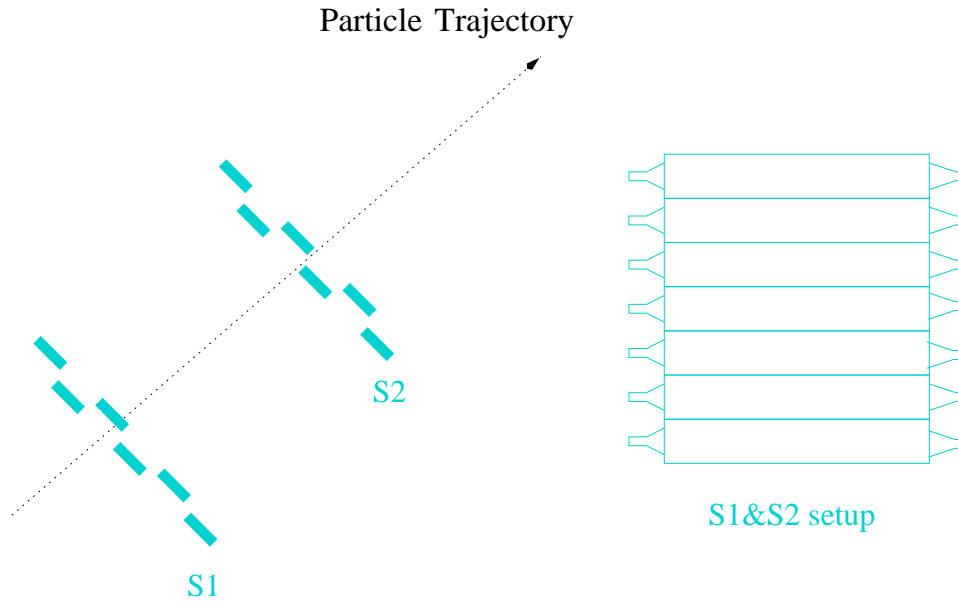


Figure 2-18: The scintillator planes (S1&S2) layout

Two scintillator planes (S1 and S2) are located 1.5 m and 3.5 m downstream of the center of focal plane and are perpendicular to the normal central ray. As can be seen in Fig. 2-18, each scintillator plane consists of six scintillator paddles which overlap by 5 mm each. A 2-inch photo-multiplier tube is mounted on either side of the paddle. If a photo-multiplier tube fires, both an Analog-Digital Converter (ADC) and a Time-Digital Converter (TDC) signal will be sent to the data acquisition system. The trigger of the data acquisition is formed by the TDC signals of S1 and S2 with the proper logic. The active area of S1 is about $170 \text{ cm} \times 35 \text{ cm}$ and that of S2 is about $220 \text{ cm} \times 54 \text{ cm}$. The spectrometer acceptance is smaller than the geometric limits of the scintillator active areas. This ensures a high trigger efficiency.

How to use the scintillators and proper electronic logic to set up triggers is discussed in section 2.7.1.

2.6.3 Gas Čerenkov

The Gas Čerenkov Detectors were employed in both HRSE and HRSB to separate the e^- and π^- . The Čerenkov counter is based on a phenomenon (the Čerenkov effect) that a particle will emit Čerenkov light when it moves faster than the speed of light in a particular medium. Namely $\beta_{thresh} = 1/n$ where β_{thresh} is the threshold velocity of a particle to emit Čerenkov light and n is the refractive index of the medium. The emitted Čerenkov light forms a light cone with an apex angle given by $\theta_c = \cos^{-1}(1/(\beta n))$. Therefore, the Čerenkov effect provides a way to differentiate between particles with different masses but similar momenta.

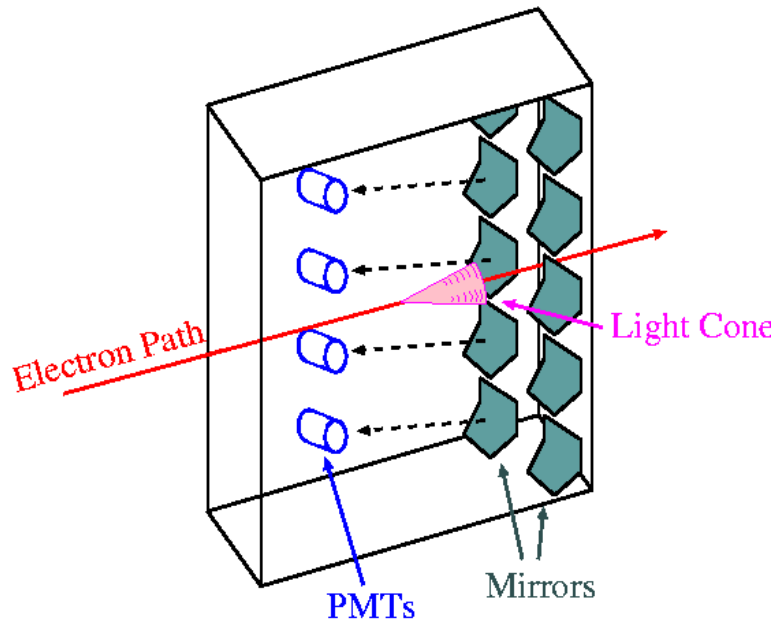


Figure 2-19: Gas Čerenkov Detector Setup

A detailed description of the Hall A Čerenkov counters is given in the Gas Čerenkov counter section of [92]. The Hall A Čerenkov detector shown in Fig. 2-19 is a rectangular stack filled with 1 atm of CO_2 , which has an index of refraction of n

$= 1.00041$. This refraction corresponds to a threshold momentum of 17 (MeV/c) for electrons and 4.8 (GeV/c) for pions. The highest momentum of Hall A HSR is about 4.0 GeV. In principal, no pion thus should be detected in the Čerenkov counter. Ten spherical mirrors are placed in front of the detector exit window and are grouped in two columns. The Čerenkov light is reflected by each mirror toward a particular photo-multiplier tube (PMT), which is located on the side of the detector box. The arrangement of these ten PMTs is to maximize the collection of the Čerenkov light. The thickness of the CO₂ gas is about 1.5 m. The average number of photoelectrons due to the Čerenkov emission is about 6 in the experiment. The electron detector efficiency theoretically can be as high as $1 - \exp(-6) \sim 99.8\%$.

2.6.4 Shower Detector

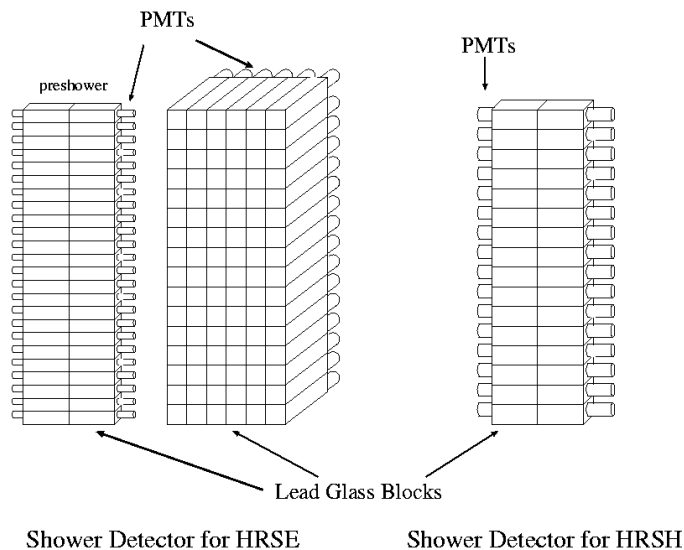


Figure 2-20: The configurations of both HRSE and HRSB shower detectors

For the accurate determination of e^- and π^- , both a shower detector and the Čerenkov detector (Fig. 2-20) were used in HRSE for experiment E95-001. The total

absorption shower counter consists of two layers. The first layer, the preshower, is made of two 48 (2×24) blocks of TF1 lead glass. Each block measures $10 \text{ cm} \times 10 \text{ cm} \times 35 \text{ cm}$. The second layer, shower detector, is made of 96 (16×6) blocks of SF-5 lead glass. Each block measures $15 \text{ cm} \times 15 \text{ cm} \times 35 \text{ cm}$. PMTs are attached to each end of the glass blocks to collect the light. The radiation lengths of both preshower and shower are 3.65 and 15.2, respectively.

When a high energy particle, such as an electron or a photon, passes through the shower counter, the interaction of the particle in the material will lead to a cascade of electrons and photons. If the radiation length of the shower is long enough, the total energy of the particle will eventually be converted to light and heat. The total amount of light emitted is proportional to the energy of the particle. For pions, most of them just pass straight through and deposit energy only by ionization and direct Čerenkov light. Therefore, plotting the energy deposition in the preshower detector versus energy deposition in the shower detector is an effective way to distinguish electrons and pions.

2.7 Hall A Data Acquisition System

2.7.1 Trigger Electronics

The electronic trigger determine whether a event will be recorded by the data acquisition system. Typically there are five S triggers and one timing trigger. The S triggers are generated mainly by timing signals of the two scintillator planes with proper logic and the timing trigger is generated by an electronic clock with 1024 Hz. The detailed logic diagram of the S trigger electronic is presented in Fig. 2-21 and Fig. 2-22.

- S1 trigger: both scintillator planes fire and a S-ray logic is satisfied in E-arm.
- S2 trigger: only one of scintillator planes fires and Gas Čerenkov Detector fires

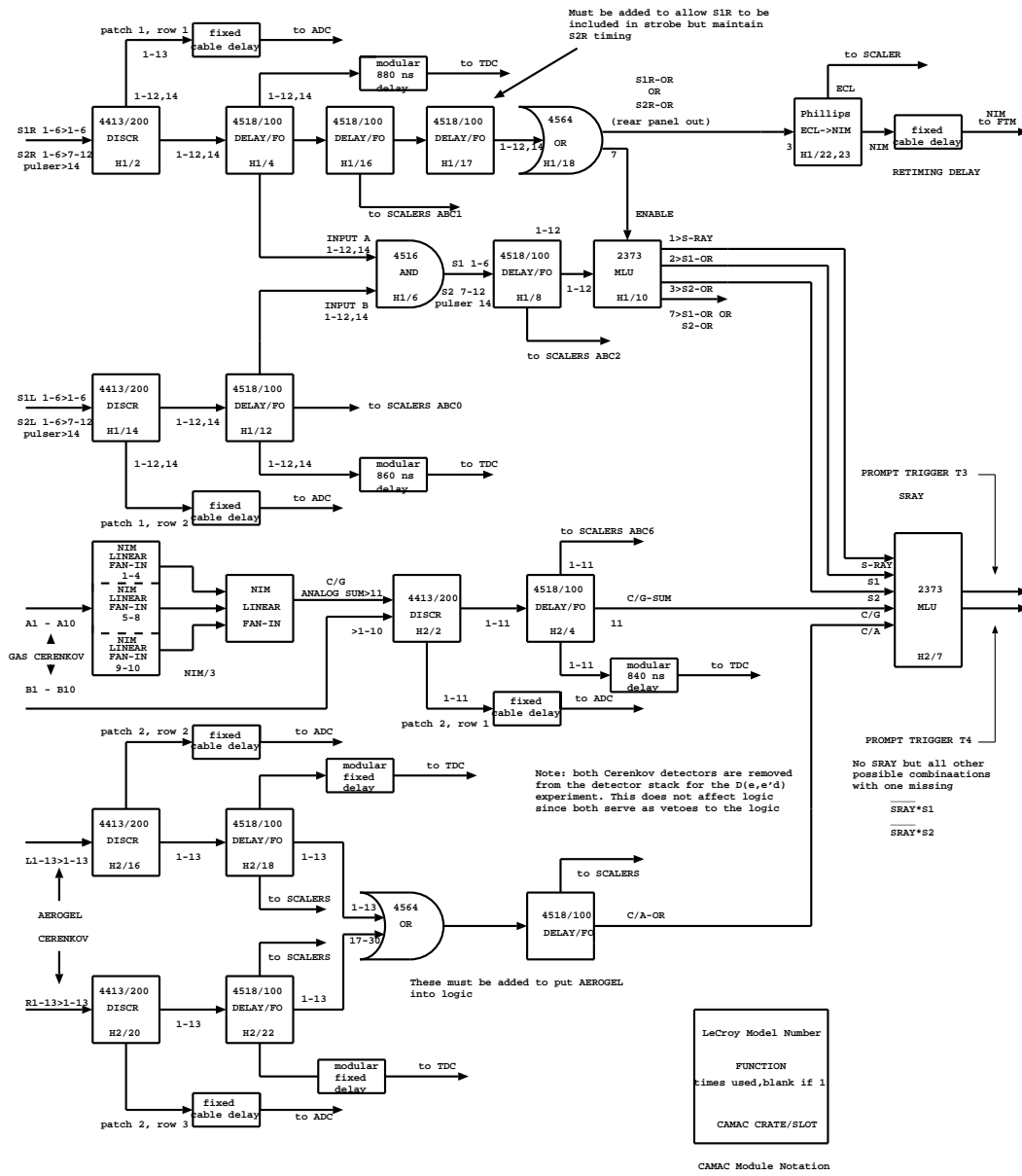
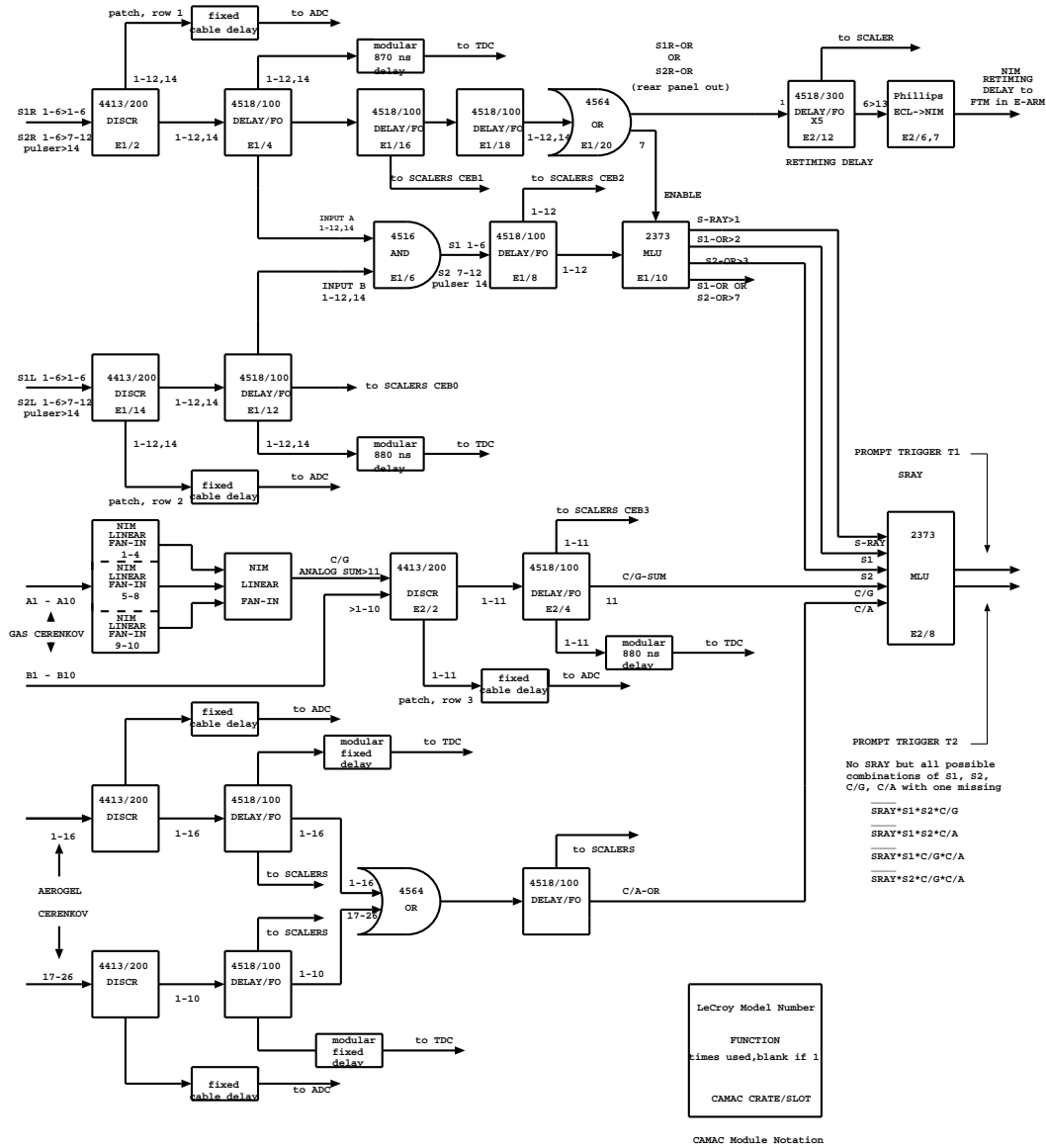


Figure 2-21: H-arm trigger Setup



HALL A ELECTRON PROMPT TRIGGER DESIGN 11/13/97

Figure 2-22: E-arm trigger Setup

(only an electron is picked up) .

- S3 trigger: same as the S1 but for H-arm.
- S4 trigger: same as the S2 but for H-arm.
- S5 trigger: coincident trigger (S1 and S3 with certain timing gate) .

The S-ray logic is defined in the following manner: If the paddle n of one of scintillator plane fires (it also means that the signals from two sides of the paddle n are discriminated) , then on the other paddle, the hit must be from one of the three paddles $n-1$, n , $n+1$.

S1 and S3 (or S5 for coincident event) taken as good triggers with S2, S4 are sent to the Trigger Supervisor (TS) and then to scalars. The Trigger Supervisor synchronizes the readout crates, administers the deadtime logic of the entire system, and prescales various trigger inputs.

2.7.2 Data Acquisition

The Hall A data acquisition is schematically displayed in Fig. 2-23. For each spectrometer, there are one VME crate, one Trigger Supervisor (TS) and one Fastbus crate which is placed inside the spectrometer shielding house. All Time to Digital Converters (TDC) and Analog to Digital Converters (ADC) used in Hall A are Fastbus based. Fastbus electronics provide higher data acquisition rates compared with CAMAC. The scalars feed into the VME crate. The data acquisition software package, CODA [93] was used for the data acquisition and the interface of CODA was displayed on an HP-9000 computer in the counting house. CODA consists of three components:

- a Read Controller (ROC) which interfaces with the detector package through a dedicated fast Ethernet line. During the experiment, the Trigger Supervisor

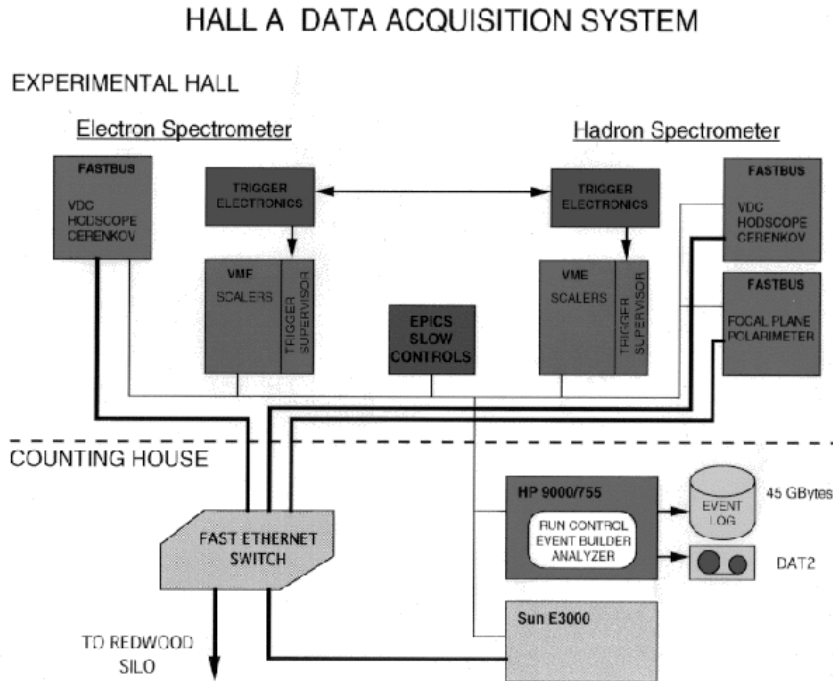


Figure 2-23: Data Acquisition Setup

controls the state of the run, and generates various of triggers to read out from ROCs.

- an event Builder (EB) which builds events from the event pieces arriving from each ROC and incorporates all of necessary CODA header information.
- an online Analyzer/Data Distribution (ANA/DD) which analyzes/writes the events to hard disk and then transfers to tape. We used Halla A online analyzer dhist, dataspv and ESPACE to analyze data and generate diagnostic histograms. These programs depend on the DD system to store data from the data stream.

The events are grouped through different event type in the data file. A few special events, which include the status of the run, appear at the beginning of the data file. A physics event is directly related to the type of a S trigger and dominates the data file. For example, the event type T1 is related to the S1 trigger. In Chapter 4, how to use T1 & T2 or (T3 & T4) events to study scintillator efficiencies is included. In addition, the scaler event and the EPICS event are written to the data stream every a few seconds. The scaler contains the accumulated number on each scaler modules. The sampled beam current and beam position information as well as the magnet information are written to the data stream as the EPICS event through Lab slow control software, EPICS [96].

Chapter 3

Data Analysis

3.1 Overview

A considerable advantage of an asymmetry measurement over a cross-section measurement is that the result is much less dependent on the usual normalizations such as detector efficiencies, target density, absolute charge measurement, spectrometer acceptance and deadtime of data acquisition, which are often difficult to determine. Asymmetry is therefore a very clean physical signature. On the other hand, the asymmetry measurement is potentially subject to false asymmetries resulting from the helicity dependences in the experiment apparatus and the product of the beam and target polarization must be determined with high accuracy.

The final goal of the E95-001 data analysis is to obtain the physics quasi-elastic asymmetry ($A_{T'}$) and extract G_m^n from the asymmetry using theoretical calculations. The quasi-elastic asymmetry, which is defined as the difference of the pure quasi-elastic cross-section with respect to different beam helicity over the sum of the pure quasi-elastic cross-section, can be written as:

$$A_{phys}^{qe} \equiv \frac{\sigma^{qe} \uparrow - \sigma^{qe} \downarrow}{\sigma^{qe} \uparrow + \sigma^{qe} \downarrow}, \quad (3.1)$$

where $\sigma^{qe} \uparrow (\downarrow)$ stands for the quasi-elastic differential cross-section ($\frac{d\sigma^{qe}}{dE' d\Omega}$) with respect to the helicity plus (minus) of the electron beam. As mentioned before, if the polarization direction of ${}^3\text{He}$ target is parallel (perpendicular) to the momentum transfer vector, \vec{q} of the virtual photon, the quasi-elastic asymmetry is only dependent on the transverse response function $R_{T'}$ (the transverse-longitudinal response function $R_{TL'}$). The physics quasi-elastic asymmetry can be obtained from the raw asymmetry.

The raw asymmetry is given as following:

$$A_{raw}^{qe} = \frac{Y^{qe} \uparrow - Y^{qe} \downarrow}{Y^{qe} \uparrow + Y^{qe} \downarrow} \quad (3.2)$$

$$= A_{exp}^{qe} \times P_b P_t. \quad (3.3)$$

Here $Y^{qe} \uparrow (\downarrow)$ is the raw quasi-elastic yield normalized by the live time and the charge for different helicity, A_{exp}^{qe} is the experimental asymmetry, and P_b and P_t are the polarizations of beam and target respectively. The yield, $Y^{qe} \uparrow (\downarrow)$, is comprised of three main parts: ${}^3\text{He}$ yield, N_2 yield (Y^{N2}) and empty target cell yield (Y^{empty}). In addition, according to the kinematic region the ${}^3\text{He}$ yield is also divided into two separated yields: the elastic radiative tail (Y^{ert}) and quasi-elastic (without radiative correction) (Y_{nrc}^{qe}) contributions. As a result, the total raw yield is linear to the sum of all four yields, namely, $Y^{qe} \uparrow (\downarrow) = Y_{nrc}^{qe} \uparrow (\downarrow) + Y^{ert} \uparrow (\downarrow) + Y^{N2} + Y^{empty}$. Equation 3.3 can therefore be rewritten as

$$A_{raw}^{qe} = \frac{Y_{nrc}^{qe} \uparrow + Y^{ert} \uparrow + Y^{N2} + Y^{empty} - (Y_{nrc}^{qe} \downarrow + Y^{ert} \downarrow + Y^{N2} + Y^{empty})}{Y_{nrc}^{qe} \uparrow + Y^{ert} \uparrow + Y^{N2} + Y^{empty} + Y_{nrc}^{qe} \downarrow + Y^{ert} \downarrow + Y^{N2} + Y^{empty}} \quad (3.4)$$

$$= \frac{Y_{nrc}^{qe} \uparrow + Y^{ert} \uparrow - (Y_{nrc}^{qe} \downarrow + Y^{ert} \downarrow)}{Y_{nrc}^{qe} \uparrow + Y^{ert} \uparrow + Y_{nrc}^{qe} \downarrow + Y^{ert} \downarrow} \times \frac{1}{1 + R^{empty} + R^{N2}} \quad (3.5)$$

with $R^{empty(N2)} = \frac{Y^{empty(N2)}}{Y_{nrc}^{qe} + Y^{ert}}$. In terms of the polarizations of both the target and the beam denoted as P_t and P_b respectively, now A_{raw}^{qe} is

$$A_{raw}^{qe} = \frac{A_{nrc}^{qe} + \eta A^{ert}}{(1 + \eta)(1 + R^{empty} + R^{N2})} \times P_b P_t, \quad (3.6)$$

where

$$\begin{aligned} \eta &= \frac{Y^{ert}}{Y_{nrc}^{qe}}, \\ A_{nrc}^{qe} &\equiv \frac{\sigma_{nrc}^{qe\uparrow} - \sigma_{nrc}^{qe\downarrow}}{\sigma_{nrc}^{qe\uparrow} + \sigma_{nrc}^{qe\downarrow}} \\ &= \frac{Y_{nrc}^{qe\uparrow} - Y_{nrc}^{qe\downarrow}}{Y_{nrc}^{qe\uparrow} + Y_{nrc}^{qe\downarrow}} \times \frac{1}{P_b P_t}, \\ A^{ert} &\equiv \frac{\sigma^{ert\uparrow} - \sigma^{ert\downarrow}}{\sigma^{ert\uparrow} + \sigma^{ert\downarrow}} \\ &= \frac{Y^{ert\uparrow} - Y^{ert\downarrow}}{Y^{ert\uparrow} + Y^{ert\downarrow}} \times \frac{1}{P_b P_t}. \end{aligned}$$

Note that the quasi-elastic radiative correction of asymmetry is evaluated as the difference between the pure (physics) quasi-elastic asymmetry (A_{phys}^{qe}) and the quasi-elastic asymmetry without the quasi-elastic radiative correction (A_{nrc}^{qe}), namely

$$\Delta A_{rad}^{qe} \equiv A_{phys}^{qe} - A_{nrc}^{qe}. \quad (3.7)$$

Taking into account Equation 3.7 and 3.6, the expression of the A_{phys}^{qe} in terms of the raw asymmetry, A_{raw}^{qe} is given by

$$A_{phys}^{qe} = \Delta A_{rad}^{qe} + \frac{(1 + \eta)(1 + R^{empty} + R^{N2})A_{raw}^{qe}}{P_b P_t} - \eta A^{ert}, \quad (3.8)$$

or

$$A_{phys}^{qe} = \Delta A_{rad}^{qe} + (1 + \eta)(1 + R^{empty} + R^{N2})A_{exp}^{qe} - \eta A^{ert}. \quad (3.9)$$

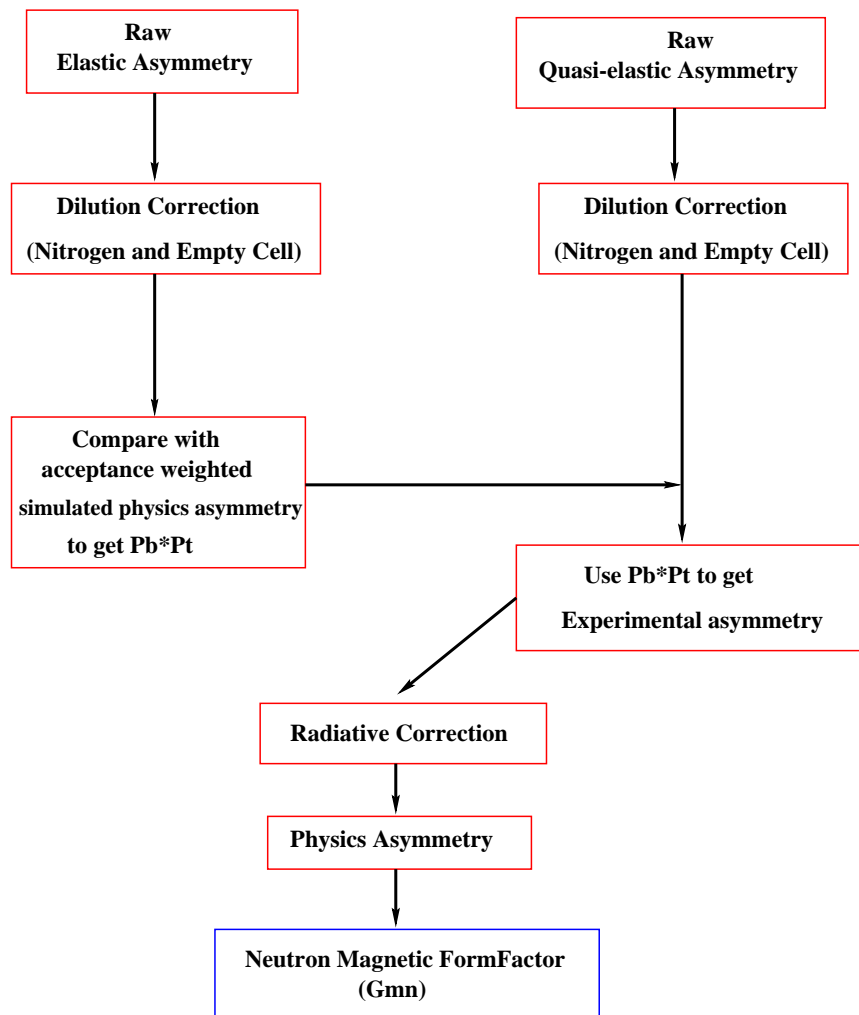


Figure 3-1: Experiment E95-001 data analysis flow chart

The procedure of E95-001 data analysis is thus shown as a flowchart in Fig. 3-1: (i), normalized raw quasi-elastic asymmetry was extracted on a run-by-run basis, and was weighted by the statistical uncertainty of each run. (ii) the physics quasi-elastic asymmetry ($A_{T'}$) was calculated by normalizing the extracted raw asymmetry by the product of the beam and target polarization and applying corrections for the dilution

factors and radiative effects. (iii) G_m^n was finally extracted with different theoretical approaches (the full Faddeev calculation by Golak *et al.* or the Plane Wave Impulse Approximation (PWIA) calculation).

Before the discussion of the data analysis, the Hall A analyzer - ESPACE will be introduced in the next section.

3.2 The Data Analyzer

The Hall A analyzer - ESPACE was employed to decode raw data file and to fill into hbook files. The Main Frame work of ESPACE was written by Dr. Eddy Offerman [94] and was adapted to Jefferson lab from Mainz. It was modified for experiment E95-001. The whole source codes are rather complex but the interface of ESPACE is relatively flexible and user-friendly.

ESPACE decodes the data files on event-by-event basis with the CODA format. Each event contains both the ADC and TDC information from the different detectors. Based on the ADC and TDC information, further data analysis of ESPACE reconstructs many physics quantities such as Time of Flight (ToF), Particle identification information (PID), the focal plane vertex quantities (x_{fp} , y_{fp} , θ_{fp} , ϕ_{fp}) and the target vertex quantities (x_{tg} , y_{tg} , θ_{tg} , ϕ_{tg}) which is calculated from focal vertex quantities using the HRS optic data base.

I developed several software packages such as the helicity check package, the current check package, the scaler check package, and the bpm and raster check package so that the analysis can be carried out more efficiently without going through the deep level ESPACE analysis for many of the online monitoring and the systematic studies.

3.3 Quasi-Elastic Raw Asymmetry

As mentioned before, the experimental raw asymmetry of quasi-elastic scattering is extracted from the normalized yield with different helicity in each run. The knowledge of experimental raw asymmetry along with the dilution factor, radiative correction and the product of the beam and target polarization allows for the calculation of the physics asymmetry. In order to minimize the false asymmetry effect, the data taking was carried out with four different configurations corresponding to the combination of the target polarization direction and the electron beam helicity definition. While either target polarization direction with respect to three momentum transfer \vec{q} , is flipped 180° or the beam helicity definition is reversed by inserting or taking out a half-wave plate at the polarized electron injector gun, the sign of the raw asymmetry is reversed, as shown in Tab. 3.1, but the magnitude should remain the same within a statistical uncertainty in an idea case.

	h +	h -
$\theta^* = 0^\circ$	+	-
$\theta^* = 180^\circ$	-	+

Table 3.1: Raw asymmetry sign with four configurations

However, in practice, the target polarization direction at lab, θ_{spin}^1 for six different quasi-elastic kinematics (shown in Table 3.3) varies from -67.3° to -53.4° . In order to minimize the systematic uncertainty due to uncertainty of the target polarization direction, θ_{spin} was kept in a certain direction around -60° but was only flipped occasionally. The flipped angle of the target polarization direction is not exact 180° but was found to be 180.9° (243.6° - 62.5°). θ_{spin} we used is about $-62.5^\circ \pm 0.5^\circ$. The corresponding target polarization direction with respect to three momentum

¹ θ_{spin} is target spin direction with respect to beam line at the lab frame.

$$\theta^* = 0^\circ$$

	$Q^2=0.1$	$Q^2=0.2$	$Q^2=0.3$
θ_{spin}	-67.3°	-58.9°	-63.6°
	$Q^2=0.4$	$Q^2=0.5$	$Q^2=0.6$
θ_{spin}	-59.9°	-56.5°	-53.4°

Table 3.2: The corresponding target spin direction in the lab, θ_{spin} at the quasi-elastic peak for six different kinematics as the target spin direction with respect to three momentum transfer \vec{q} , θ^* is equal to zero.

transfer \vec{q} , θ^* at the quasi-elastic peak region for six different kinematic settings of the experiment, which is listed in Tab. 3.3, was not always perfectly aligned along \vec{q} , yet experimentally close enough to the \vec{q} direction. Contributions to the physics asymmetry due to $R_{TL'}$ result from those θ^* s are determined from PWIA to be less than 2% at all six kinematic settings. The magnitude of the raw asymmetry shown in Fig. 3-2 therefore changes slightly due to the variation of the target polarization direction, the uncertainty of the beam and the target polarization direction, the statistical uncertainty of the measurement, and the false asymmetry. By adding the absolute value of the experimental asymmetries, A_{exp} of all four configurations, the false asymmetry which is less sensitive to the change of the target polarization direction and the beam helicity will be canceled.

To make sure that the result of the raw asymmetry is reliable, the false asymmetry checks are crucial before the raw asymmetry is corrected by the lifetime, dilution, radiative correction, etc. The sources of the false asymmetry are from the detector efficiency, the e^-/π^- separation, the helicity, the beam position and the charge. These issues will be discussed in detail in the next chapter.

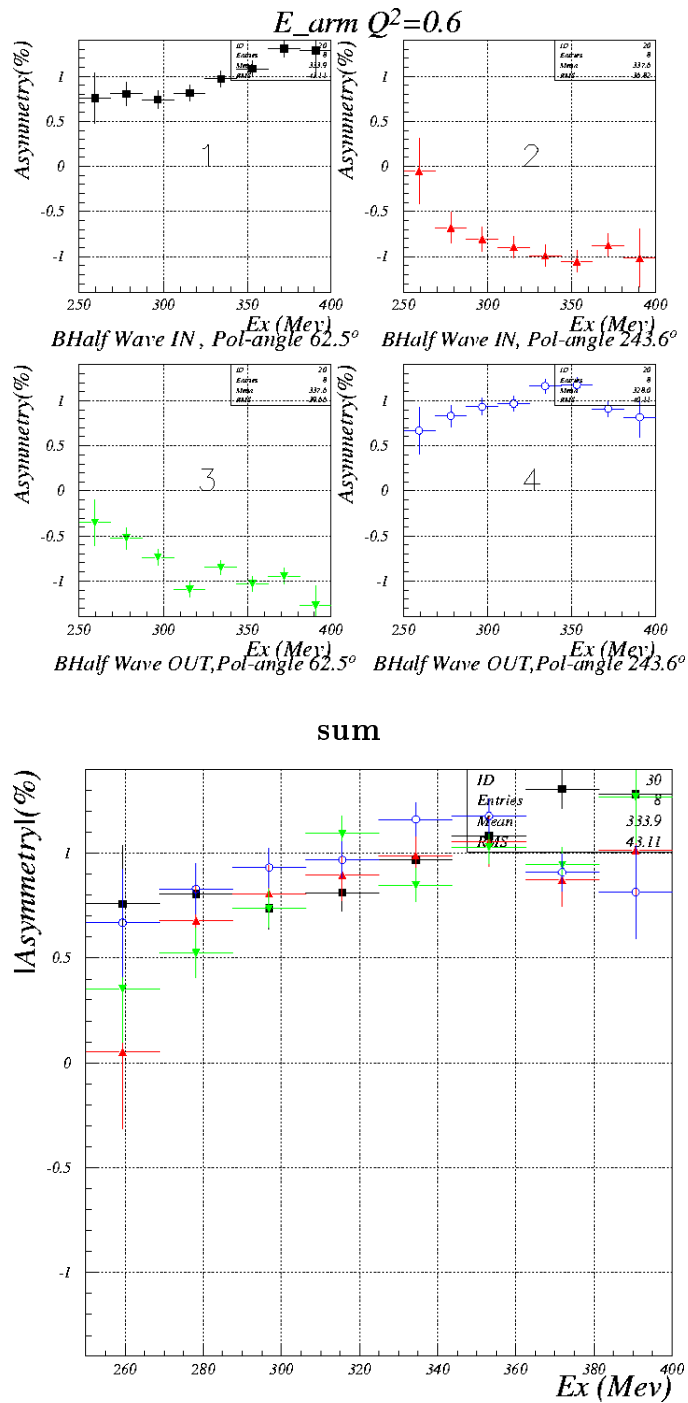


Figure 3-2: The Quasi-elastic raw asymmetry, A_{raw} for four different configurations at $Q^2 = 0.6$ ($(\text{GeV}/c)^2$) plotted as an example.

E-arm	$Q^2=0.1$	$Q^2=0.2$	$Q^2=0.3$
ω_{peak}	60(MeV)	110(MeV)	168(MeV)
E-arm	$Q^2=0.4$	$Q^2=0.5$	$Q^2=0.6$
ω_{peak}	220(MeV)	274(MeV)	328(MeV)

	$Q^2=0.1$	$Q^2=0.2$	$Q^2=0.3$
θ_{spin}	$\theta_{\omega_{peak}}^*$	$\theta_{\omega_{peak}}^*$	$\theta_{\omega_{peak}}^*$
$-62.5^\circ \pm 0.5^\circ$	4.8°	3.6°	0.9°
$-243.6^\circ \pm 0.5^\circ$	3.7°	4.7°	0.2°
	$Q^2=0.4$	$Q^2=0.5$	$Q^2=0.6$
θ_{spin}	$\theta_{\omega_{peak}}^*$	$\theta_{\omega_{peak}}^*$	$\theta_{\omega_{peak}}^*$
$-62.5^\circ \pm 0.5^\circ$	2.6°	6.2°	8.9°
$-243.6^\circ \pm 0.5^\circ$	3.7°	7.2°	10.0°

Table 3.3: The target spin direction configurations for six different kinematics. Here θ^* at the quasi-elastic peak is referred to as $\theta_{\omega_{peak}}^*$ and the ω value at quasi-elastic peak, ω_{peak} is listed in the upper table.

3.4 Elastic Polarimetry

During the experiment, the HSRH was employed as the online polarimetry monitoring the product of the beam and the target polarization. The practicality of the polarimetry is based on the fact that elastic scattering process is well known and the electro-magnetic form factor of ^3He is well measured at low Q^2 . In general, the ^3He elastic asymmetry can be expressed in terms of the ^3He charge and magnetic form factors, F_c and F_m , as

$$A_{el} = \frac{\Delta}{\Sigma} = -\frac{2\tau\mu_A^2 v_{T'} \cos\theta^* F m^2 + 2\sqrt{2\tau(1+\tau)}\mu_A Z v_{TL'} \sin\theta^* \cos\phi^* F m F c}{(1+\tau)Z^2 v_L F c^2 + 2\tau\mu_A^2 v_T F m^2}, \quad (3.10)$$

$$(3.11)$$

where the form factors have been normalized to

$$F_c(Q^2 = 0) = F_m(Q^2 = 0) = 1. \quad (3.12)$$

In this formula Z is the nuclear charge, μ_A is defined in terms of the magnetic moment of ^3He as $(m_{He}/m_n) \mu_{He}$, and all other variables are defined in Chapter 1. The measured elastic asymmetry approximately equals to $P_b P_t \times A_{el}$ despite the radiative tail correction, energy loss, HRSR acceptance, HRSR resolution etc. Thus $P_b P_t$ can be measured and monitored through the measurement of the experimental elastic asymmetry. $P_b P_t$ is shown in Equation 3.7 as the crucial physics quantity to get the quasi-elastic physics asymmetry. In fact, the systematic uncertainty of quasi-elastic physics asymmetry is dominated by the uncertainty of $P_b P_t$. In order to minimize the uncertainty of $P_b P_t$, the ^3He elastic asymmetry needs to be weighted with all kinds of the effects such as the HRSR resolution and the HRSR acceptance. A Monte-Carlo simulation seems the only way to correctly include the entire effects which will distort the elastic asymmetry distribution in terms of the electron scattering angle (ϕ_{target}) and the outgoing momentum (Δ_{target}). So the Hall A Monte-Carlo software package (MCEEP) was modified for this purpose.

3.4.1 MCEEP

The MCEEP was designed to simulate coincidence (e, e'X) experiments by averaging theoretical models over an experimental acceptance. The entire software was written in Fortran and supported by P. E. Ulmer [95] and MCEEP users. Although the program and its name were initially created with (e, e'p) in mind, MCEEP is applicable to any single particle emission experiment provided with the appropriate physics routines, as well as (e, e') elastic. For our case, the model for the ^3He elastic scattering is added. MCEEP employs a uniform random sampling method to popu-

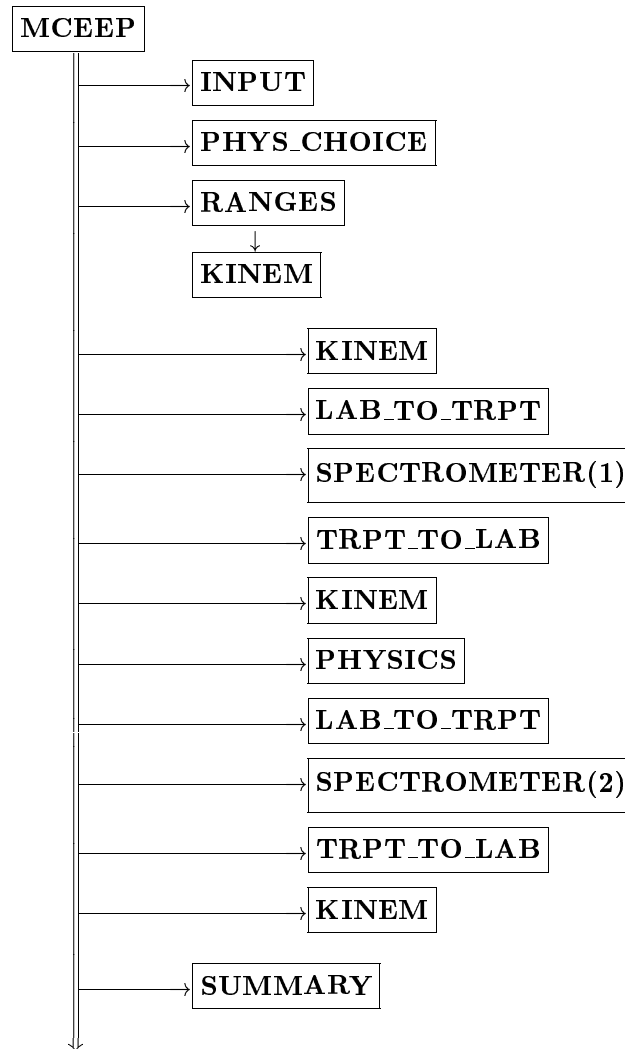


Figure 3-3: Block diagram of the main routines called by MCEEP. Subroutines are to the right of the double arrow and are called in order reading down the page. Indented subroutines are within the main Monte-Carlo event loop. For clarity, only the main routines are shown

late the experimental acceptance. This method allows us to obtain good statistics for small cross-section in the presence of a dominant contribution by a relatively small number of events. An event is defined in MCEEP as any combination of variables which completely specifies the reaction in the laboratory. For each event, weights which correspond to the relevant observables (cross sections, polarization, etc.) are computed according to a user selected physics model. The main frame of version of 2.3 MCEEP is demonstrated in Fig 3-3.

In order to simulate the ^3He elastic process, first the option 30 for the ^3He elastic is added in the subroutine of PHYS_CHOICE. Then the acceptance functions for both arms are included in the subroutine of SPECTROMETER (1). (However, only the acceptance function for H-arm was used in simulating the elastic scattering.) Subsequently, the updated calculations of the cross-section and asymmetry of the ^3He elastic scattering with the mostly recent data of the ^3He elastic form factors are available for the subroutine of PHYSICS. Finally, the effects such as radiative correction, energy loss and multiple scattering are taken into account along the event transportation. In later sections, the issues about the acceptance and the interaction between a charge particle and a medium will be discussed.

3.4.2 Acceptance

A detected electron leaving from the scattering chamber travels all the way to VDC and generates the output ADC and TDC signals from VDC wires. Along the path, however, not all electrons can arrive at VDC and produce the signals because of the geometric limit of the spectrometer, the deflection caused by the interactions between electrons and mediums, and VDC detector inefficiency. The acceptance is a tool to describe the possibility of finding an electron at the perfect VDC chamber (without the inefficiency) within a certain scattering angle and momentum range. Thus the acceptance can be expressed as a function of possibility in terms of the scattering

angle, momentum and the scattering position at the target. The acceptance is so complex that the acceptance used in the simulation often can not perfectly agree with reality. Compared with the experiment acceptance and the simulation acceptance

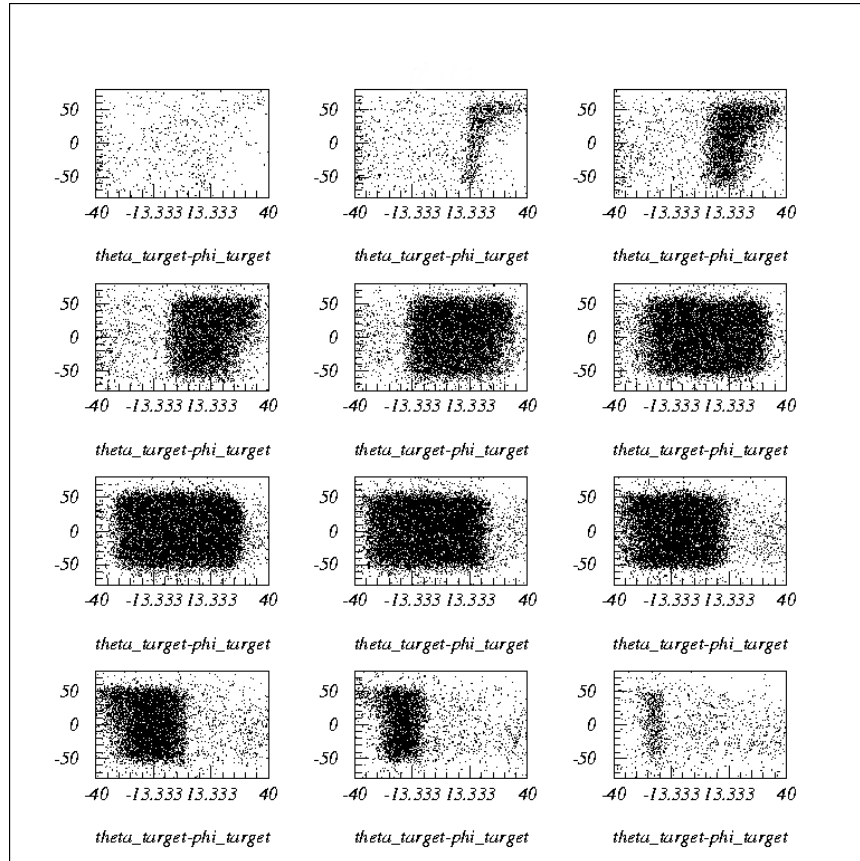


Figure 3-4: The experiment acceptance is plotted as a function of ϕ_{target} vs θ_{target} with 10mm y_{target} long scanning from $y_{target} = -60\text{mm}$ to $y_{target} = 60\text{mm}$.

in Fig. 3-4 and Fig. 3-5, the shape of the diagram demonstrates that the acceptance which has been modified and used in MCEEP is quite reasonable. This acceptance function pushes the elastic simulation further closer to the final goal. In addition, the simulation of the interaction between a charged particle and a medium is another key factor for a good simulation. In the next sections, the interactions between the

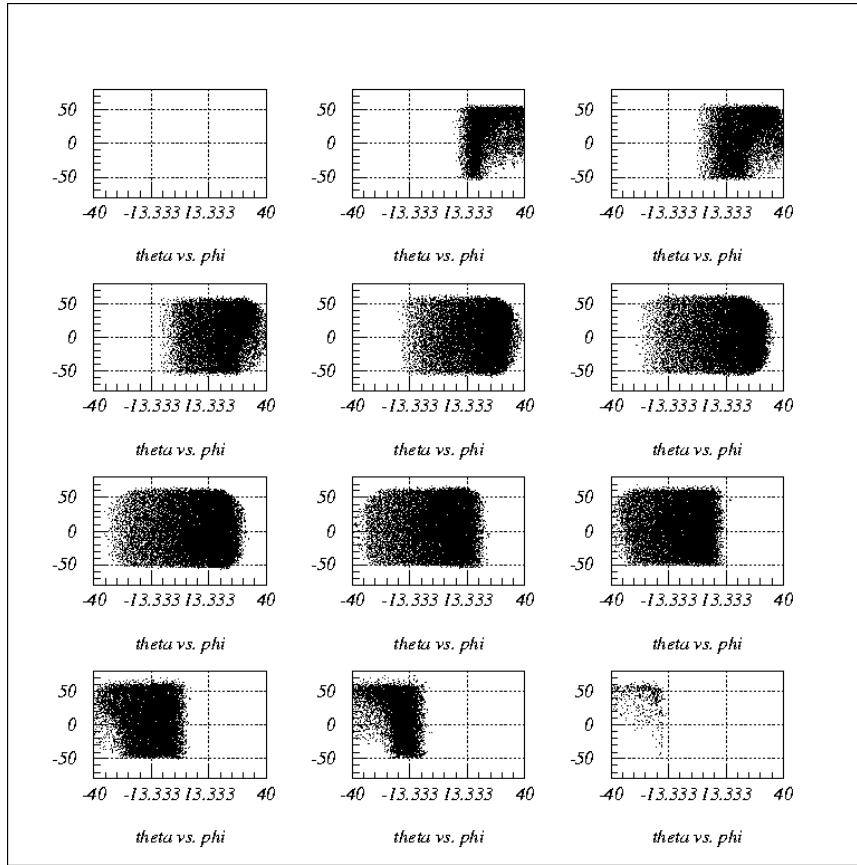


Figure 3-5: The simulation acceptance is plotted as a function of ϕ_{target} vs θ_{target} with 10mm y_{target} long scanning from $y_{target} = -60\text{mm}$ to $y_{target} = 60\text{mm}$.

particle (electron) and mediums are therefore discussed.

3.4.3 Energy Loss

A charged particle (electron) moving through a material may ionize or excite the atoms of that material at the expense of the energy. This energy loss is subject to appreciable fluctuations about the the most probable energy loss ΔE_{mp} , which is

defined as following, [78]

$$\Delta E_{mp} = \frac{2\pi ne/4 z^2 t}{m_e c^2 \beta^2 \rho} \left[\ln \frac{4\pi ne/4 z^2 t}{I^2 (1 - \beta^2) \rho} - \beta^2 + 0.198 - \delta - U \right] \quad (3.13)$$

$$, \quad (3.14)$$

with

n: the number of the electrons per cm³ in the material,

ρ : the density of the material in g/cm³,

I: the mean excitation energy of the material in eV,

z: the charge of the incident particle,

t: the thickness of the material in g/cm²

$m_e c^2 = 0.511$ MeV, the rest mass of the electrons,

$\beta = v/c$, where v is the velocity of the particle.

For relativistic electrons ($\beta \sim 1$, $z = 1$), as $\frac{2\pi ne/4 z^2 t}{m_e c^2 \beta^2 \rho} = \frac{0.1536 z^2 Z}{A}$, Equation 3.13 can be rewritten in the simple form:

$$\Delta E_{mp} = 0.1536 \frac{Zt}{A} [19.26 + \log(t/\rho + 1.0^{-5})], \quad (3.15)$$

with Z: the effective mass of medium, and A: the effective atomic mass.

The shape of the energy loss depends on the value of the κ : [79]

$$\kappa = \frac{\xi}{E_{max}} \quad (3.16)$$

with:

$$\xi = \frac{2\pi c^2 e/4 z^2 n t}{m_e c^2 \beta^2} = \frac{0.1536 z^2 Z t}{A \beta^2}.$$

The maximum energy transfer in the collision E_{max} from the incident particle to

atomic electrons, is approximately given as:

$$E_{max} = \begin{cases} \frac{2m_e v^2}{1-\beta^2} & \text{for incident heavy particles} \\ \frac{T_e}{2} & \text{for incident electrons} \end{cases} \quad (3.17)$$

Calculating the energy loss distribution requires different theoretical treatments for various energy transfer regions. κ measures the contribution of the collisions with energy transfer close to E_{max} . The correlation between the κ and chosen theoretical models for energy loss is:

$$\begin{cases} \kappa \leq 0.01 & \text{Landau distribution (thin layer) [79]} \\ 0.01 < \kappa \leq 10.0 & \text{Vavilov distribution [80]} \\ 10.0 < \kappa & \text{Gaussian distribution [81]} \end{cases} \quad (3.18)$$

The Landau distribution ($\kappa \leq 0.01$) was chosen because during the experiment, the incident electron and the scattered electron passed the thin entrance window (0.13/0.142 mm) and the target glass wall (≈ 1.2 mm) respectively. The distribution is asymmetric with a long high-energy loss tail and a broad peak. The expression of the observed energy loss ΔE in term of the most probable energy loss E_{mp} is given by

$$\Delta E = \lambda \times \xi + \Delta E_{mp}, \quad (3.19)$$

where the distribution of λ is slightly different from the universal Landau distribution. For electrons passing through the glass side wall, the energy loss is displayed in the Fig 3-6.

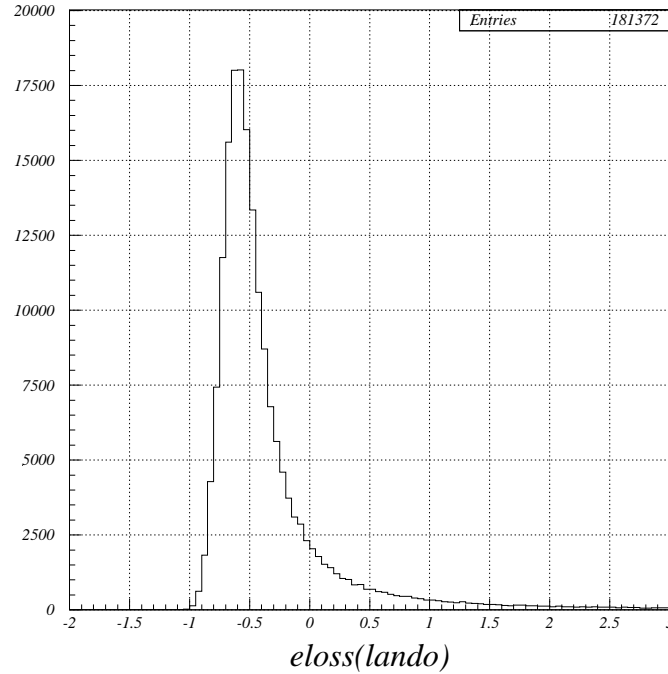


Figure 3-6: The distribution of the simulated elastic electron events versus eLoss which is denoted as the energy loss (ΔE) at $Q^2 = 0.1$ when the electron passes through the side wall of the target glass cell.

3.4.4 Multiple Scattering

Due to the interaction with the Coulomb field of the nuclei, a charged particle (electron) is deflected by many scatters, mostly at small angles. The deflected angle (θ_0) between the directions projected on a plane of a particle before and after traversing a thickness, t of medium roughly follows a Gaussian distribution. A simple form for the multiple Coulomb scattering of singly charged particles is widely use:

$$\theta_0 \approx \frac{15MeV}{E\beta^2} \sqrt{\frac{t}{X_0}}, \quad (3.20)$$

where X_0 is the radiation length of the medium. The formula can introduce large errors because it ignores significant dependences on path-length and Z of the medium. To compensate for this, a similar formula was given by [75, 76]:

$$\theta_0 \approx \frac{14.1 \text{ MeV}}{E\beta^2} \sqrt{\frac{t}{X_0}} [1 + 0.038 \log(\frac{t}{X_0})]. \quad (3.21)$$

Equation 3.21 which doesn't take into account the β and z dependence of the incident particle was employed in the simulation. The more subtle equation was developed by [77]:

$$\theta_0 \approx \frac{S_2}{E\beta^2} \sqrt{\frac{t}{X_0}} [1 + \epsilon \log(\frac{z^2 t}{X_0 \beta^2})], \quad (3.22)$$

where S_2 and ϵ are about 14.1 MeV and 0.038.

3.4.5 Bremsstrahlung

The Bremsstrahlung radiation can be separated into two main categories:

- internal bremsstrahlung: Emission of the real and virtual photon in the field of the scattering nucleus.
- External bremsstrahlung: Emission of the real photons when electrons pass through materials before or after the scattering.

Internal bremsstrahlung

Feynman diagrams for the internal bremsstrahlung processes are given in Figure 3-7. Based on the knowledge of the energy resolution of the spectrometer ΔE , the internal bremsstrahlung can be recognized as the soft photon emission, where the energy of emitted photon (E_γ) is less than ΔE and hard photon emission where E_γ is above the ΔE . The hadron photon emission in upper part of Fig. 3-7 (the so-called

“Radiative Tail correction”) tends to reduce the apparent cross section by shifting the events to higher missing energies, and can be treated as two “external equivalent radiators” [63] with one placed before and one after the scattering each with a thickness of:

$$t_{eq}^{bre} = \frac{1}{b} \frac{\alpha}{\pi} \left[\ln \frac{Q^2}{m_e^2} - 1 \right], \quad (3.23)$$

with:

$$b = \frac{4}{3} \left\{ 1 + \frac{1}{9} \left[\frac{Z+1}{Z+\xi} \right] \left[\ln(183Z^{\frac{-1}{3}}) \right]^{-1} \right\},$$

and

$$\xi = \frac{\ln(1440Z^{\frac{-2}{3}})}{\ln(183Z^{\frac{-1}{3}})}.$$

The “Radiative Correction” is the correction applied to a basic scattering process due to emission and re-absorption of the virtual photons and to the emission of any number of real soft photons with total energy less than ΔE . This correction involves all the diagrams shown in Figure 3-7.

The radiative correction (“Radiative Tail” + “Radiative Correction”) was first deduced for elastic scattering by Schwinger [61]. It has since been well studied and extended to inelastic scatterings. Following the method of Mo and Tsai [63], the experimental cross-section at elastic peak can be written in terms of the pure one-photon exchange cross section and radiative correction as:

$$\frac{d\sigma}{d\Omega dE} = \left(\frac{d\sigma}{d\Omega dE} \right)_{1\gamma} (1 + \delta_{T_{sai}}(\Delta E)) \quad (3.24)$$

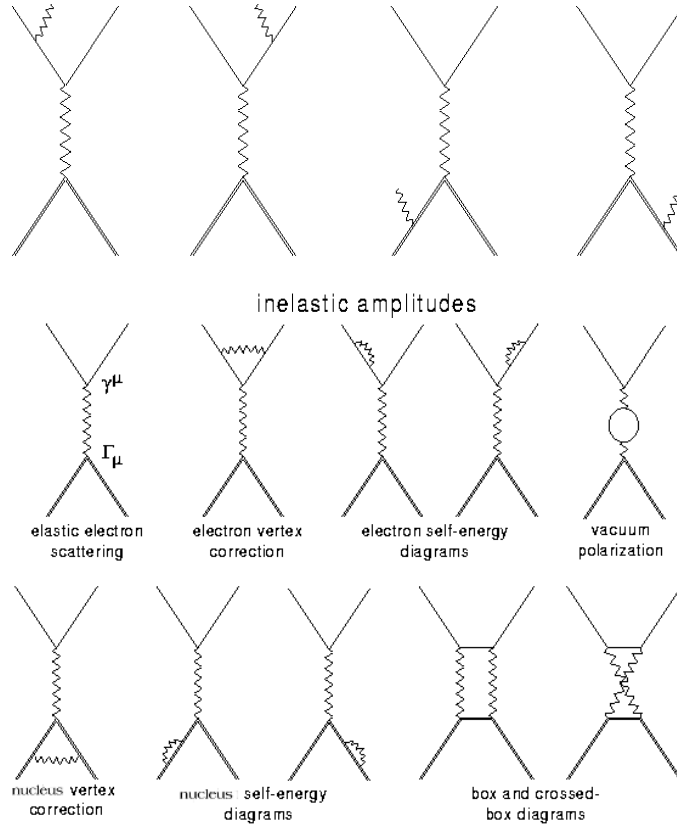


Figure 3-7: The internal bremsstrahlung

The expression for $\delta_{T_{sai}}$, taking into account both the kinematic effect due to target recoil and the dynamic effect due to photon mission by the target, can be written as [63, 64]

$$\begin{aligned} \delta = & \frac{-\alpha}{\pi} \left(\frac{28}{9} - \frac{13}{6} \ln \left(\frac{Q^2}{m_e^2} \right) + \left(\ln \left(\frac{Q^2}{m_e^2} \right) - 1 + 2Z \ln \eta \right) \left(2 \ln \frac{E}{\Delta E} - 3 \ln \eta \right) \right. \\ & - \Phi \left(\frac{E' - E}{E'} \right) - Z^2 \ln \frac{E'_t}{M_t} + Z^2 \ln \frac{M_t}{\eta \Delta E} \left(\frac{1}{\beta'_t} \ln \frac{1 + \beta'_t}{1 + \beta'_t} - 2 \right) \\ & \left. + \frac{Z^2}{\beta'_t} \left\{ \frac{1}{2} \ln \frac{1 + \beta'_t}{1 + \beta'_t} \ln \frac{E'_t + M_t}{2M_t} - \Phi \left[- \left(\frac{E'_t - M_t}{E'_t + M_t} \right)^{\frac{1}{2}} \left(\frac{1 + \beta'_t}{1 - \beta'_t} \right)^{\frac{1}{2}} \right] \right\} \right\} \end{aligned}$$

$$\begin{aligned}
& + Z \left[\Phi \left(-\frac{M_t - E'}{E} \right) - \Phi \left(-\frac{M_t(M_t - E')}{2E'E'_t - M_tE} \right) \right. \\
& + \Phi \left(-\frac{2E'(M_t - E')}{2E'E'_t - M_tE} \right) + \ln \left| \frac{2E'E'_t - M_tE}{E(M_t - 2E')} \right| \ln \left(\frac{M_t}{2E'} \right) \Big] \\
& - Z \left[\Phi \left(-\frac{E'_t - E'}{E'} \right) - \Phi \left(-\frac{M_t(E'_t - E')}{2EE'_t - M_tE'} \right) \right. \\
& + \Phi \left(-\frac{2E(E'_t - E')}{2EE'_t - M_tE'} \right) + \ln \left| \frac{2EE'_t - M_tE'}{E'(M_t - 2E)} \right| \ln \left(\frac{M_t}{2E} \right) \Big] \\
& - Z \left[\Phi \left(-\frac{M_t - E}{E} \right) - \Phi \left(\frac{M_t - E}{E} \right) \right. \\
& + \Phi \left(\frac{2(M_t - E)}{M_t} \right) + \ln \left| \frac{M_t}{2E - M_t} \right| \ln \left(\frac{M_t}{2E} \right) \Big] \\
& Z \left[\Phi \left(-\frac{M_t - E'}{E'} \right) - \Phi \left(\frac{M_t - E'}{E'} \right) \right. \\
& + \Phi \left(\frac{2(M_t - E')}{M_t} \right) + \ln \left| \frac{M_t}{2E' - M_t} \right| \ln \left(\frac{M_t}{2E'} \right) \Big] \\
& - \frac{\alpha}{\pi} \left(-\Phi \left(\frac{E - E'}{E} \right) + \frac{Z^2}{\beta'_t} \left\{ \Phi \left[\left(\frac{E'_t - M_t}{E'_t + M} \right)^{\frac{1}{2}} \left(\frac{1 - \beta'_t}{1 + \beta'_t} \right)^{\frac{1}{2}} \right] \right. \right. \\
& \left. \left. - \Phi \left[\left(\frac{E'_t - M_t}{E'_t + M} \right)^{\frac{1}{2}} \right] + \Phi \left[\left(-\frac{E'_t - M_t}{E'_t + M} \right)^{\frac{1}{2}} \right] \right\} \right), \tag{3.25}
\end{aligned}$$

And Φ is the Spence function defined by

$$\Phi(x) = \int_0^x \frac{-\ln|1-y|}{y} dy, \tag{3.26}$$

where:

$Z = +3$ (electron- ^3He scattering) ,

E is the incident electron energy,

E' is the outgoing electron energy,

M_t is the target mass,

m_e is the electron mass,

ΔE is the energy resolution of the spectrometer.

The other quantities are given according to the elastic scattering kinematics. From 4-momentum conservation we have

$$P_e^\mu + P_t^\mu = P_{e'}^\mu + P_{t'}^\mu \quad (3.27)$$

Here $P_e^\mu = (E, \vec{P})$, $P_t^\mu = (M_t, 0)$, $P_{e'}^\mu = (E', \vec{P}')$, $P_{t'}^\mu = (E'_t, \vec{P}'_t)$. For relativistic electrons, we obtain the following expression:

$$Q^2 = (P_e^\mu - P_{e'}^\mu)^2 = 4EE' \sin^2(\theta/2), \quad (3.28)$$

$$E' = \frac{E}{\eta}, \quad (3.29)$$

$$\eta = 1 + \frac{2E}{M_t} \sin^2(\theta/2), \quad (3.30)$$

$$E_{t'} = E - E' + M_t, \quad (3.31)$$

$$\beta'_t = \frac{v'_t}{c} = \frac{\sqrt{E_{t'}^2 - M_t^2}}{E'_t}. \quad (3.32)$$

External bremsstrahlung

When the energy of an electron E ($E > 100 \text{ MeV}$) straggles down to energy E_1 mainly by external bremsstrahlung process after passing through t radiation length in the target, the possibility of finding the electron, $P_e^{ext}(E, E_1, t)$ is given by Tsai [62] as:

$$P_e^{ext}(E, E_1, t) = \frac{bt}{\Gamma(1+bt)} \left(\frac{E - E_1}{E} \right)^{bt} \frac{1}{E - E_1} \quad (3.33)$$

The general formula of the cross section for electrons of incident energy E to scatter at angle θ_{scat} to final energy E' from a target of T radiation length can be described as [63]:

$$\frac{d\sigma_{exp}(E, E', \theta_{scat})}{d\Omega dE'} = \int_0^T \frac{dt}{t} \int dE_1 \int dE'_1$$

$$P_e(E, E_1, t) \frac{d\sigma_{rad}(E_1, E'_1, \theta_{scat})}{d\Omega dE'_1} P'_e(E'_1, E', T - t), \quad (3.34)$$

where:

$P_e(E, E_1, t)$ is the probability of finding an electron starting at initial energy E straggling down to energy E_1 after passing through t radiation length in the target,

$P'_e(E'_1, E', T - t)$ is the probability of finding an electron after scattering at E'_1 straggling down to energy E' through the rest of the target,

$\frac{d\sigma_{rad}(E_1, E'_1, \theta_{scat})}{d\Omega dE'_1}$ is the cross-section for elastic scattering at incident energy E_1 to final energy E'_1 at the scattering angle θ_{scat} with internal radiation correction.

Using Eqs 3.23, 3.24, and 3.33, Eq. 3.34 can be rewritten as [82]:

$$\begin{aligned} \frac{d\sigma_{exp}(E, E', \theta_{scat})}{d\Omega dE'} &= \int dE_1 \frac{bT'_b}{E - E_1} \left(\frac{E - E_1}{E} \right)^{bT'_b} \frac{1}{\Gamma(1 + bt_b)} \\ &\quad \frac{d\sigma(E_1, \theta_{scat})}{d\Omega} (1 + \delta_{T_{sai}} - \delta_{teq}) \\ &\quad \frac{bT'_a}{E'_1 - E'} \left(\frac{E'_1 - E'}{E'_1} \right)^{bT'_a} \frac{1}{\Gamma(1 + bt_a)}, \end{aligned} \quad (3.35)$$

where:

$$\begin{aligned} T'_b &= t_b + t_{eq} \\ T'_a &= t_a + t_{eq} \\ E'_1 &= \frac{E_1}{1 + \frac{2E_1}{M_t} \sin^2(\theta_{scat})} \quad (\text{elastic confinement}). \end{aligned}$$

Here, t_a and t_b are the radiation length of the real radiators before and after the scattering. Because $\delta_{T_{sai}}$ includes the contribution from ‘‘Radiative Tail’’ and the replacement of ‘‘Radiative Tail’’ is the two ‘‘external equivalent radiators’’, δ_{teq} is

subtracted from $\delta_{T_{sai}}$ where δ_{teq} is given by [63]

$$\begin{aligned}\delta_{teq} = & - (bt_{eq}^{bre} \ln(E/\eta^2 \Delta E)) \\ & + bt_{eq}^{bre} \ln(E'/\Delta E).\end{aligned}\tag{3.36}$$

Using Eq. 3.23 and $\eta = E/E'$, δ_{teq} can be written as:

$$\delta_{teq} = \frac{-\alpha}{\pi} \left(\ln \left(\frac{Q^2}{m_e^2} \right) - 1 \right) \left(2 \ln \frac{E}{\Delta E} - 3 \ln \eta \right),\tag{3.37}$$

of which items can be found in the expression of $\delta_{T_{sai}}$.

3.4.6 Results of $P_b P_t$

Before we can get to the point of calculating $P_b P_t$ from A_{el} , it is necessary to compare the data analysis results of other physics quantities (except A_{el}) including θ_{target} , ϕ_{target} , y_{target} , p_{target} , missing mass spectra and deduced values, such as the beam energy and the spectrometer momentum setting, with the simulation. Such a comparison gives us a glimpse of the quality of the simulation. However, only comparisons about the beam energy, the momentum setting, and the cross-section will be discussed in detail.

As we mentioned before, the simulation of the elastic scattering provides additional measurement of the beam energy. Assuming that the scattering angle and the energy loss are well known, one can extract the beam energy and the spectrometer central momentum setting with a high accuracy, by matching of the spectrum of scattering momentum (Δ_{target}) verse the scattering angle (ϕ_{target}) and the spectrum of the excitation energy (E_x) from the simulation with spectra from the data. Here the spectrum of ($\Delta_{target}, \phi_{target}$) corresponding to the elastic kinematic equation is written

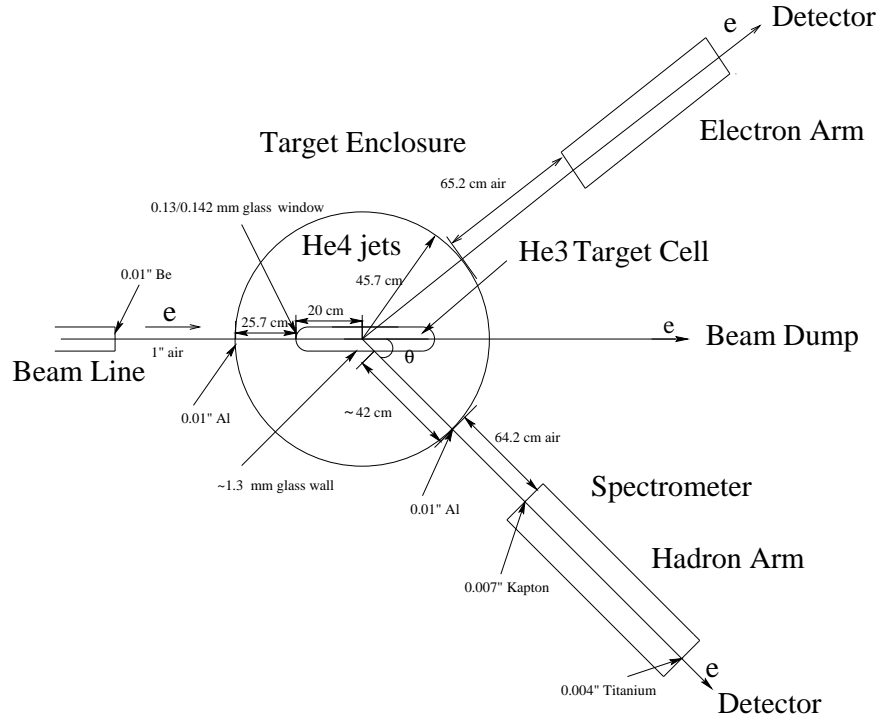


Figure 3-8: The material, which particle goes through, layout

as:

$$E'_e = \frac{E_e - E_{loss1}}{1.0 + E_e \frac{1.0 - \cos(\phi_0 + \phi_{target})}{M_{3He}}} - E_{loss2} \quad (3.38)$$

with the spectrometer central scattering angle setting being ϕ_0 , the mass of 3He , M_{3He} , energy losses before and after scattering, E_{loss1} and E_{loss2} . The Δ_{target} is defined as

$$E'_e = \left(1 + \frac{\Delta_{target}}{100}\right) \times P_0 \quad (3.39)$$

with the spectrometer central momentum setting being P_0 . The excitation energy,

E_x is given as

$$E_x = \sqrt{M_{3He}^2 + 2M_{3He}(E_e - E'_e) - 2E_e E'_e(1.0 - \cos(\phi_0 + \phi_{target}))} - M_{3He}. \quad (3.40)$$

The geometric parameters of the medium, which particle goes through, within the simulation software are shown in Fig. 3-8 and their radiation lengths, X_0 are listed in Tab. 3.4. The results of the beam energy (shown in Fig. 3-9) extracted independently

Absorber	Material	Rad Length, X_0 (g/cm^2)
	Upstream	
Beamline Vacuum Window	Be, 0.01" thickness	65.19
Gap between Windows	Air, 1" gap	36.66
Target Chamber Window	Al, 0.01" thickness	24.01
Target Chamber Gas	4He , 25.7 cm	94.32
Target Entrance Window	Glass, .13/.142 mm	28.3
Target	3He , 9.98 amg	70.74
	Downstream	
Target Side Wall	Glass(ge180) 1.2/1.3mm	19.43
Target Chamber Gas	4He , 42.0 cm	94.32
Chamber Exit Window	Al, 0.01" thickness	36.66
Gap between Windows	Air, 64.2cm gap	24.01
Magnets Entrance Window	0.007" Kapton	40.56
Magnets Exit Window	0.004" Titanium	16.17

Table 3.4: The medium radiation length, X_0

from the eP measurement, (the Arc measurement), and the 3He elastic measurement agree within the experimental uncertainty for both the 1pass data and the 2 pass data. However the results of the spectrometer central momentum setting (shown in Fig. 3-9) from the 3He elastic measurement and the spectrometer NMR measurement do not agree. The reason for the discrepancy, later pointed out in [117], was due to

the nonlinearity between the driving current and the magnetic field, which caused the failure of the calibration constant of the NMR measurement as the driving current was set far away from the calibration current. In fact, the NMR result is expected to be lower than the real value of the magnetic field, and the larger the driving current (magnetic field) is, the bigger the discrepancy between the NMR result and real magnetic field value is. The momentum setting from the simulation fitting is ($\approx 0.2\%$) bigger than the NMR result and therefore may be very close to the real value.

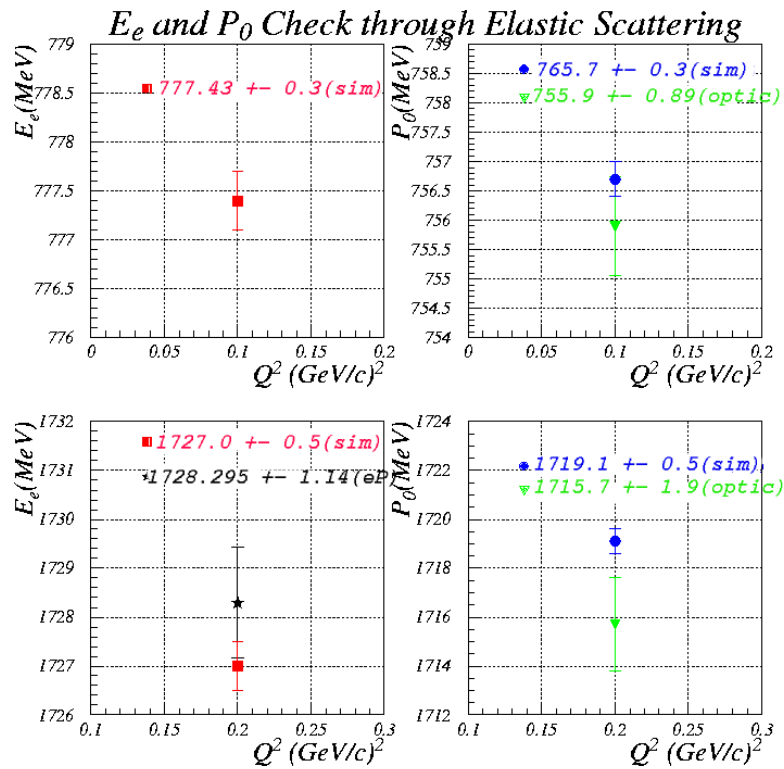


Figure 3-9: The spectrometer central momentum setting P_0 and the incident energy E_e from three independent means: ep elastic(eP), ^3He elastic(sim), and the optic database(optic)

The normalized yield of the data for the ^3He elastic scattering shown in Fig. 3-10

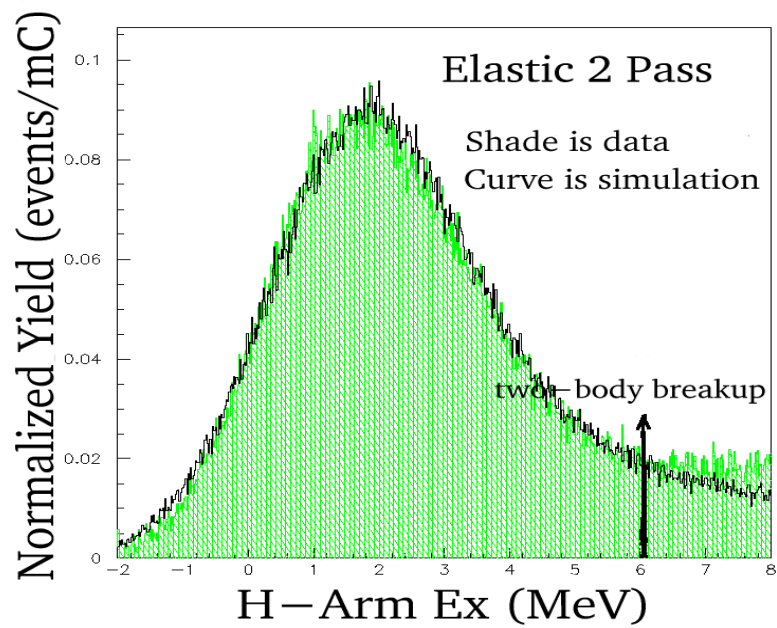
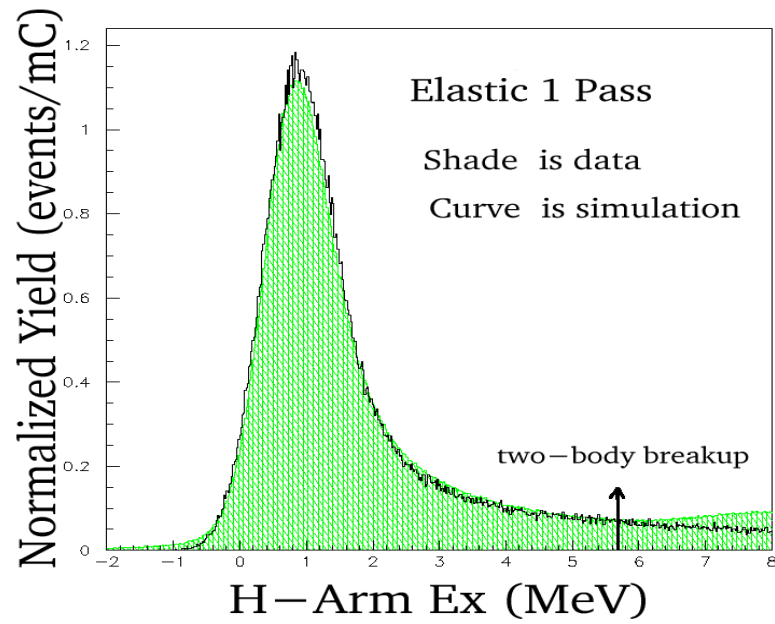


Figure 3-10: The comparisons between data and simulation for $Q^2 = 0.1$ and 0.2 . The two-body breakup energy is about 5.5 MeV.

Cuts	A_{el}^{sim}
$\Delta: [-1.5\%, 1\%]$	5.840%
Ex: [-3MeV, 3MeV]	5.844%
$\theta_{target}: [-30mr, 30mr]$ & Ex: [-3MeV, 3MeV]	5.817%
$\phi_{target}: [-30mr, 30mr]$ & Ex: [-3MeV, 3MeV]	5.848%
$y_{target} + offset: [-30mm, 30mm]$ & Ex: [-3MeV, 3MeV]	5.848%
Ex: [-1.5MeV, 1.5MeV]	5.848%

Table 3.5: Variation of A_{el}^{sim} for 1 Pass kinematic setting and target spin -62.5° with different cuts

Cuts	A_{el}^{sim}
$\Delta: [-3\%, -0.5\%]$	5.681%
Ex: [-3MeV, 3MeV]	5.569%
$\theta_{target}: [-30mr, 30mr]$ & Ex: [-3MeV, 3MeV]	5.503%
$\phi_{target}: [-30mr, 30mr]$ & Ex: [-3MeV, 3MeV]	5.598%
$y_{target} + offset: [-30mm, 30mm]$ & Ex: [-3MeV, 3MeV]	5.570%
Ex: [-1.5MeV, 1.5MeV]	5.570%

Table 3.6: Variation of A_{el}^{sim} for 2 Pass kinematic setting and target spin -62.5° with different cuts

is not only normalized by the total charge, live time of data acquisition system and detector inefficiency, but also corrected by the N_2 and empty target cell backgrounds. On the other hand, the simulation result is only corrected by the charge normalization. As the normalized yield is directly proportional to the corresponding cross section, the relative difference of the normalized yield equals to the relative difference of the cross section. Some conclusions we can draw from Fig. 3-10 are following: First the cross-section from simulation is about 2-3% larger than the cross-section from data. Secondly the relative difference tends to get bigger if the missing mass is further beyond the elastic peak region. A few reasons are expected to explain this behavior. One is that the equivalent radiators theory for the radiative tail correction of the internal bremsstrahlung is the peaking approximation. Thus the calculation became

$ A_{el}^{sim} $		
θ_{spin}	1 Pass	2 Pass
-62.5°	0.05848	0.05570
-243.6°	0.05762	0.05496

Table 3.7: The simulated elastic asymmetry, $|A_{el}|$ for different target polarization direction, θ_{spin} and kinematic setting

less precise on radiation tail as the missing mass is further away from the elastic peak region. Another is the uncertainty of the N_2 and empty target cell dilution listed in Tab. 3.8. Lastly quasi-elastic events sneak into the elastic tail by reasons such as multiply scattering and bremsstrahlung effects. Overall, the agreement between the data and simulation is good.

In order to get A_{el} from the simulation, not only the strength of the effects, such as radiative correction, but also the spin dependence of the effects needs to be taken into account. The spin dependence of the effects mainly includes the spin dependence $\delta_{T_{sai}}$ and the depolarization of electron beam through collisions and ionization process. The depolarization effect is included in the simulation, and the spin dependence of $\delta_{T_{sai}}$ is so small that it is ignored. In addition, the magnitude of A_{el} may strongly depend on the acceptance. If it is the case, the uncertainty of A_{el}^{sim} from the simulation due to the uncertainty of the acceptance of the simulation will be large. In Table 3.6, the simulated asymmetry A_{el}^{sim} is found to have little dependence on the acceptance. Therefore, the simulated asymmetry A_{el}^{sim} s for Q^2 values of $0.1 (GeV/c)^2$ and $0.2 (GeV/c)^2$ are listed in Tab. 3.7 with a systematic uncertainty due to the acceptance of 0.1%.

$P_b P_t$ is determined by the following formula:

$$P_b P_t = \frac{A_{el}^{exp}}{A_{el}^{sim}} \times f_{N2} f_{empty} \quad (3.41)$$

with the elastic dilution factors: f_{N2} and f_{empty} from $N2$ and empty target cell respectively. f_{N2} and f_{empty} are given in Tab. 3.8. The average $P_t P_b$ is $0.208 \pm 0.001 \pm$

H-arm Q^2	$(f_{N2} - 1)(2.2 \pm 0.5 \text{ psi})$	$(f_{empty} - 1)$
0.1	1%	< 0.1%
0.2	3.07%	< 0.2%

Table 3.8: The elastic dilution factors: f_{N2} and f_{empty} for two elastic data sets

0.005, where the uncertainties are statistical and systematic, respectively [104]. The systematic uncertainties of $P_b P_t$ are list in Table 3.9. The systematic uncertainties are dominated by the theoretical uncertainties due to the experimental uncertainties of Fc and Fm in calculating of the theoretic asymmetry A_{el} from the simulation. For the 1pass data ($Q^2 = 0.1$), the uncertainty of the calculation of A_{el} is about 1.3% and for the 2pass data ($Q^2 = 0.2$), it is about 1.7%. Combining the polarization of the beam P_b results from Møller measurement, as shown in Tab. 2.4 and the polarization of the target P_t results from NMR measurement, the average $P_t P_b$ can also be obtained to be 0.215 ± 0.013 with total systemic uncertainty [104]. The results of those two independent techniques agree within a relative difference of 4%. The difference, we expect, is caused by factors such as the beam-induced depolarization and the temperature uncertainty of the target cell. This is because the ^3He elastic measurement took place as the electron beam was going through the target and, on the contrary, the NMR measurement took place with beam off. Indeed, the consistency of these two measurement provides an additional support of the results of the simulation.

In addition, using $P_b P_t$ in Eq. 3.41 and the polarization of th beam, P_b from Møller measurement, we also can get the polarization of the target, P_t and compare with P_t from NMR measurement. The comparison is shown in Fig. 3-11 and these two P_t results can agree with each other within 5% after MNR measurement is properly calibrated.

H-arm $Q^2=0.1$

Item	Uncertainty	$\frac{\delta P_b P_t}{P_b P_t}$ %
target spin direction	0.5°	0.69
Fc,Fm	$1.5 \times 10^{-3}, 3.0 \times 10^{-3}$	1.0
electron beam energy	± 1 MeV	0.20
central momentum setting	± 3 MeV	0.30
acceptance		0.10
radiation length	3	0.10
empty target cell subtraction		0.02
N2 background subtraction	± 2	0.05
	total	1.3

H-arm $Q^2=0.2$

Item	Uncertainty	$\frac{\delta P_b P_t}{P_b P_t}$ %
target spin direction	0.5°	0.65
Fc,Fm	$1.4 \times 10^{-3}, 1.2 \times 10^{-3}$	1.5
electron beam energy	± 1 MeV	0.20
central momentum setting	± 3 MeV	0.30
acceptance		0.10
radiation length	3	0.10
empty target cell subtraction		0.01
N2 background subtraction	± 2	0.02
	total	1.7

Table 3.9: Systematic uncertainty in determining $P_t P_b$ from the elastic asymmetry measurement.

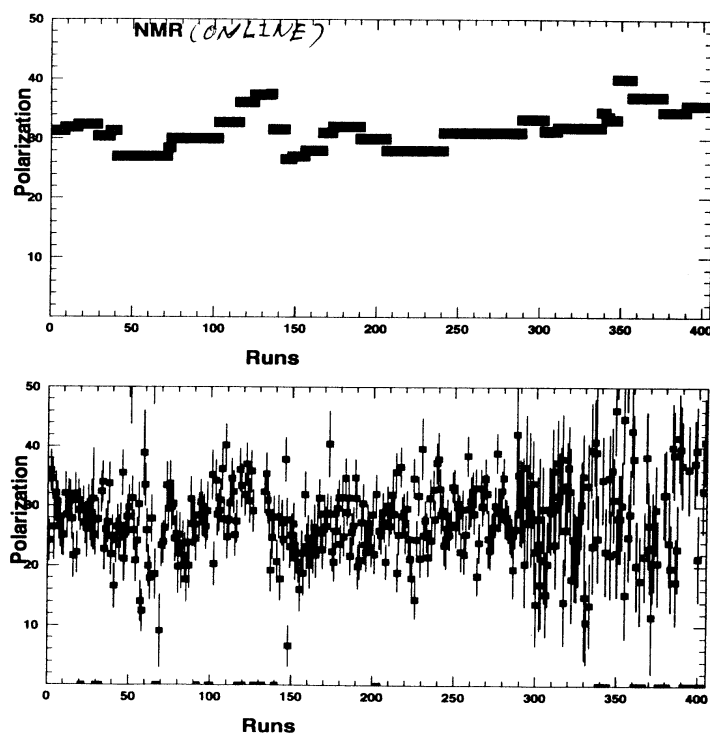


Figure 3-11: The target polarization, P_t from the NMR measurement in the upper panel, and P_t from the Møller measurement & elastic polarimetry in the lower panel.

3.5 Dilution Factor

Electrons are not only scattered by the ^3He nuclei but also by the windows of the target cell and N_2 nuclei. The magnitude of the raw asymmetry caused by the beam and target polarization will drop because in the equation of asymmetry, the denominator, which is the total yield of the scattered electron, gets bigger but the numerator, which is the difference of the yields with respect to the different beam helicity, remains the same. The dilution corrections due to the N_2 and empty target cell backgrounds is therefore introduced in Equation 3.8 in order to extract the physics quasi-elastic asymmetry. For dilution corrections due to the N_2 , the calculation is

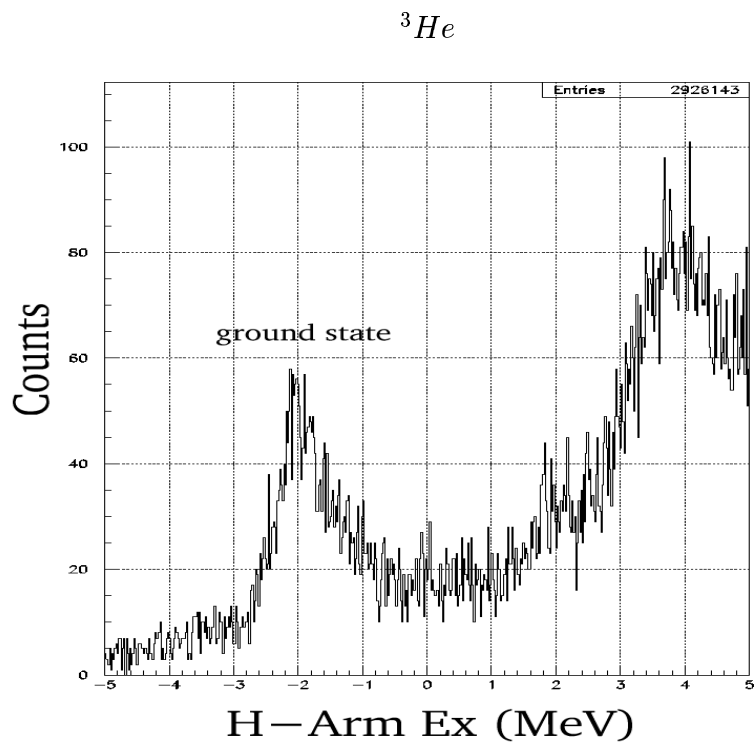
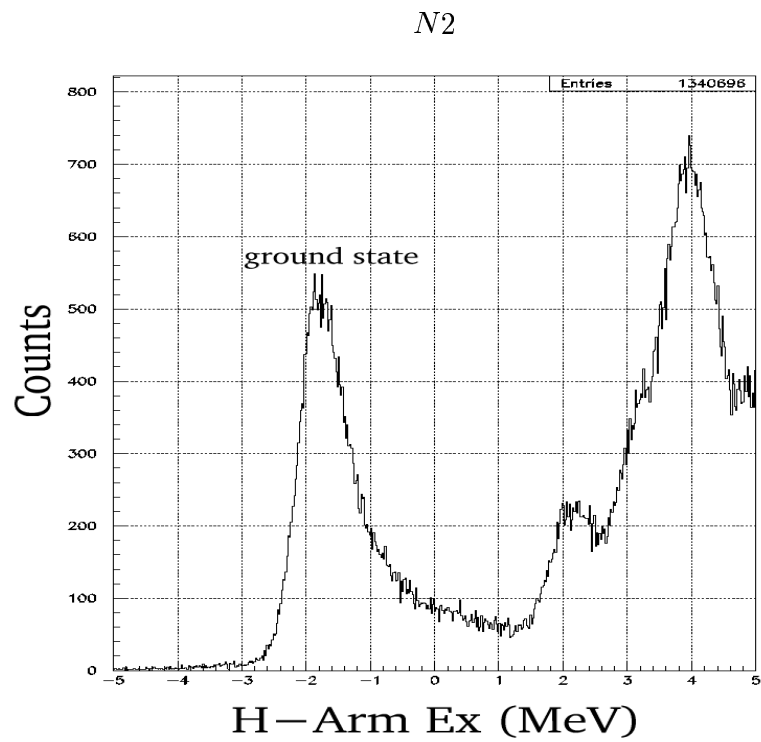


Figure 3-12: Excitation energy, Ex for N_2 reference and 3He target. The most left peak is related to the ground state of N_2 and others are related to excitation states of N_2 .

difficult because the amount of N_2 in the ^3He target cell need to be determined. To get the result of the dilution factor of N_2 , one has to determine the N_2 pressure in the ^3He target using a pure N_2 reference cell with a known N_2 pressure first, then scale a pure N_2 yield according to the N_2 pressure in ^3He target cell, and finally calculate the dilution factor using the scaled N_2 yield divided by the ^3He quasi-elastic yield.

The determination of the N_2 pressure in the target cell is the following: several N_2 elastic peaks shown in Fig. 3-12: the most left peak related to the ground state of N_2 and others related to excitation states of N_2 in the N_2 excitation energy spectrum are clearly observed from data taken with the ^3He target cell. In order to get the normalized N_2 elastic yields, the yields of those elastic peaks are corrected with backgrounds such as ^3He gas, the entrance window of target, and the target wall, then are normalized with charge, deadtime and efficiencies. Compared with the normalized N_2 elastic yield of one of elastic peaks from ^3He target cell ($Y_{N_2}^{target}$) and such yield from a pure N_2 reference cell ($Y_{N_2}^{ref}$) with a known N_2 pressure (P_{N_2}), one can get the N_2 pressure in the ^3He target, which is the $\frac{Y_{N_2}^{target}}{Y_{N_2}^{ref}} \times P_{N_2}$, because the physical sizes and running conditions of two cells are similar. The N_2 pressure in the ^3He target from this determination process is obtained as 2.2 ± 0.05 psi. The uncertainty of the N_2 pressure in the ^3He target contributes to the main error of the N_2 dilution factors.

In fact, the empty target cell background can not be directly measured because we can not pump out gas inside the target cell without destroying the target. The physical size of the reference target cell is close to that of the target cell. Thus assuming the empty target cell yield is equal to the empty reference cell yield, we can obtain the result of the dilution factor of the empty target cell using the empty reference cell yield divided by the ^3He quasi-elastic yield. Because of the difference of wall thickness between the target and the reference cells and the dependence of the empty target cell yield on the beam position, the yield from the empty ^3He target

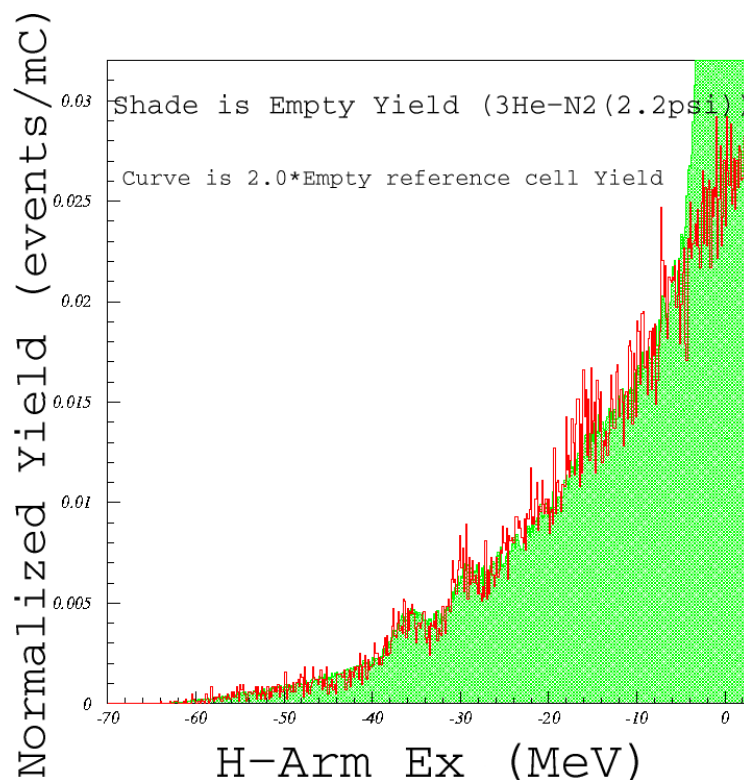


Figure 3-13: The dilution factors of the empty target cell for 1 Pass kinematic in H-arm cell may not be equal to the empty reference cell yield with a central beam position of $(X_{beam} = 0, Y_{beam} = 0)$. In fact, Fig. 3-13 shows that the yield of the empty ^3He target cell is about twice the empty reference cell yield with a central beam position of $(X_{beam} = 0, Y_{beam} = 0)$. One therefore needs to enlarge the dilution factor of the empty target cell by a factor of 2 in order to correct the raw asymmetry properly. This factor may vary during the experiment². In addition, the well matching of two curves (in Fig. 3-13) indicates that the N_2 pressure we determined is accurate.

The empty target cell and the N_2 dilution factors (R^{empty} and R^{N_2}) at six different Q^2 are listed in Table 3.10.

²In data analysis, we assume this factor is 1 and we introduce a correction for G_m^n in Tab. 5.6

$$Q^2=0.1$$

$\omega(\text{MeV})$	R^{N^2}	R^{empty}
(25.0, 35.0)	0.06918	0.0396
(35.0, 45.0)	0.05379	0.0346
(45.0, 55.0)	0.04227	0.0297
(55.0, 65.0)	0.03889	0.0296
(65.0, 75.0)	0.04369	0.0361
(75.0, 85.0)	0.05468	0.0503
(85.0, 95.0)	0.06918	0.0720
(95.0, 105.0)	0.07097	0.1058

$$Q^2=0.2$$

$\omega(\text{MeV})$	R^{N^2}	R^{empty}
(75.0, 85.0)	0.0626	0.0462
(85.0, 95.0)	0.0516	0.0417
(95.0, 105.0)	0.0444	0.0375
(105.0, 115.0)	0.0426	0.0394
(115.0, 125.0)	0.0463	0.0455
(125.0, 135.0)	0.0548	0.0588
(135.0, 145.0)	0.0666	0.0788

$$Q^2=0.3$$

$\omega(\text{MeV})$	R^{N^2}	R^{empty}
(100.0, 120.0)	0.086310	0.0106505
(120.0, 140.0)	0.059532	0.0078850
(140.0, 160.0)	0.049766	0.0070951
(160.0, 180.0)	0.052771	0.0082114
(180.0, 200.0)	0.065888	0.0115666
(200.0, 220.0)	0.085988	0.0171267
(220.0, 240.0)	0.103261	0.0236398

$$Q^2=0.4$$

$\omega(\text{MeV})$	R^{N^2}	R^{empty}
(140.0, 160.0)	0.09711	0.01190
(160.0, 180.0)	0.07368	0.00845
(180.0, 200.0)	0.05843	0.00688
(200.0, 220.0)	0.05339	0.00692
(220.0, 240.0)	0.05667	0.00836
(240.0, 260.0)	0.06642	0.01141
(260.0, 280.0)	0.08397	0.01672
(280.0, 300.0)	0.09570	0.02052

$$Q^2=0.5$$

$\omega(\text{MeV})$	R^{N^2}	R^{empty}
(190.0, 210.0)	0.09711	0.01231
(210.0, 230.0)	0.07368	0.00935
(230.0, 250.0)	0.05843	0.00785
(250.0, 270.0)	0.05339	0.00765
(270.0, 290.0)	0.05667	0.00835
(290.0, 310.0)	0.06642	0.00880
(310.0, 330.0)	0.08397	0.01556
(330.0, 350.0)	0.09570	0.02049

$$Q^2=0.6$$

$\omega(\text{MeV})$	R^{N^2}	R^{empty}
(250.00, 268.75)	0.08417	0.01128
(268.75, 287.50)	0.06754	0.00862
(287.50, 306.25)	0.05680	0.00835
(306.25, 325.00)	0.05349	0.00810
(325.00, 343.75)	0.05707	0.00949
(343.75, 362.50)	0.06618	0.01205
(362.50, 381.25)	0.08145	0.01610
(381.25, 400.00)	0.08937	0.01859

Table 3.10: The dilution factors: R^{N^2} and R^{empty} for six Q^2 values of quasi-elastic kinematics of the experiment

3.6 Quasi-elastic Radiative Correction and Elastic Tail Correction

In general, in order to extract physics asymmetry of the one-photon exchange contribution of a scattering, one needs to correct the experimental asymmetry with the radiative corrections (RC). In our case, A^{ert} , η and ΔA_{rad}^{qe} introduced in Chapter 2 need to be calculated from the radiative correction. There are two basic methods to calculate the model independent QED radiative correction. The first one, which we used to obtain A_{el} with Mo and Tsai calculation, is connected with the introducing of an artificial parameter ΔE separating the momentum phase space into soft and hard parts. The presence of the artificial parameter ΔE is a disadvantage of this method. The calculation of the soft photon part is performed in soft photon approximation, in which the photon energy is considered to be small with respect to all momenta and masses. Thus the parameter should be chosen as small as possible to reduce the region evaluated approximately. However it can not be chosen too small because of possible numerical instabilities in calculating the hard-photon emission. In late seventies Bardin and Shumeiko developed an approach [65] of extraction and cancellation of infrared divergence without introducing this artificial parameter ΔE . This approach was then applied to the calculation of electromagnetic correction to the lepton current for deep inelastic scattering (DIS) [70] as well with some approximation taking into account the contribution of net soft photon emission. The exact expressions for the lowest order QED RC to polarized DIS of polarized leptons by polarized light nuclei including targets of spin 1 such as deuterium are presented in [66]. Based on these formulae Fortran code POLRAD [67] are constructed.

The formulae for calculating the RC cross-section is given by

$$\sigma_{RC} = \sigma^{in} + \sigma^{el} + \sigma^q + \sigma^v \quad (3.42)$$

Here $\sigma^{in}, \sigma^{el}, \sigma^q$ are contributions of radiative tails from continuous spectrum, of the elastic scattering radiative tail, and of the radiative tail from the quasi-elastic scattering respectively. σ^v is the virtual photon contribution. The explicit expression for σ^{el}, σ^q can be found in [66, 69].

For the lowest-order QED correction (α^1 correction), the infrared-free sum of σ^v and σ^{in} is calculated by

$$\sigma^v + \sigma^{in} = \frac{\alpha}{\pi} (\delta_R^{IR} + \delta_{vert} + \delta_{vac}^l + \delta_{vac}^h) \sigma_o + \sigma_F^{in}, \quad (3.43)$$

where σ_o is the Born cross-section, δ_{vert} is the lepton vertex correction, $\delta_{vac}^l + \delta_{vac}^h$ are the vacuum polarization by the leptons and hadrons respectively, and the quantity δ_R^{IR} appears when the infrared divergence is extracted in accordance with Bardin and Shumeiko method from σ^{in} . These corrections are given by formulae (20-25) of ref. [66]

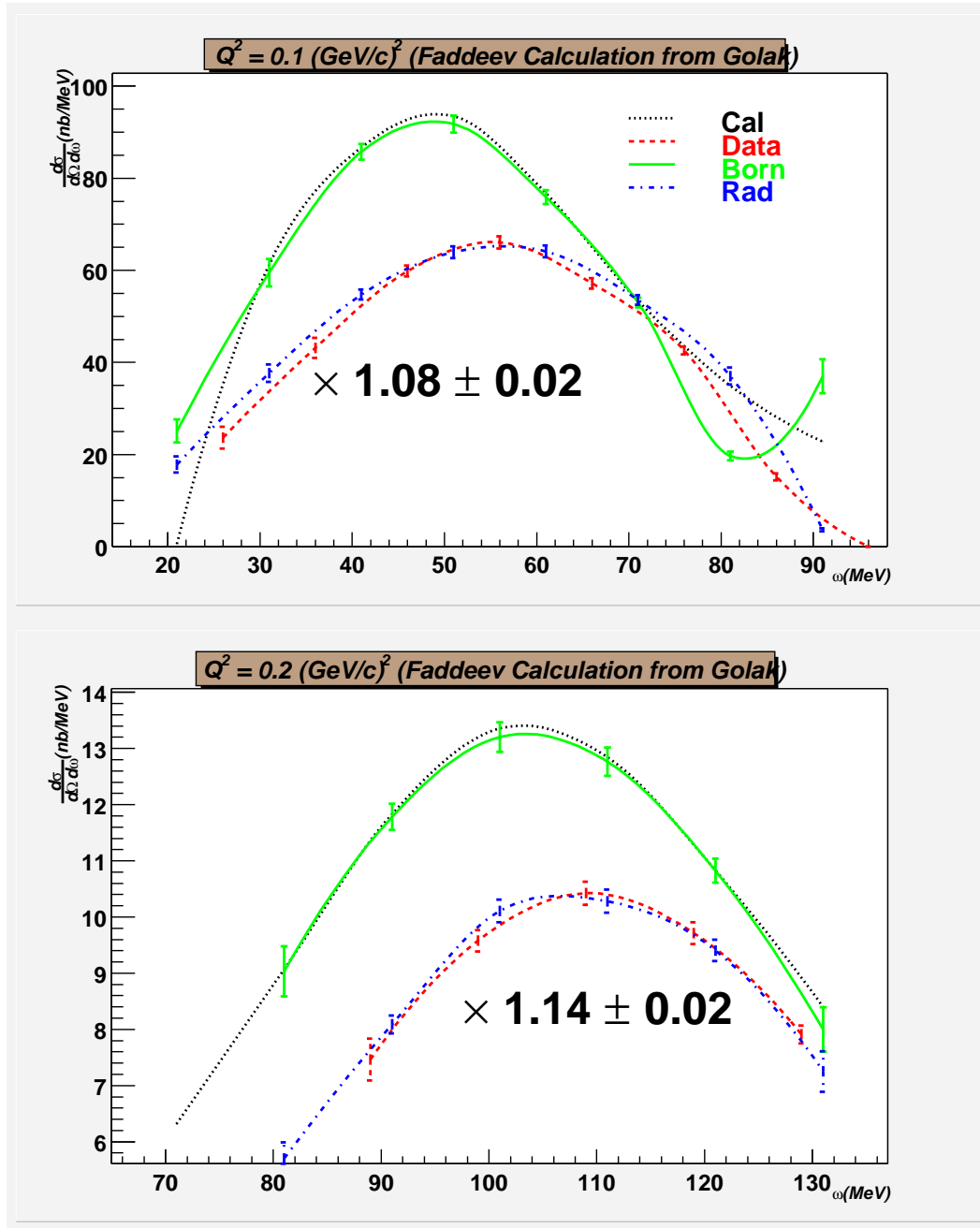
Taking into account the contribution of multi-soft-photon emission, i.e. by using the so-called “exponentiation” procedure [68], thus we have

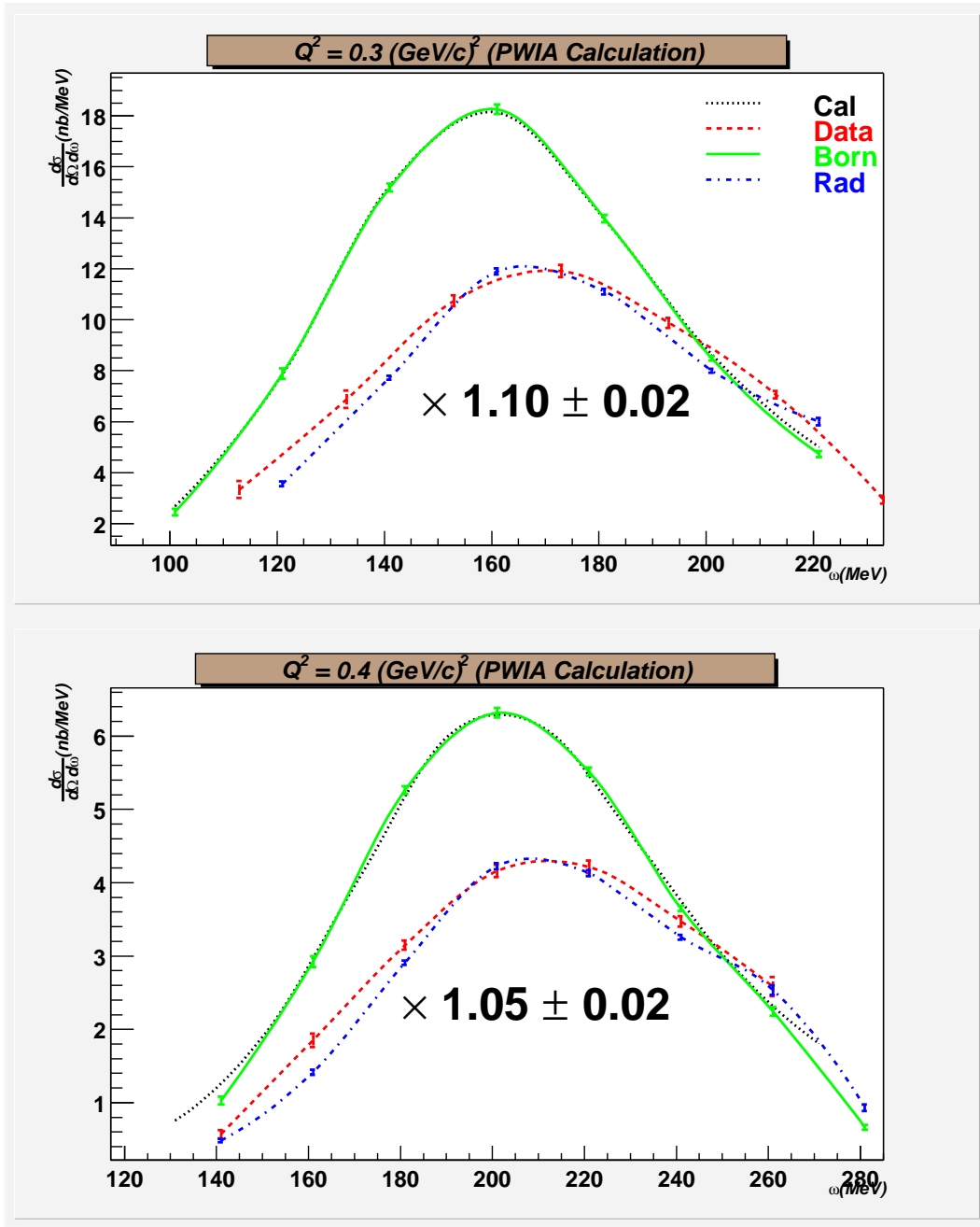
$$\sigma_{RC} = e^{\frac{\alpha}{\pi} \delta^{inf}} (\delta_{IR}^R + \delta_{vert} + \delta_{vac}^l + \delta_{vac}^h - \delta^{inf}) \sigma_o + \sigma_F^{in} + \sigma^{el} + \sigma^q. \quad (3.44)$$

Following same formulae as POLRAD does, the C++ code called Polarized Radiative Correction was developed for longitudinally polarized electron scattering on a polarized ^3He nucleus. For the details of this work, we refer to [72]. In Table 3.11, the radiative corrections (RC) are listed. Using Polarized Radiative Correction, we are also able to study the unpolarized quasi-elastic yield for $^3\text{He}(e, e')$. In Fig. 3-14, the extracted cross-section from the simulation without radiative correction (called “Born”), the cross-section from the calculation using a central kinematic setting (called “Cal”), the extracted cross-section from the simulation with radiative correction (called “Rad”), and the extracted cross-section from data (called “Data”) are

shown in terms of the energy transfer ω for six different Q^2 . The systematic uncertainty in the extraction of the cross-section is estimated as the difference between “Born” and “Cal”, which is about 2%.

Conclusions drawn from the study for the unpolarized cross-section are three-folds. First, “Rad” using Golak’s full calculation at Q^2 value of 0.1 or 0.2 (GeV)² is roughly 10% higher than “Data”. Secondly, “Rad” using PWIA at Q^2 values above 0.2 (GeV)² is roughly 5% higher than “Data”, and as Q^2 goes higher, the PWIA calculation, “Rad” gets closer to the experimental result, “Data”. One should bear in mind that both our knowledge of the spectrometer acceptance and the knowledge of the nuclear response functions goes into the comparison between data and simulation. Although the cross-section from quasi-elastic simulation is 5-10% higher than the cross-section from data, such agreement is still reasonable considering the facts that the experiment focuses on asymmetry instead of cross-section measurement, and the radiative correction on experimental asymmetry in quasi-elastic peak region is not sensitive to the radiative correction on cross-section. Lastly, one therefore can still get the quasi-elastic radiative correction with a small theoretical uncertainty.





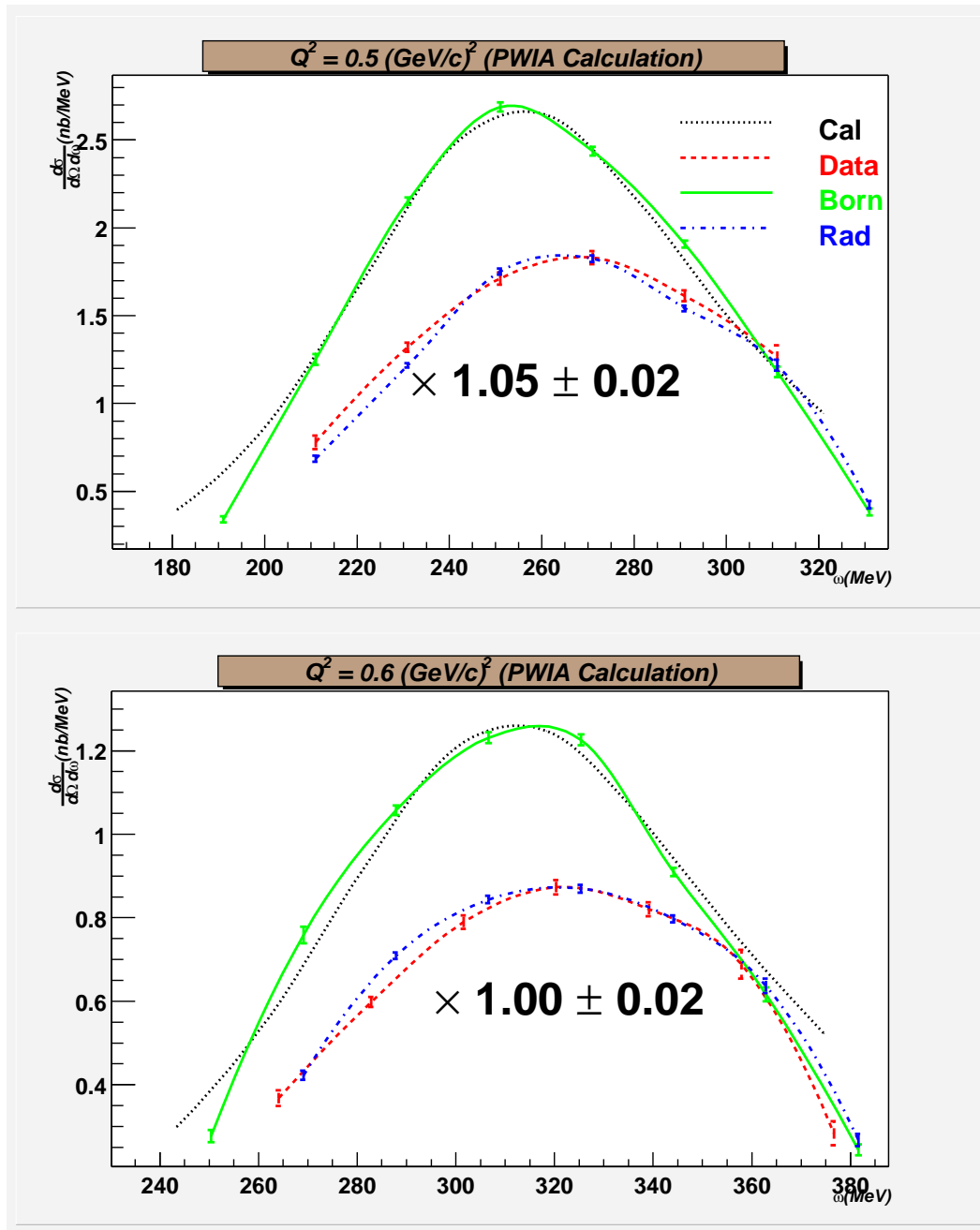


Figure 3-14: The comparison among the extracted quasi-elastic cross-sections. The extracted cross-section from the simulation without radiative correction is referred to as “Born”, the extracted cross-section from the simulation with radiative correction is referred “Rad”, the cross-section from the calculation is referred to as “Cal”, and the extracted cross-section from data is referred to as “Data”. The number on the graph is the ratio of “Rad” and “Data”, and “Data” is scaled with this ratio in the graph.

$$Q^2=0.1$$

$\omega(\text{MeV})$	$\Delta A_{rad}^{qe}(full)$	η	A^{ert}
(25.0, 35.0)	0.00255924	0.0015696	0.31091
(35.0, 45.0)	-0.000946766	0.0017870	0.09042
(45.0, 55.0)	-0.00150382	0.0019268	0.04352
(55.0, 65.0)	-0.00159346	0.0019548	0.02987
(65.0, 75.0)	-0.00238483	0.0021690	0.02765
(75.0, 85.0)	-0.00337165	0.0022534	0.03010
(85.0, 95.0)	-0.00696778	0.0025300	0.04410

$$Q^2=0.2$$

$\omega(\text{MeV})$	$\Delta A_{rad}^{qe}(full)$	η	A^{ert}
(75.0, 85.0)	-0.00163502	0.00910	0.0350807
(85.0, 95.0)	-0.00127525	0.00572	0.0335841
(95.0, 105.0)	-0.000489976	0.00403	0.0321326
(105.0, 115.0)	-0.000496957	0.00331	0.0306573
(115.0, 125.0)	-0.000265174	0.00310	0.0293742
(125.0, 135.0)	-0.00124063	0.00340	0.0277448
(135.0, 145.0)	-0.00311851	0.00340	0.0277448

$$Q^2=0.3$$

$\omega(\text{MeV})$	$\Delta A_{rad}^{qe}(pwia)$	η	A^{ert}
(100.0, 120.0)	-0.0020209	0.00356	0.0340388
(120.0, 140.0)	-0.0003281	0.00111	0.0302019
(140.0, 160.0)	-0.0013839	0.00056	0.0277632
(160.0, 180.0)	-0.0016440	0.00046	0.0244447
(180.0, 200.0)	-0.0029524	0.00051	0.0217933
(200.0, 220.0)	-0.0055601	0.00069	0.0198347
(220.0, 240.0)	-0.0092538	0.00102	0.0176836

$$Q^2=0.4$$

ω (MeV)	$\Delta A_{rad}^{qe}(pwia)$	η	A^{ert}
(140.0, 160.0)	-0.0019626	0.00027	0.232462
(160.0, 180.0)	-0.0022663	0.00011	0.190677
(180.0, 200.0)	-0.0009377	0.00006	0.158488
(200.0, 220.0)	-0.0012033	0.00005	0.131781
(220.0, 240.0)	-0.0023750	0.00005	0.109443
(240.0, 260.0)	-0.0047388	0.00007	0.091837
(260.0, 280.0)	-0.0071162	0.00011	0.070185
(280.0, 300.0)	-0.0080000	0.00011	0.070185

$$Q^2=0.5$$

ω (MeV)	$\Delta A_{rad}^{qe}(pwia)$	η	A^{ert}
(190.0, 210.0)	-0.0020000	0.00002	-----
(210.0, 230.0)	-0.0008205	0.00002	-----
(230.0, 250.0)	-0.0009572	0.00001	-----
(250.0, 270.0)	-0.0017815	0.00002	-----
(270.0, 290.0)	-0.0023846	0.00002	-----
(290.0, 310.0)	-0.0045448	0.00002	-----
(310.0, 330.0)	-0.0069334	0.00002	-----
(330.0, 350.0)	-0.0075000	0.00002	-----

$$Q^2=0.6$$

ω (MeV)	$\Delta A_{rad}^{qe}(pwia)$	η	A^{ert}
(250.00, 268.75)	-0.0008097	0.00004	-----
(268.75, 287.50)	-0.0016557	0.00004	-----
(287.50, 306.25)	-0.0016192	0.00004	-----
(306.25, 325.00)	-0.0018354	0.00004	-----
(325.00, 343.75)	-0.0027080	0.00004	-----
(343.75, 362.50)	-0.0047085	0.00004	-----
(362.50, 381.25)	-0.0069011	0.00004	-----
(381.25, 400.00)	-0.0088891	0.00004	-----

Table 3.11: ΔA_{rad}^{qe} , η and A^{ert} for six Q^2 values. Because η is too small for the last two Q^2 kinematic settings, A^{ert} is not necessary to calculate.

Chapter 4

False Asymmetry and Systematic Uncertainty

In helicity-dependent asymmetry measurement, any helicity-correlated variation other than the helicity-dependent cross-section will cause additional asymmetry (so-called false asymmetry) which dilutes the physics asymmetry. In this chapter, various false asymmetries will be discussed in detail. The false asymmetries from some helicity-dependent variables can be determined for each run. One can therefore make a direct correction to the experimental asymmetry. These variables are termed correctable helicity-dependent variables. Some of the helicity-dependent variables cause false asymmetries which are smaller than the statistical uncertainty of the measured asymmetry. One can only identify them and assign a systematic uncertainty based on the false asymmetry. So these variables are named negligible helicity-dependent variables. For helicity-independent variables, one can check if their asymmetries are consistent with zero.

Based on these considerations, the DAQ dead time is categorized as a correctable helicity-dependent variable. Beam position shift, beam current, helicity determination, and the pion contamination are categorized as the negligible helicity-dependent

variables, due to of which the false asymmetries are smaller than the statistical uncertainty and thus only their contribution to the systematic uncertainty can be estimated. Other variables such as N_2 contribution, empty target cell contribution, the scintillators efficiency, and the VDC efficiency are testified as helicity-independent variables.

4.1 Correctable Helicity-dependent Variables

4.1.1 Data Acquisition Deadtime

When the signals from the detectors are gathered and a trigger is generated from the trigger supervisor, the event builder will help to build one event for DAQ (Data Acquisition) system. However, not all scattered particles will be able to generate events which goes into the data stream. One main reason is that a scattered particle can be excluded by the acceptance of the spectrometer. Other reasons for loss of event are the trigger inefficiency and the DAQ deadtime which also includes the computer network deadtime. It is reasonable to believe that the acceptance of the spectrometer is not helicity-dependent but trigger inefficiency and DAQ deadtime possibly are. In fact, there is ample evidence that the DAQ deadtime is strongly correlated to the beam helicity. We will discuss the helicity dependence of the DAQ deadtime in this section and the helicity dependence of the trigger efficiency will be discussed in the next section.

A number of factors can contribute to the DAQ deadtime and its fluctuation. As far as we know, the main factors are the event length, the event rate, and the computer system deadtime. The DAQ deadtime therefore is expressed as a function of the event length, the event rate, and the computer system deadtime. To show the correlation between the DAQ deadtime and the beam helicity, the difference of the DAQ deadtime with respect to the different helicities, Δ_{dt} is calculated as the

following:

$$\begin{aligned}
\Delta_{dt} &= Dt_{DAQ}^+ - Dt_{DAQ}^- \\
&= Dt_{DAQ}(L_{event}^+, R_{event}^+, Dt_{comp}^+) - Dt_{DAQ}(L_{event}^-, R_{event}^-, Dt_{comp}^-),
\end{aligned} \tag{4.1}$$

where L_{event} and R_{event} are the event length and the event rate respectively, Dt_{comp} is the deadtime of the DAQ computer system, and +, - refer to the two helicity states. Furthermore, Δ_{dt} can be rewritten in terms of the derivatives of L_{event} , R_{event} , and Dt_{comp} as:

$$\Delta_{dt} = \frac{\partial Dt_{DAQ}}{\partial L_{event}} \delta L_{event} + \frac{\partial Dt_{DAQ}}{\partial R_{event}} \delta R_{event} + \frac{\partial Dt_{DAQ}}{\partial Dt_{comp}} \delta Dt_{comp}, \tag{4.2}$$

and because δR_{event}^{mean} is equals to δR_{event} , and δL_{event}^{mean} is equals to δL_{event} , thus Δ_{dt}^{mean} is

$$\Delta_{dt}^{mean} = \frac{\partial Dt_{DAQ}}{\partial L_{event}} \delta L_{event} + \frac{\partial Dt_{DAQ}}{\partial R_{event}} \delta R_{event} + \frac{\partial Dt_{DAQ}}{\partial Dt_{comp}} \delta Dt_{comp}^{mean}, \tag{4.3}$$

Here δ is the operator representing the difference with respect to the different beam helicity, and mean is operator representing the average on an event basis.

Because the computer system deadtime is independent of the beam helicity, the δDt_{comp}^{mean} equals zero and the mean value of Δ_{dt} does not depend on the computer system deadtime. However, the shape of the distribution of Δ_{dt} is mainly a result of the computer system deadtime fluctuation .ie. $\Delta_{dt} = \Delta_{dt}(Dt_{comp})$. For the event length, the difference is also naturally expected to be zero. But due to the error that the Møller signal is triggered by the helicity signal, the Møller results are wrongly put into the data stream when the beam helicity pulse is positive. As a result, the event lengths for different helicities were not identical during the data taking and

the discrepancy between these two event lengths is about two words. Fortunately, the time slot for each event to be written into the data stream is not fully occupied. Therefore, the difference in the DAQ deadtime with respect to the different helicities is insensitive to the event length.

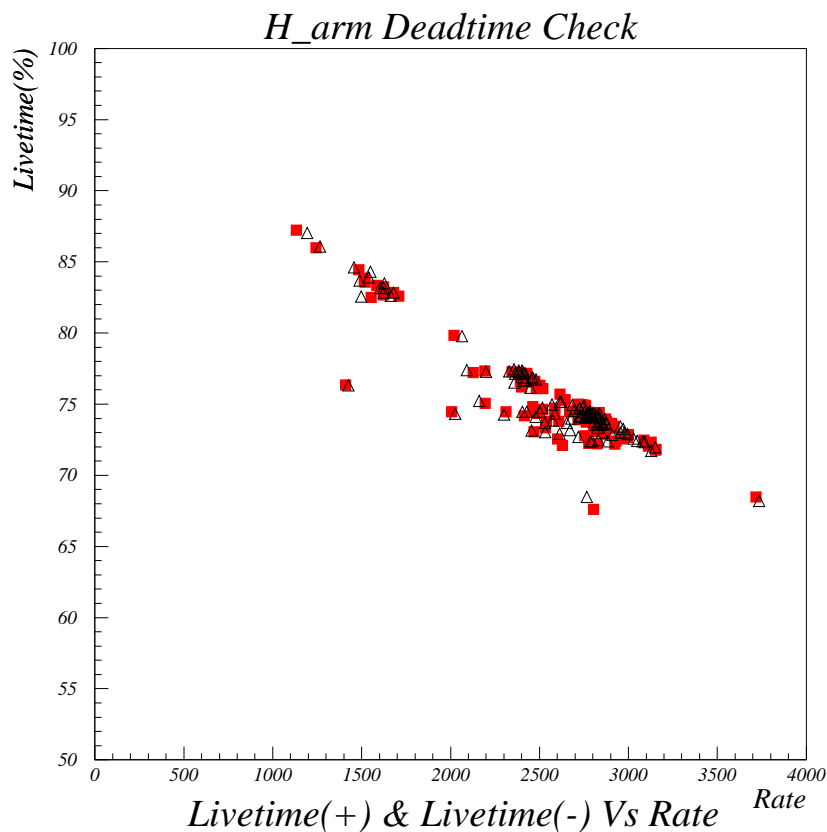


Figure 4-1: The DAQ livetime vs. rate with respect to helicities. The hollow triangle is the DAQ livetime for helicity + and the solid square is the DAQ livetime for helicity -.

This statement has been verified by the fact that the slopes of the DAQ deadtime¹ as function of the event rate are almost the same for the two different helicities in

¹Deadtime = 1 - Livetime

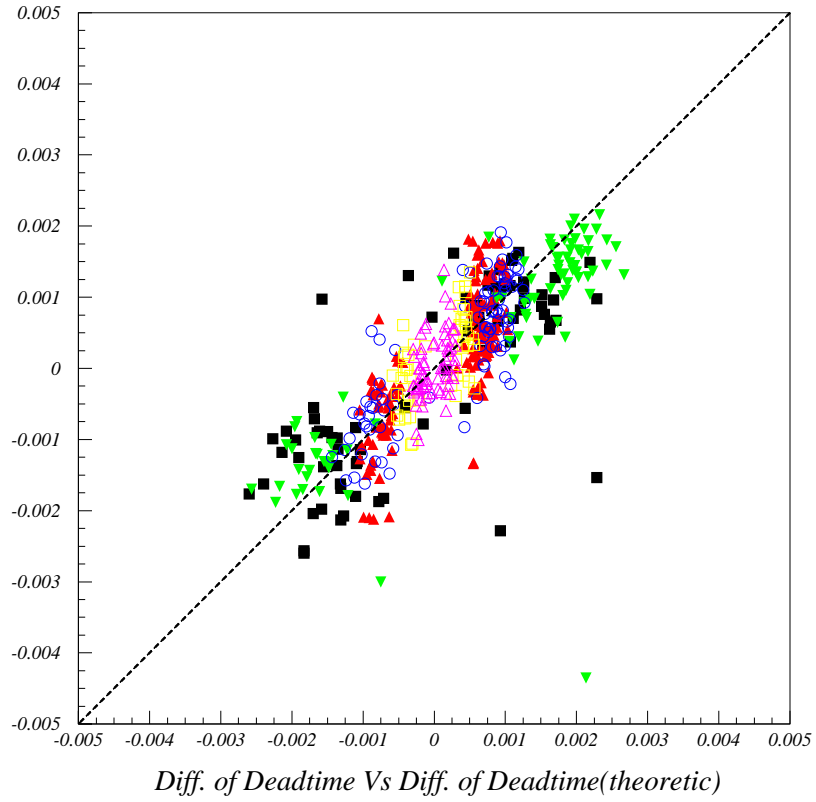


Figure 4-2: The comparison between the livetime and the calculated live time. The different shapes of the data points represent six different Q^2 data sets.

Fig 4-1. Therefore, Equation 4.3 is simplified as:

$$\Delta_{dt}^{mean} = \frac{dDt_{DAQ}}{dR_{event}} \delta R_{event}, \quad (4.4)$$

and the distribution of the difference in the DAQ deadtime for the different beam helicities is given according to the previous discussion, as:

$$\Delta_{dt} = \Delta_{dt}(\Delta_{dt}^{mean}, Dt_{comp}) \quad (4.5)$$

Knowledge of the slope of the DAQ deadtime in terms of the event rate - $\frac{dDt_{DAQ}}{dR_{event}}$, which is shown in Fig 4-1, allows us to calculate the mean value of Δ_{dt} by using Equation 4.4. The expected and the observed values of the mean value of Δ_{dt} for six different Q^2 are displayed in Fig. 4-2.

The discrepancy between the expected and the observed values are less than 10ppm. Therefore, even though the DAQ deadtime causes a false asymmetry of about a few percent, the uncertainty in the physics asymmetry due to the DAQ deadtime is less than 10ppm.

4.2 Helicity-independent Variables

4.2.1 N2 Asymmetry and Empty Target Cell Asymmetry

As we have stated before, the N2 yield and the empty target cell yield contribute to the total experimental yield because of the composition of the ^3He target cell. As a consequence, not only do the yields from N2 and the empty target dilute the physics asymmetry, but their false asymmetries will also contribute to the systematic uncertainty of the physics asymmetry. In Table 4.2.1, the asymmetries and the uncertainties of N2 and the empty target cell(which deduce from the empty reference cell) for E-arm at six different settings of the experiment are listed. The false asymmetries from the N2 calibration runs & the empty reference cell runs are consistent with zero within the statistical uncertainty of the measurements. Thus the N2 yield and the empty target yield cell are listed as the helicity-independent variables.

$$Q^2=0.1$$

ω (MeV)	A^{N^2} (%)	A^{empty} (%)
(25.0, 35.0)	-0.84515 ± 0.28172	0.82933 ± 0.84966
(35.0, 45.0)	0.01400 ± 0.15288	-0.55789 ± 0.44155
(45.0, 55.0)	0.13654 ± 0.12614	0.35587 ± 0.34944
(55.0, 65.0)	0.05341 ± 0.11510	-0.20434 ± 0.30676
(65.0, 75.0)	0.06881 ± 0.10755	-0.17110 ± 0.27511
(75.0, 85.0)	0.13020 ± 0.10333	-0.07454 ± 0.25075
(85.0, 95.0)	-0.06956 ± 0.10350	0.31191 ± 0.23607

$$Q^2=0.2$$

ω (MeV)	A^{N^2} (%)	A^{empty} (%)
(75.00, 85.00)	0.97817 ± 0.49205	-0.98871 ± 2.44558
(85.00, 95.00)	0.28337 ± 0.22676	0.09444 ± 1.07211
(95.00, 105.00)	-0.01443 ± 0.18132	-0.35547 ± 0.83853
(105.00, 115.00)	-0.07099 ± 0.16744	0.34674 ± 0.74068
(115.00, 125.00)	0.03706 ± 0.15719	0.74098 ± 0.67626
(125.00, 135.00)	-0.18251 ± 0.15026	0.83226 ± 0.61832
(135.00, 145.00)	-0.17630 ± 0.15839	-0.32135 ± 0.62113

$$Q^2=0.3$$

ω (MeV)	A^{N^2} (%)	A^{empty} (%)
(100.00, 120.00)	0.10560 ± 0.19924	0.45206 ± 2.05152
(120.00, 140.00)	0.09104 ± 0.12749	0.33473 ± 1.30145
(140.00, 160.00)	0.09572 ± 0.10852	-1.84191 ± 1.06311
(160.00, 180.00)	0.23470 ± 0.09848	-1.08136 ± 0.92478
(180.00, 200.00)	-0.17045 ± 0.09281	0.02171 ± 0.83278
(200.00, 220.00)	-0.03300 ± 0.09049	-0.82540 ± 0.76703
(220.00, 240.00)	-0.00891 ± 0.09137	-1.56561 ± 0.72944

$$Q^2=0.4$$

$\omega(\text{MeV})$	$A^{N2}(\%)$	$A^{empty}(\%)$
(140.00, 160.00)	2.53907 ± 0.62193	-10.89210 ± 7.23575
(160.00, 180.00)	-0.03986 ± 0.26535	0.54389 ± 2.96045
(180.00, 200.00)	-0.22542 ± 0.19247	0.36451 ± 2.06901
(200.00, 220.00)	-0.19114 ± 0.17131	0.56586 ± 1.80953
(220.00, 240.00)	-0.01259 ± 0.15915	-1.28657 ± 1.60706
(240.00, 260.00)	0.18473 ± 0.15179	-0.31942 ± 1.45974
(260.00, 280.00)	0.06695 ± 0.14849	-0.21873 ± 1.34449
(280.00, 300.00)	-0.05311 ± 0.16671	-2.00882 ± 1.42624

$$Q^2=0.5$$

$\omega(\text{MeV})$	$A^{N2}(\%)$	$A^{empty}(\%)$
(190.00, 210.00)	0.24199 ± 2.42251	-10.98305 ± 16.66667
(210.00, 230.00)	-0.94622 ± 0.75487	5.23905 ± 5.45545
(230.00, 250.00)	0.33673 ± 0.50686	-5.38372 ± 3.62500
(250.00, 270.00)	0.55504 ± 0.44864	2.16476 ± 3.16070
(270.00, 290.00)	0.46118 ± 0.41570	5.04289 ± 2.79946
(290.00, 310.00)	0.20007 ± 0.39473	1.01205 ± 2.55238
(310.00, 330.00)	-0.52387 ± 0.38327	3.61357 ± 2.35637
(330.00, 350.00)	0.18610 ± 0.42018	-2.12898 ± 2.44704

$$Q^2=0.6$$

$\omega(\text{MeV})$	$A^{N2}(\%)$	$A^{empty}(\%)$
(250.00, 268.75)	2.84574 ± 1.21046	39.14284 ± 17.40777
(268.75, 287.50)	-0.51921 ± 0.46909	4.57681 ± 6.88428
(287.50, 306.25)	-0.00162 ± 0.33301	-6.39566 ± 5.16398
(306.25, 325.00)	-0.15136 ± 0.30035	-7.54859 ± 4.38951
(325.00, 343.75)	0.09235 ± 0.28070	5.17497 ± 3.91630
(343.75, 362.50)	-0.05791 ± 0.26698	-2.11396 ± 3.57371
(362.50, 381.25)	-0.22279 ± 0.25717	1.25371 ± 3.23762
(381.25, 400.00)	0.37900 ± 0.27248	3.00891 ± 3.38449

Table 4.1: The false asymmetry contributions in E-arm from $N2$ and the empty target cell backgrounds

4.2.2 Trigger Efficiency

When a scattered particle from the target passes through two scintillator layers (S1 and S2), that experiment event is considered as a good event. But not all good events will fire the photo tubes in the two layers and generate a good trigger: T1 for e-arm and T3 for h-arm. A good event without a good trigger will not be written into CODA or will be recorded as a T2 or T4 event which indicates that only one of S1 and S2 fired. In order to get the cross-section from events with good triggers (T1 events or T3 events) , one need to study the trigger efficiency carefully and correct the yield for the trigger inefficiency. While the physics asymmetry doesn't directly depend on the trigger efficiency, the false asymmetry due to the trigger inefficiency will affect the physics asymmetry.

A good trigger is generated with the following scintillator paddle configuration. The configuration consists of one scintillator paddle in S1 and one scintillator paddle in S2 and these two paddles are also subject to the S-ray logic. The trigger efficiency is therefore a function of the efficiency of each paddle so that it varies from place to place. Even though the scintillator efficiency is a different concept from the trigger efficiency, the trigger efficiency is sometimes called the scintillator efficiency because they are closely related. To demonstrate the relationship between the trigger efficiency and the scintillator efficiency of each paddle, let's assume that the number of events ,of which tracks are parallel to the central ray of the spectrometer and paddle n in S1 plane and paddle n in S2 plane are fired, is N^{n-n} , the efficiency of paddle n in S1 plane is ϵ_1 , and the efficiency of paddle n in S2 plane is ϵ_2 (in Fig. 4-3). As a result, the number of the T1 trigger (n-n), which fired paddle n in S1 and paddle n in S2, (N_{T1}^{n-n}), the number of the T2 trigger (n-*), which fired the paddle n in S1 only, (N_{T2}^{n-*}), and the number of the T2 trigger (*-n), which fired paddle n in S2 only,

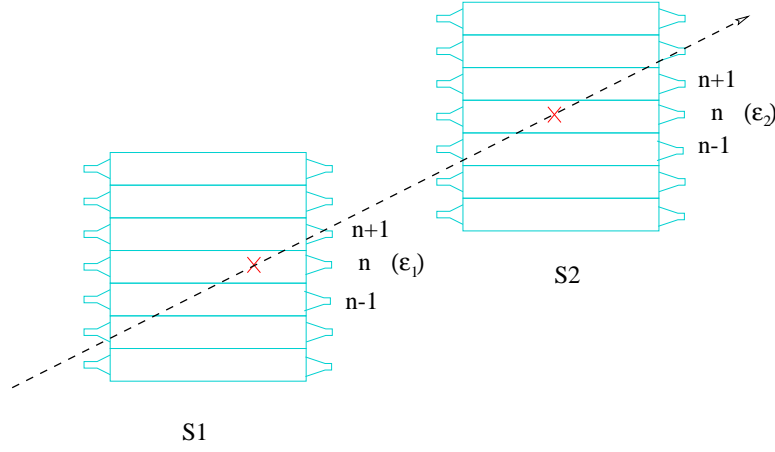


Figure 4-3: The definitions of the scintillator efficiencies

(N_{T2}^{*-n}) are :

$$\begin{aligned}
 \epsilon_1 \epsilon_2 N^{n-n} &= N_{T1}^{n-n} \\
 (1 - \epsilon_2) \epsilon_1 N^{n-n} &= N_{T2}^{n-*} \\
 (1 - \epsilon_1) \epsilon_2 N^{n-n} &= N_{T2}^{*-n}
 \end{aligned} \tag{4.6}$$

Because the definition of the trigger efficiency (ϵ_{T1}^{n-n}) is known as the number of good triggers T1 (N_{T1}^{n-n}) over the number of total event (N^{n-n}), we could simply rewritten the Eq. 4.6 in terms of the trigger efficiency or inefficiency as:

$$\begin{aligned}
 \epsilon_1 \epsilon_2 &= \epsilon_{T1}^{n-n} \\
 (1 - \epsilon_2) \epsilon_1 &= 1 - \epsilon_{T2}^{n-*} \\
 (1 - \epsilon_1) \epsilon_2 &= 1 - \epsilon_{T2}^{*-n},
 \end{aligned} \tag{4.7}$$

where $1 - \epsilon_{T2}^{n-*}$ and $1 - \epsilon_{T2}^{*-n}$ are trigger inefficiencies in the S2 plane and the S1 plane respectively. As the number of T1 triggers (N_{T1}^{n-n}) and that of T2 triggers in

S1 plane, (N_{T2}^{n-*}) and S2 plane, (N_{T2}^{*-n}) are measured during the experiment, one is able to calculate the number of events, N_{T1}^{n-n} and the efficiencies of both paddles, ϵ_1 and ϵ_2 using the Eq. 4.6. Next the trigger efficiency, ϵ_{T1}^{n-n} can be easily obtained by multiplying ϵ_1 and ϵ_2 .

Instead of going through a complicated calculation to get the scintillator efficiencies, one can just use an approximation, that scintillator efficiency is given by the number of T1 triggers divided by the sum of the T1 triggers and T2 triggers. If the scintillator efficiencies are over 90%, the results from this simple approximation are very close to those obtained in the full calculation. But if a large inefficiency of a scintillator paddle is observed during an experiment, the full calculation is very necessary to obtain the scintillator efficiencies and to correct the yield. In fact, the yield for the E94-010 experiment [105, 106, 108] (on Measurement of the Neutron (^3He) Spin Structure Function at low Q^2 : a Connection Between the Bjorken and Drell Hearn Gerasimov (GDH) Sum Rule) was successfully recovered using the full calculation when the output amplitude of a few scintillator PMTs (Photon Multiplier Tubes) dropped off.

Before the final results are presented, a few other issues about the full calculation need to be mentioned. One issue is the trigger prescale factor. In order to avoid a high DAQ deadtime, the triggers are always scaled down with prescale factors in real experiments. The number of triggers in the full calculation therefore needs to be multiplied by the prescale factors. Another issue is the correction due to those events whose tracks are far from the central ray. In the full calculation, the track of the event is assumed to go through the paddle with the same index in S1 plane as in S2 plane. Therefore, the track of N_{T2}^{n-*} event or N_{T2}^{*-n} event are supposed to pass through both S1 and S2 planes with the same paddle index. In reality, some of the tracks of these events will go through S1 and S2 with different paddle number. In order to satisfy the assumption, the number of N_{T2}^{n-*} event (or the number of N_{T2}^{*-n} event) needs to

be corrected by the factor which equals to the ratio of the N^{n-n} and the total number of events, $N^{n-n} + N^{n,n\pm 1} + N^{n,n\pm 2} + \dots$ (or $N^{n-n} + N^{n\pm 1,n} + N^{n\pm 2,n} + \dots$). A practical estimate of this factor for the number of $N_{T_2}^{n-*}$ event (or the number of $N_{T_2}^{*-n}$ event) is the ratio of the $N_{T_1}^{n-n}$ and sum of the $N_{T_1}^{n-n}$ and $N_{T_1}^{n,n-1}$ (or $N_{T_1}^{n-1,n}$). If most of the tracks of the scattered particles satisfy the S-ray logic, this estimate will be very close to the real value of the correction factor. Besides this correction, the background including cosmic rays is an additional issue which needs to be carefully considered in the full calculation. In this way, one can get the scintillator efficiencies more precisely.

In the Fig. 4-4, the scintillator efficiencies ($\epsilon_1 \times \epsilon_2$) are plotted against different paddle configuration for E-arm $Q^2 = 0.2$ kinematic setting (as an example). In order to further understand the helicity dependences of the scintillator efficiencies, the difference of the scintillator efficiencies with respect to the beam helicity is checked and is shown in Fig. 4-5. No helicity-dependence has been observed in the scintillator efficiencies for the six different Q^2 settings as shown in Fig. 4-6 since the difference of the scintillator efficiencies with respect to the beam helicity is consistent with zero within statistical uncertainty.

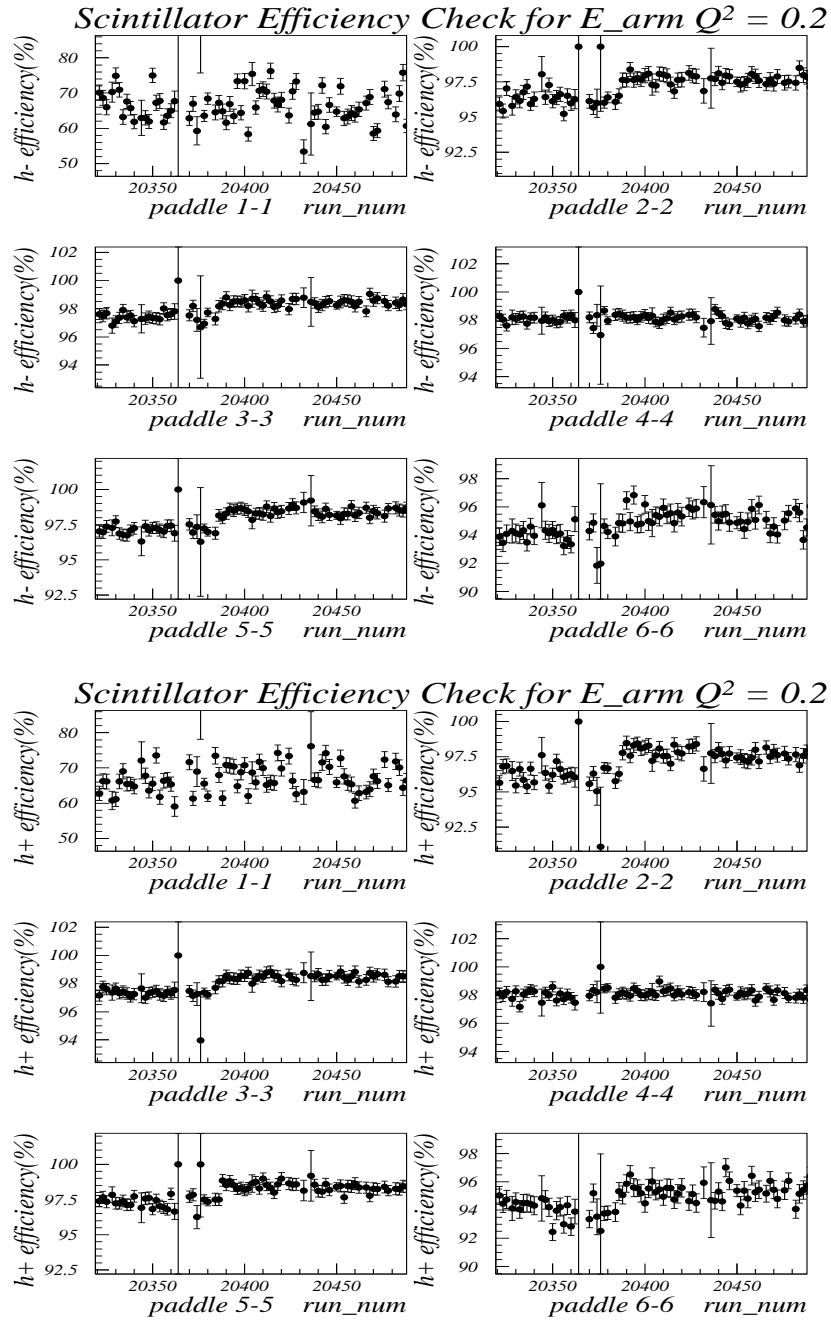
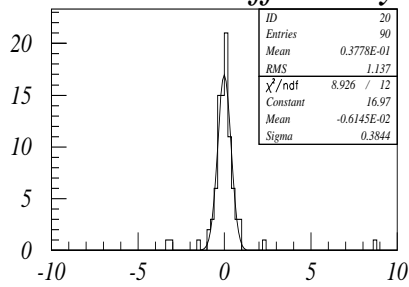
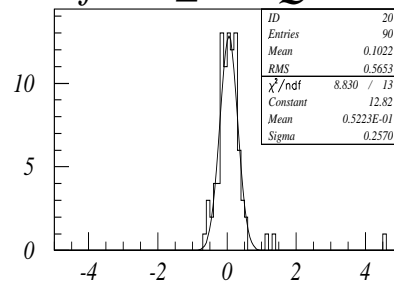


Figure 4-4: The scintillator efficiencies ($\epsilon_1 \times \epsilon_2$) vs. run number with different paddle configuration. The reason for the low determined efficiencies on the paddler 1-1 and the paddler 6-6 is because of cosmic ray contamination.

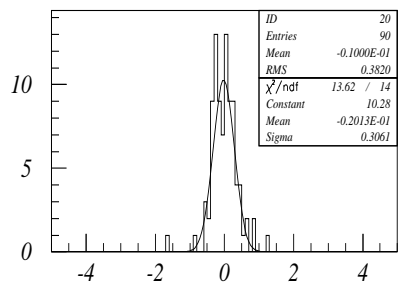
Scintillator Efficiency Check for $H_arm Q^2 = 0.2$



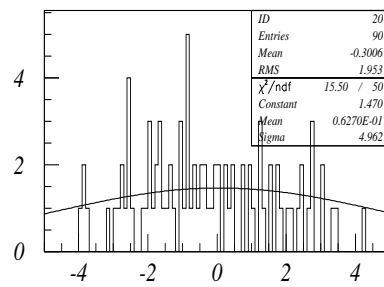
paddle 1-1 diff-eff



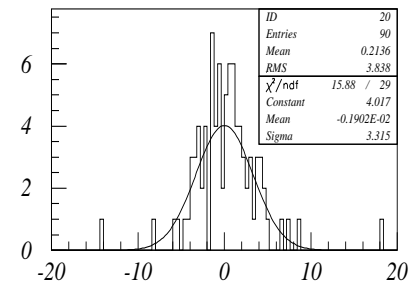
paddle 2-2 diff-eff



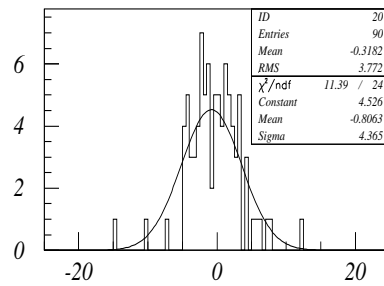
paddle 3-3 diff-eff



paddle 4-4 diff-eff



paddle 5-5 diff-eff



paddle 6-6 diff-eff

Scintillator Efficiency Check for $E_{arm} Q^2 = 0.2$

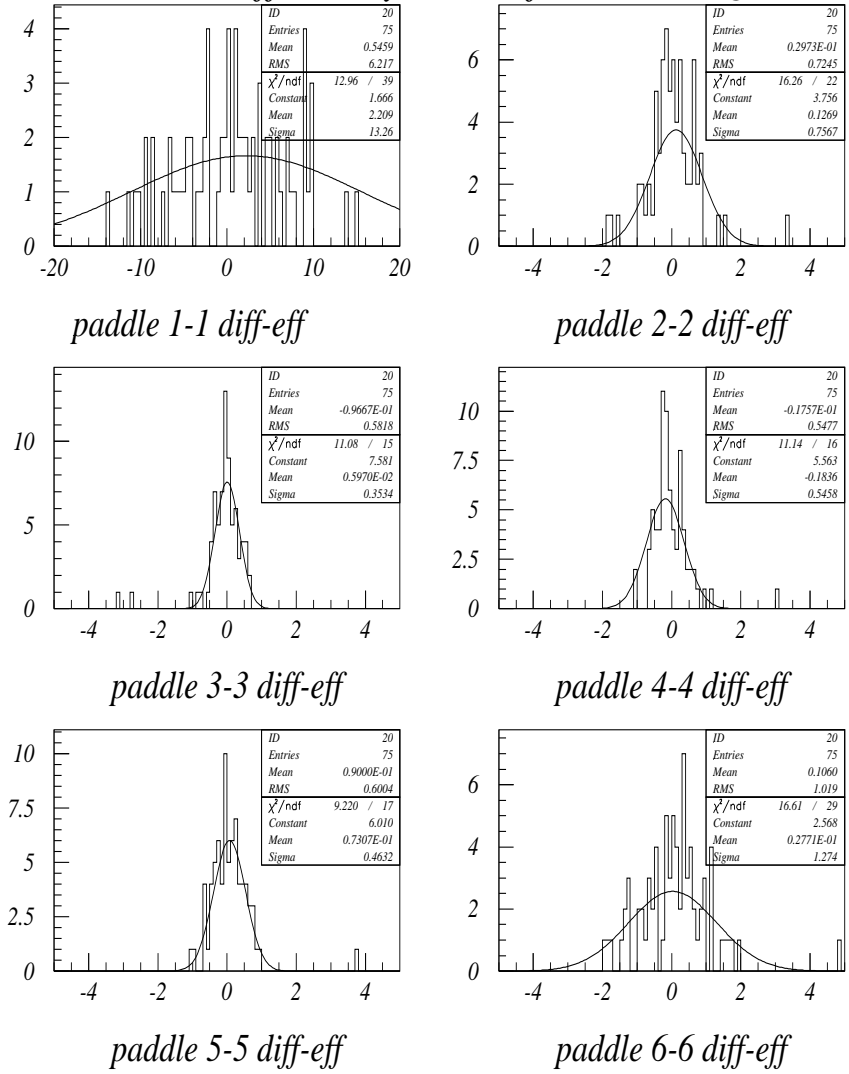


Figure 4-5: The difference of the scintillator efficiencies regarding the beam helicity vs. run number for the different paddle configurations.

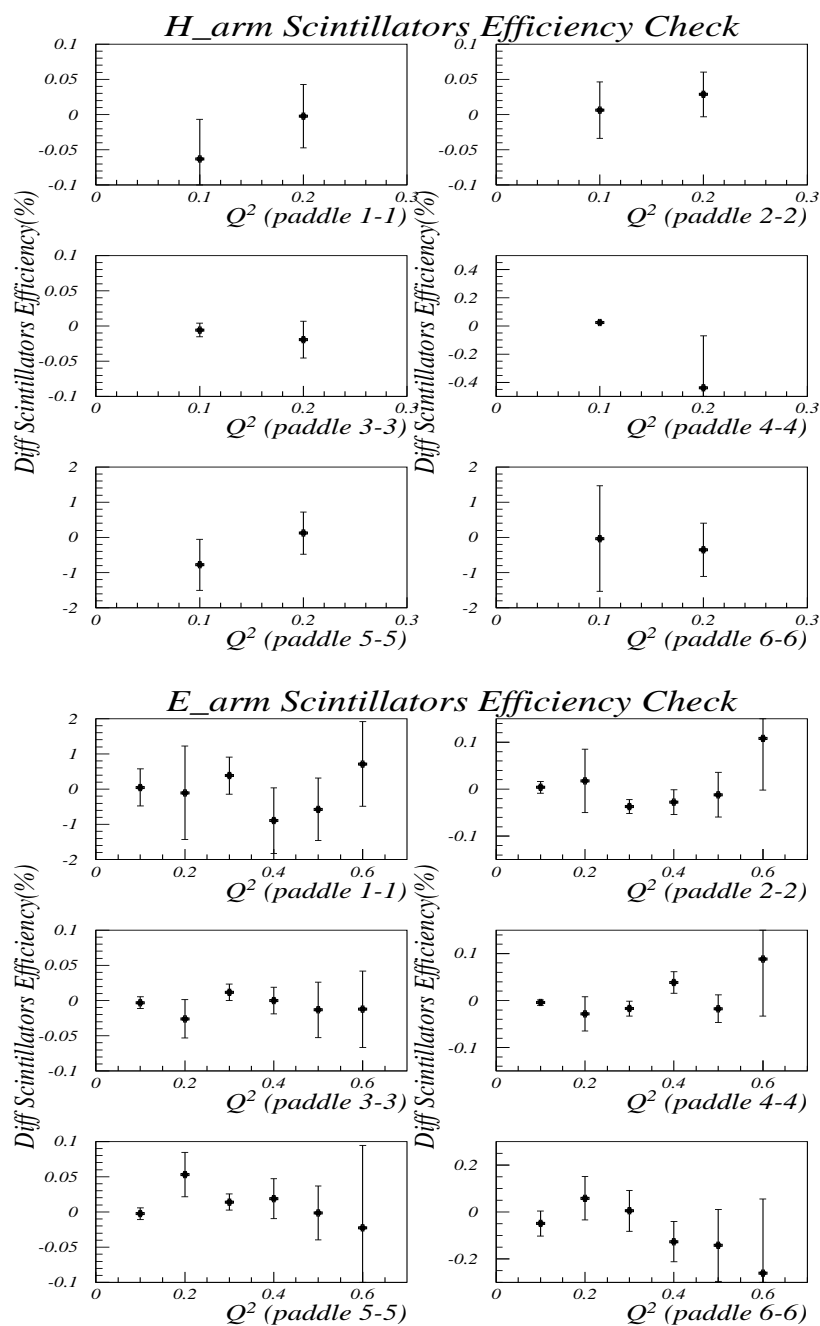


Figure 4-6: Overall study of the correlation between the helicity and the scintillator efficiencies

4.2.3 VDC Efficiency

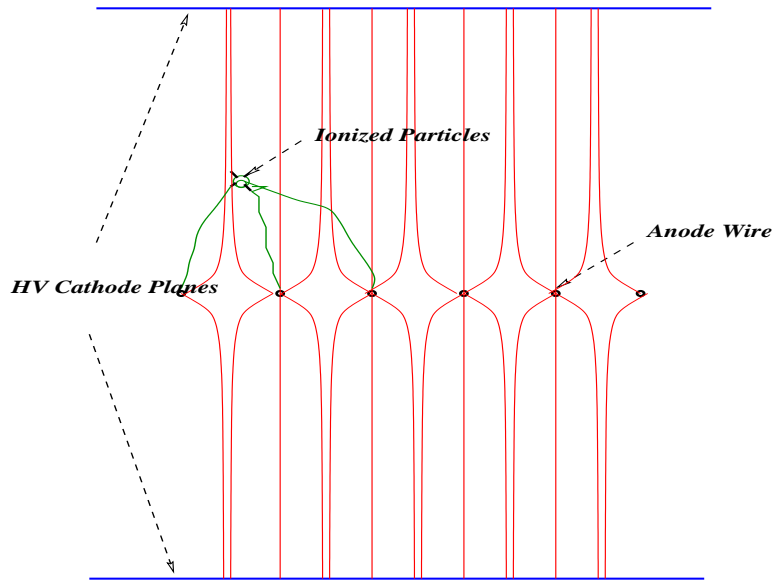
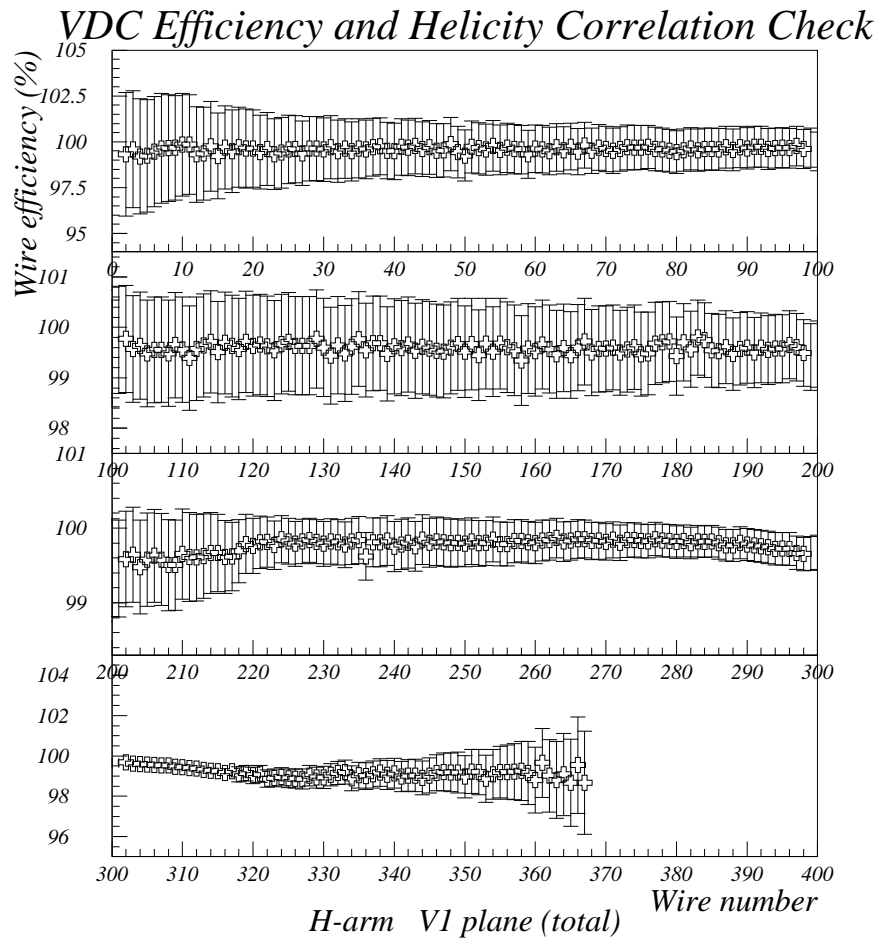


Figure 4-7: The collecting process of vdc signal

The VDC detector plays a major role in the whole detector package in each arm. Knowledge of the position and the direction of a scattered particle at the focal plane along with a good understanding of the spectrometer optics allows us to precisely determine the track of the scattered particle. As we mentioned before, the VDC detector consists of two sets of the wire chambers. Each set of the wire chambers includes two 368-wire wire chambers (one U and one V) and the directions of wires in two wire chambers are normal to each other. When a scattered particle passes through a wire chamber, the ionized particles are generated along the trajectory of the scattered particle, and they are forced to move toward or away from the wires in a strong electric field which are created by the high voltage between the anode wires and the cathode plate. From the timing information of each wire TDC, one can figure out the position of the trajectory in the set of wire chambers as it goes through a set



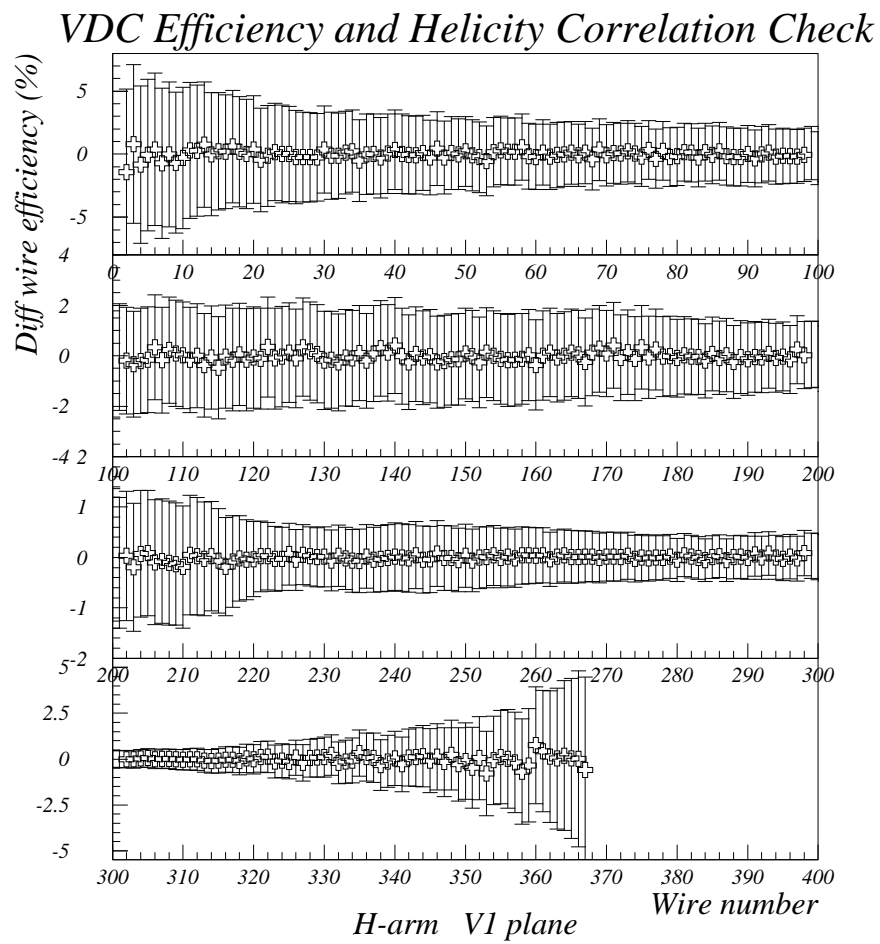


Figure 4-8: VDC wire efficiencies & difference of efficiencies at V1 planes in H-arm (as an example)

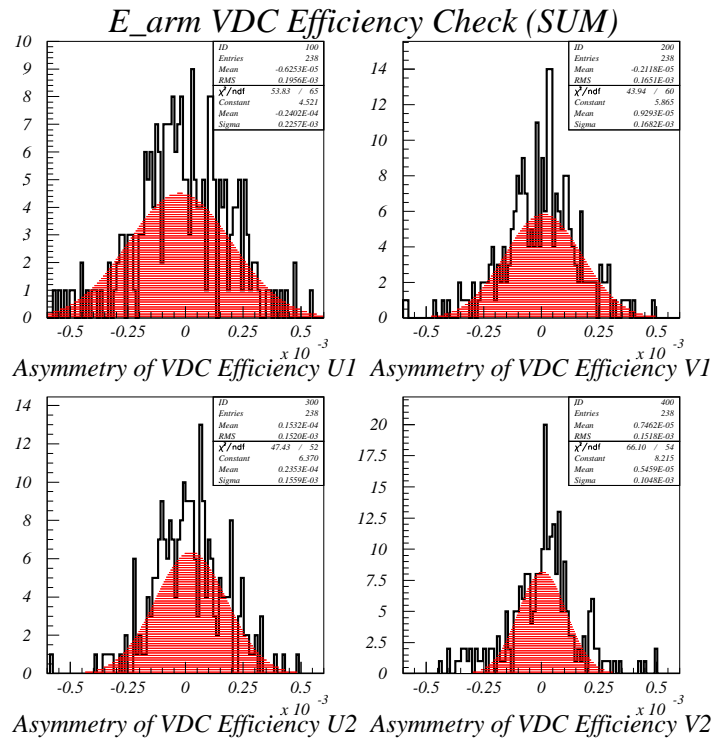


Figure 4-9: The difference of vdc wire efficiencies vs. vdc planes

of wire chambers. Using the position information from all two set of wire chambers, the trajectory of the particle can be calculated. In fact, four or five wires instead of one wire, will fire when the scattering particle passes through a wire chamber. As a result, the position and the direction of a scattering particle are extracted and optimized from the cluster position of each set of wire chambers. Although it is very complicated to quantify the overall VDC efficiency, the wire efficiency is the other quantity which is commonly used.

The wire efficiency is defined as the probability for a wire to fire while its neighboring wires fire and form a cluster. It is clear that the VDC will perform well if each wire functions efficiently. The wire efficiency of each wire for four wire chambers

or four VDC planes is shown in Fig. 4-8, and is found to be above 99%. Thus the VDC worked very well during the period of the E95-001 data taking. Also the wire efficiency or VDC efficiency is found to be helicity-independent since the difference of the wire efficiency with respect to the beam helicity as shown in Fig. 4-9 is consistent with zero.

4.3 Negligible Helicity-dependent Variables

4.3.1 Beam Position Shift

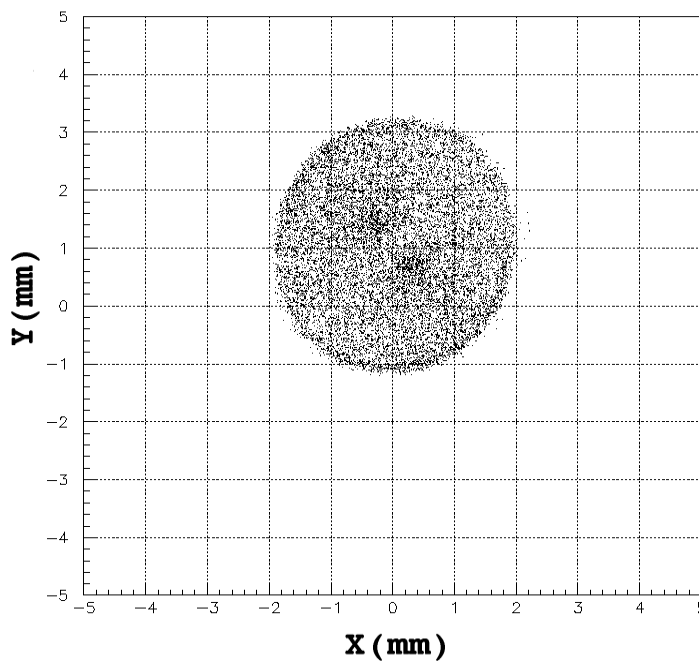


Figure 4-10: Beam spot at target position

The electron beam is rastered by two sets of the steering magnets and its shape turns into a circular beam spot 4mm diameter (shown in Fig. 4-10) at the target

position. This reduces the beam-induced heat on the target front and back windows. The central position of the beam spot shifts and is regulated in a range $[-0.5\text{mm}, 0.5\text{mm}]$ for both x and y positions, as monitored by BPM03A. The entire target cell or empty reference cell consists of a glass cylinder and two very thin windows fused onto each side of a glass cylinder, and the thickness of the window and the glass wall vary from place to place. In the Fig. 4-11, the yield of an empty reference cell with

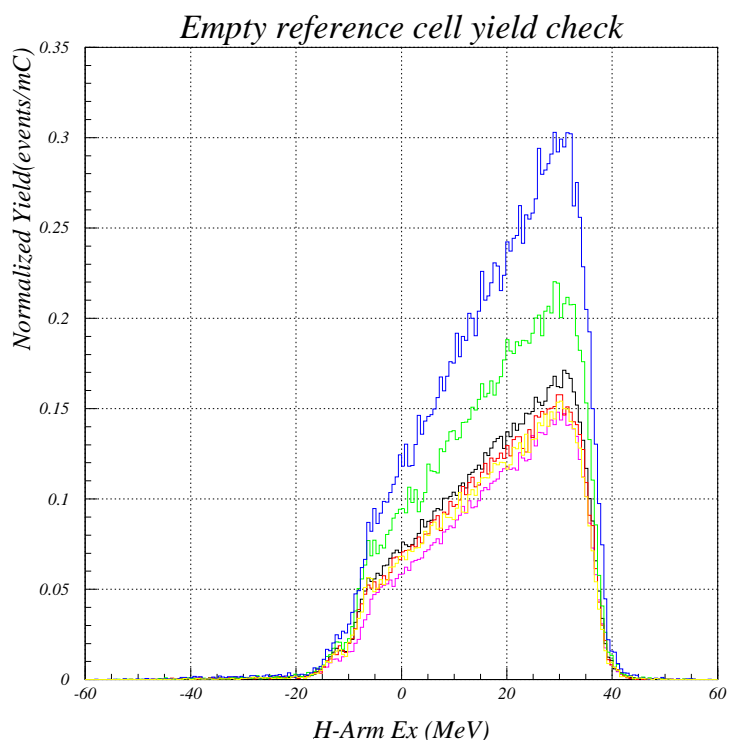


Figure 4-11: The empty reference cell yields with different beam positions and their beam positions vary within a few mm

different central beam positions is shown and due to the variations of the thickness of the windows, the yield has been found to be dependent on the central beam position. As a consequence, the yield from empty target cell, whose central beam position varies within $\pm 0.5\text{mm}$ for x and y positions, may not be equal to the yield of the empty

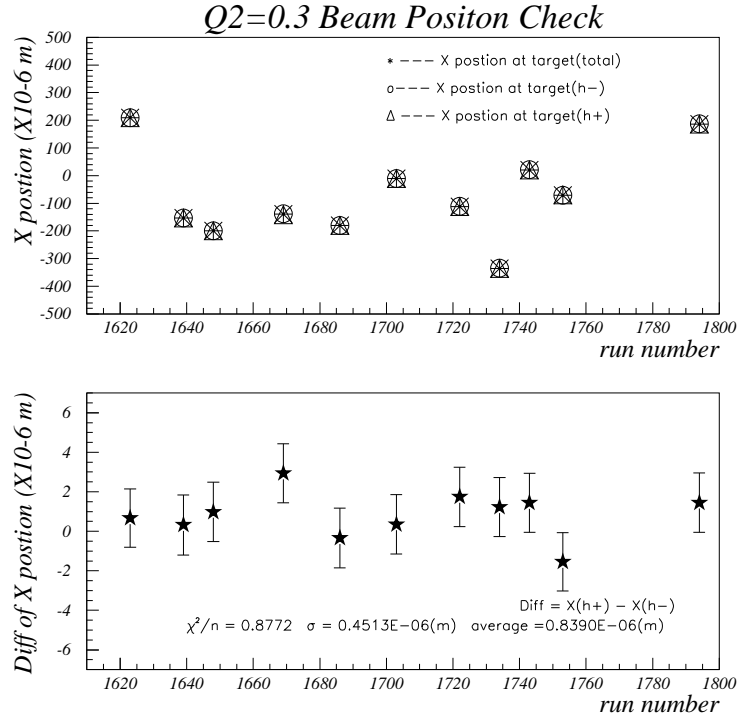


Figure 4-12: The variation of beam spot with helicities

reference cell with the central beam position at zero. To get the dilution factor from the empty target cell background, the yield from the empty target cell is obtained from the yield of the empty reference cell multiplied by an overall factor, which is determined by using the elastic, N₂, and empty reference cell runs. The value of the over factor changes within a range from 1 to 2 during the experiment.

For the false asymmetry due to the variation of both the central beam position and the front window thickness of the target cell (A_{false}^{bp}), an estimation can be written in terms of the empty yield as:

$$A_{false}^{bp} = \eta \frac{dY_{empty}}{2dl \times Y_{empty}} (BP_+ - BP_-), \quad (4.8)$$

where Y_{empty} is the yield from empty target cell which is approximately the yield from the target front window, BP_+ and BP_- are the central beam position for helicity plus and helicity minus respectively, dl is the difference of the beam position with respect to the beam helicity, and η is the ratio of the empty yield to the total yield and is less than 0.1%.

On one hand, the largest empty yield shown in Fig. 4-11 can be 2-3 times larger than the smallest one and the distance between the corresponding central beam positions for these two empty yields are only a few mm apart. On the other hand, the difference of the central beam positions between the two beam helicities is found (in Fig. 4-12) to be less than $10 \mu\text{m}$. The A_{false}^{bp} is estimated to be at most 5×10^{-6} . Thus, compared to the statistical uncertainty of the experiment asymmetry ($\approx 22 \times 10^{-5}$), the helicity correlated false asymmetry due to the variation of the target window thickness can be neglected.

4.3.2 Beam Helicity Determination

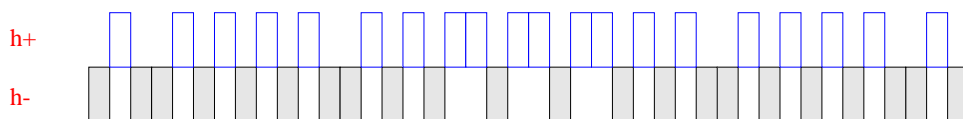


Figure 4-13: The variation of beam spot with helicities

Jefferson Lab's polarized electron source is achieved by an electron gun with a strained GaAs photocathode and a circularly polarized laser operated at a wavelength near the GaAs semiconductor's energy difference between the valence and conductive bands. The helicity of the electrons induced by the laser light directly relates to the spin direction of the photons. When the spin direction of the photons (or the circular polarization direction of the laser) flips, the sign of the electron helicity

reverses. Knowledge of the circular polarization direction of the laser therefore allows us to determine the beam helicity. During the experiment, the circular polarization direction of the laser was switched by changing the high voltage of a Pockel's cell which can provide a voltage tunable optical retardation. By continuously monitoring the input high voltage of the Pockel's cell on an event by event basis, one can determine the circular polarization direction of the laser light and thus the beam helicity for each event. The beam helicity pulses (the high voltage pulse of a Pockel's cell) shown in Fig 4-13 was 1 Hz for the first five Q^2 sets and 30 Hz for the last Q^2 set ($Q^2=0.6$ (GeV/c)²).

Fig 4-14 shows the different combinations of two input high voltages of the Pockel's cell (s_{minus} and s_{plus}) and their redundant copies (g_{minus} and g_{plus}) for e-arm. The logic to determine the helicity is listed in Tab. 4.2. The ambiguity for

	$s_{minus} \leq h_{logic}$	$s_{minus} > h_{logic}$
$s_{plus} \leq h_{logic}$		h-
$s_{plus} > h_{logic}$	h+	

Table 4.2: Helicity configuration

the determination of an event's helicity status appears if both s_{minus} and s_{plus} for the event are below h_{logic} or above the h_{logic} . Typically, for one out of one hundred thousand events, the helicity status is undetermined. However, the statistical fluctuation of the difference in the total number of events for each helicity is much larger than the total number of the unknown helicity state events. Thus, the effect of the ambiguity in the helicity determination is not a problem for this experiment.

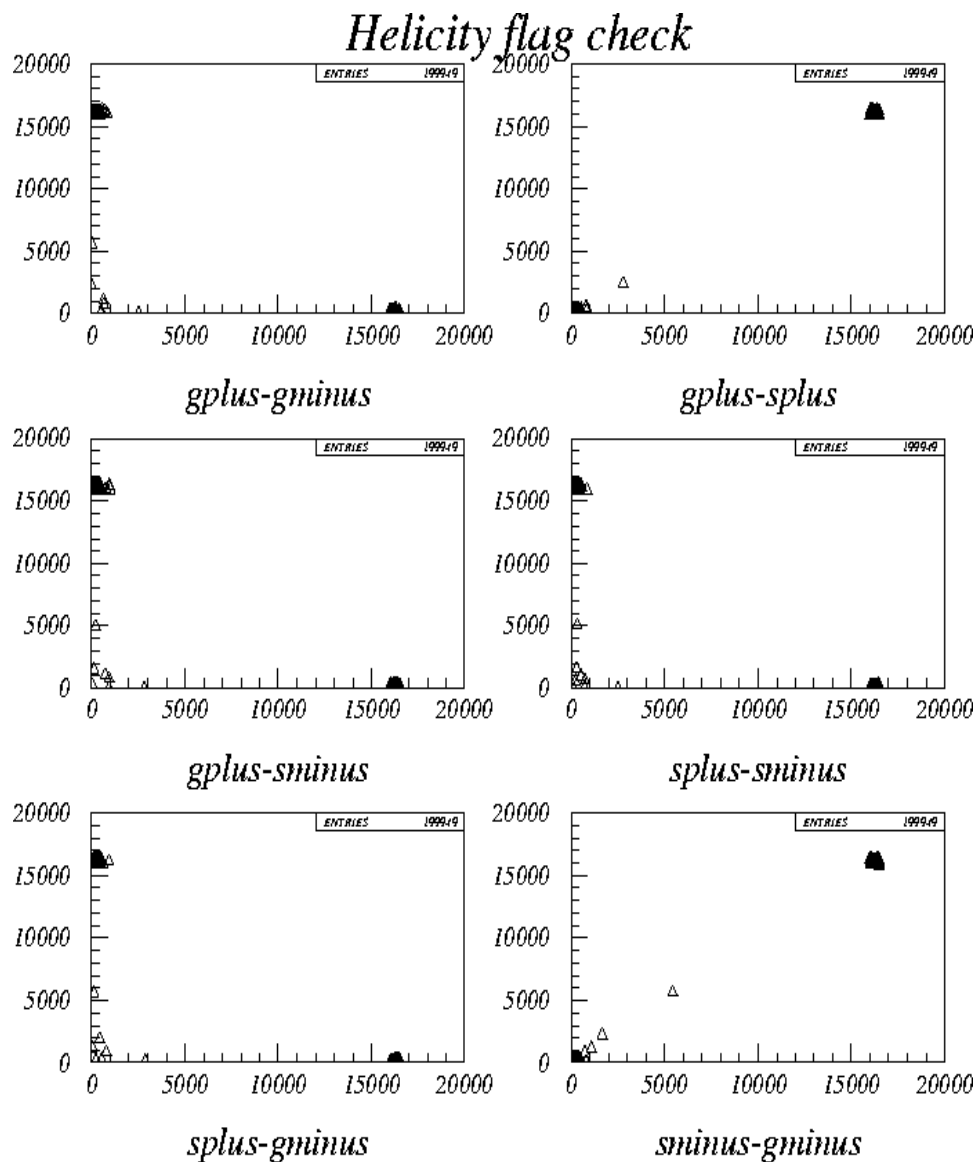


Figure 4-14: The combinations of two input high voltages of the Pockel's cell and their copy

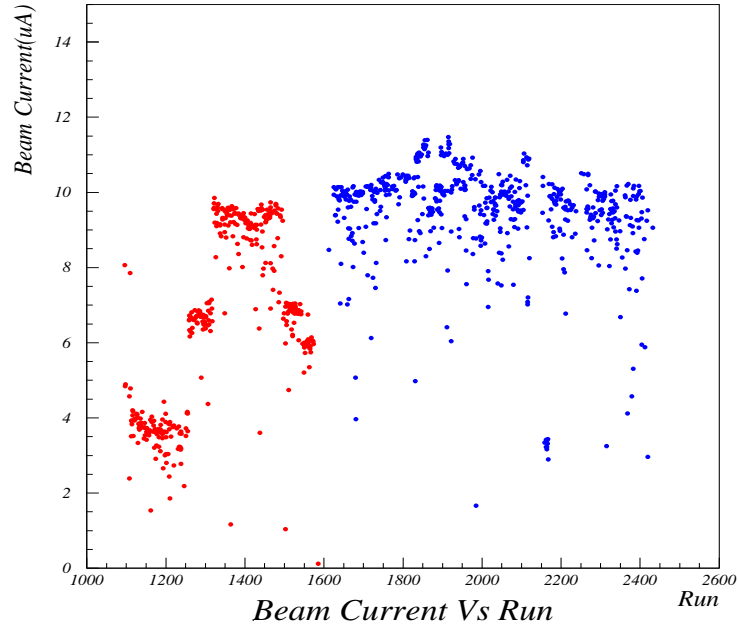


Figure 4-15: The beam current summary

4.3.3 Beam Current

As we have mentioned before, the experimental asymmetry can be written in terms of the normalization factors; the detector efficiencies, ϵ_{det} , the trigger lifetime, Lt , and the total charge, C , as followings:

$$A^{exp} = \frac{Y_{normal}^+ - Y_{normal}^-}{Y_{normal}^+ + Y_{normal}^-}, \quad (4.9)$$

where

$$Y_{normal}^{\pm} = \frac{N^{\pm}}{\epsilon_{det}^{\pm} Lt^{\pm} C^{\pm}}. \quad (4.10)$$

The measured charge for each run is given as:

$$C_{run} = \sum (C_{scaler}(i+1) - C_{scaler}(i)) \times f(I), \quad (4.11)$$

where

i is the index which indicate the number of the scaler event, $C_{scaler}(i)$ is the total charge which is measured through the BCMs and record into the i th scaler event, T_{scaler} is the time recorded into the i th scaler event, and $f(I)$ is the BCM current calibration number which depends on the beam current, $I(\propto \frac{C_{scaler}(i+1)-C_{scaler}(i)}{T_{scaler}(i+1)-T_{scaler}(i)})$.

The BCM current calibration number (for BCMx10) strongly depends on beam current. In Tab. 4.3, the current-dependent calibration numbers for different current monitors are also listed. Due to lack of full knowledge of the BCM current calibration,

I(μ A)	u1	d1	u3	d3	u10	d10
32.93	1307 \pm 2.3	1461 \pm	4019 \pm 7.1	4532 \pm 8	12228 \pm 21.5	14279 \pm 25.2
19.96	1305 \pm 0.8	1457 \pm	4010 \pm 2.5	4511 \pm 2.9	12196 \pm 7.7	14244 \pm 9
9.96	1307 \pm 1	1458 \pm	4014 \pm 3	4511 \pm 3.4	12191 \pm 9.1	14241 \pm 10.6
4.936	1314 \pm 1.8	1461 \pm	4025 \pm 5.5	4515 \pm 6.2	12188 \pm 16.8	14246 \pm 20.4
2.003	1332 \pm 2.07	1471 \pm	4054 \pm 6.3	4523 \pm 7	12170 \pm 18.9	14246 \pm 22.2
1.0672	1357 \pm 1.2	1487 \pm	4098 \pm 3.6	4536 \pm 4.2	12150 \pm 11.1	14257 \pm 13.1
1.9808	1335 \pm 1.8	1475 \pm	4065 \pm 5.3	4534 \pm 5.6	12201 \pm 16.1	14282 \pm 18.8
1.0696	1357 \pm 1.6	1487 \pm	4095 \pm 5	4534 \pm 5.6	12145 \pm 15.1	14251 \pm 17.9
0.4856	1428 \pm 2.1	1537 \pm	4228 \pm 6.3	4599 \pm 6.8	12173 \pm 18.3	14376 \pm 21.6
0.2011	1580 \pm 1.4	1653 \pm	4520 \pm 3.6	4731 \pm 3.6	12154 \pm 10.3	14583 \pm 12.4

Table 4.3: The calibration numbers of Beam Current Monitor(BCM)

we are not able to calculate C_{run} according to the definition in Eq. 4.11. Instead, the

* C_{run} ² is calculated by

$$*C_{run} = \sum (C_{scaler}(i+1) - C_{scaler}(i)) \times f(15\mu A). \quad (4.12)$$

If the beam current for the positive helicity is close enough to the beam current for the negative helicity within two neighboring helicity pulses, then Eq. 4.12 is a good approximation for calculating the experimental raw asymmetry. Before proving this statement, we group the two neighboring helicity pulses which include one positive and one negative helicity pulses. Typically, each helicity pulse is about a few hundred milliseconds long. In each group i , A^{exp} is given as the function, g of both C_i^+ the charge with respect to positive helicity and C_i^- the charge with respect to negative helicity according to Eq. 4.11.

$$\begin{aligned} A^{exp} &= g(C_i^+, C_i^-) \\ &= g(f(I_i)(C_{scaler}^+(i), C_{scaler}^-(i))) \\ &= g(C_{scaler}^+(i), C_{scaler}^-(i)). \end{aligned} \quad (4.13)$$

The last statement is true because if both C_i^+ and C_i^- vary proportionally, the A^{exp} remains same according to Eq. 4.9. Because A^{exp} is the same for each group of helicity pulses, then

$$\begin{aligned} A^{exp} &= g\left(\sum_i C_{scaler}^+(i), \sum_i C_{scaler}^-(i)\right) \\ &= g(f(15\mu A)\left(\sum_i C_{scaler}^+(i), \sum_i C_{scaler}^-(i)\right)) \\ &= g(*C_{run}^+, *C_{run}^-) \end{aligned} \quad (4.14)$$

However, this approximation gives rise to a false asymmetry because of the vari-

²To distinguish C_{run} defined in Eq. 4.11, the definition is called $*C_{run}$

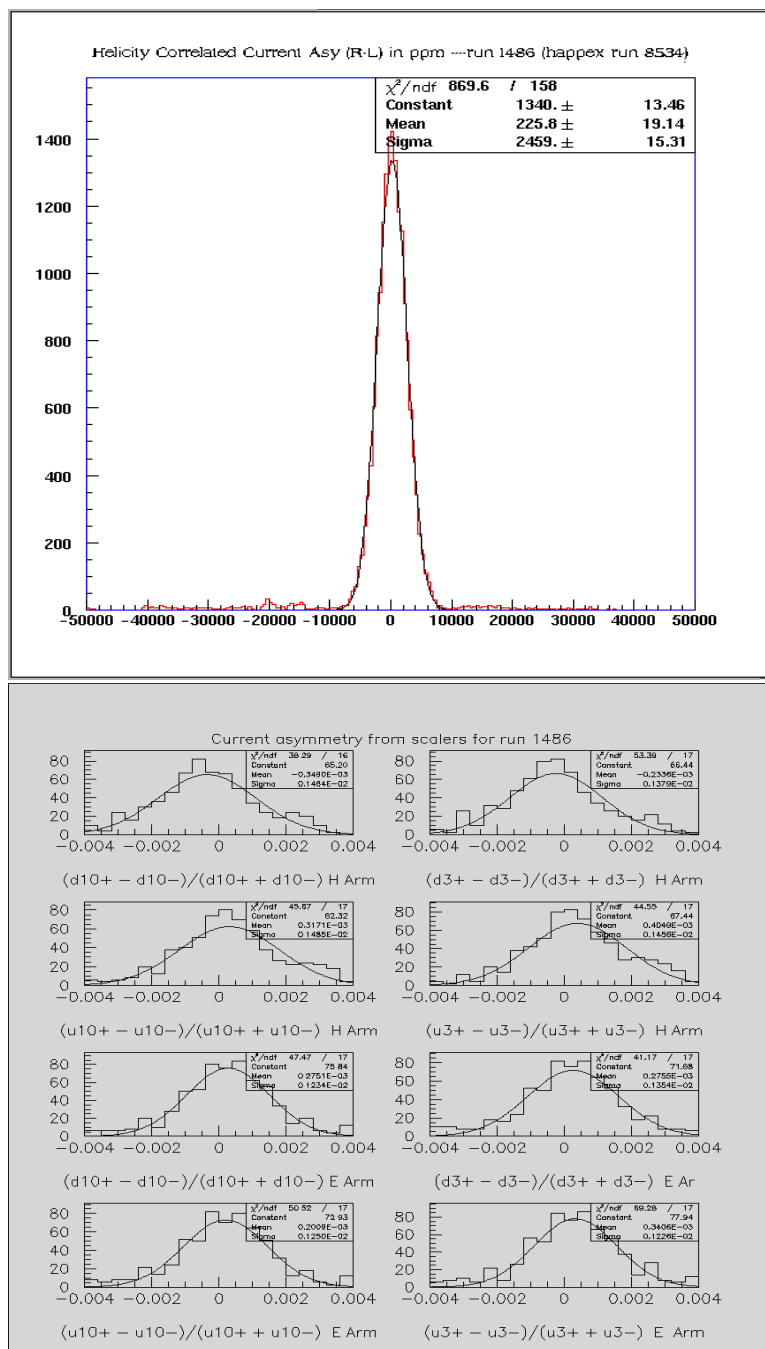


Figure 4-16: The current asymmetry from two independent instruments. Upper Graph is the result from the independent DAQ for Happex experiment (which we used during our experiment to check the current asymmetry); Lower one is the results from upstream BCM and downstream BCM

ation in the beam current with time. The Fig. 4-16 shows asymmetry of the beam current with respect to the helicities, the A_c . The False asymmetry is estimated by

$$\begin{aligned}\Delta_c &= \frac{df(I)}{dI} \times A_c \times \frac{15\mu A}{f(15\mu A)}, \\ &\sim \frac{16}{19\mu A} \times 2.5 \times 10^{-3} \times \frac{15\mu A}{14242}, \\ &\sim 2 \times 10^{-6}.\end{aligned}\tag{4.15}$$

Here using the current calibration number of dx10 results in Tab. 4.3, one can get those numbers in Eq. 4.15.

In fact, the real Δ_c value will be even smaller because the beam current is found to be stable around 10-15 μA for most of experiment (Fig. 4-15). Hence we can ignore the false asymmetry associated with beam current.

4.3.4 Pion Contamination

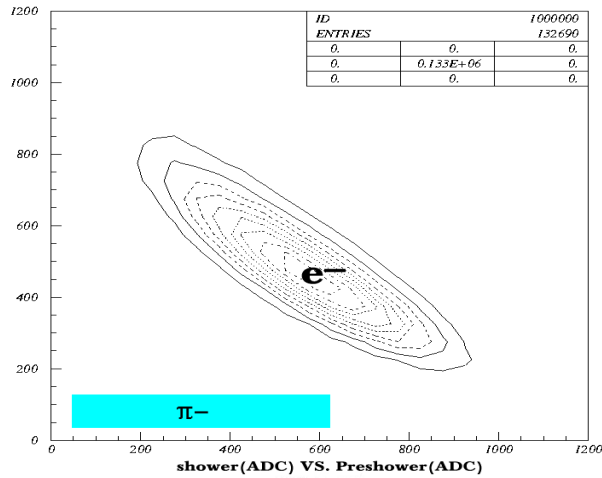


Figure 4-17: The particle id information on e^-/π^- using shower vs. preshower

The pion Asymmetry can be a source of false asymmetry to the physics asymmetry if a lot of the pions event are misidentified as the electron events. Fortunately, the power of the particle identity (ID) is enforced by two sets of independent detectors - the shower counters (Preshower & Shower) and the Čerenkov detector in E95-001 experiment. After the good electrons shown in Fig. 4-17 are selected by the Preshower and Shower ADC signals, only a few good electron events will not fire the Čerenkov detector. The ratio of the misidentified electrons to good electrons is less than 0.1%. In addition, the pion yield is a function of energy transfer ω and increases as the energy transfer ω becomes larger. The experimental ω acceptance is not close to the one pion threshold and therefore the pion yield is relative small compared to the electron yield. The pion contamination is consequently very small due to these two factors and the effect of the pion contamination to the measured asymmetry has been found to be negligible.

Chapter 5

Results

5.1 Introduction

In this Chapter, the experimental asymmetries and the extracted neutron magnetic form factor, G_m^n are presented. G_m^n is extracted precisely from the recent Faddeev calculation (Golak *et al.*) which includes both FSI and MEC at Q^2 values of 0.1 and 0.2 (GeV/c)². The uncertainties of G_m^n at these Q^2 values are comparable to those of recent experiments with deuterium targets. However, theoretical uncertainties of the extracted G_m^n from PWIA at higher Q^2 values are larger compared to the systematic and statistical uncertainties. The reliable extraction of G_m^n at higher Q^2 values requires improved theoretical calculations including FSI, MEC and relativistic effects.

5.2 Elastic Asymmetry

The ${}^3\vec{H}e$ elastic asymmetry was measured in the HRSB spectrometer as a monitor of the product of the beam and target polarization so that the 3He quasi-elastic asymmetry measured in the HRSE spectrometer can be determined with high precision.

The measured elastic asymmetries within the elastic peak region in the missing mass spectrum together with the statistical uncertainties for four configurations of beam helicity & target spin at six Q^2 kinematic settings are listed in Table 5.2. In addition, the momentum acceptance of HRS is large enough to allow us to study not only the ${}^3\vec{H}e$ asymmetry in the elastic peak region but also in the breakup region (the elastic threshold region), where effects of final state interaction (FSI) and meson exchange current (MEC) are expected to be large. The extraction of form factors is usually model-dependent. Significant constraints on the theoretical calculations are provided by 3He asymmetry at Q^2 values of 0.1 and 0.2 $(\text{GeV}/c)^2$ in the breakup region. The detailed work on asymmetry study in the breakup region is contained in Ref. [72].

$$|A_{el}^{exp}(\%)|$$

Q^2	$-62.5^\circ \&\text{in}$	$-62.5^\circ \&\text{out}$	$-243.6^\circ \&\text{in}$	$-243.6^\circ \&\text{out}$
0.1	1.333 ± 0.027	1.043 ± 0.027	1.067 ± 0.02	1.208 ± 0.030
0.2	1.078 ± 0.037	1.177 ± 0.027	1.190 ± 0.021	1.102 ± 0.023
0.3	1.251 ± 0.096	1.222 ± 0.048	1.107 ± 0.067	1.206 ± 0.075
0.4	1.181 ± 0.055	1.314 ± 0.061	1.168 ± 0.06	1.258 ± 0.057
0.5	1.265 ± 0.042	1.307 ± 0.039	1.200 ± 0.045	1.184 ± 0.041
0.6	1.258 ± 0.049	1.301 ± 0.047	1.110 ± 0.05	1.096 ± 0.05

Table 5.1: $|A_{el}^{exp}|$ results for four configurations of beam helicity & target spin at six quasi-elastic kinematic settings. -62.5° and -243.6° are the target spin directions with respect to the incident electron beam direction (convention: standing facing the beam dump, + for left side of beamline and - for right side of beamline). In/out refers to the beam half-wave plate status.

5.3 Quasi-elastic Transverse Asymmetry $A_{T'}$

The 3He quasi-elastic transverse asymmetry $A_{T'}$ has been extracted from the yield of spin-dependent inclusive quasi-elastic scattering as a function of electron energy

transfer ω . Corrections to $A_{T'}$, such as the quasi-elastic radiative effect, elastic radiative tail, the dilution effect, etc., have been discussed in Chapter 3. The extracted quasi-elastic transverse asymmetry $A_{T'}$ is shown in Fig. 5-1, together with calculations by Salmè *et al.* [46–48] (AV18 & Höhler form factor parameterization) for six different kinematics and by Golak *et al.* [41] (Bonn & Höhler form factor parameterization) for the first four kinematics. The theoretical approach for ${}^3\vec{H}e(\vec{e}, e')$ scattering by Salmè and that by Golak are quite different. Salmè's calculations are based on the PWIA picture including the Coulomb interaction between protons within 3He nucleus, while Golak's calculations are non-relativistic and have used the Faddeev equations to include the final state interaction fully and the meson exchange current partially. The data at low Q^2 are in good agreement with Golak's full calculations. On the contrary, the PWIA calculations from Salmè describe the data at high Q^2 much better.

The acceptance of the HRSE spectrometer is roughly $\pm 5\%$ for the momentum, ± 30 msr for the in-plane angle, ± 60 msr for the out-of-plane angle. The acceptance effect on the calculated asymmetry $A_{T'}$ is estimated using Monte-Carlo simulations with PWIA calculations and the effect has been found to be negligible. The target spin angle was aligned to either -62.5° or -243.6° with respect to the electron beam direction with an uncertainty of $\pm 0.5^\circ$. The systematic error due to the target spin angle uncertainty on $A_{T'}$ is also found to be negligible. The uncertainties of $A_{T'}$ include the systematic uncertainty and the statistical uncertainty. The systematic uncertainty is dominated by the systematic uncertainty in the determination of the product of beam and target polarizations. In Fig. 5-1, the statistical uncertainty is shown as error bar and the dark band is the systematic uncertainty.

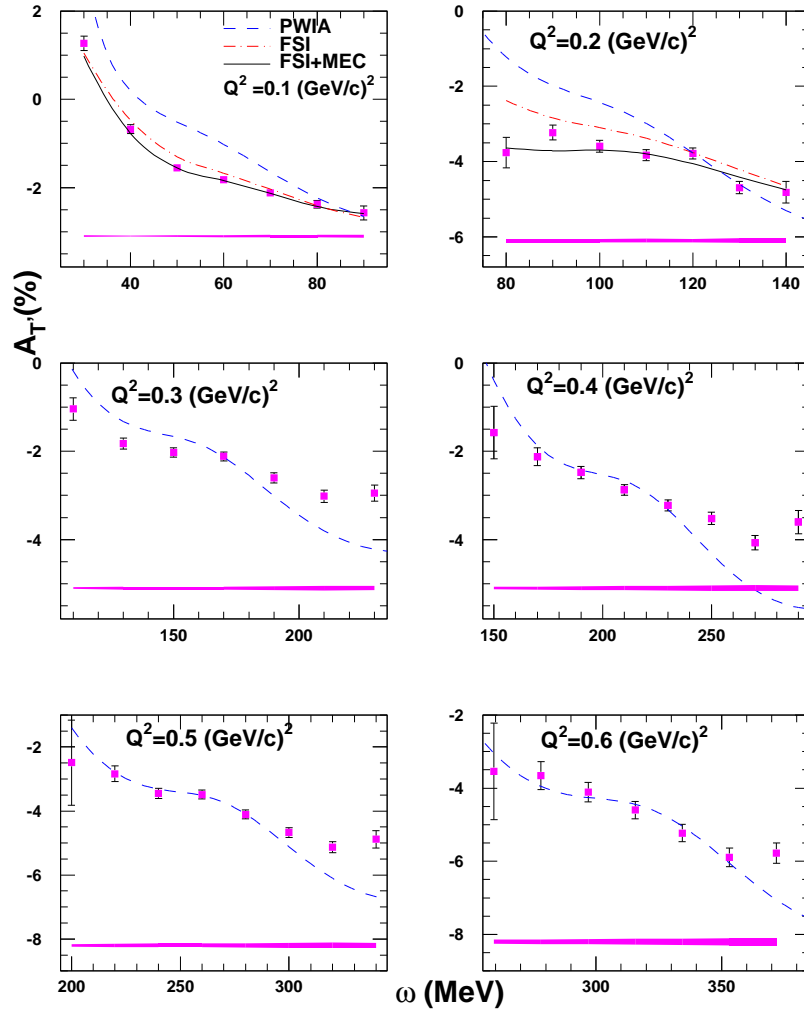


Figure 5-1: The $A_{T'}$ results vs. the energy transfer, ω . The error bar is the statistical uncertainty and the error band is the systematic uncertainty.

$Q^2=0.1$

ω	$A_{T'}(\%)$	stat. uncertainty(%)
30.0	1.267070	0.166237
40.0	-0.680063	0.100537
50.0	-1.557210	0.075991
60.0	-1.826670	0.070497
70.0	-2.124070	0.077014
80.0	-2.378600	0.090310
90.0	-2.574840	0.160527

 $Q^2=0.2$

ω	$A_{T'}(\%)$	stat. uncertainty(%)
80.0	-3.763600	0.405147
90.0	-3.231710	0.197098
100.0	-3.590200	0.157531
110.0	-3.830670	0.147266
120.0	-3.786220	0.147600
130.0	-4.690820	0.165051
140.0	-4.816910	0.286003

 $Q^2=0.3$

ω	$A_{T'}(\%)$	stat. uncertainty(%)
110.0000	-1.042760	0.252434
130.0000	-1.822610	0.122984
150.0000	-2.027040	0.105675
170.0000	-2.116020	0.100975
190.0000	-2.600350	0.114496
210.0000	-3.015910	0.139167
230.0000	-2.948640	0.183839

$Q^2=0.4$

ω	$A_{T'}(\%)$	stat. uncertainty(%)
150.0	-1.574490	0.597719
170.0	-2.122460	0.202996
190.0	-2.481120	0.136140
210.0	-2.875170	0.122627
230.0	-3.229750	0.125304
250.0	-3.520590	0.140853
270.0	-4.067350	0.163936
290.0	-3.603550	0.265501

 $Q^2=0.5$

ω	$A_{T'}(\%)$	stat. uncertainty(%)
200.0	-2.489060	1.335240
220.0	-2.836430	0.245948
240.0	-3.450710	0.161918
260.0	-3.485600	0.141956
280.0	-4.107000	0.140032
300.0	-4.669120	0.152375
320.0	-5.127510	0.172977
340.0	-4.883820	0.270675

 $Q^2=0.6$

ω	$A_{T'}(\%)$	stat. uncertainty(%)
259.3750	-3.538010	1.322410
278.1250	-3.656840	0.382556
296.8750	-4.110020	0.269067
315.6250	-4.600920	0.240890
334.3750	-5.231400	0.238051
353.1250	-5.888730	0.253478
371.8750	-5.775230	0.278148
390.6250	-6.001840	0.414913

Table 5.2: $A_{T'}$ results for different energy transfer, ω

Sources	uncertainty $\frac{\delta A_{T'}}{A_{T'}} (\%)$
$P_t P_b$ (H-arm $Q^2=0.1$, E-arm $Q^2 =0.1, 0.2(0.193)$)	1.3
$P_t P_b$ (H-arm $Q^2=0.2$, E-arm $Q^2=0.3 - 0.6$)	1.7
empty target subtraction	0.4
N2 background subtraction	0.1
QE radiative correction	0.3
elastic radiative tail	0.3
acceptance	0.5
HC scintillator eff.	0.1
HC VDC efficiency	0.1
HC computer deadtime	0.1
HC beam current shift	0.1
HC beam motion	0.1
pion contamination	0.1
TOTAL	
(H-arm $Q^2=0.1$, E-arm $Q^2 =0.1, 0.2(0.193)$)	1.3
(H-arm $Q^2=0.2$, E-arm $Q^2=0.3 - 0.6$)	1.7

HC: Helicity-correlated

Table 5.3: Systematic errors in $A_{T'}$ measurement.

5.4 Extraction of the Neutron Magnetic Form Factor

As we mentioned before in Chapter 1, the ^3He quasi-elastic transverse asymmetry can be written as a function of the neutron magnetic form factor based on PWIA:

$$A_{T'}(G_m^n) = \frac{1 + aG_m^{n\ 2}}{b + cG_m^{n\ 2}}. \quad (5.1)$$

Here $|a| \gg 1$, and $b > c$ at low Q .

The ^3He quasi-elastic transverse asymmetry therefore can be expanded as a Taylor series around an expected G_m^n value - G_0 :

$$A_{T'}(G_m^n) = A_{T'}(G_0) + \frac{dA_{T'}}{dG_m^{n\ 2}}(G_0) \times (G_m^{n\ 2} - G_0^2) + O((G_m^{n\ 2} - G_0^2)^2) \quad (5.2)$$

In a particular G_m^n unit, for instance, the Höhler parameterization, G_0 can be chosen as 1. As a result, $A_{T'}(G_m^n)$ can be rewritten as:

$$A_{T'}(G_m^n) = A_{T'}(1) + \frac{dA_{T'}}{dG_m^{n\ 2}}(1) \times (G_m^{n\ 2} - 1) + O((G_m^{n\ 2} - 1)^2), \quad (5.3)$$

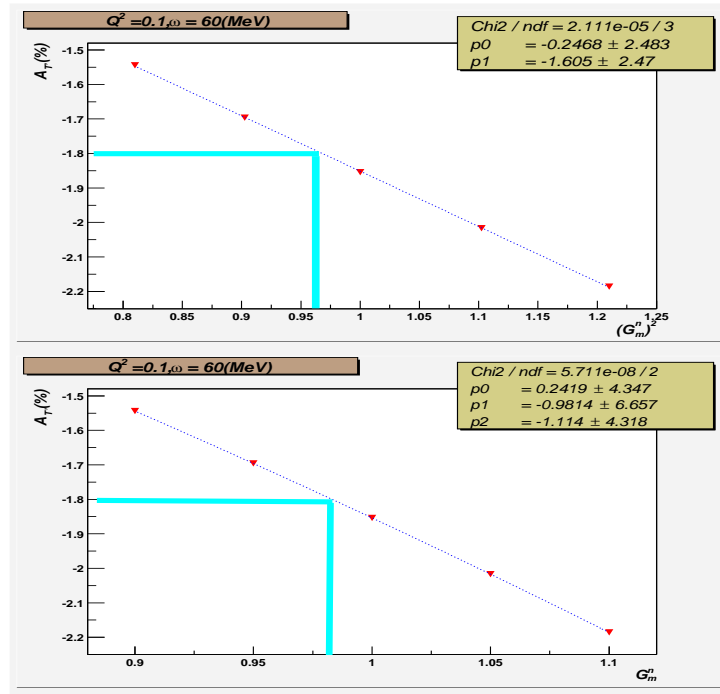
or

$$A_{T'}(G_m^n) = P_0 + P_1 G_m^{n\ 2}, \quad (5.4)$$

where $P_0 = A_{T'}(1) - \frac{dA_{T'}}{dG_m^{n\ 2}}(1)$, and $P_1 = \frac{dA_{T'}}{dG_m^{n\ 2}}(1)$.

From Equation 5.4, G_m^n can be simply expressed as a function of the $A_{T'}(G_m^n)$:

$$G_m^n = \sqrt{\frac{A_{T'}(G_m^n) - P_0}{P_1}} \quad (5.5)$$

Figure 5-2: The fitting process for P_0 and P_1

The expression of G_m^n in Eq. 5.5 indicates that G_m^n can be extracted from the measured ^3He quasi-elastic transverse asymmetry $A_{T'}$ if the theoretical calculation of P_0 and P_1 is practical. As a matter of fact, P_0 and P_1 can be calculated by fitting the G_m^n dependence of theoretical calculation of $A_{T'}(G_m^n)$. The upper panel of Fig 5-2 is an example of the fitting procedure displayed in Eq. 5.5. Following the same spirit, $A_{T'}(G_m^n)$ can also be generally expanded as:

$$A_{T'}(G_m^n) = P_0 + P_1 G_m^n + P_2 G_m^{n^2}, \quad (5.6)$$

where $P_0 = A_{T'}(1) - \frac{dA_{T'}}{dG_m^n}(1) + \frac{1}{2} \frac{d^2 A_{T'}}{d^2 G_m^n}(1)$, $P_1 = \frac{dA_{T'}}{dG_m^n}(1) - \frac{d^2 A_{T'}}{d^2 G_m^n}(1)$, and $P_2 = \frac{1}{2} \frac{d^2 A_{T'}}{d^2 G_m^n}(1)$.

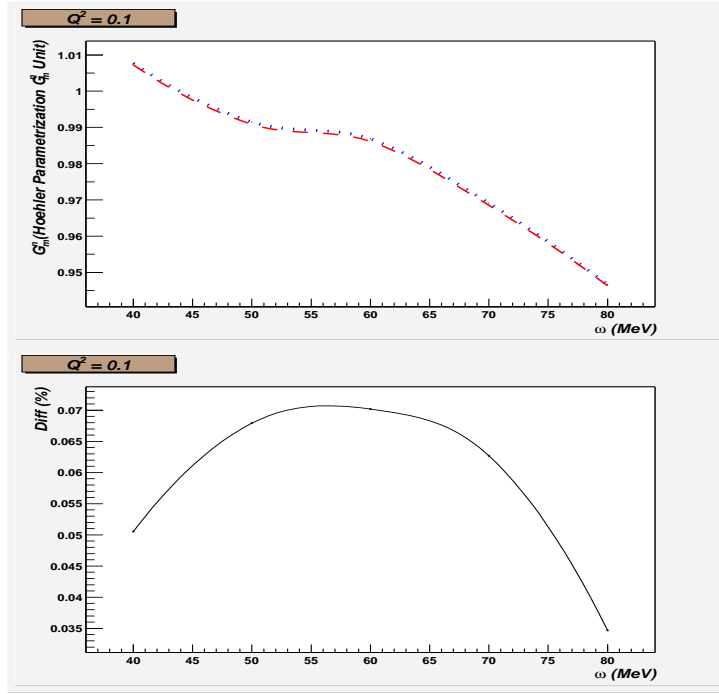


Figure 5-3: The extraction of G_m^n as a function of energy transfer ω . In the upper panel, the long-dashed line is the results from Eq. 5.5 and the dotted line is the results from Eq. 5.7. The difference between these two is plotted in the lower panel.

G_m^n is therefore given as:

$$G_m^n = \frac{-P_1 + \sqrt{P_1^2 - 4P_2(P_0 - A_{T'})}}{2 \times (P_0 - A_{T'})} \quad (5.7)$$

The corresponding fitting procedure using Eq. 5.7 is presented in the bottom panel of Fig 5-2. The extracted G_m^n results from these two methods are very close to each other. The comparison between these two is plotted in the upper panel of Fig. 5-3 and the difference of 0.1% shown in the bottom panel can be neglected. For all six Q^2 kinematics using either the full calculation or PWIA, the difference between these two methods is also found to be negligible. Therefore, $A_{T'}$ in the vicinity of the ${}^3\text{He}$ quasi-elastic peak, calculated from the full calculation or PWIA, is confirmed to be

a function of $(G_m^n)^2$, though the full calculation includes FSI and MEC.

P_0 and P_1 in Eq.5.5 extracted from different theoretic models for different Q^2 kinematics are listed In Tab. 5.4 and Tab. 5.5. Using P_0 and P_1 for different energy transfer (ω) bin, one can extract G_m^n and study the ω dependence of the extraction of G_m^n . In Fig. 5-3, The extracted G_m^n results for $Q^2 = 0.1 (GeV/c)^2$ is plotted as a function of energy transfer, ω .

The final $G_m^n(Q^2)$ results can be obtained by either extracting G_m^n from the weighted $A_{T'}$ of neighboring bins around the quasi-elastic peak, or taking the weighted average of the extracted G_m^n s, which are around the quasi-elastic peak. Before the G_m^n results are presented in terms of Q^2 , a few issues concerning the uncertainty of the extraction of G_m^n need to be further investigated. First, we discuss the ω dependence of the extraction of G_m^n . From a theoretically point of view, the G_m^n results depend on the Q^2 value only and the curve of the extracted G_m^n as a function of ω is supposed to be flat as shown in Fig.5-3, because Q^2 changes only a few percent due to the variation of ω . However, the curve in Fig. 5-3 are quite different from what we expect and it changes rapidly. Therefore, the two different ways to get $G_m^n(Q^2)$ and the uncertainty of energy transfer may contribute to the uncertainty of G_m^n . In fact, the uncertainty of G_m^n from two different procedures is found to be minimal. The uncertainty of G_m^n due to the uncertainty of energy transfer is estimated and is listed in Tab. 5.6. Secondly, how to categorize the uncertainty of G_m^n is discussed. The major sources of the uncertainty of G_m^n can be grouped as the statistical uncertainty, the systematic uncertainty, and the theoretical uncertainty. The first two uncertainties are mainly due to the uncertainty in $A_{T'}$ and the ω dependence of the extraction of G_m^n . The theoretical uncertainty of G_m^n can be estimated and categorized based on each piece of the input¹ and reaction mechanism included in the calculations. Due to the lack of a theoretical calculation including all the major input and nuclear reaction

¹Such as NN potential, nucleon form factor(proton), relativity.

mechanisms, the theoretical uncertainty of G_m^n is largest among all three uncertainties of G_m^n . The theoretical uncertainties of Golak's calculation at $Q^2 = 0.1 - 0.4 \text{ (GeV/c)}^2$, and the uncertainties of PWIA calculation at $Q^2 = 0.1 - 0.6 \text{ (GeV/c)}^2$ are listed in Table 5.6. Reliable extraction of G_m^n using Golak's calculation for Q^2 value above 0.3 (GeV/c)^2 is not possible, because the uncertainty of the relativistic effect in Golak's calculation becomes too large for $Q^2 > 0.3 \text{ (GeV/c)}^2$. Lastly, we will present the work related to final-state-interaction (FSI), meson-exchange-current (MEC), relativistic effect, and nucleon off-shell effect one-by-one in detail.

$$Q^2 = 0.1$$

$\omega(\text{MeV})$	$G_m^n(\text{Höhler})$	δG_m^n	P_1	P_0
40	0.941211	0.0380199	-1.40475	0.564369
50	0.985531	0.0252055	-1.52956	-0.0715907
60	0.992271	0.0221387	-1.60457	-0.246806
70	0.984745	0.0227149	-1.72149	-0.454699
80	0.967547	0.0253019	-1.84451	-0.651866

$$Q^2 = 0.2$$

$\omega(\text{MeV})$	G_m^n	δG_m^n	P_1	P_0
90	0.912083	0.0309718	-3.4886	-0.32956
100	0.974806	0.0236836	-3.41169	-0.348253
110	0.998004	0.0218621	-3.3748	-0.46933
120	0.947922	0.0228056	-3.41384	-0.718693
130	1.02279	0.0229946	-3.50893	-1.02013

$$Q^2 = 0.3$$

$\omega(\text{MeV})$	G_m^n	δG_m^n	P_1	P_0
130	0.874738	0.0293524	-2.39495	0.00992881
150	0.913938	0.0243736	-2.37195	-0.0457906
170	0.908758	0.0238018	-2.33413	-0.188397
190	0.94786	0.0253536	-2.38219	-0.460099
210	0.946367	0.0294092	-2.50014	-0.776762

$$Q^2 = 0.4$$

$\omega(\text{MeV})$	G_m^n	δG_m^n	P_1	P_0
210	0.942175	0.0204864	-3.17657	-0.0553468
230	0.976398	0.020654	-3.10673	-0.267935
250	0.982551	0.023034	-3.1118	-0.516439

Table 5.4: The G_m^n results for different ω bins extracted with full calculation by Golak *et al.*

$$Q^2 = 0.1$$

$\omega(\text{MeV})$	$G_m^n(\text{Höhler})$	δG_m^n	P_1	P_0
40	1.30121	0.0304171	-1.27009	1.47036
50	1.33588	0.0213616	-1.33147	0.818903
60	1.25247	0.0198896	-1.41497	0.392962
70	1.14159	0.0213729	-1.57822	-0.0673053
80	1.04187	0.0247508	-1.75107	-0.477829

$$Q^2 = 0.2$$

$\omega(\text{MeV})$	G_m^n	δG_m^n	P_1	P_0
90	1.17494	0.0253623	-3.30709	1.33371
100	1.16666	0.0208301	-3.24116	0.821328
110	1.12157	0.0198883	-3.30101	0.321746
120	1.00321	0.0210395	-3.49648	-0.267276
130	1.01211	0.0217802	-3.74369	-0.855941

$$Q^2 = 0.3$$

$\omega(\text{MeV})$	G_m^n	δG_m^n	P_1	P_0
130	1.10052	0.0235999	-2.36761	1.0449
150	1.07739	0.0216222	-2.26813	0.605751
170	0.997109	0.0219284	-2.30906	0.179707
190	0.915608	0.0247578	-2.52545	-0.483172
210	0.844858	0.0300783	-2.73822	-1.06141

$$Q^2 = 0.4$$

$\omega(\text{MeV})$	G_m^n	δG_m^n	P_1	P_0
190	1.00956	0.0210499	-3.20314	0.783533
210	1.0334	0.0191167	-3.10368	0.439268
230	0.985952	0.0198014	-3.2091	-0.110182
250	0.877533	0.0231903	-3.46071	-0.855617
270	0.842546	0.026414	-3.68313	-1.45276

$$Q^2 = 0.5$$

$\omega(\text{MeV})$	G_m^n	δG_m^n	P_1	P_0
240	1.01734	0.0195646	-4.06753	0.759064
260	0.996831	0.0181332	-3.92669	0.416244
280	1.00249	0.017521	-3.98617	-0.100922
300	0.945954	0.0190221	-4.23405	-0.880369
320	0.886108	0.021706	-4.49667	-1.59678

$$Q^2 = 0.6$$

$\omega(\text{MeV})$	G_m^n	δG_m^n	P_1	P_0
296.875	0.987237	0.0280953	-4.85037	0.617337
315.625	1.01866	0.0251349	-4.70415	0.280464
334.375	1.01784	0.0244747	-4.77797	-0.281447
353.125	1.00305	0.0254375	-4.96721	-0.891164
371.875	0.880874	0.0300281	-5.25781	-1.6955

Table 5.5: The G_m^n results for different ω bins extracted with PWIA calculation by Salmè *et al.*

Q²=0.1		
contribution	uncertainty	$\frac{\delta G_M^n}{G_M^n}(\%)$
Systematic:		
$A_{T'}$	1.3%	0.65
ω determination	± 3 MeV	0.3(full), 3.0(pwia)
total		0.71(full), 3.1(pwia)
Theoretical:		
NN Potential		0.45
G_E^p	0.5%	0.44
G_M^p	0.4%	0.21
G_E^n	100.0%	0.14
off-shell		-2.1 ~ -1.2(full), 0.5(pwia)
FSI		0.5(full), -27.8 ~ +0.5(pwia)
MEC		1.0(full), -4.4 ~ +1.0(pwia)
Three Body force		-0.7 ~ 0.0
Coulomb effect		1.0
Relativistic effect		0.5
total*		-2.32 ~ +1.32(full), -30.97 ~ -0.73(pwia)
Q²=0.2		
contribution	uncertainty	$\frac{\delta G_M^n}{G_M^n}(\%)$
Systematic:		
$A_{T'}$	1.3%	0.65
ω determination	± 3 MeV	0.6(full), 3.0(pwia)
total		0.88(full), 3.1(pwia)
Theoretical:		
NN Potential		0.4
G_E^p	0.83%	0.53
G_M^p	0.8%	0.35
G_E^n	100.0%	0.13
off-shell		-1.7 ~ -0.7(full), 0.5(pwia)
FSI		0.5(full), -11.2 ~ +0.5(pwia)
MEC		1.0(full), -3.45 ~ +1.0(pwia)
Three Body force		-1.0 ~ 0.0
Coulomb effect		1.0
Relativistic effect		-0.8 ~ +0.5(full), 0.5(pwia)
total*		-2.65 ~ +1.95(full), -15.38 ~ +0.58(pwia)

* Because of the dilution factor of empty target cell may be twice of the dilution factor of empty reference cell at Q² values of 0.1 and 0.2 (GeV/c)², we enlarge G_m^n by a factor of 1.5% for six Q² values

$Q^2=0.3$		
contribution	uncertainty	$\frac{\delta G_M^n}{G_M^n}(\%)$
Systematic:		
$A_{T'}$	1.7%	0.85
ω determination	± 3 MeV	1.3(full), 1.4(pwia)
total		1.55(full), 1.64(pwia)
Theoretical:		
NN Potential		0.5
G_E^p	1.0%	0.56
G_M^p	1.0%	0.52
G_E^n	100.0%	0.17
off-shell		-1.6 \sim -0.9(full), 0.5(pwia)
FSI		0.5(full), -4.5 \sim +0.5(pwia)
MEC		1.0(full), -1.8 \sim +1.0(pwia)
Three Body force		-1.1 \sim 0
Coulomb effect		1.0
Relativistic effect		-2.0 \sim +0.5(full), 0.5(pwia)
total*		-3.34 \sim +2.74(full), -5.44 \sim +2.55(pwia)
$Q^2=0.4$		
contribution	uncertainty	$\frac{\delta G_M^n}{G_M^n}(\%)$
Systematic:		
$A_{T'}$	1.7%	0.85
ω determination	± 3 MeV	0.45(full), 0.45(pwia)
total*		0.96(full), 0.96(pwia)
Theoretical:		
NN Potential		0.45
G_E^p	1.0%	0.46
G_M^p	1.0%	0.56
G_E^n	100.0%	0.08
off-shell		-1.4 \sim -0.6(full), 0.5(pwia)
FSI		0.5(full), -1.8 \sim +0.5(pwia)
MEC		1.0(full), -1.2 \sim +1.0(pwia)
Three Body force		-1.2 \sim 0.0
Coulomb effect		1.0
Relativistic effect		-1.5 \sim +0.5(full), 0.5(pwia)
total*		-3.12 \sim +1.92(full), -2.49 \sim +2.79(pwia)

Q²=0.5		
contribution	uncertainty	$\frac{\delta G_M^n}{G_M^n}(\%)$
Systematic:		
$A_{T'}$	1.7%	0.85
ω determination	± 3 MeV	0.15
total		0.86
Theoretical:		
NN Potential		0.4
G_E^p	1.0%	0.38
G_M^p	1.0%	0.6
G_E^n	100.0%	0.38
off-shell		0.5
FSI		-0.7 \sim +0.5
MEC		0.5
Three Body force		-1.3 \sim 0.0
Coulomb effect		1.0
Relativistic effect		0.5
total*		-1.26 \sim +2.78(pwia)
Q²=0.6		
contribution	uncertainty	$\frac{\delta G_M^n}{G_M^n}(\%)$
Systematic:		
$A_{T'}$	1.7%	0.85
ω determination	± 3 MeV	0.10
total		0.86
Theoretical:		
NN Potential		0.4
G_E^p	1.0%	0.32
G_M^p	1.0%	0.64
G_E^n	100.0%	0.69
off-shell		0.5
FSI		0.5
MEC		0.5
Three Body force		-1.3 \sim 0.0
Coulomb effect		1.0
Relativistic effect		0.5
total*		-1.40 \sim +3.10(pwia)

Table 5.6: The uncertainties in G_m^n for six Q^2 kinematic settings. The lower limit of uncertainty of on FSI and MEC effects of PWIA calculation is the difference between full calculation and PWIA calculation, and the upper limit is equals to the uncertainty of full calculation.

FSI & MEC

Although the plane wave impulse approximation (PWIA) describes the dominant physics reaction mechanism of the ${}^3\vec{H}e(\vec{e}, e')$ quasi-elastic scattering, it is not sufficient to satisfy the requirement of the high precision experiment - E95-001. There are two major effects which are ignored by PWIA calculation. The first effect is the final state interaction (FSI), which describes the interaction between the scattered nucleon and the remaining nucleons involved. Comparing the curves named “relativistic fsi”, which is the non-relativistic Faddeev calculation with FSI effects corrected by relativistic effects, with the curves named “relativistic pwia”², which is the pwia calculation, around the quasi elastic peak region in Fig 5-4, one can extract the FSI effect from Golak’s calculation for four different Q^2 settings. In general, the faster the scattered nucleon departs from the recoiling nucleus, the smaller is the FSI effect. Due to this very reason, the FSI effect on the ${}^3\text{He}$ quasi-elastic transverse asymmetry $A_{T'}$ decreases with increasing Q^2 . In Fig 5-6, we extrapolate the FSI effect on the ${}^3\text{He}$ quasi-elastic transverse asymmetry $A_{T'}$ for the last two Q^2 values (0.5, 0.6 (GeV/c)²). The results in Table 5.7 show that the uncertainty due to FSI in $A_{T'}$ becomes smaller as Q^2 value increases.

	$Q^2=0.1$	$Q^2=0.2$	$Q^2=0.3$
$\frac{A_{T'}^{fsi} - A_{T'}^{pwia}}{A_{T'}^{pwia}} (\%)$	55.67	22.40	9.01
	$Q^2=0.4$	$Q^2=0.5$	$Q^2=0.6$
$\frac{A_{T'}^{fsi} - A_{T'}^{pwia}}{A_{T'}^{pwia}} (\%)$	3.63	1.46*	0.59*

* extrapolated values

Table 5.7: Contribution due to FSI effects in $A_{T'}$.

²To distinguish non-relativistic pwia which we generate, the general pwia calculation is called relativistic pwia calculation

The other effect is the meson-exchange current (MEC) effect which is due to the interaction between the nucleons in the target nucleus. The meson exchange current (MEC) effect will give a correction of the hadronic current to a single nucleon current. In chapter 1, a few items of two body current of MEC and resonances have been shown in Fig. 1-7. Due to divergence issue on the hadronic current, Golak's calculation is not able to complete all six Q^2 settings but the first four low Q^2 settings. If the MEC effect on asymmetry changes randomly in terms of Q^2 , we can only estimate the MEC effect from Golak's calculation up to $Q^2=0.4$. However, based on the studies from Golak's calculation on the quasi-elastic ${}^3\vec{H}e(\vec{e}, e')$ process for the first four Q^2 values, the MEC effect on asymmetry around the quasi-elastic peak is found to exponentially decrease as Q^2 increases in Fig 5-5. This conclusion is also supported by the studies using the Arenhövel's calculation on the quasi-elastic $\vec{d}(\vec{e}, e')$ process [50] for six Q^2 values in Fig 5-7. In the impulsive picture, both MEC effects on asymmetry from the quasi-elastic $\vec{d}(\vec{e}, e')$ process, $((A_{T'}^{full} - A_{T'}^{fsi})(\vec{d}(\vec{e}, e')))$ and from the quasi-elastic ${}^3\vec{H}e(\vec{e}, e')$ process, $((A_{T'}^{full} - A_{T'}^{fsi})({}^3\vec{H}e(\vec{e}, e')))$ are in the same order of magnitude. For the last two Q^2 settings (0.5, 0.6 (GeV/c)²), we therefore estimate the MEC effects on ${}^3\text{He}$ quasi-elastic transverse asymmetry $A_{T'}$ around the quasi-elastic peak using $(A_{T'}^{full} - A_{T'}^{fsi})(\vec{d}(\vec{e}, e'))$, which are listed in Tab. 5.8

	$Q^2=0.1$	$Q^2=0.2$	$Q^2=0.3$
$\frac{A_{T'}^{full} - A_{T'}^{fsi}}{A_{T'}^{full}}({}^3\vec{H}e(\vec{e}, e'))(\%)$	8.8	6.9	3.6
$\frac{(A_{T'}^{full} - A_{T'}^{fsi})(\vec{d}(\vec{e}, e'))}{A_{T'}^{full}({}^3\vec{H}e(\vec{e}, e'))}(\%)$	13.9	5.8	1.8
	$Q^2=0.4$	$Q^2=0.5$	$Q^2=0.6$
$\frac{A_{T'}^{full} - A_{T'}^{fsi}}{A_{T'}^{full}}({}^3\vec{H}e(\vec{e}, e'))(\%)$	2.4		
$\frac{(A_{T'}^{full} - A_{T'}^{fsi})(\vec{d}(\vec{e}, e'))}{A_{T'}^{full}({}^3\vec{H}e(\vec{e}, e'))}(\%)$	1.6	0.9	0.5

Table 5.8: Contribution due to MEC effects in $A_{T'}$.

Relativistic Correction

The full calculation of Golak *et al.* in which the final state interaction (FSI) and the meson exchange current (MEC) are taken into account is non-relativistic. As Q^2 increases, the calculation becomes unreliable because of relativistic effects. As a result, the full calculation at $Q^2 = 0.1, 0.2 ((GeV/c)^2)$ only is considered to be accurate enough to be used to extract G_m^n with small theoretical uncertainty. In order to study the impact of the relativistic effect on the full calculation quantitatively, we have modified PWIA calculation from the relativistic framework to the non-relativistic framework in accordance with the non-relativistic framework of Golak's calculation. The changes due to relativistic effect on both the inclusive cross-section and the transverse asymmetry of ${}^3\vec{H}e(\vec{e}, e')$ have been studied. The main modifications consist of three parts. The first part is to change the relativistic kinematics into the non-relativistic kinematics; the second part is to modify the many-fold integration of the inclusive cross-section of ${}^3\vec{H}e(\vec{e}, e')$, based on the non-relativistic kinematics. Specifically the phase space of the integration and the integral ranges of the Fermi momentum and the missing mass are changed; the third part is to change the relativistic hadronic current into the non-relativistic hadronic current. The exact formulas of the non-relativistic current and the relativistic current we used have been studied and written in [111, 112]. In Fig. 5-8 and Fig. 5-9, the comparisons of both the inclusive cross-section and the transverse asymmetry $A_{T'}$ of the quasi-elastic scattering ${}^3\vec{H}e(\vec{e}, e')$ between the non-relativistic PWIA calculation and the relativistic calculation are shown. From the results, one can see that the non-relativistic results for the inclusive cross-section and the transverse asymmetry $A_{T'}$ are shifted by a certain energy transfer ω compared to those with relativistic effect. The magnitude of the ω shift is equal to the difference between the energy transfer calculated in the non-relativistic PWIA and that calculated in the relativistic PWIA. Therefore, the conclusion, which we make, is that among the three major changes which we discussed above, the mod-

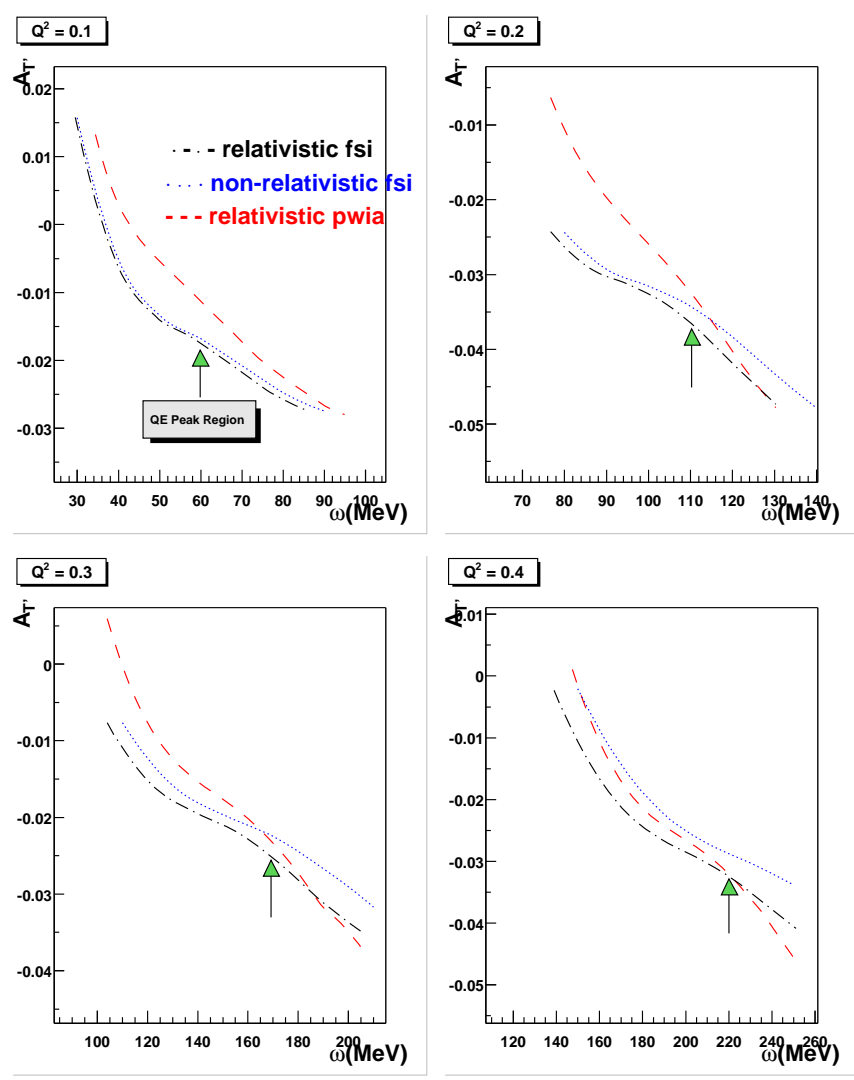


Figure 5-4: FSI effect study. The long dashed line is a relativistic pwiA calculation (to distinguish non-relativistic pwiA which we generate, the general pwiA calculation is called relativistic pwiA calculation), the dotted line is a non-relativistic Faddeev calculation with FSI effects, and the dot-dashed the non-relativistic Faddeev calculation with FSI effects corrected by relativistic effects. Comparing the long dashed line and dot-dashed line, one can find contributions due to FSI effects in A_T' .

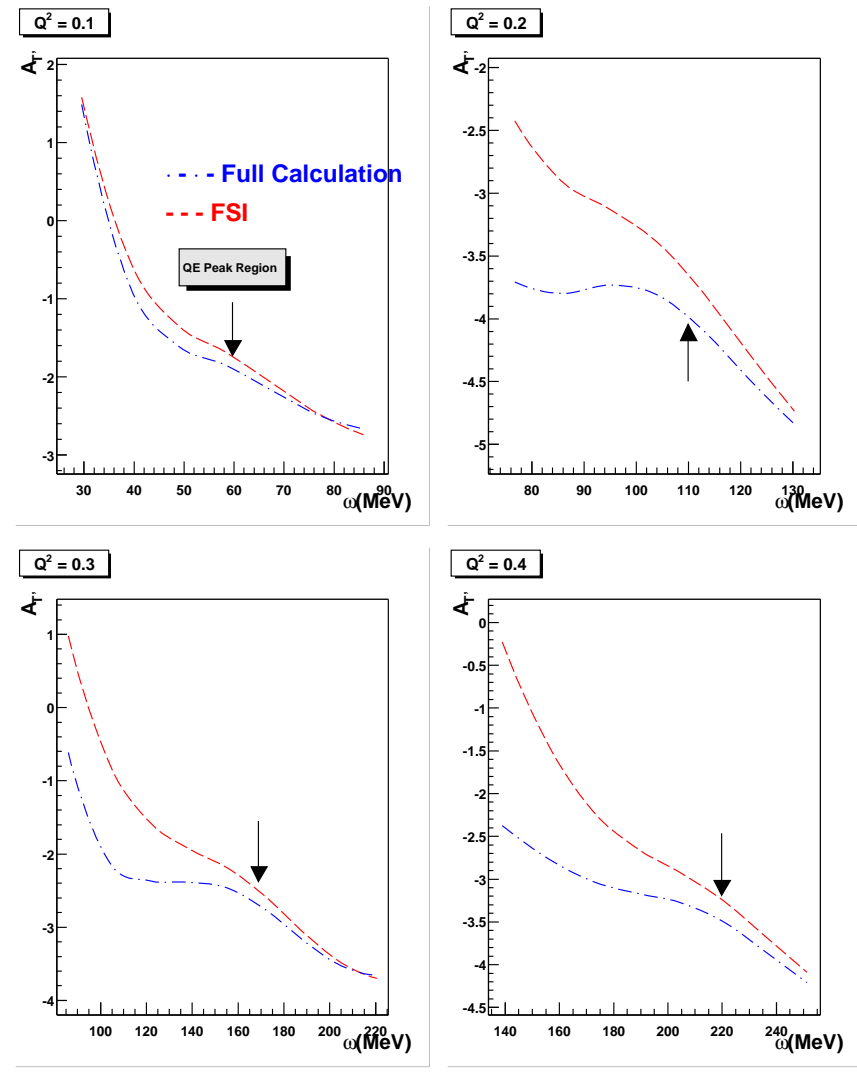


Figure 5-5: MEC effect study. Comparing the full calculation and the calculation with FSI effects, one can find contributions due to MEC effects in A_T' .

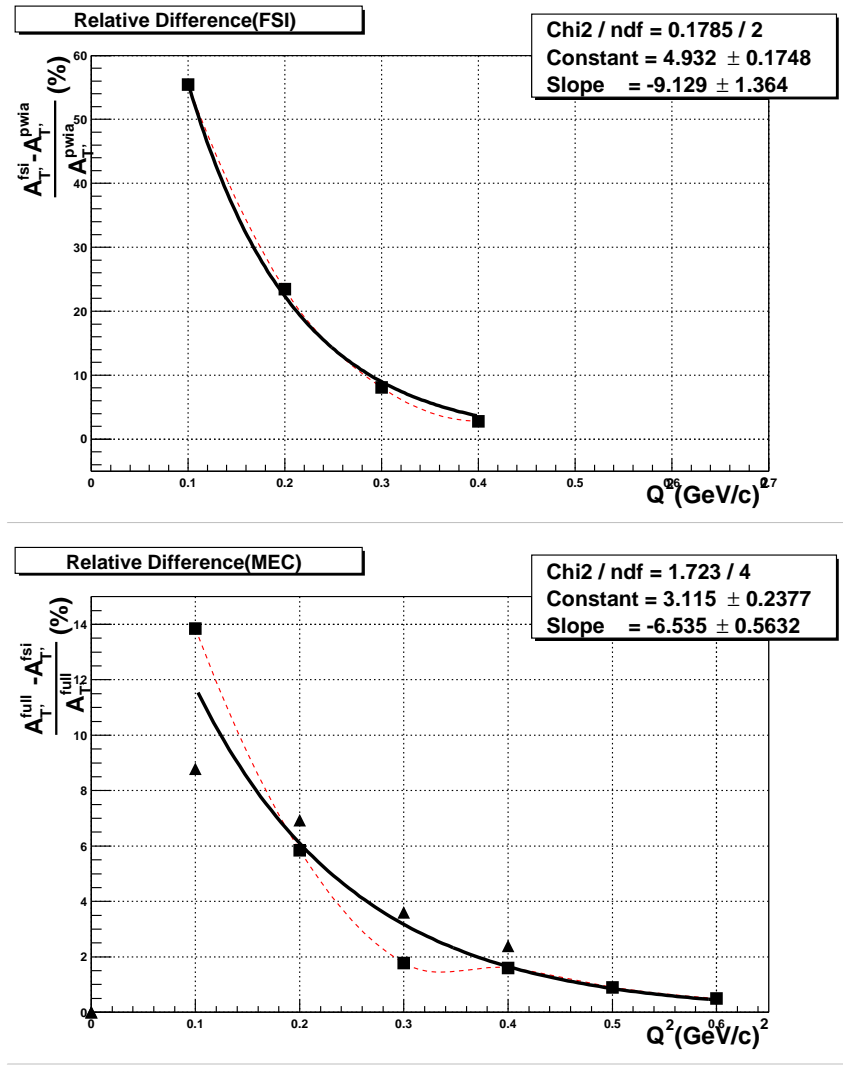


Figure 5-6: MEC and FSI effects on $A_{T'}$ for ${}^3\vec{H}e(\vec{\nu}, e')$. The upper graph is FSI effects and the lower one is MEC effects. For MEC effects, the solid triangle is from $\frac{A_{T'}^{full} - A_{T'}^{fsi}}{A_{T'}^{full}}({}^3\vec{H}e(\vec{\nu}, e'))(\%)$ (0.1 - 0.4 $(GeV/c)^2$) and the solid square is from $\frac{(A_{T'}^{full} - A_{T'}^{fsi})(\vec{d}(\vec{\nu}, e'))}{A_{T'}^{full}({}^3\vec{H}e(\vec{\nu}, e'))}(\%)$ (0.1 - 0.6 $(GeV/c)^2$).

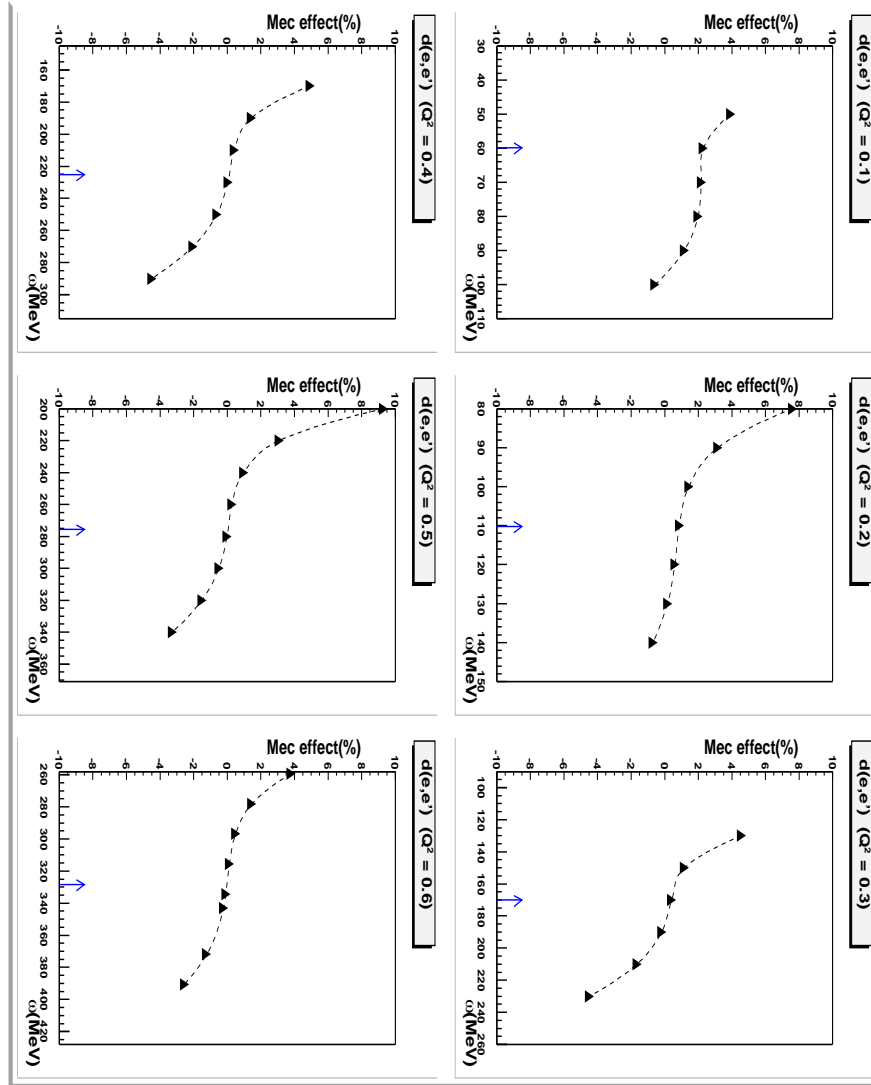


Figure 5-7: MEC effect on asymmetry for $\vec{d}(\vec{e}, e')$ process, $\frac{A_{T'}^{full} - A_{T'}^{fsi}}{A_{T'}^{full}}(\vec{d}(\vec{e}, e'))$ (%) calculated by Arenhövel *et al.* [50]. The arrow points the quasi-elastic peak position.

ification of the kinematics have a dominant effect on the inclusive cross-section and the transverse asymmetry $A_{T'}$.

Based on this study on relativistic effect, we developed a “recipe” [114] to correct for the non-relativistic results. The “recipe” includes to first-order an ω shift and to first-order a relativistic correction for non-relativistic hadronic current. In Fig. 5-9, the overall $A_{T'}$ results of “nr+relativistic correction” have a good agreement with those with relativistic effect. As Q^2 goes higher, the “recipe” (first-order correction) becomes less precise. As a result, the difference between these two results becomes large as Q^2 increases.

Non-relativistic and Relativistic approach (Paris potential)

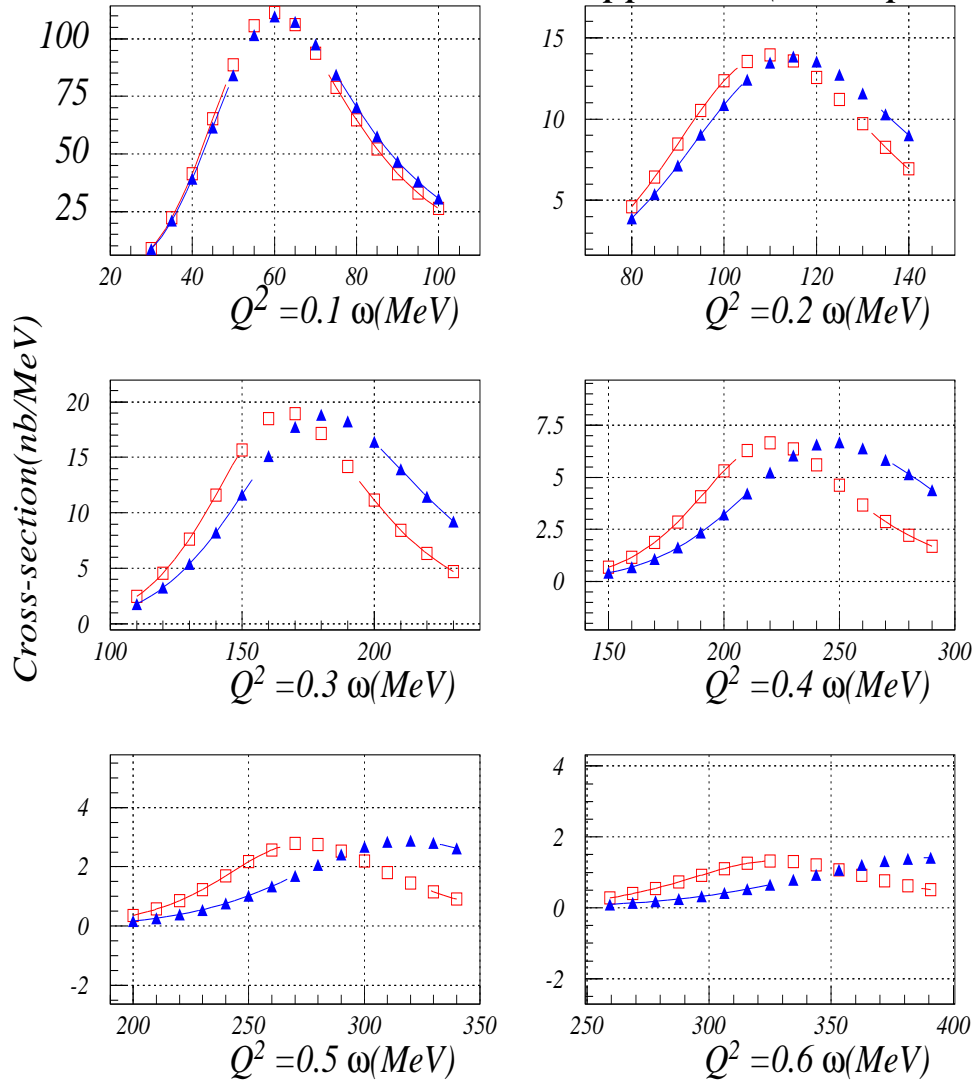


Figure 5-8: Relativistic effect on cross-section. The open square is a relativistic pwia calculation and the solid triangle is a non-relativistic pwia calculation which we developed.

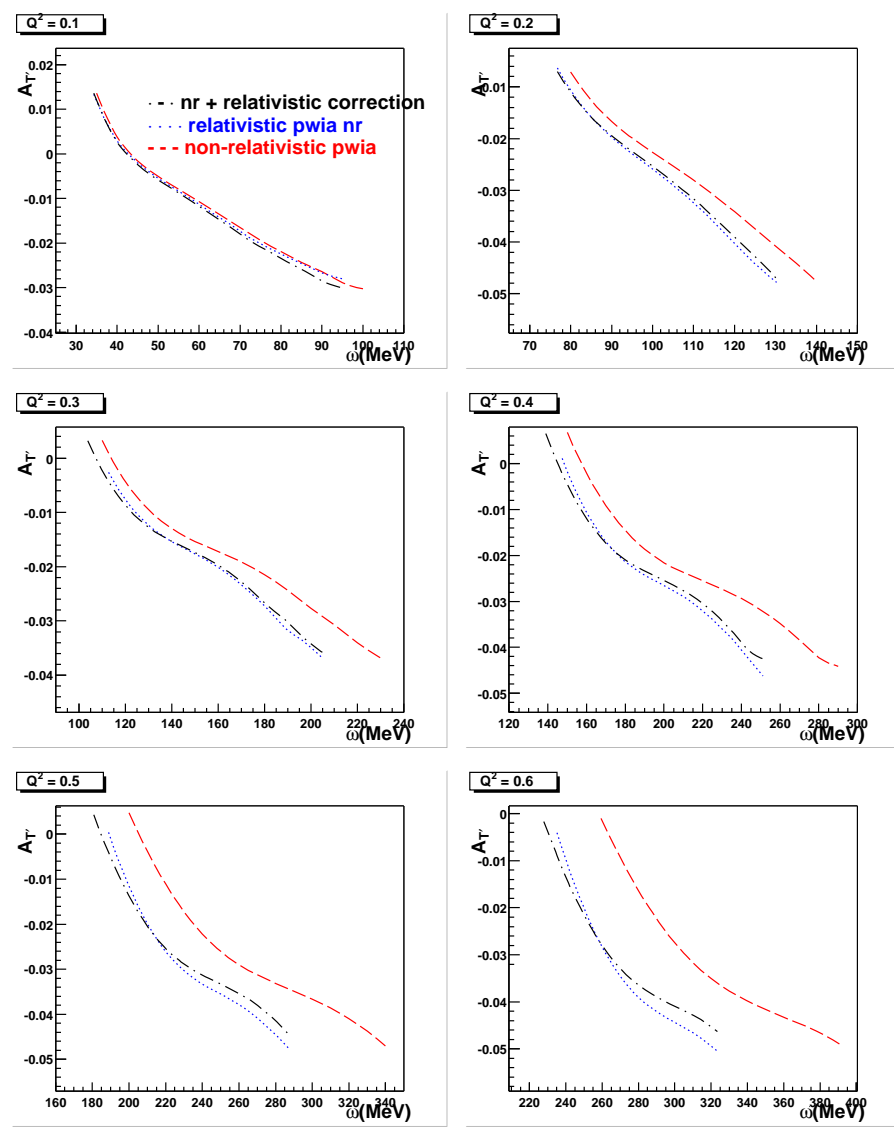


Figure 5-9: Relativistic effect on A_T . The long dashed line is a non-relativistic pwia calculation which we developed, the dot-dashed line is the non-relativistic pwia calculation with relativistic corrections, and the dotted line is a relativistic pwia calculation.

Offshell effect

Furthermore, there is no concept of the off-shell nucleon within the target nucleus in the non-relativistic framework. But in reality, the nucleon within the target nucleus may not always be a on-shell nucleon. The off-shell effect results in a discrepancy between the extracted neutron magnetic form factor G_m^n from the quasi elastic scattering ${}^3\vec{H}e(\vec{e}, e')$ through Golak's calculation or the PWIA calculation and the neutron magnetic form factor G_m^n of a free neutron. Due to the lack of the full knowledge of an off-shell nucleon, we develop a "on-shell" prescription [114] together with one of de Forest half-offshell prescriptions [35], such as cc1, cc2, ncc1 and ncc2 to study the changes of $A_{T'}$ and G_m^n caused by the off-shell effect. The PWIA calculation is chosen to be modified for studying the off-shell effect. The whole process to study the off-shell effect is to build a "on-shell" prescription based on one of de Forest's half off-shell prescriptions and to study the difference between these two prescriptions, which can be simply demonstrated as:

$$\sigma \sim \int \int Sp(P_m, \epsilon_m) \times (\sigma^{half-off}(P_m, \epsilon_m) \leftrightarrow \sigma^{on}(P_m)) dP_m d\epsilon_m, \quad (5.8)$$

where

P_m is Fermi momentum of a nucleon,

ϵ_m is the missing energy of the target nuclei, ${}^3\text{He}$,

$Sp(P_m, \epsilon_m)$ is the spectral function of ${}^3\text{He}$,

$\sigma^{half-off}(P_m, \epsilon_m)$ is the vertex of the virtual photon scattering on the off-shell nucleon as a function of the P_m and ϵ_m , and $\sigma^{on}(P_m)$ is the vertex of the virtual photon scattering on on-shell nucleon as a function of P_m only. Because for a on-shell nucleon, its energy and momentum are correlated, ϵ_m will be determined as P_m is known.

The results in Fig. 5-10, 5-11 and 5-12 (which are based on cc1 forms) shows that off-shell effect may have very little effect on the value of $A_{T'}$. The upper limit and

the lower limit for the off-shell effect in Tab. 5.6 are obtained from the $A_{T'}$ difference between the on-shell form and cc1 form, and from the $A_{T'}$ difference between the on-shell form and cc2 form respectively. Moreover, these results lead as a strong support for the accuracy of the value of the extracted G_m^n with Golak's calculation at low Q^2 settings.

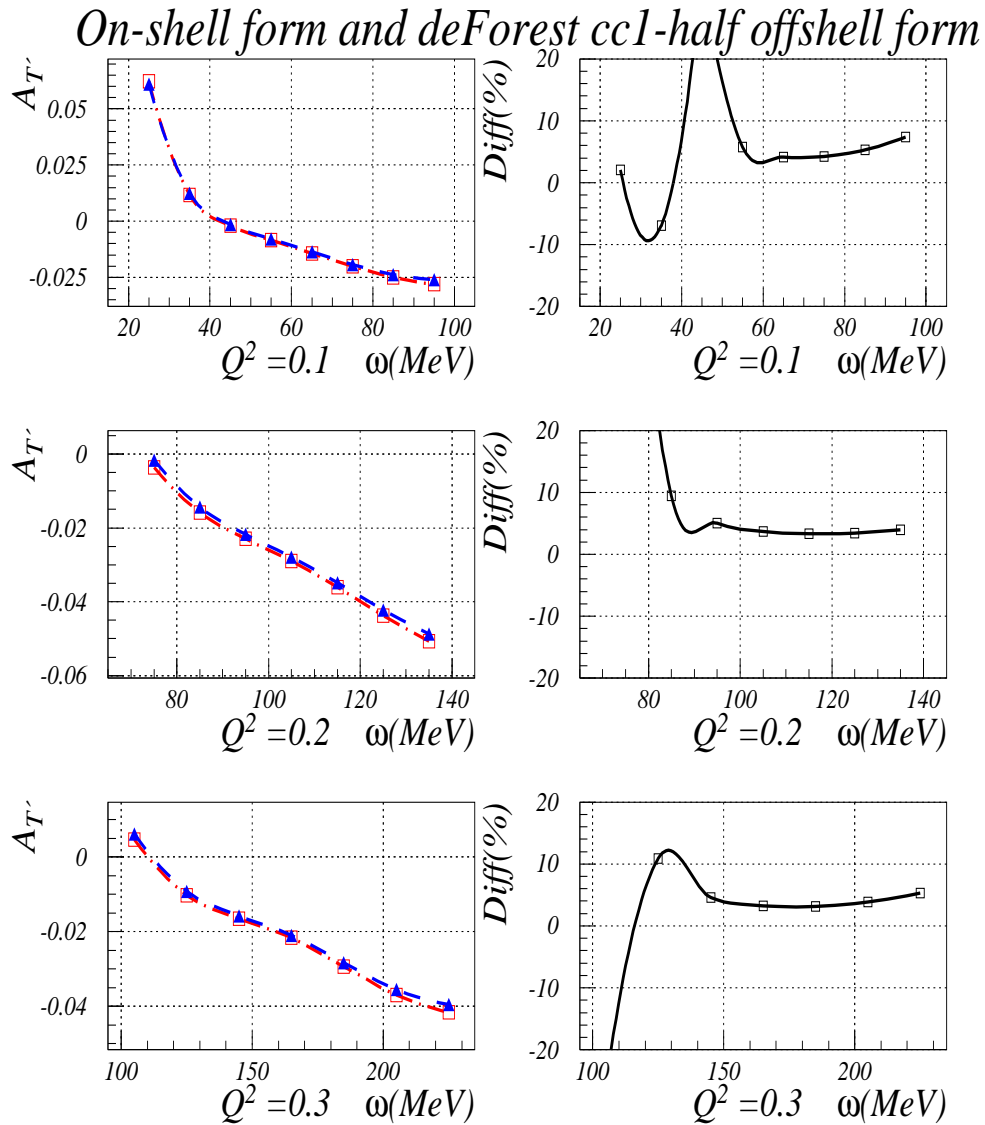


Figure 5-10: Off-shell effect on $A_{T'}(1)$. The open square is a PWIA calculation using *cc1* half-offshell form and the solid triangle is a PWIA calculation using on-shell form which we developed. Here $Diff.$ is the relative difference between two calculations, which is defined as the difference over the average.

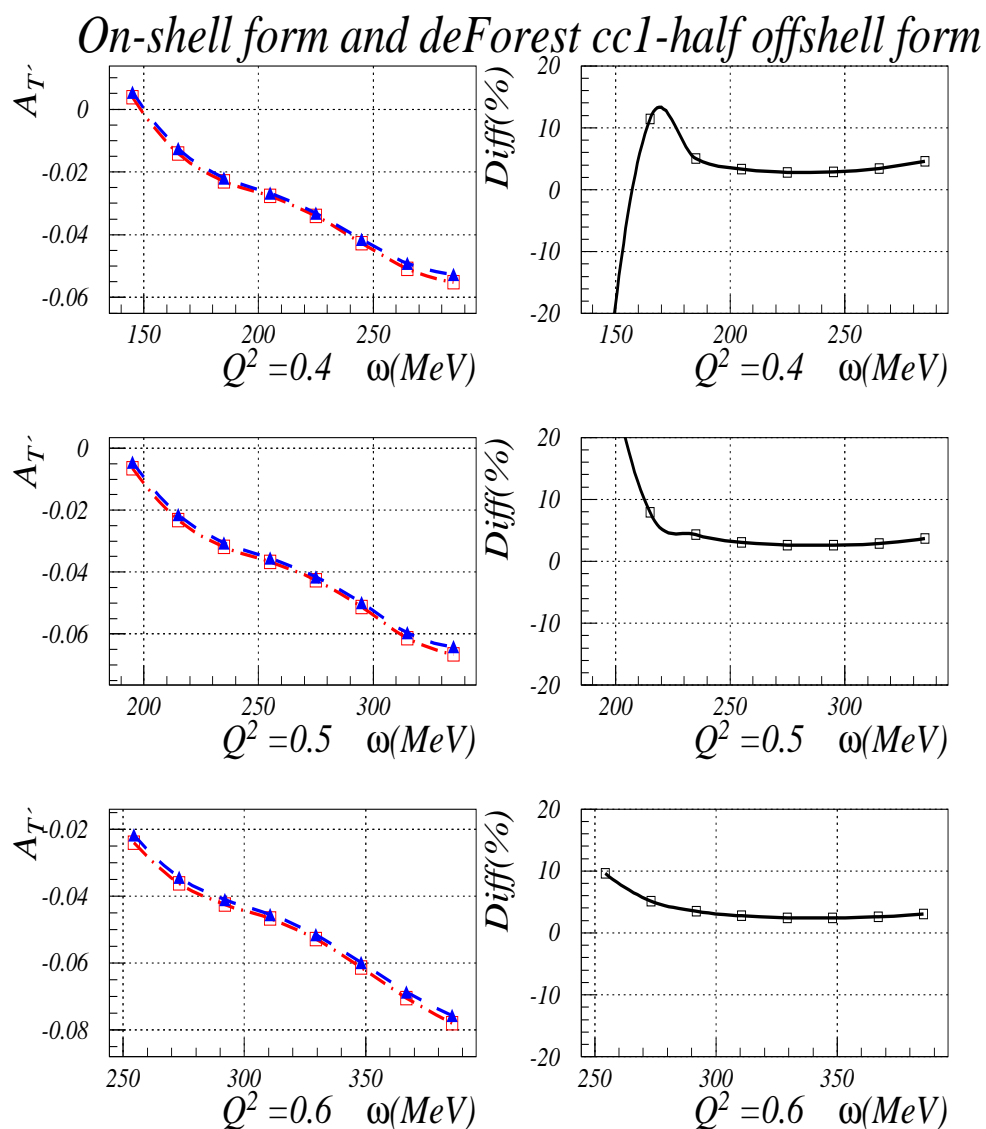


Figure 5-11: Off-shell effect on $A_{T'}'(2)$. The open square is a PWIA calculation using cc1 half-offshell form and the solid triangle is a PWIA calculation using on-shell form which we developed. Here $Diff.$ is the relative difference between two calculations, which is defined as the difference over the average.

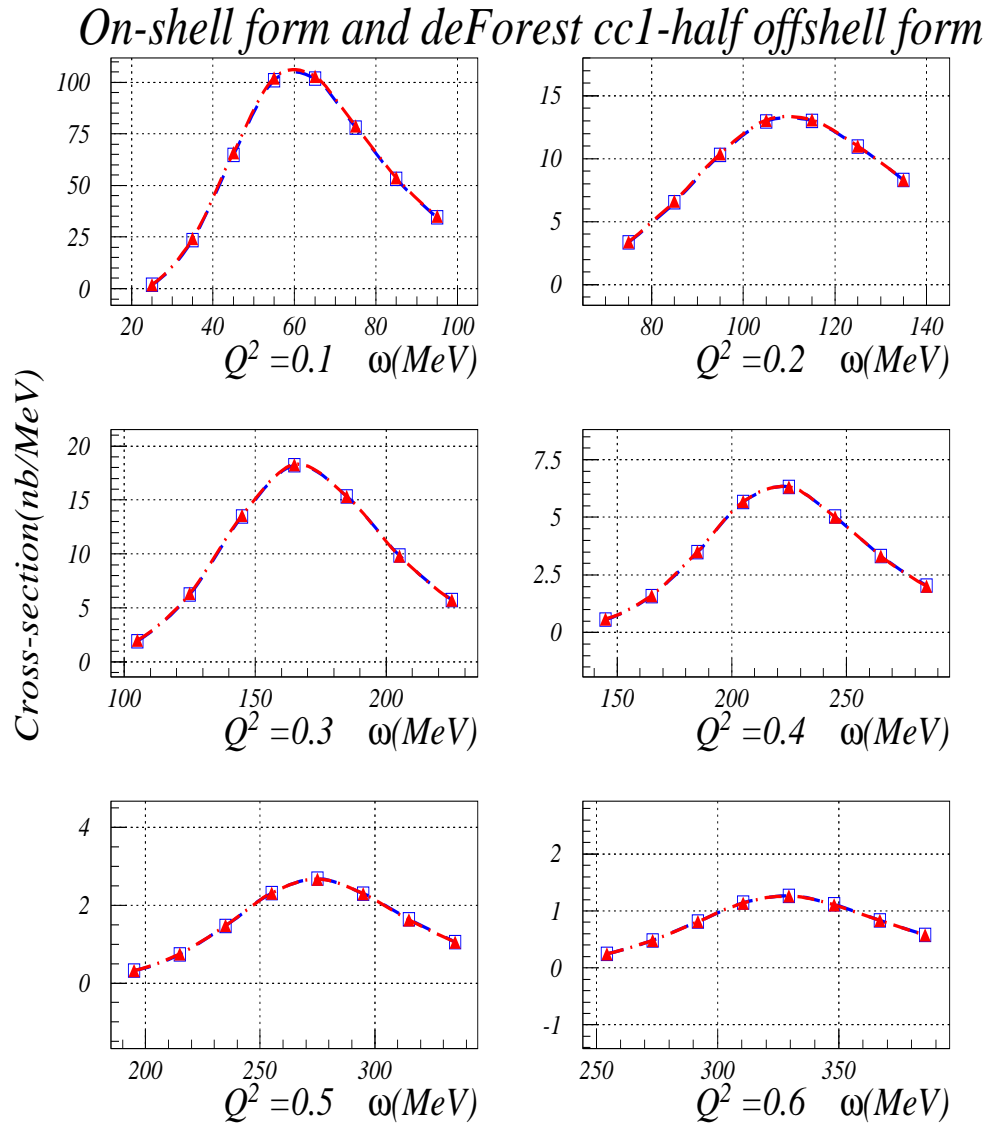


Figure 5-12: Off-shell effect on cross-section. The open square is a PWIA calculation using cc1 half-offshell form and the solid triangle is a PWIA calculation using on-shell form which we developed.

As noticed before, G_m^n is extracted through two calculations, PWIA calculation and Golak's full calculation. Both PWIA and Golak's full calculation have their own limitations. Golak's full calculation is reliable for the extraction of G_m^n at low Q^2 settings ($Q^2 = 0.1, Q^2 = 0.2$ (GeV/c)²), while PWIA is more reliable at high Q^2 settings ($Q^2 = 0.5, Q^2 = 0.6$ (GeV/c)²). The extracted G_m^n results using Golak's calculation are presented in the upper table of Tab. 5.9 at Q^2 values of 0.1 to 0.4 (GeV/c)², and the extracted G_m^n results using the PWIA calculation are presented in the lower table of Table 5.9 at Q^2 values of 0.1 to 0.6 (GeV/c)². Combining two independent groups of the extracted G_m^n results³, the extracted G_m^n results with the minimum theoretical uncertainty are plotted in Fig 5-13, which include two low Q^2 results from Golak's calculation and four high Q^2 results from PWIA calculation. In addition, the presented G_m^n results are the extracted G_m^n values at the quasi-elastic peak. The reasons are following: i) the theoretical uncertainty is the largest among all uncertainties, ii) the theoretical uncertainty is smallest at the quasi-elastic peak, and iii) thus the average value of the extracted G_m^n weighted total uncertainty is dominated by the G_m^n value at the quasi-elastic peak.

5.5 Discussion

The present data on G_m^n are shown in Figure 5-13 together with the recently determined data sets (later than 1990) and some recent calculations (shown in Figure 1-2 too). The measurements by Markowitz *et al.* and Bruins *et al.* are inconsistent with recent G_m^n results from ratio measurement at Mainz by Kubon and Anklin *et al.* and may be due to the lack of the corrections for neutrons that miss the neutron detector. This argument is possible supported by the extracted G_m^n at low Q^2 region from this experiment. In addition, the most recent G_m^n results from ratio mea-

³The extracted G_m^n results from calculation by Salmè *et al.* and from Golak's full calculation.

Overall PWIA Results

Q^2 (GeV/c) ²	G_m^n (Höhler)	Höhler/Dipole	G_m^n Dipole	stat. $\frac{\delta G_m^n}{G_m^n}$ %	sys. $\frac{\delta G_m^n}{G_m^n}$ %	theo. $\frac{\delta G_m^n}{G_m^n}$ %
0.1	1.252	0.9696	1.214	0.9869	3.1	-30.97/-0.73
0.193	1.122	0.9644	1.082	1.129	3.1	-15.38/+0.58
0.3	1.005	0.9675	0.9723	1.352	1.64	-5.44/+2.55
0.4	1.010	0.9742	0.9842	1.448	0.96	-2.49/+2.79
0.5	1.001	0.9824	0.9837	1.352	0.86	-1.26/+2.78
0.6	1.018	0.9912	1.009	1.547	0.86	-1.40/+3.10

Overall Full Calculation Results

Q^2 (GeV/c) ²	G_m^n (Höhler)	Höhler/Dipole	G_m^n Dipole	stat. $\frac{\delta G_m^n}{G_m^n}$ %	sys. $\frac{\delta G_m^n}{G_m^n}$ %	theo. $\frac{\delta G_m^n}{G_m^n}$ %
0.1	0.9927	0.9696	0.9625	1.359	0.71	-2.32/+1.32
0.1			0.966	1.4	1.0	
0.193	0.9980	0.9644	0.9656	1.348	0.88	-2.65/+1.95
0.193			0.962	1.3	1.0	
0.3	0.9088	0.9675	0.8793	1.527	1.55	-3.34/+2.74
0.4	0.9593	0.9742	0.9346	1.512	0.96	-3.12/+1.92

Table 5.9: The presented G_m^n results from PWIA calculation by Salmè *et al.* and full calculation by Golak *et al.* are the extracted G_m^n results at quasi-elastic peak. The bold numbers are the published G_m^n values from this experiment [58]. In addition, the extracted G_m^n results at Q^2 values of 0.3 and 0.4 (GeV/c)² from full calculation and PWIA calculation seem to suggest that FSI and MEC effects may be overestimated in full calculation at Q^2 values of 0.3 and 0.4 (GeV/c)².

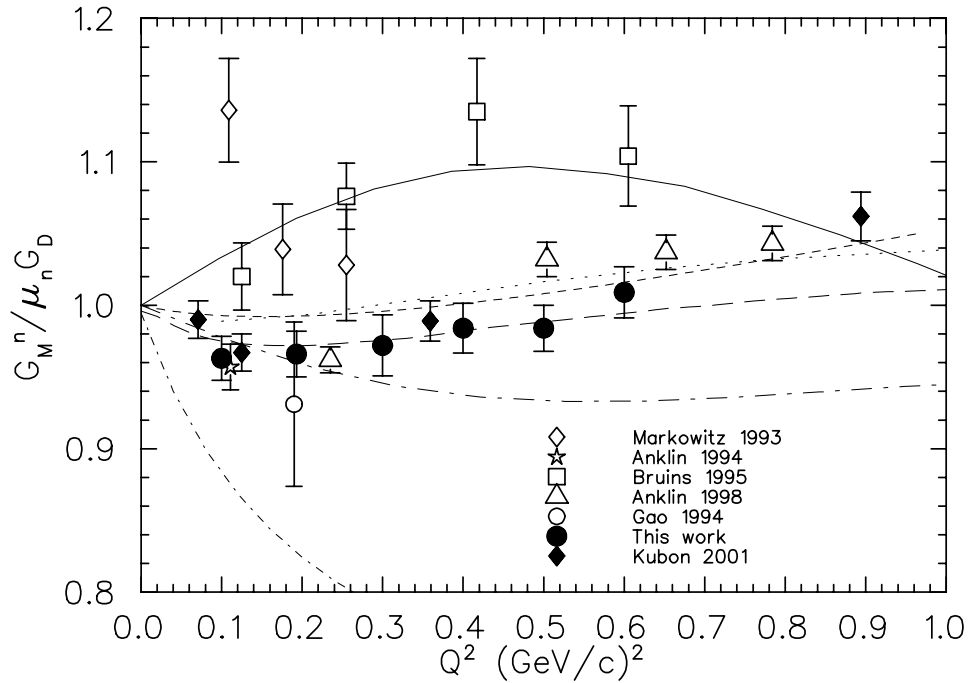


Figure 5-13: The word G_m^n data since 1990. The figure shows the results of the present measurement (● This work), the Bonn [55] (□), the MIT-Bates [39] [40] (○, ◇), the Mainz/PSI [57] [59] (△, ◆), and the NIKHEF/PSI [56] (☆), in comparison to various model calculations. Solid: Lu *et al.* [25], dot: Lomon [13], long dash: Mergell *et al.* [7], short dash: Holzwarth [24], long dash-dot: Kubis *et al.* [12], long dash-dot: Schlumpf *et al.* [17], and short dot-dash: Bo-Qian Ma [21].

surement at Mainz by Kubon and Anklin *et al.* [59] are shown in Figure 5-13. The agreement between the most recent deuterium measurements and ^3He measurements is very satisfactory within experimental uncertainties for Q^2 up to 0.6 (GeV/c)^2 . This small difference may be caused by the systematic uncertainty of the absolute neutron detection efficiency determination, the theoretical uncertainties due to FSI (mostly charge exchange scattering) for the deuterium measurement, or due to the theoretical uncertainties in PWIA calculation for the ^3He measurement.

As we mentioned before in Chapter 1, the model of calculations by Kubis *et al.* [12] (long dash) and by Lomon (dot) [13] are categorized as vector meson dominance

model (VDM), the model of calculation by Schlumpf *et al.* [17] (long dot-dash) is categorized as relativistic constituent quark model (RCQM), the model of calculation by Bo-Qian Ma *et al.* [21] (short dot-dash) is categorized as diquark model, the model of calculation by Lu *et al.* [25] (solid) is categorized as cloudy bag model (CBM) with a bag radius of 0.9 fm, and the model of calculation by Holzwarth *et al.* [24] (short dash) is categorized as Skyrme/soliton model. The soliton model calculation by Holzwarth *et al.* and the extended Gari-Kröumpelmann calculation by Lomon seem describe the proton form factor ratio well in Fig. 1-1. However, these calculations are larger than the G_m^n data at Q^2 values less than $0.4 (GeV/c)^2$, and fall into a gap between the G_m^n results from this work (\bullet) and the G_m^n results from Anklin *et al.* [56, 57] (\star, Δ) and Kubon *et al.* [59] (\blacklozenge) as Q^2 value goes higher than $0.4 (GeV/c)^2$. While exist many nucleon form factor calculations, none of model calculations is able to describe the proton and neutron form factors from both low Q^2 to higher Q^2 regions well at the same time.

Therefore, it is still early to make a final conclusion on G_m^n data. We note that a further investigation is clearly needed. In addition, all model calculations, except the lattice QCD calculation, are semi-phenomenological models. A lattice QCD calculation is based on the first principle QCD and thus is in principle most fundamental. However, the lattice QCD calculation is not in the stage to give precise results yet. In the future, a well developed lattice QCD calculation, I believe, will describe the precise proton and neutron data well and may finally explain the inconsistency between data and theoretical model calculations.

Chapter 6

Conclusion

We have precisely measured the transverse asymmetry, $A_{T'}$ from the quasi-elastic ${}^3\vec{H}e(\vec{e}, e')$ process and extracted the neutron magnetic form factor, G_m^n at Q^2 values of 0.1 to 0.6 $(GeV/c)^2$, because the transverse asymmetry $A_{T'}$ is very sensitive to the neutron magnetic form factor, G_m^n at the quasi-elastic kinematic region. At low Q^2 ($Q^2 < 0.3 (GeV/c)^2$), the extracted G_m^n results from the non-relativistic Feddeev calculation by Golak *et al.* agree with the G_m^n results from the most recent deuterium experiment well, and the total uncertainty of 2% in G_m^n from this experiment is comparable with those from the most recent deuterium experiment. As Q^2 is larger than 0.3 $(GeV/c)^2$ where the theoretical uncertainty in the extracted G_m^n results from PWIA calculation by Salmè *et al.* increases and is about 2-4%, the agreement between those two is still roughly within one σ . Here σ includes systematic and statistical uncertainties.

The uncertainties in G_m^n at Q^2 values of 0.3 and 0.4 $(GeV/C)^2$ from this work are dominated by the theoretical uncertainty. Therefore, a reliable theoretical calculation included relativity, FSI, and MEC effects is needed in order to precisely extract G_m^n from $A_{T'}$ at those Q^2 values, and thus this work is a challenge and an opportunity for a few-body physics theorist.

Bibliography

- [1] M. Jones *et al.*, Phys. Rev. Lett. **84**, 1398 (2000)
- [2] O. Gayou *et al.*, Phys.Rev.Lett. **88** (2002) 092301
- [3] F. Iachello *et al.*, Phys. Lett. **B43** (1973) 191
- [4] M. Gari and W. Krümpelmann, Z. Phys. **A322** (1985) 689
- [5] M. Gari and W. Krümpelmann, Phys. Lett. **B274** (1992) 159
- [6] G. höhler *et al.*, Nucl. Phys. **B114** (1976) 505
- [7] P. Mergell, U.-G. Meissner, D. Drechsel, Nucl. Phys. **A596**, 367 (1996)
- [8] H.W. Hammer *et al.*, Phys. Lett. **B385** (1996) 343
- [9] U.-G. Meissner, Phys. Rep. **161**, 213 (1988)
- [10] U.-G. Meissner, Nucl. Phys. **A623** (1997) 340c
- [11] U.-G. Meissner, Nucl. Phys. **A666&667** (2000) 51c
- [12] B. Kubis and U.-G. Meissner, Nucl. Phys. **A679**, 2001.
- [13] Earle L. Lomon nucl-th/0203081
- [14] P.L. Chung and F. Coester, Phys. Rev. **D44** (1991) 229

-
- [15] I.G. Aznauryan, Phys. Lett. **B316** (1993) 391
- [16] F. Schlumpf, Phys. Rev. **D44**, 229 (1993)
- [17] F. Schlumpf, J. Phys. **G20**, 237 (1994)
- [18] F. Cardarelli *et al.*, Phys. Lett. **B357**, 267(1995)
- [19] E. Pace *et al.*, Nucl. Phys. **A666&667**, 33c (2000)
- [20] F. Cardarelli and S. Simula J. Phys. Rev. **C62**, 065201-1 (2000)
- [21] Bo-Qiang Ma, Di Qing, Ivan Schmidt, Phys.Rev. **C65** (2002) 035205
- [22] G. Hellstern. R. Alkofer, M. Oettel, H. Reinhardt, Nucl.Phys. **A627** (1997) 679-709
- [23] T.H.R. Skyrme, Proc. Roy. Soc. Lon. **260** (1961) 127-138
- [24] G. Holzwarth, Z.Phys.**A356** (1996) 339-350, hep-ph/0201138
- [25] D.H. Lu, A.W. Thomas, A.G. Williams, Phys. Rev. **C57**, 2628 (1998)
- [26] D.H. Lu *et al.*, Nucl. Part. Phys. **26** (2000) L75
- [27] D.H. Lu *et al.*, Nucl. Phys. **A684**, 296 (2001)
- [28] Walter Wilcox, hep-lat/9608095
- [29] S.J. Dong, K.F. Liu, A.G. Williams, Phys. Rev. **D58**, 074504 (1998)
- [30] M. Göckeler, R. Horsley, D. Pleiter, P.E.L. Rakow, G. Schierholz, hep-ph/0108105
- [31] B. Blankleider and R.M. Woloshyn. Phys. Rev. **C29** (1984) 538
- [32] J.L. Friar *et al.* Phys. Rev. **C42** (1990) 2310

-
- [33] R.-W. Schulze and P.U. Sauer. Phys. Rev. **C48** (1993) 38
- [34] A.S. Raskin and T.W. Donnelly. Ann. Phys. **191** (1989) 78
- [35] J.A. Caballero, T.W. Donnelly and G.I. Poulis. Nucl. Phys. **A555** (1993)
- [36] C.E. Jones *et al.*, Phys. Rev. **C47**, 110(1993)
- [37] A.K. Thompson *et al.*, Phys. Rev. Lett. **68**, 2901 (1992)
- [38] M. Meyerhoff *et al.*, Phys. Lett. **B327**, 201 (1994)
- [39] H. Gao *et al.*, Phys. Rev. **C50**, R546 (1994); H. Gao, Nucl. Phys. **A631**, 170c (1998).
- [40] P. Markowitz *et al.*, Phys. Rev. **C48**, R5 (1993).
- [41] J. Golak *et al.* Phys. Rev. **C63**, R034006 (2001).
- [42] T. de Forest *et al.*, Nucl. Phys. **A392** (1983) 232
- [43] J.A. Callballero and T.W. Donnelly *et al.*, Nucl. Phys. **A555** (1993) 709
- [44] S. Ishikawa and J. Golak *et al.* Phys. Rev. **C57**, R39 (1998).
- [45] S. Ishikawa and H. Kamada *et al.* Phys. Lett. **B339** , (1994) 293.
- [46] A. Kievsky, E. Pace, G. Salmè and M. Viviani, Phys. Rev. **C56** (1997) 64-75
- [47] C. Ciofi degli Atti, E. Pace and G. Salmè, Phys.Rev. **C51** (1995) 1108-1119
- [48] A. Kievsky, M. Viviani and S. Rosati, Phys. Rev **C52** (1995) 15-19
- [49] W. Leidemann, E. L. Tomusiak and H. Arenhövel, Phys. Rev **C43** (1991) 1022
- [50] H. Arenhövel *et al.*, Few-Body Syst. **15**, 109 (1993)

-
- [51] L.D. Faddeev. Soviet Phys. JETP, **12**, (1961) 1014
- [52] J. Golak and H. Witala *et al.*, Phys. Rev. **C52** , (1995) 1216.
- [53] J. Golak and H. Kamada *et al.*, Phys. Rev. **C51** , (1995) 1638.
- [54] D.O. Riska, Phys. Scr. **31**, 471 (1985)
- [55] E.E. W. Bruins *et al.*, Phys. Rev. Lett. **75**, 21 (1995)
- [56] H. Anklin *et al.*, Phys. Lett. **B336**, 313 (1994)
- [57] H. Anklin *et al.*, Phys. Lett. **B428**, 248 (1998)
- [58] W. Xu, D. Dutta, F Xiong *et al.*, Phys. Rev. Lett. **85** (2000) 2900
- [59] G. Kubon, H. Anklin *et al.*, Phys. Lett. **B524**, 26 (2002)
- [60] J. Jourdan *et al.*, Phys. Rev. Lett. **79**, 5186 (1997)
- [61] J. Schwinger, Phys. Rev. **76** (1949) 790.
- [62] Y.S. Tsai *et al.*, Phys. Rev. **122** (1961) 1898
- [63] L.W. Mo and Y.S. Tsai *et al.*, Rev. Mod. Phys. **41** (1969) 205
- [64] L.C. Maximon and J.A.Tjon *et al.*, Phys.Rev. **C62** (2000) 054320
- [65] D.Yu. Bardin, N.M. Shumeiko Nucl. Phys. **B127** (1977) 242
- [66] I. Akushevich, N. Shumeiko, J.Phys. 1994. V. **G20**. P.513-521
- [67] I. Akushevich, A. Ilyichev, N. Shumeiko *et al.*, Comput. Phys. Commun. 1997.
V.104. P201-244
- [68] N.M. Shumeiko, Yad. Fiz. **29** (1979) 1571

-
- [69] I. Akushevich, A. Ilyichev, N. Shumeiko arXiv:hep-ph/0106180 v1 18 June 2001
- [70] T.V. Kuchto, N.M. Shumeiko, Nucl. Phys. **B219** (1983) 412-436
- [71] F. Xiong, D. Dutta, W. Xu *et al.*, Phys.Rev.Lett. **87** (2001) 242501
- [72] F. Xiong, thesis MIT(unpublished)
- [73] B. Mueller *et al.*, Phys. Rev. Lett. **78**, 3824 (1997)
- [74] K.A Aniol *et al.*, Phys. Rev. Lett. **82**, 1096 (1999)
- [75] V.L.Highland. Nucl. Inst. and Meth.,129-497,1975
- [76] V.L.Highland. Nucl. Inst. and Meth.,161-171,1979
- [77] G.R. lynch and O.I. Dahl technical Report LBL-28165
- [78] R.M. Sternheimer and R.F.Peirls *et al.*, Phys.Rev. **B3**, 3681, (1971)
- [79] A.Crispin and G.N Fowler, Rev. Mod. Phys. **42**, 290, (1970)
- [80] U. Fano, Ann. Rev. Nucl. Sci. **13**, 1, (1960)
- [81] K.R. Symon, Harvard University, Ph.D Thesis (1948)
- [82] A.T. Katramatou, SLAC NPAS-TN-86-8 (1986)
- [83] E.J Brash, R.D. Ransome, and C.W. de Jager, Status Report on Activities in Hall A, (1999)
- [84] R. Prepost and T. Maruyama, Annual Review of Nuclear Particle Science **45**, 41 (1995)
- [85] R. Alley *et al.*, Nucl. Instr. Meth. **A365**, 1 (1995)
- [86] A. Glamazdin, Fizika **B8**, 91 (1999)

-
- [87] K. Unser, IEEE Trans. Nucl. Sci. **16**, 934 (1969)
- [88] K. Unser, IEEE Trans. Nucl. Sci. **28**, 2334 (1981)
- [89] K.G. Fissum *et al.*, “Vertical Drift Chambers for the hall A high Resolution Spectrometers”, to be submitted to Nucl. Instrum. Meth. in 1999
- [90] C.Leathers B.S. Thesis MIT (1996)
- [91] R.H. Wechsler B.S. Thesis MIT (1996)
- [92] “Hall A experiment equipment operations manual”, ed. by S.Nanda(2000)
- [93] CODA User’s Manual
- [94] E. Offermann, ESPACE Manual.
- [95] MCEEP User’s Manual
- [96] http://www.cebaf.gov/accel/documents/epics_doc.html
- [97] L.D. Schearer F.D. Colegrove and G.K. Walters. Phys. Rev., **132**(6) (1963) 2561
- [98] Bouchiat *et al.* Phys. Rev., **82**(3) (1960) 373
- [99] M. Wagshul and T. Chupp, Physical Review, **A49**, 3854 (1994)
- [100] T. Killian, Physical Review **27**, 578 (1926)
- [101] T. Chupp *et al.*, Physical Review **C36**, 2244 (1987)
- [102] A. B.-A. Baranga *et al.*, Physical Review Letters **80**, 2801 (1998)
- [103] M.V. Romalis, Ph.D. thesis, Princeton University(1997)
- [104] O.N. Ozkul, Senior thesis, MIT (2000)

-
- [105] I. Kominis, Ph.D. thesis, Princeton University(2001)
- [106] J.S. Jensen, Ph.D. thesis Caltech (2000)
- [107] J.S. Jensen, “Cell Wall Thickness Measurements for E94-010 and E95-001” report, March 6, 2000 (Unpublished)
- [108] Alexandre Deur, Ph.D. thesis University Blaise Pascal (2000)
- [109] A. Abramgam, Principle of Nuclear magnetism, (Oxford University Press 1961)
- [110] G.D. Cates *et al.*, Phys. Rev. **A38**, 5092 (1988)
- [111] S. Jeschonnek and T.W. Donnelly, Phys. Rev. **C57**, 2438 (1998)
- [112] F. Ritz, H. öller, T. Wilbois, and H. Arenhövel, Phys. Rev. **C55**, 2214 (1997)
- [113] H. Gao, J.R. Calarco, H. Kolster, A proposal to the MIT-Bates PAC (2001)
- [114] private communication with T.W. Donnelly
- [115] private communication with Robert Michaels
- [116] private communication with Xiaodong Jiang
- [117] private communication with Liyanage Nilianga